Convection in high pressure ice layers of Saturn's and Jupiter's icy moons

Laëtitia Lebec

THESE de DOCTORAT DE
L'UNIVERSITE CLAUDE BERNARD LYON 1

Ecole Doctorale N° 52
Physique et Astrophysique de Lyon (PHAST)

Discipline : Planétologie

Soutenue publiquement le 11/09/2023, par :
Laëtitia LEBEC

Convection in high pressure ice layers of Saturn's and Jupiter's icy moons

---

Devant le jury composé de :

DAVAILLE, Anne	Dir. de recherche	CNRS/Univ. Paris-Saclay	Rapporteure
SOTIN, Christophe	Professeur	Nantes Univ.	Rapporteur
QUANTIN-NATAF, Cathy	Professeure	Univ. Claude Bernard Lyon1	Présidente
TOBIE, Gabriel	Dir. De recherche	CNRS/Nantes Univ.	Examinateur
LABROSSE, Stéphane	Professeur	ENS de Lyon	Directeur de thèse

ABSTRACT

In our planetary system, there are many planetary objects known as icy moons. Several of these moons home a subsurface liquid ocean mainly composed of water, which also classifies them as ocean worlds. Small icy moons, as Enceladus or Europa, are composed of an ocean between an icy surface and a rocky core, allowing strong interactions between liquid water and rocks, which make them interesting for the search for life in the solar system. However, on large icy moons as Ganymede or Titan, a layer of high-pressure (HP) ices may exist between the ocean and the rocky core due to the high pressure experienced by these moons composed of a very deep hydrosphere. At first glance, this layer prevents direct contact and exchanges of salts, and possibly nutrients, between the rocky core and the ocean. Therefore, the question is: are those exchanges possible and could they be efficient?

This PhD thesis focuses on several aspects not considered in the few previous studies carried out on this subject. The first one is the effect of the phase equilibrium at the interface between the high-pressure ice layer and the ocean. It can be modelled as a phase change boundary condition and drastically changes the dynamics, allowing a non-zero radial velocity at the top interface. We show that this boundary condition eases the convection and allows, under certain conditions for various planetary bodies, melt to form at the interface between the core and the high-pressure ice shell, which enhances the exchanges between the core and the ocean.

Secondly, we added salts into our model to study their effect on the overall dynamics. The few studies already existing on this topic focused only on pure water ice, while the oceans of these moons are likely to be composed of salty water. Part of these salts may come from the interactions with the core, hence the importance of studying the efficiency of these exchanges. By adding salts to our model, we show that there are two regimes for how the salts behave in the high-pressure ice layer, depending on how much they affect the ice density. We also show that efficient exchanges of salts can happen through the high-pressure ice shell and that, depending on the regime just mentioned, a significant amount of salts can reach the ocean. Finally, the results obtained by including salts from the core in the high-pressure ice layer highlighted the possible formation of a thin highly-salted basal ocean between the core and the ice, which we started to study in this PhD thesis.

RÉSUMÉ

Dans notre système solaire, les lunes glacées font partie des corps célestes qui intriguent le plus. En effet, certaines de ces lunes, nommées ainsi en raison de leur surface entièrement recouverte de glace, abriteraient un océan sous-glaciaire. Or, selon Cockell et al. [2016], l'existence d'un solvant comme l'eau liquide est essentielle à l'habitabilité d'un corps céleste. Ainsi, lorsqu'on parle de recherche de vie dans l'Univers, la présence d'eau liquide, même si elle n'est pas en surface, est un critère très important. Plusieurs indices tendent à prouver l'existence de cet océan sous-glaciaire, notamment les mesures de gravité pour Titan, effectuées par la mission Cassini-Huygens, ainsi que son très grand coefficient de marées k2 [Iess et al., 2012] qui implique des déformations internes importantes au cours de son orbite. Pour Ganymède, Saur et al. [2015] ont montré que la présence d'un océan sous-glaciaire pouvait être déduite en observant les oscillations des ovales auroraux, qui ne sont que de $2^\circ \pm 1.3$ pour Ganymède d'après les mesures effectuées par le télescope spatiale Hubble. D'après cette étude, ce degré d'oscillations correspond à l'existence d'un océan interne.

La présence de cet océan ne suffit cependant pas à caractériser ces lunes comme habitables. On s'intéresse également à la composition de leur partie rocheuse, que l'on nommera juste manteau dans ce résumé par soucis de simplicité. En ce qui concerne les lunes glacées de Jupiter et Saturne, d'après Tobie et al. [2014], leur accrétion serait arrivée tôt dans la vie du système solaire. Ces lunes ce seraient formées à partir du disque circumplanétaire de leurs planètes respectives, ce qui signifie qu'elles devraient posséder des éléments volatiles comme NH_3, CH_4 et CO_2 en abondances proto-solaires. Il est également admis, d'après Sotin et al. [2021], que la composition des roches formant leur manteau devrait être proche de celles de chondrites carbonées. Ainsi, ces lunes seraient composées d'une épaisse hydrosphère, d'un manteau riche en silicates et, si elles sont totalement différenciées comme cela est supposé être le cas pour Ganymède, d'un noyau riche en fer. Concernant la composition de leur océan, il est probable que celui de Titan contienne principalement des sels ioniques lourds tels que NaCl ou $MgSO_4$ [Sotin et al., 2021]. Pour Ganymède, les mesures spectrométriques effectuées par la mission Galileo [Soderlund et al., 2020] sont compatibles avec $MgSO_4$ comme principal sel océanique. Ces deux lunes glacées possèdent donc un océan sous-glaciaire composé d'eau salée. Ces sels peuvent venir de la différentiation de la lune, ou

bien provenir d'intéractions avec le manteau. Une exigence essentielle à l'habitabilité d'un corps planétaire est justement la capacité de son manteau à échanger des minéraux et des sels avec l'océan. Sur les petites lunes glacées comme Encelade et Europe, dont l'hydrosphère n'est pas assez épaisse pour que la pression dépasse les 200 MPa [Soderlund et al., 2020], la structure interne est composée d'un océan contenu entre une couche de glace Ih à la surface et un manteau rocheux. Cela permet des intéractions très fortes entre le manteau et l'océan, ce qui est favorable à l'habitabilité de ces lunes. En revanche, sur les grandes lunes glacées comme Ganymède et Titan, l'hydrosphère est très épaisse et la pression à l'interface avec le manteau est de $1500 - 1\ 700$ MPa pour Ganymède et de $650 - 850$ MPa pour Titan [Soderlund et al., 2020], ce qui est suffisamment élevé pour justifier l'existence d'une couche de glace de haute pression entre l'océan et le manteau. À première vue, cette couche de glace, dont l'épaisseur encore mal contrainte est estimée à plusieurs centaines de kilomètres, empêche un contact direct entre le manteau et l'océan, ce qui a longtemps été vu comme un obstacle à l'habitabilité de ces grandes lunes glacées [Noack et al., 2016]. Cependant, les échanges sont-ils réellement impossible à travers cette couche de glace de haute pression ? Les intéractions entre le manteau et l'océan dans le cas de ces lunes sont contrôlées par l'efficacité des transferts de chaleur et de masse. La chaleur peut être transportée à travers la couche de glace de haute pression soit par conduction, qui est un processus plutôt inefficace, ou par convection. La capacité à convecter de cette couche de glace dépend du nombre de Rayleigh, qui mesure l'importance des forces motrices par rapport aux forces résistantes. Si le nombre de Rayleigh est inférieur à une valeur critique, qui dépend des conditions aux limites, les transferts de chaleur à travers la couche de glace de haute pression ne se font que par conduction.

L'objectif de cette thèse est de prolonger le travail effectué par Choblet et al. [2017], Kalousová et al. [2018], Kalousová and Sotin [2018, 2020] sur les transferts de chaleur et de masse à travers une couche de glace de haute pression en étudiant les effets de paramètres non considérés dans ces études. Dans le chapitre 2, on étudie les effets du changement de phase à l'interface entre la couche de glace de haute pression et l'océan. Cette étude est réalisé en ne considérant que la convection à l'état solide à travers une couche de glace de haute pression composée d'eau pure. Dans un second temps, on ajoute des sels dans la glace et/ou dans l'océan pour étudier leurs effets sur la dynamique (chapitre 3), mais toujours en ne considérant que la convection à l'état solide. En effet, aucune exploration complète des effets des sels sur l'efficacité des transferts de chaleur et de masse à travers une couche de glace de haute pression à l'intérieur des grandes lunes glacées n'a encore été réalisé. Les résultats du chapitre 3 nous ont également poussés à nous intéresser à la possibilité de l'existence d'un océan très salé entre la couche de glace de haute pression et le manteau ainsi qu'aux potentielles implications pour l'efficacité des transferts de chaleur et de masse à travers cette couche de glace. Cette thèse a pour objectif de répondre à plusieurs questions:

- Les transferts de masse à travers une couche de glace de haute pression sont-ils possibles et quelle est leur efficacité ?
- Comment le changement de phase à l'interface entre la couche de glace de haute pression et l'océan impacte-il l'efficacité des transferts de chaleur et de masse à travers

cette couche de glace ?

- Comment un flux de sels provenant du manteau impacte-il l'efficacité des transferts de masse et la dynamique en général ? Ces sels peuvent-ils être efficacement transportés du manteau vers l'océan ?

- Comment l'existence d'un mince océan d'eau très salée entre le manteau et la couche de glace de haute pression affecte-elle la dynamique et l'efficacité des transferts de masse ?

- Finalement, l'existence d'une couche de glace de haute pression entre le manteau et l'océan dans les grandes lunes glacées et exoplanètes océan est-elle un réel obstacle à l'habitabilité de ces objets ?

Dans le chapitre 2, on étudie les effets sur la dynamique du changement de phase à l'interface entre la glace de haute pression et l'océan dans les grandes lunes glacées ou les exoplanètes océan. Cet effet mécanique peut être modélisé comme une condition aux limites de changement de phase. Cette condition implique une vitesse radiale non nulle à travers l'interface, ce qui augmente significativement l'efficacité des transferts de masse à travers la couche de glace de haute pression. L'objectif de ce chapitre est de montrer comment les transferts de chaleur et de masse sont affectés par ce changement de phase. En raison des contraintes visqueuses qui s'appliquent dans le solide, une topographie se forme à l'interface entre la glace et l'océan. Si l'équilibre thermique est vérifié à l'interface, la température devrait être égale à la température de fusion tout au long de celle-ci. Puisqu'elle est soumise à des variations topographiques, cela signifie qu'à une même profondeur la température est latéralement variable. La convection dans l'océan agit contre ces variations en effaçant les reliefs positifs par fusion, ce qui permet à la glace contenue dans les panaches chauds ascendants de fondre dans l'océan, et les reliefs négatifs par cristallisation de l'eau liquide, qui s'accrète à la glace. La compétition entre le temps nécessaire pour effacer la topographie et le temps nécessaire pour la former contrôle l'efficacité du changement de phase à l'interface. Ce ratio est noté Φ et nommé "paramètre de changement de phase". Cette condition aux limites a déjà été étudiée par Deguen [2013], Deguen et al. [2013], Labrosse et al. [2018], Morison [2020], Agrusta et al. [2020] dans le contexte de la Terre et des océans de magma et change drastiquement la convection dans une couche solide et les caractéristiques qui en résultent à amplitude finie.

Afin de quantifier les transferts de chaleur et de masse, on modélise une couche de glace de haute pression comme une coquille sphérique bidimensionnelle avec la condition aux limites correspondante au changement de phase qu'on veut étudier. On considère également un flux imposé en bas, plutôt qu'une température comme dans les études précédentes réalisées dans le contexte de la Terre. On réalise une analyse systématique de l'espace des paramètres contrôlé par le nombre de Rayleigh Ra_q et le paramètre de changement de phase Φ. Dans cette étude on ne considère que la convection à l'état solide dans une couche de glace composée d'eau pure, afin d'observer uniquement les effets du changement de phase. Cependant, nous avons tout de même calculé en post-traitement la fraction d'eau liquide qu'on pourrait attendre si

on traitait cet aspect. Premièrement, les résultats de cette étude confirment ceux obtenus précédemment sur les effets d'un changement de phase solide-liquide dans le contexte de la Terre. Le nombre de Rayleigh critique permettant le démarrage de la convection diminue avec le paramètre de changement de phase alors que la longueur d'onde correspondant au mode le plus instable augmente. Le nombre de Rayleigh attendu pour une couche de glace de haute pression dans les grandes lunes glacées comme Ganymède et Titan, ainsi que dans les exoplanètes océans, devrait être extrêmement supercritique. Pour ce régime, nous avons obtenus des lois d'échelles mettant en relation la vitesse radiale en haut de la couche de glace et la température en bas avec les paramètres de contrôle du système. En effet, ces deux variables de sorties évoluent en suivant une loi de puissance en $Ra_q^{1/2}$ (resp. $Ra_q^{1/2}$) pour la vitesse radiale et $Ra_q^{1/5}$ (resp. $Ra_q^{1/4}$) pour le nombre de Nusselt, sachant que $Nu = qd/(k\Delta T)$ (avec q le flux de chaleur provenant du manteau, d l'épaisseur de la couche de glace de haute pression et k la conductivité thermique), pour une condition rigide (resp. libre) en bas.

Ces lois d'échelles ont été appliquées à Ganymède ainsi qu'à une hypothétique exoplanète océan, en choisissant les valeurs pour l'épaisseur de la couche de glace, sa viscosité ainsi que le flux de chaleur provenant du manteau dans une fourchette raisonnable pour ces objets (voir tableau. 2.2), bien qu'assez large étant donné que ces paramètres sont encore mal contraints. Pour les deux objets, considérant un changement de phase efficace, nous avons trouvé une valeur d'environ 50 cm yr^{-1} pour la moyenne quadratique de la vitesse radiale à travers l'interface avec l'océan. Une vitesse de cet ordre de grandeur indique un transfert de masse qui devrait être plutôt efficace entre la glace et l'océan et les sels entrant dans la glace depuis le manteau (non considérés dans cette étude) devraient être facilement transportés jusqu'à l'océan. Inversement, si l'océan est déjà salé au départ, l'efficacité du transfert de masse entre la glace et l'océan devrait rapidement conduire à un équilibre chimique entre les deux couches [Bolrão et al., 2021].

A partir de la loi d'échelle entre les nombres de Nusselt et de Rayleigh, nous avons calculé la température en bas de la couche de glace de haute pression, en fonction des mêmes paramètres que pour les applications numériques du paragraphe précédent. En utilisant des valeurs de références choisies dans la gamme de valeurs pertinente pour Ganymède et pour l'hypothétique planète océan (voir § 2.4.3) on trouve une température en bas proche de la température de fusion pour les deux objets. C'est à dire que, dans ces conditions, on peut s'attendre à minima à la présence de poches d'eau liquide le long de l'interface avec le manteau, ce qui impliquerait une condition aux limites mixte (entre rigide et libre) à l'interface. La présence d'eau liquide à l'interface avec le manteau implique également des intéractions eau/roche importantes, ce qui est un critère important pour l'habitabilité de ces planètes océans.

Ces intéractions avec le manteau permettent l'enrichissement en sels de l'eau formée par la fusion de la glace de haute pression à l'interface. Si cette eau salée est moins dense que la glace pure, elle va remonter le long de la couche de glace de haute pression. Elle peut alors rester liquide tout le long de la montée et atteindre l'océan directement par convection à l'état liquide dans les panaches chaud ascendants, ou bien recristalliser en chemin, ce qui

devrait enrichir la couche de glace en sels et former un solide, probablement un assemblage polycristallin de glace d'eau salée et de sels hydratés. Dans ce cas, les sels pourraient atteindre l'océan par convection à l'état solide, si la densité de la mixture formée par la glace et les sels n'entrave pas la convection. Cet effet est mesuré par le nombre de flottabilité, c'est à dire le rapport entre l'augmentation de la densité due à l'enrichissement de la glace en sels et la diminution de la densité due à l'augmentation de la température associée à la présence de ces sels.

Dans le chapitre 3, on ajoute donc des sels dans la glace et/ou dans l'océan afin d'étudier leur effet sur la dynamique et l'efficacité des transferts de masse. Comme expliqué au dessus, la glace peut être enrichie en sels de deux façons: soit par des intéractions avec le manteau, soit par des échanges avec l'océan dans le cas où il serait déjà composé d'eau salée. Nous avons modélisé une couche de glace de haute pression comme une coquille sphérique bidimensionnelle entre un manteau rocheux et un océan de composition considérée comme homogène, afin d'étudier ces deux cas de figures. Les sels sont représentés par des traceurs lagrangiens afin de modéliser leur déplacement à travers la couche de glace de haute pression. On conserve également la condition de changement de phase à l'interface avec l'océan, ce qui permet aux sels de se dissoudre dans l'eau là où les panaches chauds ascendants atteignent l'océan, ainsi qu'un flux de chaleur fixe provenant du manteau. Notre modèle prend également en compte le flux de sels entrant dans la couche de glace depuis l'océan lors de sa recristallisation. La quantité de sels piégés dans ce processus dépend du coefficient de partage K des sels entre la glace de haute pression et l'océan à l'interface haute. Ce paramètre est bien connu pour la plupart des sels entre la glace Ih et l'eau, mais très peu d'études expérimentales ont été menées sur sa valeur entre les glaces de haute pression et l'eau. Seul le coefficient de partage pour NaCl a été mesuré par [Journaux et al., 2017]. D'après cette étude, il serait de 5×10^{-3} pour la glace VI et d'environ 0.12 pour la glace VII. Dans notre étude, afin d'isoler l'effet des sels, nous avons considéré uniquement la convection à l'état solide, comme précédemment.

Tout d'abord, nous avons considéré le cas d'un système fermé composé d'un océan d'eau salée et d'une couche de glace de haute pression pure afin d'étudier son évolution. Ce cas de figure a été étudié par Bolrão et al. [2021] dans le contexte des océans de magma. Le système fini dans tous les cas par atteindre un état stationnaire. Pour ce qui peut être considéré comme de faibles valeurs du nombre de flottabilité, qui dépend du coefficient de partage K (voir eq. 3.8), le système atteint un état d'équilibre chimique.

Nous avons également étudié le cas d'un flux de sels en provenance du manteau, avec une hydrosphère (glace HP et océan) initialement composée d'eau pure. Ce flux de sels provenant du manteau est modélisé par l'ajout d'une concentration de sels légèrement audessus de l'interface entre le manteau et la glace, ce qui correspond à ce qui se passerait si l'eau enrichie en sels à l'interface avec le manteau remontait le long de la couche de glace avant de recristalliser à une certaine hauteur, qui dépend du type de sels et du solidus. Nous avons effectué une exploration systématique de l'espace des paramètres, contrôlé par le paramètre changement de phase Φ, le nombre de Rayleigh Ra_q, le nombre de flottabilité B_{salts} et le coefficient de partage K. On observe deux régimes très distincts en fonction de la valeur du nombre de flottabilité. Pour de faibles valeurs de B_{salts}, les sels n'ont pas, ou

très peu, d'effet sur la densité de la glace et sont facilement transportés par convection à travers la couche de glace. Ainsi, tous les sels entrant dans la couche de glace depuis le manteau dans le cas de ce régime à faible B_{salts} atteignent l'océan. Pour de fortes valeurs de B_{salts}, au contraire, les sels augmentent fortement la densité de la glace et s'accumulent en bas de la couche de glace de haute pression. Il en découle une stratification de la convection plus ou moins à la hauteur à laquelle ont été ajoutés les sels dans la couche de glace. Cette hauteur simule celle de la recristallisation de l'eau salée, comme expliqué plus haut. Nous avons également obtenus des lois d'échelles pour la température en bas et la vitesse radiale en haut en fonction du nombre de Rayleigh, ainsi que pour le rapport f^o entre le flux de sels à travers l'interface avec l'océan et celui venant du manteau en fonction du nombre de flottabilité. Il est intéressant de noter que la vitesse radiale suit une loi de puissance en $Ra_q^{1/2}$, comme c'est le cas pour la convection dans la glace pure (voir chapitre 2) et n'est que faiblement affectée par la concentration en sels dans la couche de glace de haute pression. En ce qui concerne le nombre de Nusselt, $Nu = qd/(k\Delta T)$, il suit une loi de puissance en $Ra_q^{1/5}$ et la température en bas augmente avec le nombre de flottabilité. Quant au rapport de flux f^o, il suit une loi de puissance en B_{salts}^{-1}.

On applique les lois d'échelles obtenues au cas de Ganymède, pour des valeurs de référence choisies dans la fourchette raisonnable pour cette lune (voir tableau. 3.4). Les valeurs choisies pour cette étude sont différentes de celles choisies pour l'application numérique à Ganymède du chapitre 2, qui étaient très conservatrices, mais les lois d'échelles obtenues sont cohérentes entre les deux chapitres. Ainsi, nous avons obtenus une vitesse radiale à l'interface avec l'océan de $\sim$ 3 m yr^{-1} en moyenne pour une épaisseur de glace de d = 450 km et de $\sim$ 1.3 m yr^{-1} en moyenne pour une épaisseur de glace de d = 200 km, ce qui peut se traduire par un transfert de masse efficace à travers l'interface. Ainsi, tous les sels qui atteignent l'interface devraient se dissoudre facilement dans l'océan. Concernant le flux de sels à travers l'interface avec l'océan, il est difficile de conclure sans connaitre la composition exacte du manteau ainsi que le flux de sels entrant depuis celui-ci, mais une première approximation pour une large gamme du nombre de flottabilité nous a permis d'obtenir un flux d'environ 10^{-6}m yr^{-1}.

Finalement, si la température à l'interface entre le manteau et la glace de haute pression atteint la température de fusion, tous les sels qui seraient venus enrichir l'océan dans le cas d'une petite lune glacée avec un manteau rocheux en contact direct avec l'océan se retrouveraient dans la glace de haute pression dans notre cas. A partir de là, deux scénarios sont possibles. Soit le flux de sels provenant du manteau est faible, ce qui signifie que l'effet sur la densité de la glace de la petite quantité de sels entrant est faible également. Dans ce cas, les sels devraient être transportés facilement à travers la couche de glace et tous les sels entrant depuis le manteau devraient atteindre l'océan, exactement comme ce serait le cas sur de petites lunes glacées, comme Encelade ou Europe, qui ne possèdent pas de couche de glace de haute pression. Dans le second cas de figure, pour un flux de sels très fort provenant du manteau, les sels vont drastiquement augmenter la densité de la glace, ce qui nous place dans le second régime pour un nombre de flottabilité élevé. Dans ce cas, les sels s'accumulent à la base de la couche de glace de haute pression et la couche convective du haut est prob-

ablement pauvre en sels. Cependant, la convection dans cette couche convective supérieure n'est aucunement entravée par la présence de ces sels et tous les sels entrant dans cette couche sont transportés à travers la glace et atteignent l'océan. Finalement, seule une petite partie des sels entrant depuis le manteau atteignent l'océan, mais sachant que le flux entrant est bien plus fort dans ce cas-ci, cette petite quantité est probablement comparable à celle entrant dans la glace et atteignant l'océan dans le cas d'un faible flux de sels. Au final, pour conclure sur cette question, cela exigerait une meilleure connaissance de ces lunes et de leur composition.

En outre, pour de fortes valeur du nombre de flottabilité, les sels qui s'accumulent en bas de la couche de glace entraînent une diminution de la température de fusion, ce qui pourrait mener à la formation d'un mince océan très salé entre le manteau et la couche de glace de haute pression. Si cette couche est moins dense que la glace de haute pression, l'eau salée va s'infiltrer dans la glace et remonter jusqu'à recristalliser, ou bien rester liquide jusqu'à atteindre l'océan. Cependant, si elle est plus dense que la glace, cette couche d'eau salée pourrait former un océan stable entre le manteau et la couche de glace de haute pression. Sa densité dépendrait de la composition du manteau de ces lunes ainsi que de la solubilité dans l'eau à haute pression des sels en question. Bien que très peu de données existent à ce sujet, une étude de Journaux et al. [2013] nous informe que la concentration de NaCl dans l'eau à haute pression à partir de laquelle ce mélange devient plus dense que la glace VI est de 146 g $kg^{-1}_{H_2O}$, c'est à dire environ 15%. Afin d'analyser les effets sur la dynamique de cet océan stable entre le manteau et la couche de glace de haute pression, on étudie un système fermé composé d'une couche de glace de haute pression modélisée comme une coquille sphérique bidimensionnelle entre deux océans. Dans ce cas de figure, on considère deux conditions aux limites de changement de phase, une en haut et une en bas de la couche de glace.

Comme nous l'avons déjà observé dans le chapitre 3, ce système fermé tend vers un état stationnaire, et même vers un état d'équilibre chimique pour de faibles valeurs du nombre de flottabilité. Pour de faibles valeurs du nombre de flottabilité et ramené à un même nombre de Rayleigh, ce système à trois couches dont deux océans tend vers cet équilibre 180 fois plus rapidement que le système à deux couches du chapitre 3. Les deux régimes observés dans le chapitre 3 sont également identifiables dans le cas de ce système à trois couches. Cependant, là où la vitesse radiale en haut dépendait très peu du nombre de flottabilité dans le cas d'un système à deux couches, dans le cas présent elle est de l'ordre de 600 fois supérieure pour les faibles nombres de flottabilité. Dans le cas du second régime pour les forts nombres de flottabilité, les sels s'accumulent en bas de la couche de glace et font barrière au changement de phase, on se retrouve alors dans un cas comparable à celui du chapitre 3, sans condition aux limites de changement de phase en bas de la couche de glace de haute pression.

La question qui se pose cependant avec ce second océan est sa faisabilité, qui dépend principalement de la composition du manteau après la différentiation de ces objets. Bien qu'on manque de données à ce sujet, le fort ratio eau/roche de ces lunes, en raison de leur épaisse hydrosphère, laisse à penser que lors de la différentiation une grande partie des éléments chimiques capables de former des sels par intéraction avec de l'eau liquide ont été piégés

dans l'hydrosphère, ce qui n'est pas en faveur de la formation de cette océan, qui nécessite une très forte accumulation de sels à l'interface entre le manteau et la couche de glace de haute pression. Cependant, plusieurs études [Castillo-Rogez et al., 2022, Reynard and Sotin, 2023] indiquent d'autres processus internes au manteau de ces lunes qui pourraient augmenter la salinité de l'océan. Tout ceci est discuté en § 4.3.

L'objectif de cette thèse est de contribuer à l'amélioration des modèles concernant la dynamique dans les couches de glaces de haute pression et de caractériser les intéractions eau/roche essentielles à la détermination de l'habitabilité des lunes glacées et des exoplanètes océans. Il n'existe que très peu d'études sur la question à l'heure actuelle et contribuer à l'amélioration de nos connaissances au sujet de l'activité interne et de l'habitabilité de ces lunes est donc essentiel. Ces études pourront également être utilisées dans le futur afin de déterminer l'habitabilité des exoplanètes océans. En outre, cette thèse s'inscrit dans la lignée des quelques études déjà existantes sur le sujet et se focalise sur plusieurs aspects importants non considérés jusqu'alors afin de répondre aux questions posées au début de ce résumé.

D'après les résultats obtenus tout au long de cette thèse et ceux des quelques études préexistantes sur le sujet, des échanges efficaces sont possibles entre le manteau et l'océan malgré la présence de cette couche de glace de haute pression. Ces échanges se font par convection, soit uniquement à l'état solide, soit à l'état liquide (qui n'a pas été traitée pendant cette thèse) pendant une partie, ou bien la totalité, de la remontée. Par conséquent, l'existence de cette couche de glace de haute pression n'est pas un réel obstacle à l'habitabilité des grandes lunes glacées, comme Ganymède ou Titan, et des exoplanètes océans. Cependant, ce critère seul n'est bien entendu pas suffisant pour conclure à l'habitabilité de ces corps. Si les échanges entre le manteau et l'océan peuvent être efficaces sous certaines conditions, conclure à ce sujet nécessite plus d'informations sur la structure interne des objets étudiés afin de mieux contraindre les modèles ainsi que sur la composition de leur manteau, afin d'estimer la quantité de sels qu'on pourrait s'attendre à voir transportée depuis le manteau vers l'océan. Ces connaissances pourraient être fournies par de futures missions spatiales autour de ces lunes.

Malgré les nombreux aspects couverts pendant ces trois années, cette thèse ne répond évidemment pas à toutes les questions sur ce vaste sujet. Premièrement, l'étude présentée dans le chapitre 4 concernant les effets de l'existence d'un océan composé d'eau très salée entre le manteau et la couche de glace de haute pression pourrait être prolongée afin de considérer d'autres nombres de Rayleigh, ainsi que l'ajout d'un flux de sels à l'interface avec le manteau. Un autre point essentiel non considéré au cours de cette thèse est le traitement complet de l'écoulement biphasique. Si la température à l'interface avec le manteau atteint la température de fusion, comme c'est le cas dans nombre des scénarios que nous avons étudiés, la glace fond et de l'eau, potentiellement chargée en sels, s'élève à travers la couche de glace par convection à l'état liquide, comme indiqué dans l'étude préliminaire de la discussion du chapitre 2. La prise en compte de l'écoulement biphasique a un impact important sur la dynamique et devrait fortement favoriser les échanges entre le manteau et l'océan. Nous avons montré dans la discussion du chapitre 2 que dans le cas où on ne considère que la convection à l'état solide, travailler avec une viscosité constante à travers la couche de glace

est suffisant. Cependant, dans le cas où l'on considérerait la convection à l'état liquide, cette hypothèse n'est plus assez robuste et il faudrait prendre en compte les variations de viscosité à travers la couche de glace avec la pression, la température, la concentration en sels et la fraction de liquide dans la glace.

REMERCIEMENTS

Ce manuscrit marque la fin de trois années de thèse et l'accomplissement d'un rêve de longue date. Ce rêve, je n'aurais pas pu l'accomplir sans l'aide et le soutien de beaucoup de monde. Une thèse, c'est trois années difficiles, qui demandent de la persévérance et du dépassement de soi. Mais pour moi, ce furent également trois belles années, durant lesquelles j'ai pu m'épanouir sur le plan professionnel et personnel. Ainsi, je voudrais remercier toutes les personnes qui ont rendu cette réussite possible.

Tout d'abord, pour bien vivre une thèse et la réussir, un bon encadrement me semble être primordial. C'est pourquoi je voudrais remercier mon directeur de thèse, Stéphane Labrosse. Premièrement, pour m'avoir laissé ma chance et avoir cru en ma capacité à mener ce travail à bien. Également, pour sa disponibilité tout au long de ces trois années, mais aussi pour la liberté et la confiance qu'il m'a accordées dans mon travail et qui m'ont permis de gagner en autonomie et de tracer petit à petit mon propre chemin.

Je souhaiterais aussi remercier toutes les personnes du LGLTPE pour leur accueil et tout particulièrement les autres doctorants : Alexandra, Valentin, Line, Asma, Valentine, Enguerrand, Marwane, Pierre-Jean, Delphine et tous les autres. Merci pour votre bonne humeur, votre enthousiasme et toutes nos soirées partagées autour d'un verre ou d'une bonne raclette. Je remercie plus spécialement Chloé Michault, Stéphane, Alexandra, Valentin et Line pour les discussions intéressantes que nous avons pu avoir lors de nos "geophysics group meeting". Enfin, merci à Maëlis Arnould et Vincent Langlois pour la confiance que vous m'avez accordée pour assurer les TD de vos cours ainsi que pour votre aide quand j'en ai eu besoin.

I am very grateful to Ondřej Čadek for inviting me to present my work and to visit their laboratory at Charles University. The ensuing discussions with Klára Kalousová and Christophe Sotin, among others, were very instructive. J'ai également reçu l'aide précieuse d'Adrien Morison que je remercie pour le temps qu'il m'a accordé. Finally, thanks to Paul Tackley for allowing us to use StagYY, and for his expertise and careful proofreading.

Je dois également beaucoup aux membres de mon comité de suivi de thèse: Gaël Choblet, Thierry Alboussière et Vincent Balter pour leurs encouragements ainsi que leurs précieux conseils. Enfin, je suis très reconnaissante envers Gabriel Tobie, Anne Davaille, Cathy

Quantin-Nataf, Christophe Sotin et Stéphane Labrosse pour avoir accepté de faire partie de mon jury de thèse, pour leur relecture attentive de mon travail ainsi que pour les discussions qui en ont découlé et, bien sur, pour m'avoir accordé mon doctorat.

Je n'en serais évidemment pas là sans mes parents, qui m'ont toujours soutenu dans mes études et dans mon choix de faire une thèse. Merci d'être venu d'aussi loin pour assister à ma soutenance et à l'accomplissement de ce rêve de longue date. Je remercie également ma tante Jeannick et ma cousine Enola pour avoir été là pendant ces trois ans et pour nos soirées partagées autour d'un bon repas et d'une tasse de thé. Plus largement, je remercie ma famille pour leur présence et leurs encouragements.

Merci à Laure, Théo, Mathilde, Florian, Sarah et Cyril, pour nos calls interminables et votre soutien malgré la distance. J'ai eu la chance pendant ma thèse de participer à un évènement de vulgarisation, "ma thèse pour les nuls", dans le cadre de la fête de la science 2022. Cet évènement est un souvenir très particulier pour moi car il a mené à de nouvelles amitiés. Je tiens donc tout d'abord à remercier Elodie Chabrol, notre formatrice, pour son enthousiasme contagieux qui nous a permis de créer des liens très forts en quelques séances seulement. Je remercie également mon groupe de "copines" (Sorry Val): Lucie, Maureen et Valentin, pour toutes nos soirées sans filtre et nos sessions post-it.

Même s'il ne lira jamais ces lignes (ou bien il me cache beaucoup de choses), je voudrais remercier mon chat, Orion, pour ses câlins pendant mes longues soirées et nuits de travail. Mais aussi pour toutes les fois où il m'a forcé à décrocher de mon ordinateur pour nettoyer ses bêtises (peut-être était-ce là son objectif?).

Pour terminer, Thomas, sans toi je n'aurais sans doute jamais trouvé le courage de commencer cette thèse. Merci de m'avoir convaincu que c'était bien ma voie et de m'avoir encouragé dans cette entreprise. Pour toutes les fois où tu m'as soutenu que j'étais parfaitement à ma place quand je doutais de moi, pour nos soirées à thème et nos séjours à Disney et bien sur pour m'avoir apporté mon lait au chocolat et mes autres lubies sans que je n'aie jamais rien besoin de demander, merci.

CONTENTS

CHAPTER 1

INTRODUCTION

When it comes to ocean worlds, one would think about the Earth and the Blue Marble, this famous photograph of the Earth taken during the Apollo 17^{th} mission on December 17th 1972, showing a water-covered blue planet. Our planet is in majority covered with liquid water, which is one important criterion for the habitability of a planetary object. But is the Earth the only planetary object in our solar system to contain so much liquid water? If the Earth is in the habitable zone of our planetary system, meaning that water can stay liquid at its surface, it is not the only one to contain an important amount of liquid water under its surface. Indeed, orbiting around the giant planets of the outer solar system exist several bodies called icy moons which have a water ocean under their icy surface. In this PhD thesis, we are going to focus on Ganymede and Titan the two largest moons of the solar system, respectively orbiting Jupiter and Saturn. In this introduction, we are also going to discuss Europa and Enceladus as a tool for comparing their interior structures. Several missions have already been sent to explore these bodies, as Cassini-Huygens, which explored Saturn and its moons from 2004 to 2017. Cassini allowed us to classify Enceladus and Titan as ocean worlds thanks to several measurements. For Enceladus, it has been inferred by gravity measurements [McKinnon, 2015] and the composition of the south pole geysers, made of water and different salts, that has been discovered during this mission and is compatible with a deep-ocean [Postberg et al., 2009, Čadek et al., 2016]. For Titan, Cassini provided us with information on its surface, atmosphere, shape and gravity field in order to better characterize its interior [Sotin et al., 2021]. The existence of a subsurface ocean has been deducted mainly from these gravity measurements and the very large tidal love number which indicates important internal deformations along its orbit [Iess et al., 2012]. For Ganymede, the subsurface ocean has not been discovered by a spacecraft but by the Hubble Space Telescope, which measured that the oscillations in Ganymede's auroral ovals were about $2^\circ \pm 1.3$ which, according to Saur et al. [2015], is typical of the existence of a subsurface ocean. However, the Jovian system also had its share of explorations with the Galileo mission from 1995 to 2003, which made several flybys of Io, Europa, Ganymede

and Callisto, the four Galilean moons of Jupiter, during these years. Galileo's spacecraft provided us with the first information about Ganymede's intrinsic magnetic field [Kivelson et al., 1996, 1997]. It also provided information about the surface of Europa consistent with the existence of a subsurface ocean, which was confirmed by electromagnetic measurements carried out by the Galileo probe [Kivelson et al., 2000]. Currently, Juno has been orbiting Jupiter since 2016 and should perform two flybys of Ganymede. During the first one in 2021, Juno took four images that improve the geological and topographic mapping of Ganymede's surface [Ravine et al., 2022]. Several future missions are already planned to further explore these moons. To improve our knowledge of the Jovian system, focusing on the habitability potential of its icy moons, JUICE [Grasset et al., 2013, for more details about the expected results of this mission] has been launched this year, on April 14^{th} 2023. It should perform a full investigation of Ganymede's hydrosphere and internal structure, but also better characterize its surface, composition and magnetic field. Several flybys of Europa are also planned to study its chemical composition to better constrain its habitability potential and give us a first overview of its subsurface. It should also provide us with information on its surface in order to choose a landing site for future missions. Another mission is planned in the Jovian system, focusing on Europa. Europa Clipper [Pappalardo et al., 2021] should be launched in 2024. Its main missions are to better characterize Europa's subsurface ocean, including its composition and chemistry. It should also provide us with new information on its surface which, in conjunction with JUICE, should help to find the most interesting landing site for future missions. Finally, the next mission planned on Saturn's icy moons is Dragonfly. Dragonfly is a rotorcraft lander that should be launched towards Titan in 2027. Its main missions [Barnes et al., 2021] are to study potential prebiotic chemistry and chemical biosignatures for water- or hydrocarbons-based life to conclude about the habitability potential of Titan. Each of these missions contributes to improving our knowledge of these moons and their potential habitability.

These missions led to the conclusion of the existence of a subsurface ocean for Ganymede, Titan, Enceladus and Europa. But is the presence of liquid water sufficient to assert that these moons are habitable? From Cockell et al. [2016], the habitability of a planetary body can be defined as its ability to sustain at least a single life form and is measured by several requirements, including the existence of a solvent as liquid water, an available source of energy usable by organisms (as photosynthesis is very unlikely to happen in deep-oceans of icy moons, it is more likely to be from a chemical origin as chemotrophy) and the existence of the essential building blocks of life as we know it: CHNOPS (carbon, hydrogen, nitrogen oxygen, phosphorus and sulfur). Another important criterion is a strong heat flux from the core, allowing hydrothermal circulation, which is the source of salts exchanges between the core and the ocean. Therefore, the presence of liquid water on those four icy moons is not enough to define them as habitable, as it depends a lot on their internal structure and chemical composition. According to current data, these moons not only contain a subsurface ocean, but an ocean composed of salted water. On Ganymede and Europa, it has been inferred by Galileo's magnetometers whose measurements revealed an inductive magnetic field consistent with the existence of a deep salty ocean [Kivelson et al., 2002]. For Titan,

it comes from the Huygens probe electromagnetic measurements [Béghin et al., 2012] but also from its tidal love number k2, which value is superior to the one expected for an ocean composed of pure water [Iess et al., 2012]. If those salts could come from the differentiation of those moons, they could also be transported from their rocky core to the ocean by several processes. According to Tobie et al. [2014], the accretion of icy moons occurred early in the life of the solar system. They would have formed from ice and rock of the circumplanetary disks of Jupiter and Saturn and should contain volatiles as NH_3, CH_4 or CO_2 in protosolar abundances. The composition of the rocks that formed their rocky core is considered close to carbonaceous chondrites [Sotin et al., 2021], whose composition is detailed in Wasson and Kallemeyn [1988]. Therefore, they are likely to be composed of a silicate-rich mantle and, if fully differentiated, an iron-rich core. According to Sotin et al. [2021], Titan's ocean is likely to be mainly composed of heavy ionic salts as NaCl or $MgSO_4$, while on Ganymede [Soderlund et al., 2020], Galileo's spectrometer readings are compatible with $MgSO_4$ as the main ocean salt.

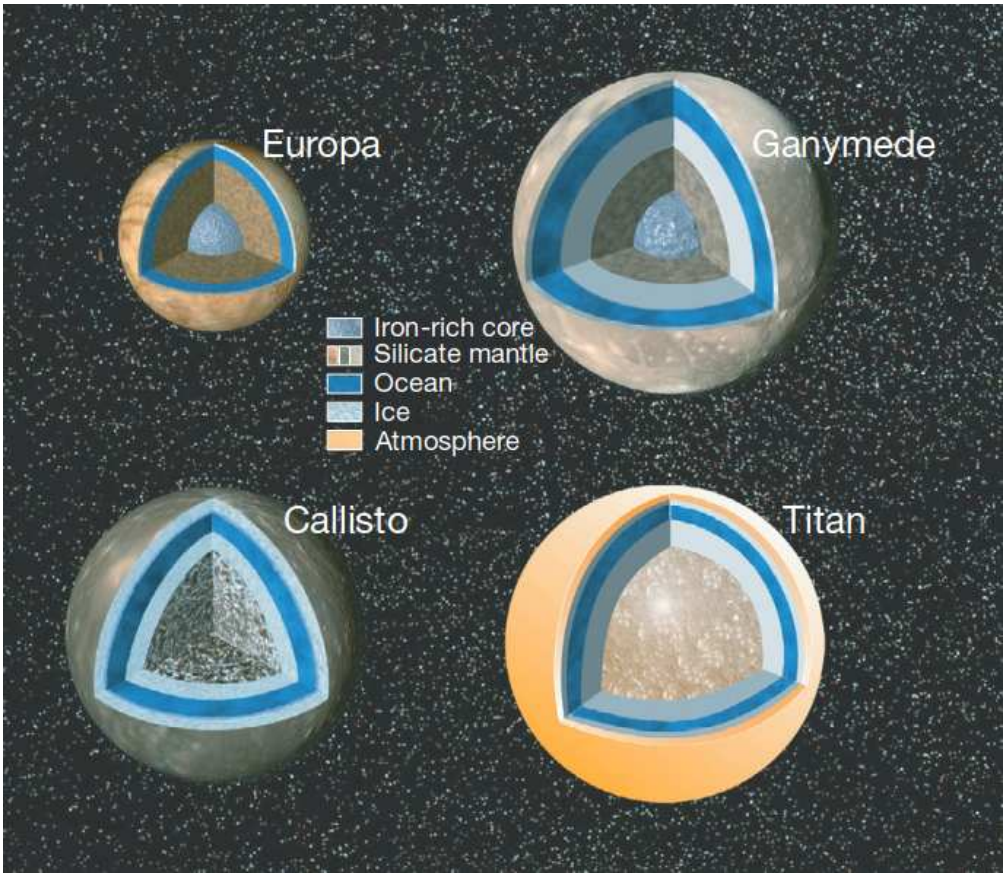

Figure 1.1: Models of the internal structures of large icy satellites and Europa from Hussmann et al. [2015].

Another condition for life to appear in high pressure environments is the existence of

strong interactions between a rocky core rich in those elements and the ocean in order for these essential salts and nutrients to reach the ocean [Picard and Daniel, 2013, Sotin et al., 2021]. On small icy moons as Europa and Enceladus, the hydrosphere is small and the pressure, inferior to 200 MPa, is too low for high-pressure (HP) ices to form [Soderlund et al., 2020] and the ocean is in direct contact with the core, allowing intensive water/rock interactions. On the other hand, on large icy moons as Ganymede and Titan, with pressures at the interface with the mantle being about, respectively, $1500 - 1\,700$ MPa and $650 - 850$ MPa [Soderlund et al., 2020], a layer of high-pressure ices may exists between the core and the ocean, preventing direct contact between both and, at first glance, decreasing the exchanges of salts from the core to the ocean. The different internal structures of these moons are summarized on fig. 1.1 from Hussmann et al. [2015].

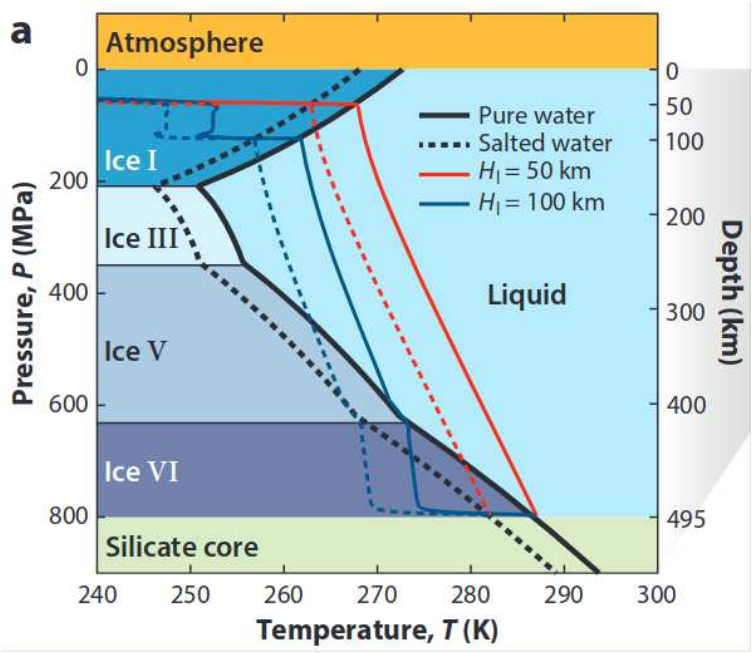

Figure 1.2: Pressure-temperature (P-T) diagram for conditions in Titan's hydrosphere. Black lines indicate the melting curve for pure H_2O (solid lines) (Wagner et al. 1994, 2011) and salty hydrosphere (dashed lines) (5 K colder). Red and blue profiles correspond to ice I shell thickness HI = 50 and 100 km, respectively. The depth on the right vertical axis is approximate and corresponds to pure hydrosphere. This figure comes from Sotin et al. [2021].

The existence of this layer made of high-pressure ices is also highly dependent on the existence and the thickness of an icy crust at the surface of the moon, as can be seen on fig. 1.2. This figure, coming from Sotin et al. [2021], shows the pressure-temperature profile in the hydrosphere of Titan for pure and salted water for two different values of the ice crust thickness. Increasing the thickness of the ice crust has two main effects visible on fig. 1.2. First, the temperature decreases for a thicker crust, which allows high-pressure ices to form at

a depth of about 400 km for a crust 100 km thick. Secondly, for a thickness of the surface ice of 50 km, the ice crust is conductive, while for an ice crust 100 km thick we can observe (see fig. 1.2) a convective profile with two boundary layers. As we have shown in this PhD thesis in the case of the upper interface between the HP ice layer and the ocean (see chapter 2), if we consider the phase change at the bottom of the icy crust (see fig. 1.2), there would be no boundary layer at the lower interface and the bottom temperature would be equal to the melting temperature. From Sotin et al. [2021], Soderlund et al. [2020] and Tobie et al. [2014] the low density of Titan's core, which is only 2 600 kg m^{-3} [Soderlund et al., 2020], and its moment of inertia (MoI) of about $0.33 - 0.34$ would imply a differentiated object ($MoI < 0.4$), but not fully differentiated, with a mantle composed of the mixture of rock and ice and probably no iron core [Tobie et al., 2014]. As can be seen on fig. 1.3 coming from

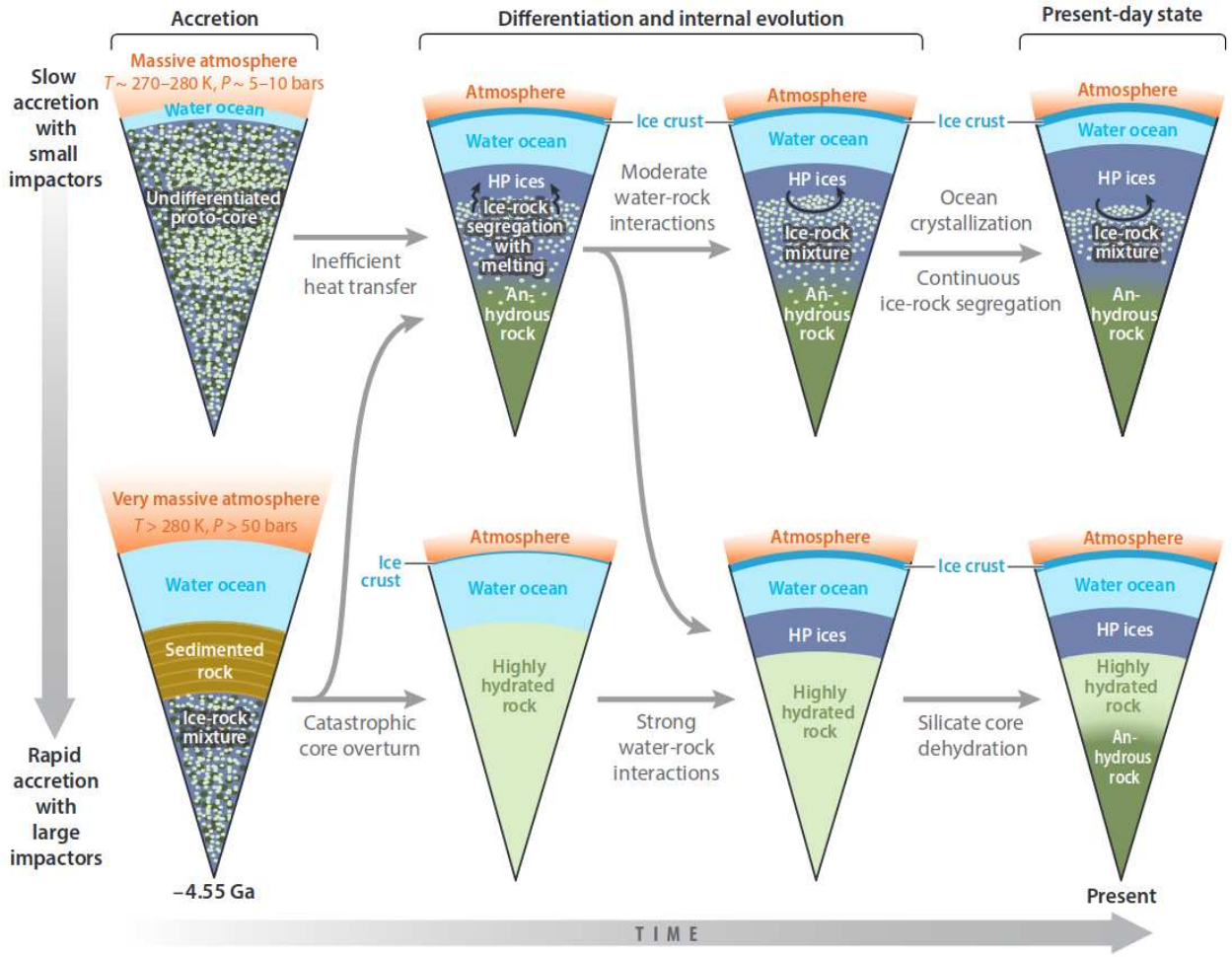

Figure 1.3: Possible evolution scenarios for the interior of Titan for different initial states. Depending mostly on the efficiency of heat transfer in the interior, different bifurcations in the evolutionary path may have occurred. Abbreviation: HP, high pressure. Figure from Sotin et al. [2021].

Sotin et al. [2021], there are two main scenarios for the formation of Titan. In both scenarios, during the accretion phase an ocean forms at the surface of Titan. During the differentiation phase, either they consider a slow accretion and small impactors, leading to a thin ocean and relatively massive atmosphere, or a fast accretion and larger impactors, leading to a very thick ocean and a very massive atmosphere. But even in the second scenario, the present-day structure remains not totally differentiated. Concerning the high-pressure ice layer, it appears only during the differentiation phase after the ice crust has already begun to develop and not before it reached a sufficient thickness, allowing direct contact between the rocky core and the ocean during a significant period of time, especially in the second scenario in which a strong water-rock interaction is possible during a longer period of time after the accretion. However, this icy crust should also not be thicker than $30 - 40$ km to maintain a subsurface liquid ocean [Tobie et al., 2014].

The low moment of inertia of Ganymede implies a fully differentiated moon with an iron-rich liquid core [Sotin et al., 2021], whose existence has been inferred by its internal magnetic field detected by Galileo's spacecraft magnetometers [Kivelson et al., 1996]. Friedson and Stevenson [1983] talk about a "runaway differentiation" which happens if the gravitational energy is large enough to melt the ice inside the moon. If the amount of silicates is sufficient, the water rises and it leads, in a planetary object mainly composed of rock and ice, to a complete differentiation between these two. Also, the existence of an iron-rich core in Ganymede is likely to be the result of a higher temperature in the core, compared to Titan, during the differentiation phase [Sotin et al., 2021].

Because of the existence of this high-pressure ice layer preventing direct contact between the core and the ocean on moons like Titan or Ganymede, whose thickness is not well-constrained yet but is estimated to be several hundreds of kilometers and expected to be thicker on Ganymede than on Titan, exchanges of salts and nutrients between the core and the ocean has long been considered non-existent and those moons as inhabitable [Noack et al., 2016]. Depending on its thickness, this layer could be composed on several ice phases, mostly ices V and VI [Vance et al., 2018]. But are exchanges really impossible through this high-pressure ice layer? The interactions between the core and the ocean in that case are controlled by the efficiency of the heat and mass transfer. Through this kind of layer, heat can be transported either by conduction, which is a rather inefficient process, or by convection. The ability of this high-pressure ice layer to convect depends on its Rayleigh number, measuring the importance of the driving force compared to the resisting ones. If it is inferior to a critical value, heat transfer through the shell happens only by conduction. As represented on fig. 1.4 from [Sotin et al., 2021], if the Rayleigh number is superior to the critical one, the prevailing mode of transfer through a thick layer of high-pressure ices is convection and the amount of chemical transported from the core to the ocean depends strongly on the ability of melting at the interface between the core and the high-pressure ice layer. Through convection, the heat and mass are transported upwards to the ocean by up-welling hot plumes.

Some studies already addressed the question of the efficiency of these exchanges through the high-pressure ice layer of Ganymede and/or Titan. To do so, Choblet et al. [2017] made

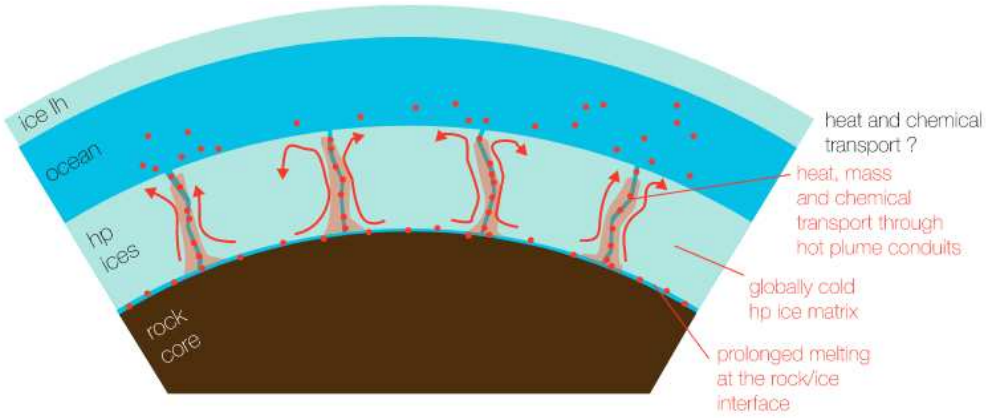

Figure 1.4: Scheme for the principle of heat pipe transfer in the HP ice mantle from Choblet et al. [2017].

a three-dimensional spherical model of a high-pressure ice layer, considering partial melting in the bulk which is instantaneously extracted into the ocean. Kalousová et al. [2018] and Kalousová and Sotin [2018] described a two-dimensional Cartesian model for a high-pressure ice layer made of ice VI, considering a two-phase flow model with partial melting in the bulk and treating melt transport through the ice, while Kalousová and Sotin [2020] did the same for Titan but considering the phase change existing in the high-pressure ice layer between ice V and ice VI. All of these studies considered a viscosity varying with pressure and temperature through the high-pressure ice shell. Kalousová and Sotin [2018], Kalousová et al. [2018], Kalousová and Sotin [2020] even included the viscosity variations due to the presence of melt in the bulk. On fig. 1.5, which comes from the study of Kalousová et al. [2018], we can observe the temperature and the porosity through the high-pressure ice layer for three values of the ice VI reference viscosity. The first column is a profile of temperature inside the shell, the second one shows the difference between the melting temperature and the temperature through the bulk, while the third and fourth column display, respectively, the porosity and porosity profile. In the first case for the lowest viscosity, the temperature reaches the melting temperature only near the top interface with the ocean, while for the intermediate viscosity it also reaches the melting temperature at the bottom interface with the core, meaning that there is melt at the bottom and top boundaries that refreezes along the way through the high-pressure ice layer. Finally, for the highest viscosity considered, the temperature reaches the melting temperature in the entire layer and we can observe the formation of stable up-welling hot plumes transporting the melt all along the way from the core to the ocean. It can also be observed looking at the porosity which is above 1% on most of the ascent. This observation is compatible with the fact that increasing the viscosity decreases the Rayleigh number, which increases the bottom temperature and the melting ability at the interface with the core. This type of figure shows that, depending on several parameters that are not well-constrained yet, as the viscosity of high-pressure ice, the thickness of this ice shell or the heat flux from the core, three main regimes can be observed

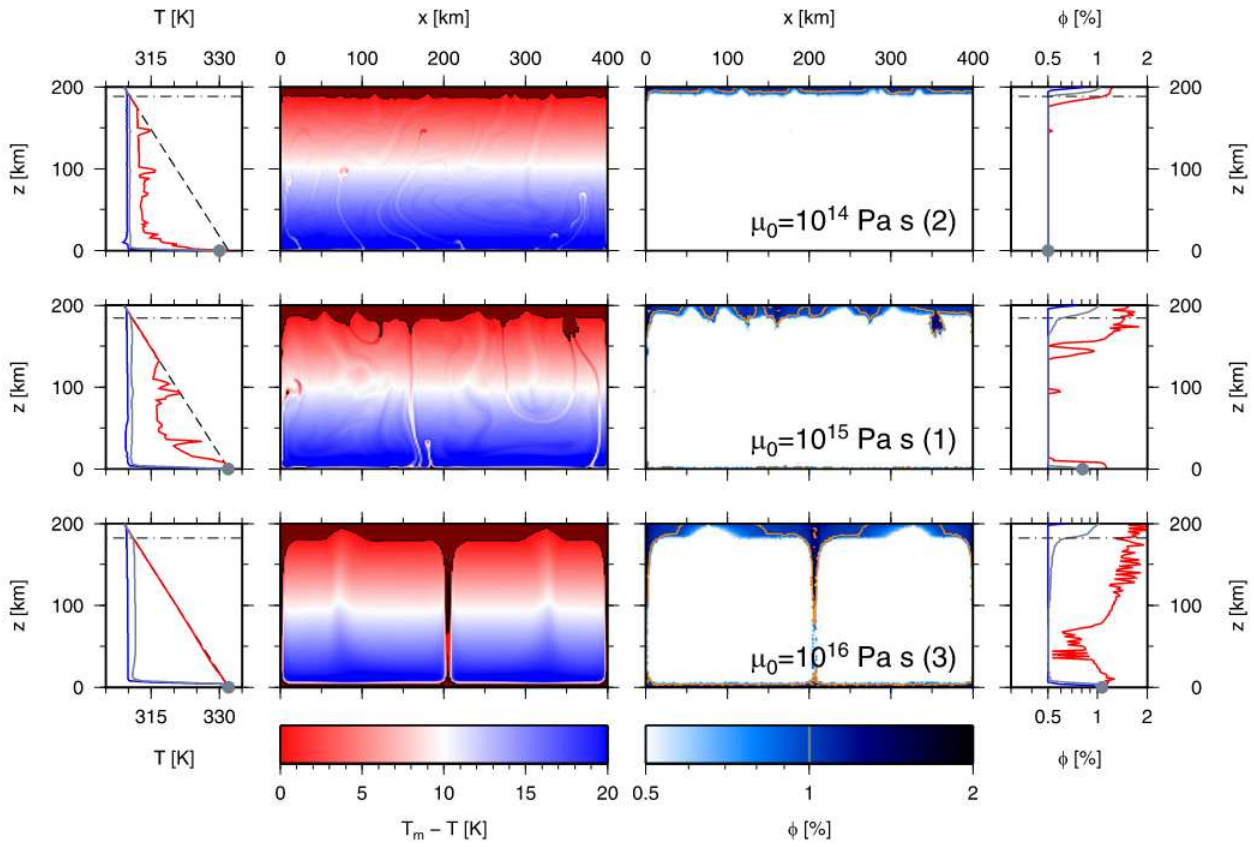

Figure 1.5: This figure comes from Kalousová et al. [2018] and shows the results for different melting point viscosities (10^{14} – 10^{16} Pa s, top to bottom, numbers in parentheses refer to simulation numbers) and in a statistical steady-state. Horizontal dot-dashed lines mark the extent of the top temperate layer. First column: temperature profiles – maximum (red), minimum (blue), horizontal average (grey), and melting temperature (dashed line); second column: difference between melting temperature and ice temperature; third column: porosity; fourth column: porosity profiles – maximum (red), minimum (blue), and horizontal average (grey). Dark red in temperature panels marks temperate ice ($T = T_m$), orange contour in porosity panels marks $\phi = 1\%$. The grey circles in the left and right panels mark the bottom boundary values of average temperature and porosity, respectively.

(which can also be divided into 4 regimes according to Kalousová and Sotin [2018]):

- If the melting temperature is not reached at the interface with the core, there is no liquid water to interact with the core and there are no exchanges of chemicals between the core and the ocean.
- If melt is produced at the bottom boundary but refreezes during the ascent, there is at least periodically indirect contact between the core and the ocean: water is enriched in chemicals at the interface with the core, it starts rising through the ice but refreezes

along the way and reaches the temperate layer at the top by convection in the solid state where it melts again, allowing the salts to dissolve in the ocean.

- If the temperature is equal to the melting temperature in stable up-welling hot plumes all the way through the high-pressure ice shell, melt is produced at the bottom interface with the core and the mixture of melt and chemicals rises and stays liquid during all the ascent, allowing direct contact between the core and the ocean through these plumes and an efficient mass transfer between both layers.

The same dynamics can be observed in the high-pressure ices of Titan [Kalousová and Sotin, 2020]. It shows that under certain conditions that still have to be better constrained by future space missions, efficient interactions could occur between the core and ocean inside these large icy moons.

These studies considered several parameters that are interesting to get closer to the physical reality of these moons, as the melting ability of the interface between the core and the ice, which is an important point for salts transport to the ocean and the two-phases convection in the high-pressure ice shell. However, one of the points they did not consider is the effect of the phase change existing at the interface between the high-pressure ice layer and the ocean. This boundary has already been studied by Agrusta et al. [2020], Deguen [2013], Labrosse et al. [2018], Morison et al. [2019] in the context of the Earth and magma oceans and they demonstrated that it greatly eases the convection and increases the mass transfer efficiency through the solid layer. Applied to large icy moons and high-pressure ice layers, at the interface between the ice and the ocean, the convective stresses in the ice create a topography of the interface. Convection in the ocean acts against these variations and erases the topography by melting and freezing. This condition implies a non-zero radial velocity at the interface which improves the exchanges of salts between the core and the ocean through the high-pressure ice layer. Also, all of these previous studies considered only pure ice. From the different references cited in this introduction, we know that the oceans of these moons are salty and that a part of these salts should come from interactions with the core.

If the effects of compositional variations have not been studied on large icy moons yet, it has been done for the Earth's mantle. Indeed, differences in isotopic compositions identified between the mid-ocean ridge basalt and the oceanic island basalt [Hofmann, 1997] have been used as an argument for a heterogeneous Earth's mantle. Therefore, the Earth's mantle should be composed of various chemical reservoirs. On Earth, partial melting at both ocean ridges and subduction zones separates chemical elements and create large-scale chemical heterogeneities. These heterogeneities are reinjected into the mantle at subduction zones and there is a competition between the processes that continuously renewed these heterogeneities and the convection in the mantle that tends to erase them [Tackley, 2000]. In any case, the system tends to a one-layer regime after a significant time and chemical diffusion completes the homogenization of the mantle [Le Bars and Davaille, 2004]. But before this homogenization process is complete, chemical heterogeneities have an important impact on the convection pattern. According to Davaille [1999], a "doming" regime of the convection composed of large oscillating domes topped with thin up-welling hot plumes could

explain the existence of hot spots (caused by the plumes) and superswells (caused by the dome itself), which is a large area of shallow seafloor with a high concentration of hot spots, on Earth. This study also suggests that the convective regime in the mantle evolved over the Earth's history, going from a highly stratified convection to the present day "doming" regime and expected to end with a complete mixing of the mantle. The other models proposed for Earth's mantle convection in order to best meet the geophysical, geochemical and seismic constraints are presented in fig. 1.6, which comes from Tackley [2000]. Finally, Le Bars and Davaille [2004] suggest that the Earth's mantle may have experienced these different types of convection over its history.

The goal of this PhD thesis is to pursue this work by studying the effect of other parameters not considered in previous studies, as the phase change mechanical boundary condition at the interface between the ice and the ocean. A second part (chapter 3) is to add salts in the high-pressure ice layer and/or in the ocean to study their effect on the overall dynamics. The results of chapter 3 also led us to investigate the possibility of the existence of a highly salted ocean between the core and the HP ice shell. This thesis addresses:

- Is mass transfer through a high-pressure ice layer possible and how efficient is it?
- How does the phase-change at the top boundary between the ice and the ocean impact the efficiency of the heat and mass transfer through the high-pressure ice layer?
- How does a flux of salts from the core impact the mass transfer efficiency and the overall dynamics? Can these salts be efficiently transferred from the core to the ocean?
- How would the existence of a thin liquid ocean composed of highly salted water between the core and the high-pressure ice shell change the dynamics and affect the mass transfer efficiency?
- Finally, is the existence of a high-pressure ice layer between the core and the ocean a real obstacle to habitability?

Chapter 2 presents the effect of the phase-change at the interface between the ocean and the high-pressure ice layer considering only pure ice and convection in the solid-state, while in chapter 3 salts have been added to the ice and/or ocean to study how they affect the overall dynamics and mass transfer efficiency through the high-pressure ice shell, still considering convection in the solid-state only. Finally, chapter 4 contains the preliminary results addressing the question of a thin, highly salted liquid layer between the core and the high-pressure ice layer, which seems to be a possible consequence of the existence of salts in the high-pressure ice layer as explained in the discussion part of chapter 3.

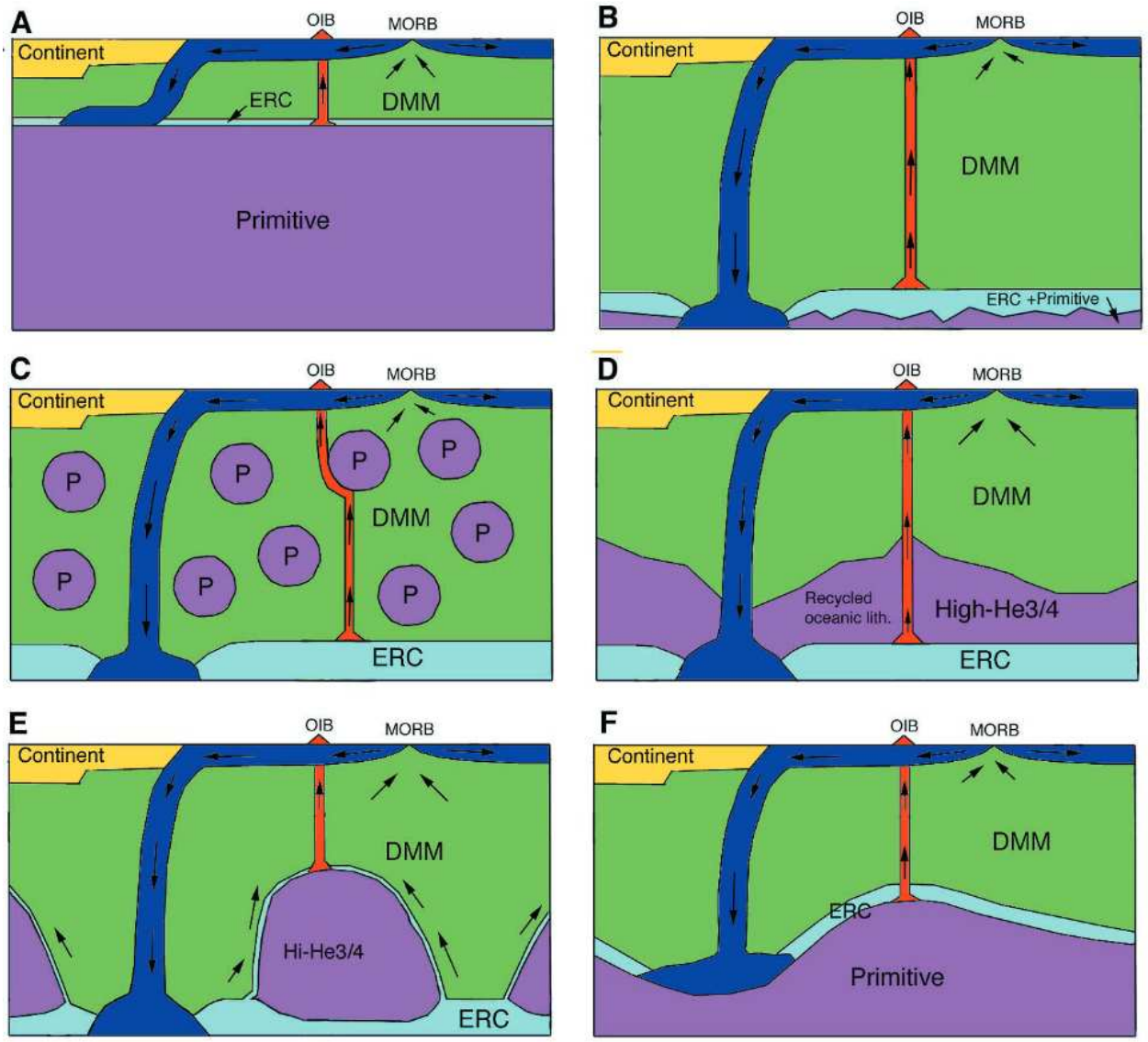

Figure 1.6: Some possible locations of mantle reservoirs and relationship to mantle dynamics. Convective features: blue, oceanic plates/slabs; red, hot plumes. Geochemical reservoirs: dark green, DMM; purple, high 3He/4He ("primitive"); light green, enriched recycled crust (ERC). (A) Typical geochemical model layered at 660 km depth [Hofmann, 1997]. (B) Typical geodynamical model: homogeneous except for some mixture of ERC and primitive material at the base. (C) Primitive blob model [Becker et al., 1999] with added ERC layer. (D) Complete recycling model [Albarède, 1998, Coltice and Ricard, 1999]. (E) Primitive piles model [developed from [Tackley, 1998]]. (F) Deep primitive layer [Kellogg et al., 1999]. Figure from [Tackley, 2000].

CHAPTER 2

SCALING OF CONVECTION IN HIGH-PRESSURE ICE LAYERS OF LARGE ICY MOONS AND IMPLICATIONS FOR HABITABILITY

Several studies have already been published on the heat and mass exchanges processes through a HP ice layer [Choblet et al., 2017, Kalousová and Sotin, 2018, Kalousová et al., 2018, Kalousová and Sotin, 2020]. But none of them considered the effect on the dynamics of the phase equilibrium at the interface between the HP ices and the ocean. This mechanical effect can be modeled as a phase-change boundary condition implying a non-zero radial velocity at this interface. The aim of this chapter is to show how the heat and mass transfer efficiency through the HP ice shell is affected by this phase change boundary condition. Due to viscous stresses in the ice, a topography is formed at the surface of the ice layer. Assuming thermal equilibrium at the upper boundary, the temperature should be equal to the melting one along the entire interface, which is subject to topographic variations. In practice, the convection in the ocean acts against the temperature lateral variations by erasing the protrusions by melting the ice, which allows the ice transported in the up-welling hot plumes to reach the ocean, or filling the hollows by freezing of the liquid water that accretes to the ice above the down-welling currents. It is done by moving latent heat from the freezing regions that supply it to the melting regions that use it. The competition between the time to erase the topography versus the time to build it controls the efficiency of the phase-change at the interface with the ocean. This ratio is denoted Φ (See § 2.3.1.2 for more details).

In this chapter we focus on two output parameters: the bottom temperature, which is directly linked to the ability of melting at the interface between the core and the ice and the radial velocity at top which is a measure of the efficiency of the mass transfer trough the HP ice layer. We build a model with a phase-change boundary condition at the top and solve the convection equations with StagYY (See § 2.3.2.2). We perform a systematic exploration of the parameter space controlled by the Rayleigh number Ra_q and the phase-change number Φ and we establish scaling laws relating the bottom temperature and the top radial velocity

to Ra_q for various values of Φ and two different bottom boundary conditions (§ 2.4.2). We use these laws to study the importance of this parameter on the efficiency of the heat and mass transfers for specific planetary bodies in § 2.4.3.

In this study, to isolate the effect of the mechanical condition, we consider only convection in the solid-state, but in § 2.5 we compute the amount of melting expected in the HP ice layer. We assume that the HP ice layer is composed only of pure ice VI and we neglect compositional effects. We also consider a constant viscosity through the HP ice layer, except for one case presented in § 2.5.

This chapter comes from our paper Lebec et al. [2023] published in Icarus in 2023. The supplementary materials are in appendix A.

2.1 Abstract

The existence of a high-pressure (HP) ice layer between the silicate core and the liquid ocean in large icy moons and ocean worlds is usually seen as a barrier to habitability, preventing a direct contact and therefore transfer of nutrients from the core to the liquid ocean. More recently, several studies challenged that hypothesis and showed that exchanges were possible under specific conditions, allowing transport of salts toward the ocean. In our study, we consider an effect not taken into account in the previous works, which is the dynamical implications of the phase equilibrium at the ice-ocean interface allowing a non-zero vertical velocity at the surface of the HP ice layer. This effect, which can be modeled as a phase change boundary condition for the ice layer, has a significant impact on the flow dynamics and enables exchanges with the ocean by fusion and crystallization at the top interface of the HP ice layer, even without partial melting in the bulk of the ice layer. For the same conditions as standard convective systems, it also leads to faster mass transfer in the bulk. These exchanges are directly linked to the melting capacity of the ice at the interface between the HP ice layer and the core, depending on the efficiency of convection in the liquid ocean. This is controlled by a dimensionless coefficient noted Φ. Considering this boundary condition at the interface between the HP ice layer and the liquid ocean, we propose a scaling of the bottom temperature and the top vertical velocity as function of the Rayleigh number, in the case of a fixed heat flux from the core, a rigid or free-slip bottom boundary and various values of Φ.

2.2 Introduction

The internal structure of large icy moons, as Ganymede or Titan, differs from that of smaller ones as Enceladus or Europa for which a direct contact exists between the core and the ocean under the icy surface [Hussmann et al., 2015]. Their composition has been studied from the data of Cassini-Huygens which explored Saturn's moons from 2004 to 2017 and Galileo missions which explored Jupiter's moons from 1995 to 2003. Currently, Juno is orbiting Jupiter and performed one close flyby of Ganymede [Ravine et al., 2022], which will also be

one of the targets of the JUICE mission [Grasset et al., 2013] around 2030 in order to better constrain several parameters of this moon. For large icy moons, as Ganymede, Callisto and Titan, owing to the phase diagram of water, a high-pressure (HP) ice layer of tetragonal ice VI and ice V, depending on the assumed thickness of the ice mantle [Vance et al., 2018], may exist between the internal liquid ocean and the rocky core [Hussmann et al., 2015], in addition to the ice Ih at the surface of the moon. The consequences of this internal structure is that the core and the ocean are not in direct contact, which has long been considered as an obstacle to their habitability by strongly limiting or even removing all interactions between these two layers. Efficient exchanges of nutrients between the core and the ocean being one of the necessary conditions for life to appear at high-pressure in a deep water ocean [Picard and Daniel, 2013], these moons were considered less favorable to habitability than smaller moons like Europa [Noack et al., 2016].

In recent years, several studies showed that, under certain conditions depending on the thickness of the HP ice layer, the viscosity of the ice and the heat flux from the core, periodically indirect contacts, or even direct contacts, could still be possible by convection through the HP ice layer. Choblet et al. [2017] described a 3D spherical model of the HP ice shell including partial melting at the bottom of the ice layer, in contact with the core, the melt being extracted instantly to the ocean. Kalousová and Sotin [2018] and Kalousová et al. [2018] described a 2D cartesian two-phase convection model including partial melting and melt transport through the HP ice layer. These studies consider the pressure and temperature dependence of the viscosity. In addition, Kalousová and Sotin [2018] and Kalousová et al. [2018] also include viscosity variations owing to the presence of melt. All those studies concluded that for various values of ice viscosity, shell thickness and heat flux from the core, mass transfers is possible between the core and the ocean through the HP ice layer by convection in a two-phase medium. A key aspect common to these models is the possibility of melting of the HP ice at the rock interface and transfer through the ice layer, as liquid channels or by solid-state convection.

While these previous papers consider the possibility of melting at the bottom of the HP ice layer and partial melting in the bulk, with various levels of approximation, they do not consider the dynamical effect of the solid-liquid phase equilibrium at the upper boundary of the HP ice layer. Indeed, several studies showed that a melting-freezing boundary drastically changes the condition for convection in a solid layer and the resulting convection characteristics at finite amplitude [Deguen, 2013, Labrosse et al., 2018, Agrusta et al., 2020, Morison, 2020]. Applied to our study, the interface between the liquid ocean and the HP ice layer can be set as a phase change boundary condition. Physically, convective stresses in the solid create a topography of the interface which can be erased by melting and freezing. It implies a non-zero radial velocity at the surface of the HP ice layer, which significantly increases the efficiency of the mass transfer through the HP ice layer. This effect can be modeled as a boundary condition for the ice layer controlled by the phase change coefficient Φ [Deguen, 2013, Labrosse et al., 2018, and references therein]. The aim of this paper is to evaluate the implications of the liquid-solid phase change boundary condition for convection in high pressure ice layer of large icy satellites and water planets.

To this end, we used a numerical model solving the convection in the HP ice layer

subject to the phase change boundary condition. We explored systematically the numerical solution depending on the dimensionless control parameters (mainly the Rayleigh number and the phase change number) and obtained scaling laws relating output parameters (bottom temperature, flow velocity) as function of these input dimensionless numbers. We show in this paper how these scaling laws can be used to make prediction on specific planetary objects, like Titan and Ganymede. We do not consider two-phase flow in the bulk of the ice layer, as done in some previous studies [Choblet et al., 2017, Kalousová and Sotin, 2018, Kalousová et al., 2018] to isolate the effect of the phase change boundary condition. We nevertheless compute, as a post-treatment, the amount of partial melting that we would expect if it was permitted, which allows us to compare our results to these previous studies.

In section 2.3 we present the physical and numerical models used to solve the convection problem. The results are described in section 2.4. These generic results are then applied to several bodies in subsection 2.4.3. In section 2.5 we discuss the limitations of the results and the possible future work. A summary and conclusion are provided in section 2.6.

2.3 Model

2.3.1 Physical model

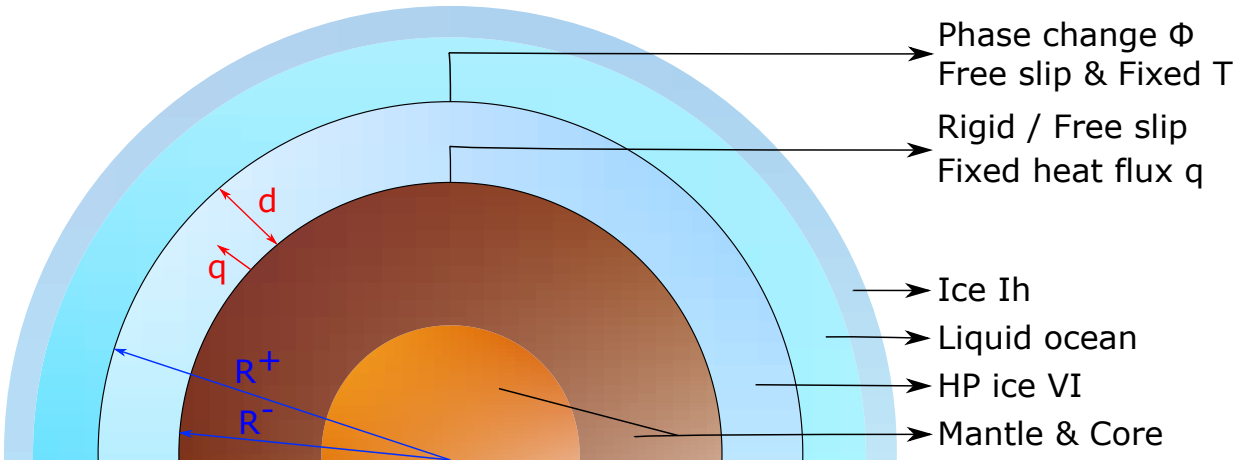

Figure 2.1: Model illustration for the interior of an ocean world with a HP ice layer in direct contact with a liquid ocean at top and a rocky core/mantle at the bottom (type IV or V of Lammer, 2013, and type H3 of Noack et al., 2016). Our numerical models treat convection in the HP ice layer.

2.3.1.1 Governing equations

We want to quantify the heat and mass transfer by convection in HP ice layers of various planetary objects, from large icy satellites like Ganymede and Titan, to water exoplanets.

The large number of control parameters with wide ranges of possible values among these objects can be reduced by the use of dimensionless equations and numbers and the principle of physical similarity [Barenblatt, 1996]. We use the thickness d of the layer as length scale, the diffusion time d^2/κ as time scale, with κ the thermal diffusivity. For an ice layer subjected to an imposed heat flux q at the bottom, the relevant temperature scale is qd/k, k being the thermal conductivity. Because we consider an incompressible model using the Boussinesq approximation, the actual value of the temperature $\tilde{T}$ (dimensional) is irrelevant to the dynamics and we set the surface temperature $\tilde{T}_{top}$ to be equal to the melting temperature. The dimensionless temperature is

$$T = k\frac{\tilde{T} - \tilde{T}_{top}}{qd}. \tag{2.1}$$

With the dynamic viscosity η, which is considered constant with pressure and temperature through the HP ice layer in our model, the thermal expansion coefficient α, the gravity acceleration g, the shell inner radius R^- (the upper radius being $R^+ = R^- + d$, see fig 2.1), the reference density ρ, we complete the set of input parameters except for that relevant to the phase change boundary condition that is introduced below (§ 2.3.1.2). Table 2.2 gives numerical values of these parameters for Ganymede and a water exoplanet. As is well known [e.g. Ricard, 2015], Rayleigh-Bénard convection in the Boussinesq approximation (and with the previous variables considered constant) is controlled by two dimensionless parameters (aside from the one associated with the phase change boundary), the Rayleigh number,

$$Ra_q = \frac{\alpha g q \rho d^4}{k\kappa\eta}, \tag{2.2}$$

and Prandtl number,

$$Pr = \frac{\eta}{\rho\kappa}. \tag{2.3}$$

The definition of the Rayleigh number given in eq. 2.2 differs from the classical one obtained for an imposed temperature difference and is relevant to the case of an imposed heat flux [Choblet et al., 2017], as considered here.

For the solid HP ice layer, the Prandtl number is large enough (of order 1×10^{20}, see table 2.2) to be considered infinite, meaning the inertia of the ice can be neglected in front of viscous forces. Then, the dimensionless conservation equations of mass, momentum and energy for thermal convection in the spherical HP ice shell under the Boussinesq approximation for an infinite Prandtl number are the following [e.g. Ricard, 2015]:

$$\boldsymbol{\nabla} \cdot \boldsymbol{u} = \boldsymbol{0}, \tag{2.4}$$

$$0 = -\boldsymbol{\nabla} p + \boldsymbol{\nabla}^2 \boldsymbol{u} + Ra_q (T - \bar{T})\hat{\boldsymbol{r}}, \tag{2.5}$$

$$\frac{\partial T}{\partial t} + \boldsymbol{u} \cdot \boldsymbol{\nabla} T = \boldsymbol{\nabla}^2 T, \tag{2.6}$$

with $\boldsymbol{u} = (v, w)$ the velocity, p the dynamic pressure, T and $\bar{T}$ the temperature and steady-state conductive temperature (see section 2.3.2.1) and $\hat{\boldsymbol{r}}$ the radial unit vector.

2.3.1.2 Solid/Liquid phase change at top boundary

The existence of a solid/liquid phase equilibrium at the top of the ice layer leads to a specific mechanical boundary condition in place of the classical non-penetrative one usually considered in convection models. This boundary condition and its implications for Rayleigh-Bénard convection have been the subject of a few previous papers [Deguen, 2013, Deguen et al., 2013, Labrosse et al., 2018, Agrusta et al., 2020, Bolrão et al., 2021] where interested readers will find all the details of the derivation of this boundary condition. Here, we only recall the basic ideas leading to this boundary condition and its implications.

At the interface between the HP ice layer and the ocean, a phase change can occur in either direction, melting or freezing. The secular evolution of the planetary object leads to a net motion of the interface, which we do not consider here since it would require a full thermal evolution model that goes beyond the scope of this paper. On the other hand, the ice flowing vertically toward the interface can cross it by melting and, conversely, liquid water can solidify and accrete to the HP ice layer above down-welling currents. In practice, this happens because the convective stresses in the ice layer generate a topography of the ice-water interface. Assuming thermal equilibrium at the interface makes its temperature equal to that of melting everywhere, but at different depths. This is equivalent to creating lateral temperature differences at the same depth in the liquid layer. Convection in the liquid layer acts against these lateral variations to erase them which in turn tends to erase the interface topography by melting and freezing. This requires transporting latent heat from regions of freezing that provide it to regions of melting that consume it. The behaviour of the boundary depends therefore on the competition between two processes, topography building by convection in the ice layer and its erasing by convective transfer in the liquid. Each process has its own timescale and their ratio decides which wins.

The timescale to build the topography at the interface is dictated by the equilibrium between the viscous stress in the ice layer and the weight of the topography and is

$$\tau_\eta = \frac{\eta}{\Delta\rho g d}, \tag{2.7}$$

with $\Delta\rho = \rho_s - \rho_l$ the density difference across the interface of the order of 100 kg m^{-3} for Ganymede [Kalousová et al., 2018], ρ_s and ρ_l being the density of the solid and the liquid, respectively. Using parameter values for Ganymede given in table 2.2 gives a timescale of order 2 to 200 yr depending on the value of η.

The timescale for erasing the topography is associated to convection in the liquid layer, with a typical flow velocity u_l, that transports latent heat L. A detailed analysis of this process [Labrosse et al., 2018, Deguen, 2013, Deguen et al., 2013] gives

$$\tau_\phi = \frac{\rho_s L}{\rho_l c_{pl} u_l \left|\frac{\partial T_m}{\partial r}\right|}, \tag{2.8}$$

with c_{pl} the specific heat of the liquid. This timescale is difficult to estimate but assuming a flow velocity of about 3×10^{-3} m s^{-1} (Computed using Gastine et al. [2016], Soderlund

[2019]) and using parameter values from table 2.2 gives a timescale of order 15 yr. Note that this theory assumes a turbulent flow in the ocean, u_l being its typical RMS value. Considering τ_ϕ to be constant in time and uniform in space amounts to two assumptions. The typical timescales for the fluctuations in the liquid are assumed small compared to that for the dynamics in the solid. In addition, the turbulence is assumed isotropic. This second assumption could be relaxed by considering a laterally varying value of τ_ϕ to take into account the effect of rotation on the dynamics of the ocean. However, a proper theory is still lacking for this type of effect to be included.

The ratio of the two timescales,

$$\Phi = \frac{\tau_\phi}{\tau_\eta}, \tag{2.9}$$

is called the phase change number and controls the behaviour of the boundary. For Ganymede, from the previous calculations, Φ would be in the range $[0.1; 10]$. This value is a very rough estimate and this range could be larger. The key point here is that the phase change at the top interface must be efficient. A detailed analysis combining the traction continuity across the boundary, the energy balance associated with latent heat and thermodynamic equilibrium at the boundary leads to a single boundary condition for the radial velocity which, in dimensionless form, is [Labrosse et al., 2018, Deguen, 2013, Deguen et al., 2013, Bolrão et al., 2021]

$$\Phi w + 2\frac{\partial w}{\partial r} - p = 0, \tag{2.10}$$

with w the radial velocity. Varying the value of Φ between 0 and ∞ makes the behaviour of the boundary evolve between end-members. In the limit case of $\Phi \to \infty$, the radial velocity at the boundary, w_{top} must tend to 0 (fig 2.3.b) and we recover the classical non-penetration boundary condition used in all previous studies of convection in icy satellites. This happens if heat transfer is inefficient in the ocean so that the weight of the topography limits its building and therefore the radial motion, as shown on fig. 2.2.a. On the other hand, for $\Phi \to 0$ fig. 2.2.b–c, the radial velocity is unconstrained and its radial gradient is set. This happens if the topography is erased by phase change faster than it is built so that its weight is never limiting radial flow. The boundary is then permeable, which is known to drastically change the convective regime [e.g. Ricard et al., 2014, Monnereau and Dubuffet, 2002, Agrusta et al., 2020] compared to the other end-member that is usually considered. With the estimates discussed above, we expect a rather low value of the phase change parameter but we explore systematically the effects of changing its value, in the range $[10^{-2}, \infty)$, since it is rather ill-constrained.

The vertical velocity varies along the boundary, depending on the convection pattern, as can be seen on fig. 2.2.c, but the mean radial velocity at the interface is null due to mass conservation. For this reason, in the following, we use the root-mean-square (RMS) of w to evaluate the efficiency of the mass transfer at the top boundary.

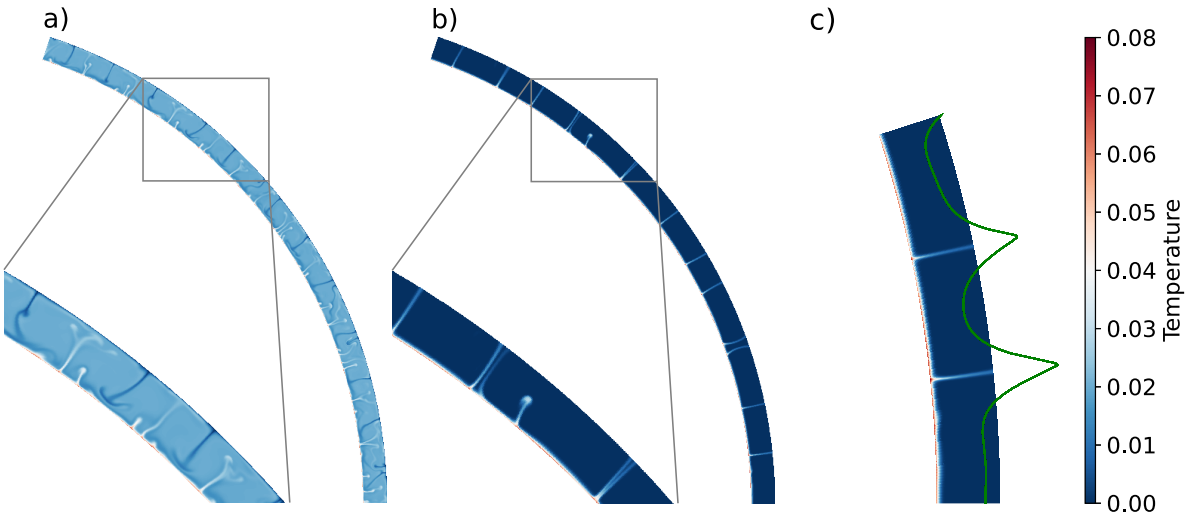

Figure 2.2: Snapshots of 1/5 of the HP ice shell for a given $Ra_q/Ra_c = 10^5$ for $\Phi \to \infty$ (a) and $\Phi = 10^{-2}$ (b). (c) is a zoom of (b) with the top radial velocity displayed in green, varying from ~ -1300 to ~ 3350 along the top boundary. The temperature scale on the right is common to all three panels.

2.3.1.3 Other boundary conditions

As can be seen on figure 2.1 and described by equation 2.2, our model is based on a fixed flux at the bottom boundary between the core and the HP ice layer and a fixed temperature at the upper boundary between the HP ice layer and the liquid ocean, which is set to 0 by rendering the temperature dimensionless. It leads to the following temperature boundary conditions:

$$T^+ = 0, \tag{2.11}$$

$$\left(\frac{\partial T}{\partial r}\right)^- = -1, \tag{2.12}$$

the $^+$ and $^-$ exponents referring to, respectively, the top and bottom boundaries. As the ice VI is in direct contact with a rocky core/mantle whose viscosity is orders of magnitudes larger than that of ice, we normally impose a non-penetrative no-slip (rigid) condition:

$$u^- = w^- = 0. \tag{2.13}$$

However, since the heat flux is fixed at the bottom, the temperature T^- varies along the bottom boundary, allowing, in some cases, pockets or even a global film of melt to form at the interface between the core and the HP ice layer, which could lubricate the boundary and lead to a free-slip BC, which would imply that:

$$\frac{\partial^2 (rw)}{\partial r^2} = 0. \tag{2.14}$$

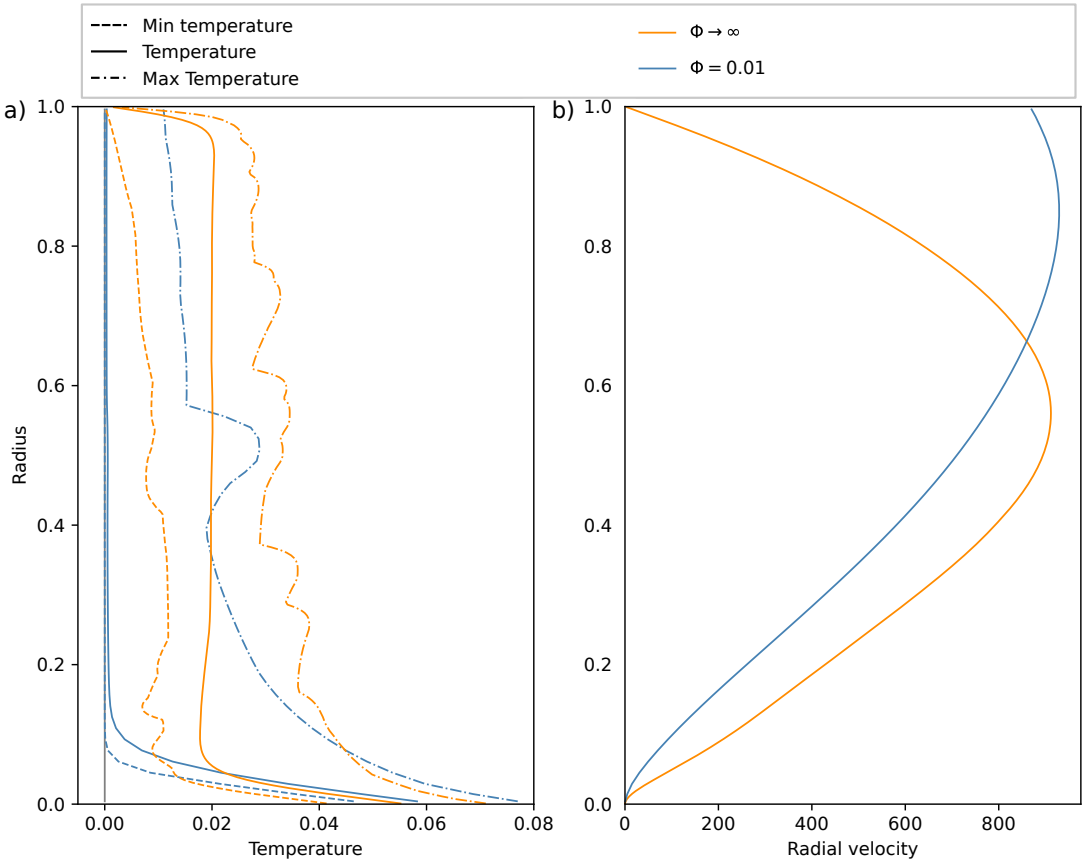

Figure 2.3: Figure of **a)** the minimum (dashed lines), maximum (dashdot lines) and horizontal average (solid lines) temperatures and **b)** the radial velocity through the HP ice layer for a given $Ra_q/Ra_c = 10^5$ for $\Phi = 10^{-2}$ (blue lines) and $\Phi \to \infty$ (orange lines). The grey line in **a)** is for a null temperature.

In practice, where melt is present at the bottom, the situation is likely intermediate between the free-slip and no-slip boundary condition, depending on the thickness of the melt layer and the roughness of the interface. For the sake of simplicity, we consider the two end-member situations of a free-slip or no-slip bottom boundary condition.

2.3.2 Numerical method

The first step of this study, for each choice of input parameters as listed in table 2.1, consists in finding the critical Rayleigh number Ra_c for the onset of convection and the associated mode. For a Rayleigh number lower than Ra_c, the heat transfer within the HP ice layer occurs only by conduction. The conditions for the onset of convection are computed using a linear stability analysis described in subsection 2.3.2.1. Having determined the critical Rayleigh number, we use a mantle convection code to compute finite amplitude solutions,

Table 2.1: Detailed parameters applied to all simulations for each study-case. When several numbers are written in cells, the model has been run for all possible combinations.

Study case	Ra_q/Ra_c	Bottom boundary	Phase change at top	Φ	γ
SC1	$1.1, 2, 3, 4, 5, 6, 7, 8, 9, 10$	Freeslip	True	$10^{-2}, 10^{-1}, 1, 10, 10^2$	0.9,0.95
			False	∞	
SC2		Rigid	True	$10^{-2}, 10^{-1}, 1, 10, 10^2$	0.9,0.95
			False	∞	
SC3	$5.10^1, 1.10^2, 5.10^2, 1.10^3,$ $5.10^3, 1.10^4, 1.10^5$	Freeslip	True	$10^{-2}, 10^{-1}, 1, 10, 10^2$	0.9,0.95
			False	∞	
SC4		Rigid	True	$10^{-2}, 10^{-1}, 1, 10, 10^2$	0.9,0.95
			False	∞	

as explained in §2.3.2.2.

2.3.2.1 Linear stability analysis

The convection equations and their boundary conditions always admit a steady motionless solution in which heat is transferred by conduction only. In the present case, the steady conduction temperature profile is:

$$\overline{T} = \frac{r^{-^2}}{r} - r^{-}\gamma, \tag{2.15}$$

where $\gamma = r^-/r^+$, r^+ (resp. r^-) the dimensionless radius of the upper (resp. lower) boundary of the HP ice layer, with $r^+ - r^- = 1$ by our choice of the thickness of the layer as length scale to render the equations dimensionless.

Using StabLinRB (`https://github.com/amorison/stablinrb`), a free computational tool for linear stability analysis developed by Stéphane Labrosse and Adrien Morison [Labrosse et al., 2018, Morison et al., 2019, Morison, 2020], we looked for the stability of the conductive solution for each study case. Infinitesimally small perturbations are written as spherical harmonics with coefficient whose radial dependency is written as a sum of Chebyshev polynomials. Using differentiation matrices for this Chebyshev collocation approach, the linearized problem for each mode is transformed into a generalized eigenvalue problem. The critical Rayleigh number is the one that makes the real part of the eigenvalue change sign and the mode which has the minimum critical Ra is the most unstable one. You can refer to the studies of Morison [2020], Labrosse et al. [2018], Deguen [2013] and Deguen et al. [2013] for further details on the method used in our study for linear stability analysis and associated spherical harmonics.

2.3.2.2 Finite amplitude models

The convection equations (2.4–2.6) subject to the boundary conditions described in § 2.3.1.2 and 2.3.1.3 are solved using the mantle convection code StagYY [Tackley, 2008] in the

spherical annulus two-dimensional geometry [Hernlund and Tackley, 2008]. The runs have been divided into four main categories, low super-criticality ($Ra_c \leq Ra_q \leq 10Ra_c$) or high super-criticality ($Ra_q > 10Ra_c$) for both free-slip and rigid mechanical boundary condition at the bottom. In each category, values of the phase change parameter Φ were varied systematically in the range 10^{-2} to ∞ (no phase change), with two values of the aspect ratio, $\gamma = 0.9$ and 0.95 (see table 2.1). The runs are pursued until a statistically steady-state is reached, which is the case when all global diagnostics (mean temperature, heat fluxes at both boundaries, RMS velocity) only fluctuate around a time-independent mean. The chosen grid size depends on the simulation study-case and boundary conditions, in the form of $ny_{tot} \times nz_{tot}$, being the number of points in the HP ice shell respectively in the horizontal and vertical directions. The resolution is deemed sufficient when the global energy balance is satisfied. We performed calculations with increasing values of nz_{tot} until this criterion was satisfied, with ny_{tot} chosen such that the cells are nearly square (detailed values can be found in the table captions of the supplementary material, see appendix A). A vertical grid refinement depending on the study case is also applied at top and bottom boundaries. The geometry of the problem is adapted to the need of each simulation in order to capture the relevant flow structure: the convection equations can be solved either on the entire ice shell or only a part of it (see § 2.4.2 for detailed explanations).

As shown by Agrusta et al. [2020], the phase change boundary condition drastically changes the behaviour of the boundary layer (and therefore the convective dynamics) compared to the classical non-penetration BC. While in the classical situation, plumes originating from the opposite boundary have to turn when reaching a non-penetration boundary, which builds a boundary layer, they can here flow directly through the boundary by melting. This process still requires to adjust the temperature to that of the boundary but this happens on a distance much smaller than the thickness of a classical boundary layer. The thickness of a classical boundary layer is set by its stability, and typically scales as $Ra^{-1/3}$ for a fixed temperature free-slip situation. On the other hand, the thickness of a phase-change boundary layer is simply set by the rate of flow toward it $\delta \sim 1/w_{top}$ and we will show below that it therefore scales as $Ra_q^{-1/2}$. This boundary layer is not driving any dynamics but needs to be resolved to balance heat correctly, which rapidly becomes prohibitive (in terms of grid spacing and therefore time-step) at high Ra_q.

For this reason, while the fixed temperature boundary condition (eq. 2.11) is applied at the top boundary for runs close to the critical value of the Rayleigh number, we adopted another thermal boundary condition for cases with a high Rayleigh number and small value of Φ, as initially introduced by Agrusta et al. [2020]. The basic idea is to remove the very thin boundary layer from the calculation and apply a boundary condition relevant to what happens physically on the edge of that boundary layer. Mathematically, it is described as an intermediate condition between Dirichlet and Neumann boundary conditions, which respectively corresponds to a fixed temperature or flux condition. The intermediate Robin boundary condition is defined by the following equation [Agrusta et al., 2020]:

$$\Gamma\theta + (1 - \Gamma)\frac{\partial\theta}{\partial r} = 0, \tag{2.16}$$

where θ is the lateral deviation of temperature compared to the mean and Γ is an approximation of the Heaviside function:

$$\Gamma = \frac{1}{2}\left[1 + \tanh\left(\pi \frac{\frac{w_0}{2} - w_{top}}{\frac{w_0}{2}}\right)\right] \tag{2.17}$$

with w_0 a threshold velocity. In our study, we used $w_0 = 5.10^{-2} Ra_q^{\frac{2}{3}}$, in order to be about half the typical scaling of the RMS velocity in convection [Agrusta et al., 2020]. This function allows the boundary condition to switch smoothly between the Neumann and Dirichlet options, depending on the flow velocity. For rapidly up-welling flows, $w_{top} > w_0$, $\Gamma \simeq 0$ and we apply $\frac{\partial \theta}{\partial r} = 0$, which is expected for a hot plume rapidly melting in contact with the liquid. For downwelling or slowly upwelling ones, $w_{top} \leq w_0$, the normal fixed temperature condition can be imposed, $\theta = 0$. The validity of this approach has been checked by comparing the results to high resolution calculations using the Dirichlet BC (eq. 2.11).

2.4 Results

2.4.1 Onset of convection

Let us first discuss the results of the linear stability analysis that give the conditions for the onset of convection. The figure 2.4 shows the convective solution at onset (linear) in the HP ice layer for various values of Φ and different bottom boundary conditions. The linear problem depends on the degree of spherical harmonics but is degenerate in terms of order. For ease of representation and for comparison with the spherical annulus geometry used for the finite amplitude calculations, we represent the sectoral harmonics (i.e. with order equal to degree) in the equatorial plane. For a free-slip BC the critical Rayleigh number Ra_c and the number of convective rolls (spherical harmonics degree at onset) l_c of the first unstable mode are always lower than for a rigid BC. Also, both Ra_c and l_c increase with Φ (fig 2.5). It is particularly interesting to note that the most unstable mode for a free-slip BC and small values of Φ ($\Phi \leq 4$) is a degree 1 mode. A similar result was obtained in previous studies with an imposed temperature at the bottom [Deguen, 2013, Morison et al., 2019] and the present calculations extend that finding to the situation of an imposed bottom heat flux.

The impact of the boundary conditions can also be observed directly on the shape of flow lines (fig. 2.4). For small values of Φ, the phase change at the top is efficient and the flow lines are open at the top interface, while they are closed when $\Phi \to \infty$. Also, for a rigid BC at the bottom and a free-slip one at the top, the convective circulation is concentrated near the top interface since horizontal motion is not limited by that type of boundary.

Then, left and middle panels of figure 2.5 show respectively the evolution of the critical Rayleigh number Ra_c and critical wave-number l_c with the phase change number at the top boundary, Φ, depending on the bottom BC and the aspect ratio γ for the HP ice shell. In all cases, the critical Rayleigh number for the onset of convection increases with Φ, with important variations in the range Φ = 1–100. For a free-slip BC the convection starts for

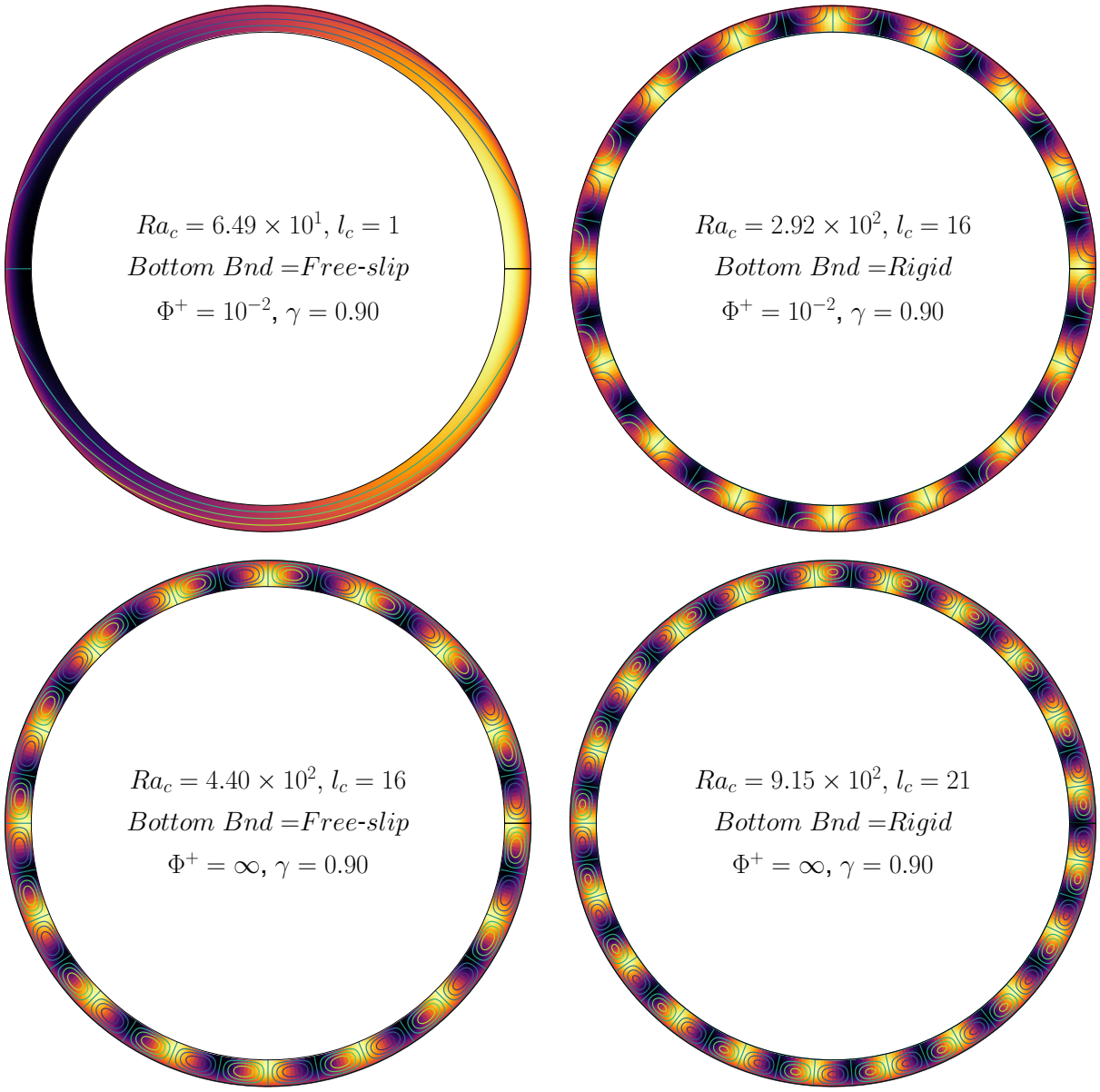

Figure 2.4: First unstable convective modes for $Ra_q = Ra_c$ as function the bottom boundary condition (Free-slip or rigid) and the value of the phase change parameter Φ. The color gives the temperature anomaly with respect to the steady conduction profile (arbitrary units, amplitude not constrained by the linear stability analysis) and the contours give the stream function. The input parameters and output critical Ra and wavenumber l_c are provided inside each shell.

lower values of Ra_c compared to a rigid BC, meaning that the convection is easier to start in that configuration. While the effect of the aspect ratio γ on Ra_c is limited, it is important for the wave-number, which is increasing with γ, except for a free-slip BC with $\Phi \leq 4$. The effect

of the aspect ratio on the wave-number for classical non-penetrating BC is well documented [Chandrasekhar, 1961] and is related to the linear stability in the case of planar layers. The large values of γ considered here make the shell close to being planar but changing γ modifies the number of convective rolls of a given aspect ratio (the one obtained for plane layers) that can fit in. The degree 1 mode obtained for low values of Φ and a free-slip bottom boundary condition can be understood when considering the flow presented on figure 2.4. In this case, down-welling occurs on the hemisphere where freezing happens, while up-welling occurs on the other hemisphere, where melting occurs. The return flow entirely happens in the liquid state, which is not treated explicitly. Such a flow in the solid minimizes the amount of deformation and, therefore, viscous resistance. For this reason, its critical Rayleigh number is much smaller than the one obtained at large values of Φ. This mode requires free-slip around the core and is suppressed when using rigid boundary conditions.

Applying the linear stability analysis to a specific ocean world as Ganymede, the critical thickness d_c of the HP ice layer for the onset of convection can be computed. The right panel of figure 2.5 shows the evolution of this parameter with Φ, depending on the bottom BC and the aspect ratio γ, using values listed in table 2.2, when considering reference values for the heat flux from the core $q = 10$ mW m^{-2} and for the viscosity of the ice $\eta = 10^{15}$ Pa s. Then, to start the convection on Ganymede considering these reference values, the minimum thickness has to be in 1.5–2.1 km range for a rigid BC and in 1–1.7 km range for a free-slip BC. For the reference HP ice thickness of 100 km, the Rayleigh is close to $Ra_q = 5 \times 10^8$ (see eq. 2.28), which is far above the critical value to onset the convection. However, in the context of planetary evolution, the thickness of the HP ice layer is expected to evolve and it is interesting to consider a full range, from the critical value to the large nominal value just mentioned. This is done using the finite amplitude convection code StagYY (§2.3.2.2).

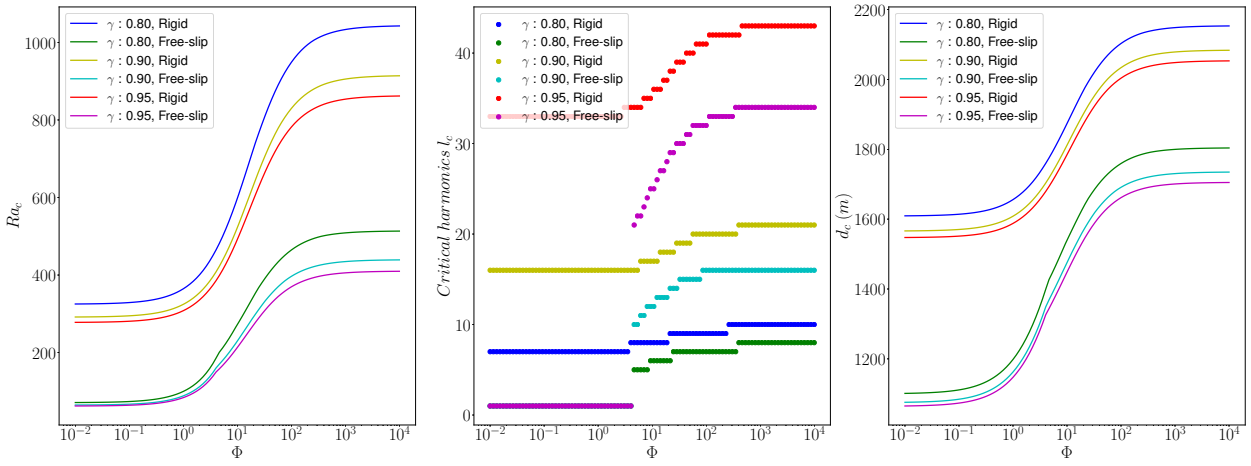

Figure 2.5: The three panels are showing, from left to right respectively, the critical Rayleigh number, critical wave-number and the minimum thickness d of the HP ice layer for the onset of convection as function of Φ, depending on the bottom boundary condition (BC) and the shell aspect ratio γ.

2.4.2 Finite amplitude calculations and scaling laws

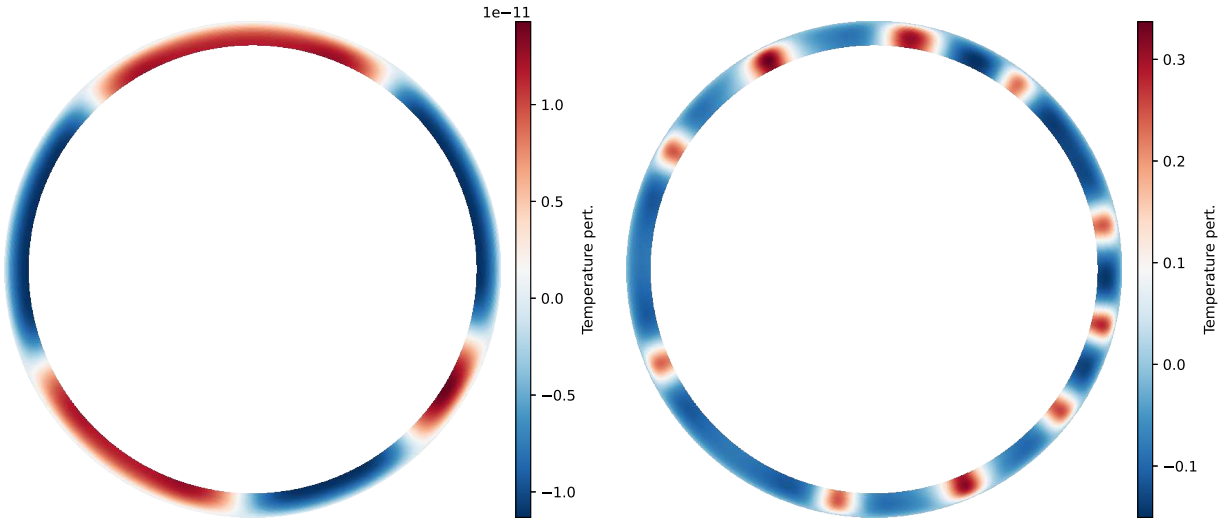

Figure 2.6: Snapshot of the perturbation temperature along the entire HP ice layer for $Ra_q = 1.1Ra_c$ (left) and $Ra_q = 2Ra_c$ (right) in the case of a free-slip BC for $\gamma = 0.9$ and $\Phi = 10^{-2}$.

We ran calculations systematically exploring a wide range of values of the main dimensionless input parameters, the Rayleigh number and the phase change number, with two values of the shell aspect ratio and two mechanical boundary conditions at the bottom. The longitudinal aperture of the HP ice layer on which the convection equations are solved is chosen carefully for each simulation in order to get at least one horizontal period. As can be seen on fig 2.5, in the case of a free-slip BC and a low value of Φ, the most unstable mode is of degree 1. Then, for low super-criticality cases, the runs have been done on the entire ice shell to capture the relevant flow structure. The figure 2.6 shows the perturbation temperature along the HP ice layer for two low super-criticality study-cases. When $Ra_q = 1.1Ra_c$ (left), a large scale flow is dominant and the simulation has to be solved on the entire ice shell. The fact that the dominant degree is not 1 but rather a combination of 2 and 3, contrary to the prediction of the linear stability analysis, can be explained by the initial conditions chosen for this calculations, a random white noise added to the steady conduction solution. Even though the degree 1 mode has a larger linear growth rate, if other modes with only slightly lower growth rates have a larger initial amplitude, they can take over and dominate in the non-linear calculation. When $Ra_q = 2Ra_c$ (right), the solution is already dominated by higher degree perturbations. In that case, as in the ones for $\Phi \geq 10$ or a rigid BC for which the critical harmonics l_c is at least around 10 (see fig 2.5), the simulations can be performed on a part of the shell to reduce the computational resources (detailed values can be found in the table captions of the supplementary material, see appendix A).

The first targets of our study concern the mass flux between the ice layer and the overlying ocean and heat transfer efficiency by convection in the ice layer. The former is quantified

by the root-mean-square (RMS, the mean being null by virtue of mass conservation) of the radial velocity at the top surface, w_{top}, while the latter is measured by the dimensionless mean temperature difference across the ice layer, $\Delta\bar{T}$, or its inverse, which, in our case of an imposed heat flux at the bottom, is precisely the Nusselt number, i.e. the ratio between the heat flux and what would be transported by steady-state conduction, $Nu = 1/\Delta\bar{T}$. In the following, we consider the lateral mean temperature $\bar{T}$, because as can be seen on fig.2.3a, its variation along the shell can be important. Fully detailed results tables and figures corresponding to the exploration of the parameters space for all cases described in table 2.1 can be found in the supplementary material (see appendix A).

Starting with the low super-criticality cases ($Ra_q \leq 10Ra_c$), figure 2.7 shows the evolution of both diagnostics, w_{top} and Nu, as function of Ra_q for both choices of bottom BC and various values of Φ. As expected, the values of w_{top} and Nu rapidly increase with Ra_q from their values at onset ($Ra_q = Ra_c$) of convection, 0 and 1, respectively. The increase rate with Ra_q gets larger when smaller values of Φ are considered. This behaviour is similar to the one obtained in a plane layer with different boundary conditions [Agrusta et al., 2020].

Figure 2.8 shows the global diagnostics w_{top} and Nu for both choices of bottom BC and various values of Φ for larger values of Ra_q (SC3 and SC4, see table 2.1). Since these diagnostics and Ra_q vary on several orders of magnitude, the plots use log-log scales. As expected, the values of w_{top} and Nu increase with Ra_q as power laws. We can also see that, for a given value of Ra_q, w_{top} and Nu increase when decreasing Φ, as the top boundary becomes progressively more permeable. The evolution of the Nusselt number saturates at some point which seems to depend on the value of Ra_q and the mechanical boundary condition at the bottom: for a rigid BC, the value for $\Phi = 100$ is similar to that for lower values at large values of Ra_q but is intermediate for small values of Ra_q. For this reason, the exponent of the $Nu = f(Ra_q)$ law is different for $\Phi = 100$ than for other choices of that parameter.

Each combination of choice of BC and Φ value leads to a power law relationship of the form:

$$w_{top} = a_w Ra_q^{\beta_w}, \tag{2.18}$$

$$Nu = \frac{1}{\Delta\bar{T}} = a_T Ra_q^{\beta_T}, \tag{2.19}$$

(a_w, β_w) being the scaling coefficients for the top radial velocity and (a_T, β_T) being those for the Nusselt number. These scaling coefficients depend on the value of the phase change number Φ and the mechanical boundary condition at the bottom.

As can be seen on figure 2.8, the exponents β_x depend on the choice of boundary condition but weakly on Φ. On the other hand, the coefficients a_x depend strongly on Φ, as shown on fig. 2.9 on which a_w is plotted as function of Φ. In the case of a rigid BC, we get $\beta_w = 0.47$–0.53, i.e. close to 1/2, and $\beta_T = 0.2$–0.22, i.e. close to 1/5. In the case of a free-slip BC, we obtain $\beta_w = 0.45$–0.55 which is also similar to 1/2 but $\beta_T = 0.22$–0.24 is close to 1/4. The differences in exponents between the free-slip and no-slip BCs have been explained with some theoretical models in a different context, notably using a fixed boundary

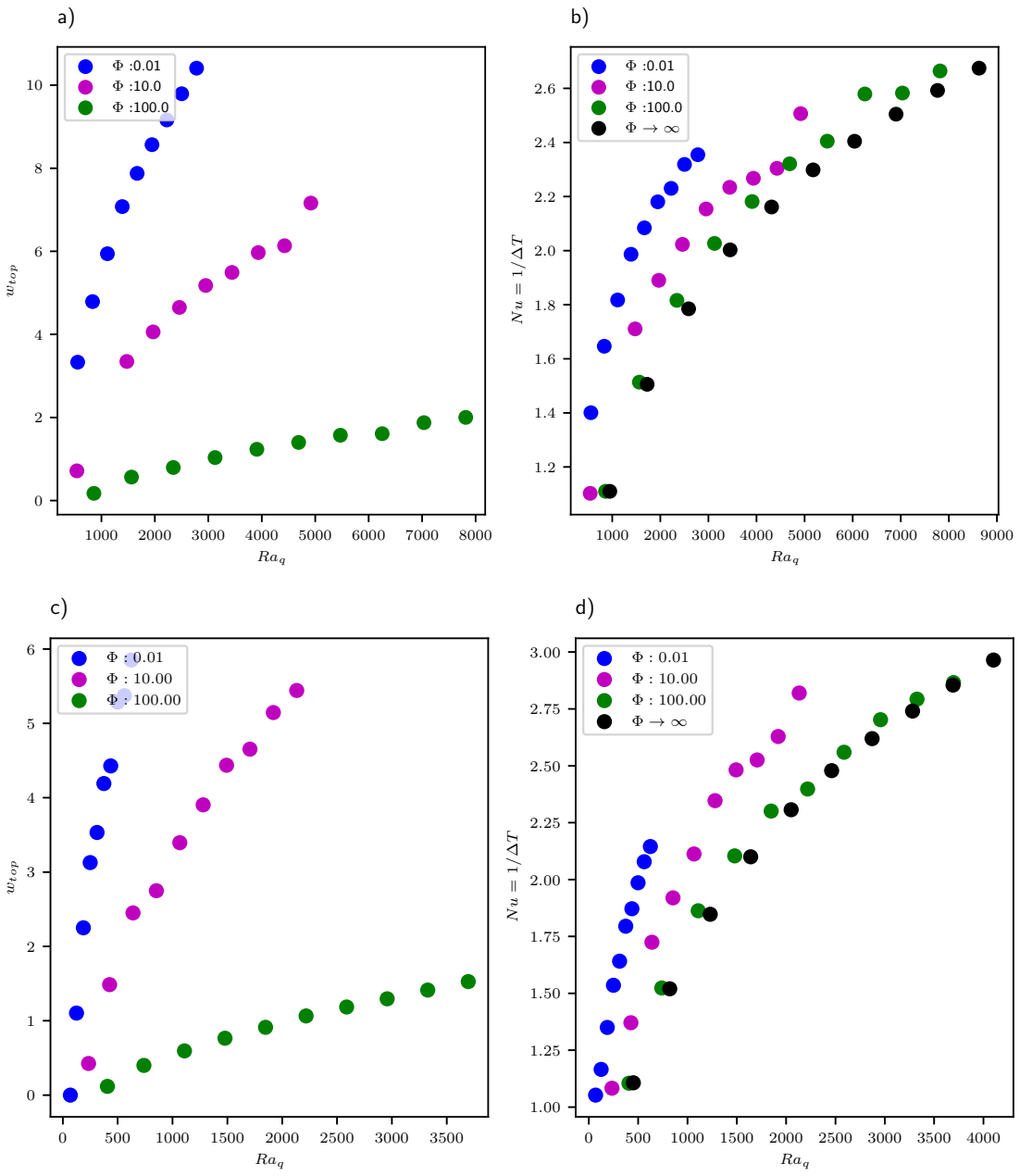

Figure 2.7: Cases $Ra_q \sim Ra_c$ for a rigid bottom BC (a)&(b) and a free-slip bottom BC (c)&(d). Left panels (a)&(c) show the dimensionless radial velocity at the top boundary of the HP ice layer, w_{top}. Right panels (b)&(d) show the dimensionless heat flux (Nusselt number). Both parameters are shown as functions of the Rayleigh Number Ra_q and for various values of Φ.

condition on both boundaries [e.g. Roberts, 1979]. Adapting that theory to the present situation falls beyond the scope of this paper but we can explain in a simpler way how β_T

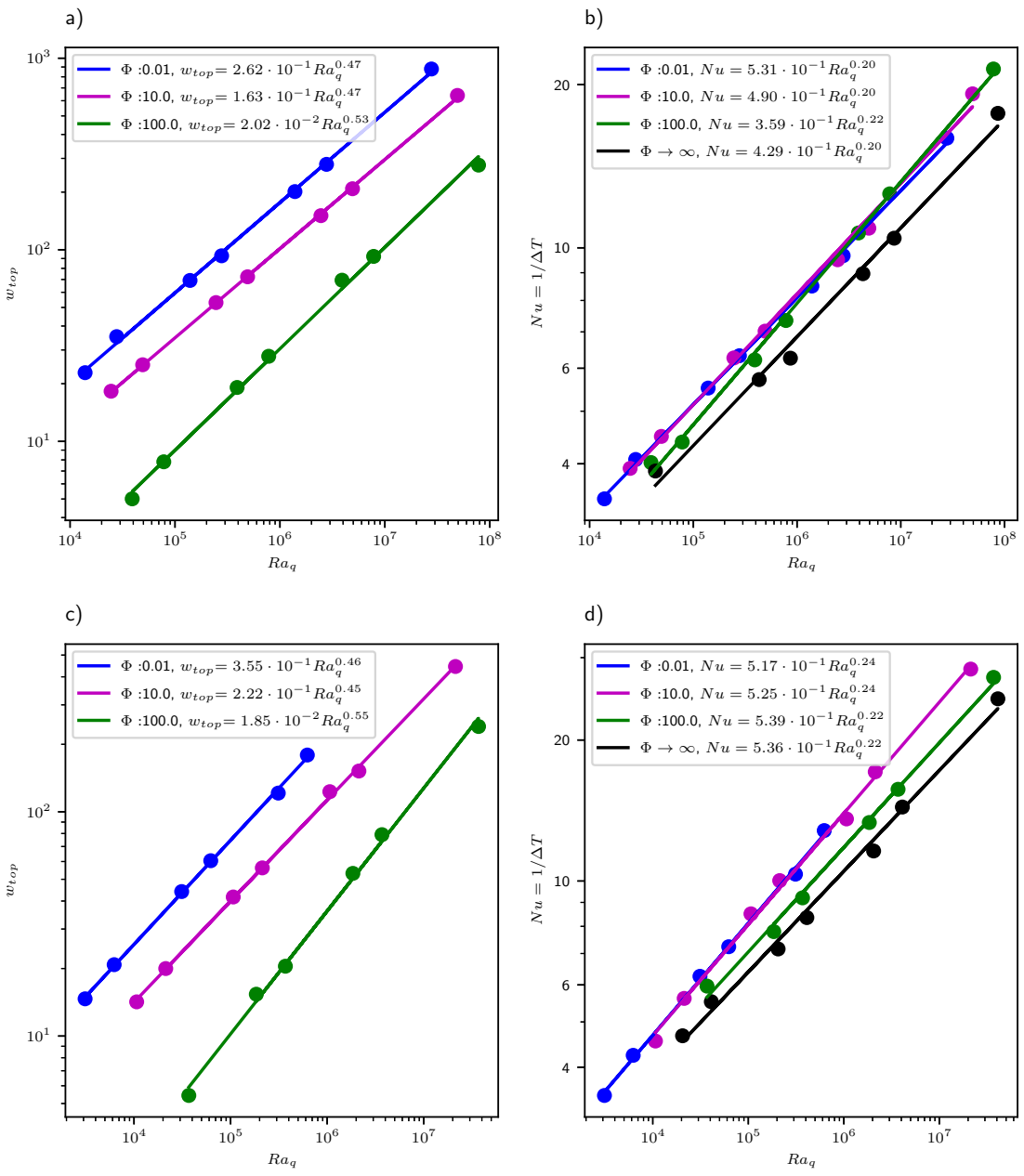

Figure 2.8: Cases $Ra_q \geq 50 Ra_c$ for a rigid bottom BC (a)&(b) and a free-slip bottom BC (c)&(d). Left panels (a)&(c) show the dimensionless radial velocity at the top boundary of the HP ice layer. Right panels (b)&(d) show the dimensionless heat flux (Nusselt number). Both parameters in function of the Rayleigh Number and for various values of Φ.

can be justified.

The β_T exponents can be obtained theoretically using the argument of the stability of boundary layers [Malkus, 1954]: the thickness of the boundary layer is set by its stability,

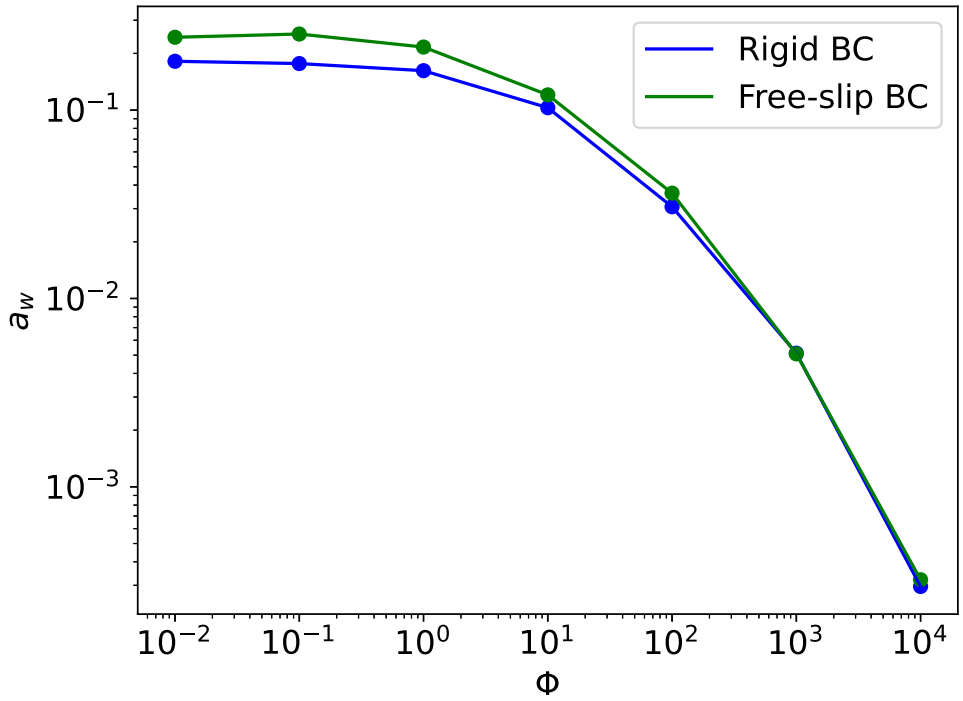

Figure 2.9: Variation of the coefficient a_w of the scaling law for the radial velocity at the top boundary as function of the phase change number Φ (See eq. 2.18). For each value of Φ, it is computed as the mean of $w_{top}/Ra_q^{\frac{1}{2}}$ over values of Ra_q.

therefore its Rayleigh number, Ra_δ. The existence of a boundary layer at the top interface depends on the value of Φ. As shown on the average temperature profiles on figure 2.3a, when $\Phi \to 0$, the boundary layer disappears at the top interface and only one boundary layer of thickness δ' has to be considered at the bottom interface, while there are two boundary layers of thickness δ' in the case $\Phi \to \infty$. For a free-slip BC at the bottom interface, when $\Phi \to 0$,

$$Ra_\delta = Ra_q \Delta\bar{T}\delta^3 = A \tag{2.20}$$

with Ra_δ the Rayleigh number of the boundary layer, $\delta = \delta'/d$ the dimensionless thickness of the boundary layer and A a constant related but not exactly equal to the critical Rayleigh number for the instability of the boundary layer [Howard, 1964, Sotin and Labrosse, 1999]. As $q' = k\frac{\Delta\bar{T}'}{\delta'}$, primed variables being dimensional, is used to scale temperature, its dimensionless value is equal to 1 and $1 = \frac{\Delta\bar{T}}{\delta}$. Combining with equation 2.20 gives

$$Nu = A^{-\frac{1}{4}} Ra_q^{\frac{1}{4}}. \tag{2.21}$$

With this simple argument, we obtain the exponent $\beta_T = 1/4$. The coefficient $a_T = A^{-\frac{1}{4}}$ cannot easily be predicted from first principles [Sotin and Labrosse, 1999].

On the other hand, when $\Phi \to \infty$, the coefficient β_T should be the same, but the variation of the a_T coefficient can be computed in order to better understand the figure 2.8. The derivation is similar but the temperature jump is now split between the two boundary layers. Neglecting the effect of curvature for simplicity, since the aspect ratio of the shell is large [see Sotin and Labrosse, 1999, for a more complete derivation], we can assume that each boundary layer takes an equal share of the total temperature jump, therefore

$$Ra_\delta = Ra_q \frac{\Delta\bar{T}}{2}\delta^3 = A \tag{2.22}$$

and the dimensionless heat flux from the core is $1 = \frac{\Delta\bar{T}}{2\delta}$. Then,

$$Nu = \frac{1}{2}A^{-\frac{1}{4}}Ra_q^{\frac{1}{4}}. \tag{2.23}$$

As expected for such a reasoning, we get the same exponent but a different expression for the coefficient, $a_T = \frac{1}{2}A^{-\frac{1}{4}}$. We can assume that the dynamics of the bottom boundary layer is entirely determined by its own stability, which implies that the value of A is independent from Φ. In that case, we expect the Nusselt number to change by a factor of 2 between the $\Phi \to 0$ and $\Phi \to \infty$ limits, which is larger but similar to what can be seen on figure 2.8 for a free-slip BC.

Using a more sophisticated theory, Roberts [1979] obtained scaling laws for convection with both free-slip and no-slip boundary conditions, both considering fixed temperature thermal boundary conditions. In both cases, he obtained a scaling relationship $Nu = aRa^\beta$, with $\beta = 1/3$ for free-slip BCs and $\beta = 1/5$ for rigid BCs. In order to compare these scaling laws to our results, we need to account for the change of definition for the Rayleigh number:

$$Ra_q = Ra\frac{q'd}{k\Delta\bar{T}'}. \tag{2.24}$$

Then,

$$q' = Nu\frac{k\Delta\bar{T}'}{d} = a\frac{k\Delta\bar{T}'}{d}\left(\frac{\alpha g\rho\Delta\bar{T}'d^3}{\kappa\eta}\right)^\beta \tag{2.25}$$

which gives us $1/\Delta\bar{T}'$ and

$$Nu = \frac{1}{\Delta\bar{T}} = \frac{1}{\Delta\bar{T}'}\frac{q'd}{k} = a^{\frac{1}{\beta+1}}Ra_q^{\frac{\beta}{\beta+1}}. \tag{2.26}$$

Finally, for a rigid BC,

$$Nu = a_T Ra_q^{\frac{1}{6}}, \tag{2.27}$$

a_T being different than previously (See figure 2.8.d for values).

2.4.3 Numerical applications to planetary objects

In this section, we show how the dimensionless results obtained in our study can be applied to various planetary objects using numerical values listed in table 2.2 to get dimensional results regarding the mass flux across the ice-ocean interface and the bottom temperature. Some parameters are assumed to be known, essentially because they are not expected to be too much in error with respect to the listed values. On the other hand, we express our results in a way that permits to see the effects of a change in the heat flux from the core, the thickness of the HP ice layer and the ice viscosity, over reference values, all having highly uncertain values.

2.4.3.1 Application to Ganymede

Ganymede is the largest moon of the solar system, with a water-ice shell thickness in the 600–900 km range [Hussmann et al., 2015]. The HP ice layer thickness is estimated between 100 and 400 km [Kalousová et al., 2018]. For this numerical application we consider a HP ice layer reference thickness of 100 km, a reference heat flux from the core of 10 mW m^{-2} and a reference ice VI viscosity of 10^{15} Pa s [Kalousová et al., 2018]. With these parameters, the Rayleigh number can be computed as

$$Ra_q = \frac{\alpha g q \rho d^4}{k\kappa\eta} = 4.85 \times 10^8 \left(\frac{q}{10 \text{ mW m}^{-2}}\right)\left(\frac{d}{100 \text{ km}}\right)^4\left(\frac{\eta}{10^{15} \text{ Pa s}}\right)^{-1} \tag{2.28}$$

It shows that the reference values give a large value of the Rayleigh number, of order 5×10^8, and larger values can be obtained for a thicker layer, a larger heat flow from the core or a lower ice viscosity. The reference value is already quite large, in particular compared to the critical value for the onset of convection for $\gamma = 0.9$, which is in the range $Ra_c = 65 - 915$, depending on the bottom BC and the value of Φ (see fig 2.4). All other parameters being kept identical, the critical value $Ra_c = 292$ for a rigid bottom BC when $\Phi = 10^{-2}$ is reached for a thickness of the ice layer around 1.6 km (see fig 2.5).

Considering first the situation for which the bottom boundary of the HP ice shell of Ganymede is a no-slip one (i.e. in the absence of liquid water to lubricate that boundary) and the phase change at the top boundary is fast, $\Phi = 10^{-2}$, with an aspect ratio $\gamma = 0.95$, from the scaling laws obtained in § 2.4.2 on figure 2.8:

$$w_{top} = 0.262 Ra_q^{0.47}\frac{\kappa}{d} = 42.9 \text{ cm yr}^{-1}\left(\frac{q}{10 \text{ mW m}^{-2}}\right)^{0.47}\left(\frac{d}{100 \text{ km}}\right)^{0.88}\left(\frac{\eta}{10^{15} \text{ Pa s}}\right)^{-0.47}, \tag{2.29}$$

$$\frac{1}{\Delta\bar{T}} = 0.531 Ra_q^{0.2}\frac{k}{qd} = 4.6 \times 10^{-2} \text{ K}^{-1}\left(\frac{q}{10 \text{ mW m}^{-2}}\right)^{-0.8}\left(\frac{d}{100 \text{ km}}\right)^{-0.2}\left(\frac{\eta}{10^{15} \text{ Pa s}}\right)^{-0.2}. \tag{2.30}$$

Table 2.2: Detailed numerical application parameters for Ganymede from Kalousová et al. [2018] and a water-rich exoplanet from Hernandez et al. [2022].
* Are the reference values used in the numerical application in section 2.4.3.1
[a] Hussmann et al. [2015].
[b] Valid for the reference thickness d of the HP ice layer chosen for Ganymede.
[c] Bridgman [1912, 1937] (Valid for the water-rich exoplanet at the ice/ocean interface).
[d] Valid at ice/ocean interface [Tchijov, 2004].

Parameter	Symbol	Ganymede	Water-rich exoplanet	Unit
Thermal expansivity	α	1.5×10^{-4}	2×10^{-4}	K^{-1}
Gravity	g	1.6	8.4	m s^{-2}
Thermal conductivity	k	1.6	1.6	$Wm^{-1}K^{-1}$
Thermal diffusivity	κ	4.3×10^{-7}	4.3×10^{-7}	m^2s^{-1}
Reference density	ρ	1390	2×10^3	kgm^{-3}
Density difference at R^+	$\Delta\rho$	160	-	kgm^{-3}
HP ice viscosity	η	$^*10^{15} - 10^{17}$	10^{17}	Pa s
Heat flux for silicate core	q	$^*10 - 40$	30	mWm^{-2}
HP ice thickness	d	$^*100 - 400$	260	km
Core radius	R^-	$1\,700 - 2\,000^a$	5 000	km
Melting temperature at R^+	T_m^+	321^b	367	K
Melting temperature at R^-	T_m^-	332^b	800	K
Pressure at R^+	P^+	$1\,378^b$	2×10^3	MPa
Pressure at R^-	P^-	$1\,600^b$	$30 \times 10^3 - 40 \times 10^3$	MPa
Latent heat	L	334^c	350^c	kJ kg^{-1}
Heat capacity	C_p	2 850	$2\,850^d$	J kg^{-1} K^{-1}

The scaling relationship for the temperature difference across the ice layer can be used to compute the mean temperature at the ice-rock interface $\bar{T}^-$ from the one at the ice-ocean interface T^+ as:

$$\bar{T}^- = \Delta\bar{T} + T^+ = 343\text{K} \tag{2.31}$$

with $T^+ = T_m^+ = 321$ K (see table 2.2) the melting temperature of ice VI at the pressure relevant for the ice-ocean boundary [Kalousová et al., 2018, Bridgman, 1912, 1937]. This temperature, obtained for our reference parameters (eq. 2.30), should be compared to the melting temperature of ice VI at the pressure relevant for the ice-rock boundary $T_m^- = 332$ K [Kalousová et al., 2018, Bridgman, 1912, 1937]. This means that taking the nominal values for all the parameters implies a large amount of melting at the bottom of the ice layer. All these parameters being quite uncertain, we can instead compute the value of any chosen

Table 2.3: Results to the numerical applications to Ganymede using parameters from table 2.2, for $\Phi = 10^{-2}$ and $\gamma = 0.95$.

Bottom BC	Rigid	Free-slip
Ra_q	4.85×10^8	4.85×10^8
w_{top} (cm yr^{-1})	42.9	47.6
$1/\Delta\bar{T}$ (K^{-1})	4.6×10^{-2}	0.1
$\bar{T}^-$ (K)	343	331

parameter such that the bottom temperature is equal to the melting one, all other parameters being kept the same. The melting temperature values T_m^- and T_m^+ respectively at the bottom and the top of the HP ice layer depend on the pressure at these corresponding depths and, then, for a fixed rocky core radius, on the thickness d of the ice shell. For example, still in the case of a rigid bottom BC, for a fast phase change $\Phi = 10^{-2}$ at the top boundary and taking the reference values for d and η, it is possible to compute the minimum value q_l of the heat flux for which $\bar{T}^- = T_m^-$ as follow:

$$q_l = \frac{k\Delta T_m}{d} a_T^{1/(1-\beta_T)} \left(\frac{\alpha g \rho d^3 \Delta T_m}{\kappa \eta} \right)^{\beta_T/(1-\beta_T)} = 4.3 \text{ mW m}^{-2} \tag{2.32}$$

with $\Delta T_m = T_m^- - T_m^+$. Note that the expression in brackets is simply the Rayleigh number of the layer based on the temperature difference ΔT_m. For a rigid BC, even a heat flux from the core as small as 4.3 mW m^{-2} could be sufficient to melt the bottom of the HP ice layer in Ganymede. This is further discussed in §2.5.

These calculations have also been performed for a free-slip BC and the results can be seen in table 2.3 for comparison. As expected, the free-slip situation leads to a convection that is faster, more efficient to transfer heat and therefore to a cooler bottom temperature. Then, $\bar{T}^-$ does not reach the melting temperature when using the reference values of table 2.2 for d, q and η. Indeed, a minimum heat flux of 11.4 mW m^{-2} would be necessary in the case of a free-slip BC for the mean temperature to equal the melting temperature. However, the obtained temperature is the lateral mean one, which varies a lot along the shell (See fig.2.3a), and is only one Kelvin under T_m^-, meaning that pockets of melt likely exist along the bottom boundary. In addition, the parameters chosen here for Ganymede are rather conservative and it is in fact likely that significant melting actually occurs.

2.4.3.2 Application to a water-rich exoplanet

To compare with a larger planetary object, a numerical application has been performed on a hypothetical ocean exoplanet modelled as described on figure 2.1, with a surface ocean instead of ice Ih. All the values considered for this application are coming from the study of Hernandez et al. [2022] with some adjustments to match the conditions used here. We

consider a rocky core/mantle of density $\rho_c = 6 \times 10^3$ kg m^{-3} with a radius $R_c = 5\ 000$ km and a HP ice shell thickness of around $d = 260$ km in order to have an aspect ratio $\gamma = 0.95$ as the scaling laws of part § 2.4.2 are computed for this value. The aspect ratio considered by Hernandez et al. [2022] is ~ 0.6 and the HP ice layer thickness considered in their study is much larger than the one used for the current numerical application. Therefore the melting temperature at the top boundary has to be adjusted and is computed as

$$T_m = T_m^+ + (T_m^- - T_m^+)\frac{P - P^+}{P^- - P^+}, \tag{2.33}$$

with

$$P = P^- - \rho g z. \tag{2.34}$$

The pressure considered in Hernandez et al. [2022] at the bottom of the HP ice layer is in the range $30-40$ GPa for a melting temperature $T_m^- = 800$ K, which corresponds to ice VII. The melting temperature at the top of their HP ice layer is $T_m^+ = 367$ K, which implies a pressure of about 2 GPa for ice VII. Then, we can compute the pressure 260 km above the ice/core boundary, which is the top of the HP ice layer in our case. This value should be in the range $25 - 35$ GPa and the melting temperature associated is around 730 K. The gravitational acceleration is computed as function of R_c and ρ_c as $g = 4\pi G \rho_c R_c/3 = 8.4$ m s^{-2} with $G = 6.67 \times 10^{-11}$ m^3 kg^{-1} s^{-2}.

The heat flux from the core depends on the composition of the star, which will imply more or less radioactivity inside the planet. If we consider a star similar to ours, the heat flux is function of the core radius. For a given concentration in heat producing elements, the total radiogenic heating in the core scales as R_c^3 while the surface scales as R_c^2 and, therefore, its contribution to the heat flux density scales as R_c. As the value of R_c chosen for our application is ~ 2.5–3 times higher than the one of Ganymede, the heat flux should be about 3 times higher. For this numerical application we consider a reference heat flux from the core of 30 mW m^{-2} and a reference ice VI viscosity of 10^{17} Pa s. With these parameters, the Rayleigh number Ra_q, the radial velocity at ocean/ice interface w_{top} and the Nusselt number $\frac{1}{\Delta \overline{T}}$ for a rigid BC and a fast phase change $\Phi = 10^{-2}$ at the top boundary have been computed as follows:

$$\begin{aligned} Ra_q = \frac{\alpha g q \rho d^4}{k \kappa \eta} = 6.7 \times 10^9 &\left(\frac{R_c}{5\ 000 \text{ km}}\right)\left(\frac{q}{30 \text{ mW m}^{-2}}\right) \\ &\left(\frac{d}{260 \text{ km}}\right)^4 \left(\frac{\eta}{10^{17} \text{ Pa s}}\right)^{-1}, \end{aligned} \tag{2.35}$$

$$\begin{aligned} w_{top} = \frac{\kappa}{d} 2.62 \times 10^{-1} \times Ra_q^{0.47} = 57 \text{ cm yr}^{-1} &\left(\frac{R_c}{5\ 000 \text{ km}}\right)^{0.47} \left(\frac{q}{30 \text{ mW m}^{-2}}\right)^{0.47} \\ &\left(\frac{d}{260 \text{ km}}\right)^{0.88} \left(\frac{\eta}{10^{17} \text{ Pa s}}\right)^{-0.47}, \end{aligned} \tag{2.36}$$

Table 2.4: Results to the numerical applications to an ocean exoplanet using parameters from table 2.2, for $\Phi = 10^{-2}$ and $\gamma = 0.95$.

Bottom BC	Rigid	Free-slip
Ra_q	6.7×10^9	6.7×10^9
w_{top} (cm yr^{-1})	57	61
$1/\Delta\bar{T}$ (K^{-1})	1×10^{-2}	2.4×10^{-2}
$\bar{T}^-$ (K)	830	772

$$\frac{1}{\Delta\bar{T}} = \frac{k}{qd} 5.31 \times 10^{-1} Ra_q^{0.2} = 1 \times 10^{-2} \text{ K}^{-1} \left(\frac{R_c}{5\ 000 \text{ km}}\right)^{0.2} \left(\frac{q}{30 \text{ mW m}^{-2}}\right)^{-0.8} \left(\frac{d}{260 \text{ km}}\right)^{-0.2} \left(\frac{\eta}{10^{17} \text{ Pa s}}\right)^{-0.2}. \tag{2.37}$$

The results can be found in table 2.4 for comparison between rigid and free-slip boundary conditions and with Ganymede numerical application given in table 2.3. Obviously, the reference Rayleigh number is higher in the case of a large ocean exoplanet than for a Ganymede-like body, meaning a more efficient convection leading to a higher Nusselt number and a lower dimensionless $\Delta\bar{T}$, but a larger dimensional temperature gap between the two HP ice layer boundaries. But, the layer being ~ 2.5 times thicker, the melting temperature gap between boundaries is also important and this should not have a huge impact on the melt production at the core/ice interface. For the same efficiency of the phase change at the top, the melting ability at the bottom of the HP ice layer, looking at the temperatures $\bar{T}^-$ obtained, are comparable to the Ganymede case, but the difference of bottom temperature between rigid and free-slip BC seems to be more pronounced in the case of a large water-rich exoplanet. In fact, for both objects, the temperature difference across the ice layer is roughly twice larger for a rigid boundary condition than for a free-slip one. Scaling back to dimensional units for a larger object leads however to larger dimensional differences. In the case computed here, $\bar{T}^-$ does not reach T_m^- for a free-slip BC but it does for a rigid boundary condition. First of all, as already discussed above for the application to Ganymede, the exact parameters for this application are subject to discussion and higher temperatures are possible. But the fact that a free-slip boundary condition leads to a lower value of the bottom temperature than a rigid one remains and this could lead to a conundrum: the free-slip BC that is justified by the presence of melt could predict its absence while the rigid BC that results from the absence of melt could predict its presence. In this case, we would expect a mixed situation with the presence of melt where the temperature is high and its absence elsewhere with a non-uniform boundary condition that depends on the local temperature. Such a situation could be the topic of future studies.

Finally, the vertical velocity at the top of the HP ice layer, w_{top}, is larger for this study case, meaning that the mass transfer between the core and the ocean should be more impor-

tant.

2.5 Discussion

The model and results presented above are simple and concentrate on one effect not considered before, the phase-change boundary condition at the upper boundary. We showed that this effect alone is sufficient to considerably alter the solution, its structure and the efficiency of heat and mass transfer. Interestingly, the temperature profiles we obtain are similar to the ones Kalousová et al. [2018] and Kalousová and Sotin [2018] obtained with a mechanical conditions that is non-penetrative for the solid but considering the possibility of partial melting in the bulk of the ice layer and extraction of the liquid.

As mentioned before, in this study we considered the HP ice layer as an isoviscous material, for the sake of simplicity, while the viscosity is expected to depend on pressure, temperature and melt fraction [Choblet et al., 2017, Kalousová and Sotin, 2018, Kalousová et al., 2018]. To get a hint on the potential effect of viscosity variations, we performed a single simulation with a depth- (pressure-) and temperature-dependent viscosity following the dimensionless Arrhenius law established so that the surface viscosity serves as reference in the Rayleigh number:

$$\eta = \exp\left(\frac{E + (1-z)V}{T+1} - E\right), \tag{2.38}$$

with E and V the dimensionless activation energy volume. The values $E = 230$ and $V = 4.6$ are chosen for the simulation to be comparable with the ones of Choblet et al. [2017]. This simulation has been ran for a rigid bottom boundary condition, $\Phi = 10^{-2}$ and $Ra_q = 10^6$.

As can be seen on fig 2.10, the lowest viscosity is located at the bottom boundary and inside the up-welling hot plumes. This is consistent with the fact that the temperature is higher in these locations and could reach the melting temperature, implying the formation of melt and a lower viscosity. Beside that obvious difference in viscosity, the thermal structure of the solution is similar to that obtained with a constant viscosity, with a boundary layer at the bottom from which hot plumes originate and a passive downward return flow whose temperature is that of the upper boundary. Comparing fig 2.11.a and fig 2.11.b, we can see that our chosen viscosity law (eq.2.38) makes it increase by 10^2 with depth and vary by more than six orders of magnitude with temperature. Also, we can observe on fig 2.11.c that the RMS radial velocity curve shape is slightly different than the one for an isoviscous calculation (as can be seen on the blue curve of fig 2.3.b). In both cases, the radial velocity increases with height in the layer, but the curvature are somewhat different. Of particular interest here are the local maximum reached in the bottom boundary layer, where the viscosity is lowest and the increase when getting close to the upper boundary, because of the decrease of the viscosity with height. When the statistically steady-state is reached, the time-averaged Nusselt number is $Nu = 12.8$ and the time-averaged radial velocity at the top is $w_{top} = 264.9$. From the scaling obtained in § 2.4.2 for a constant viscosity and the same boundary conditions (See fig 2.8.a and fig 2.8.b), the Rayleigh number corresponding to the radial

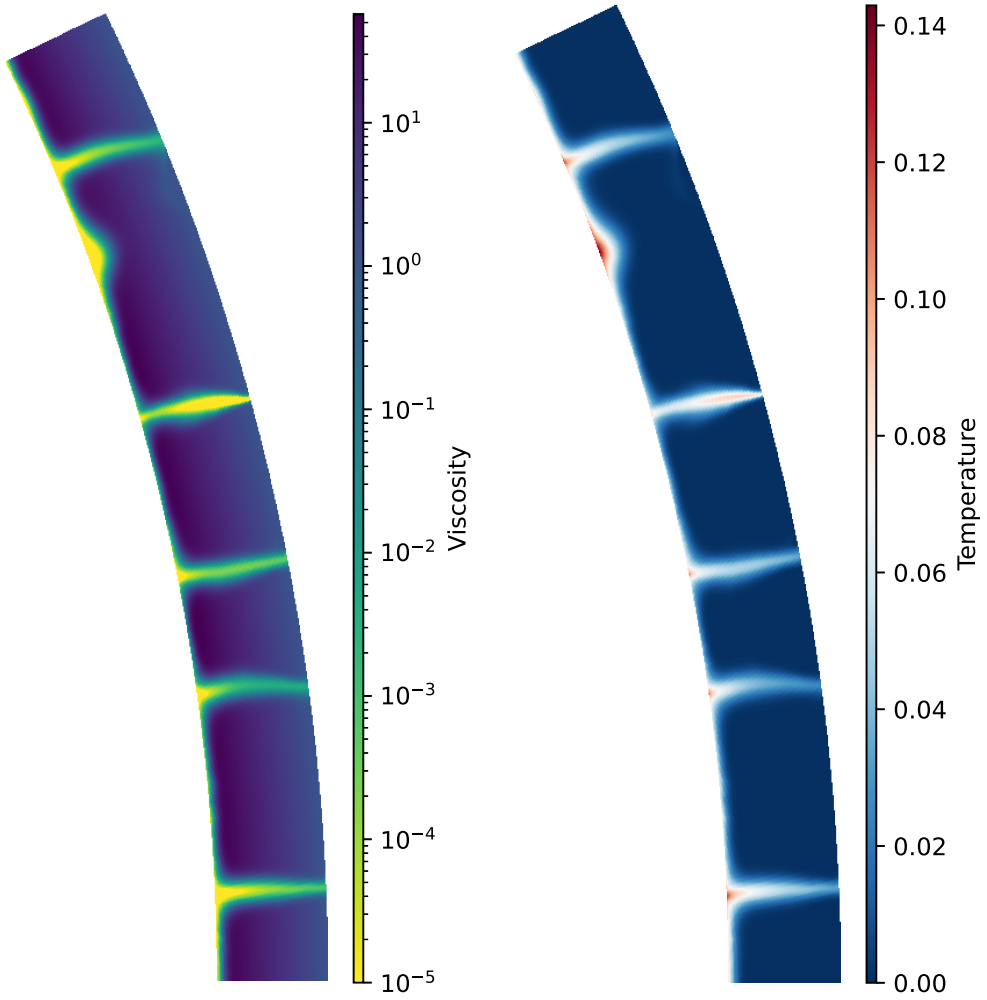

Figure 2.10: Snapshots of 1/14 of the HP ice shell for $Ra_q = 10^6$, $\Phi = 10^{-2}$ and a rigid bottom boundary condition. The left (respectively right) panel shows the viscosity variations (respectively temperature) through the HP ice layer.

velocity at the top is $Ra_w = 2.5 \times 10^6$ and the one corresponding to the Nusselt number is $Ra_{Nu} = 8.1 \times 10^6$, compared to the nominal value of 10^6 used for this calculation. It means that the calculation with this type of viscosity variation leads to results similar to those obtained with a constant viscosity but a slightly larger Rayleigh number. This is not surprising since the average viscosity is lower than one. It would however be worth exploring these effects more systematically in the future, especially if we take into account partial melting.

As already mentioned (§2.4.2), for some values of the input parameters, we predict a temperature at the bottom of the ice layer that is larger than the melting temperature. This should result in the presence of melt, either everywhere or restricted to melt pockets, since the temperature is laterally variable. This melt, containing salts by interacting with the

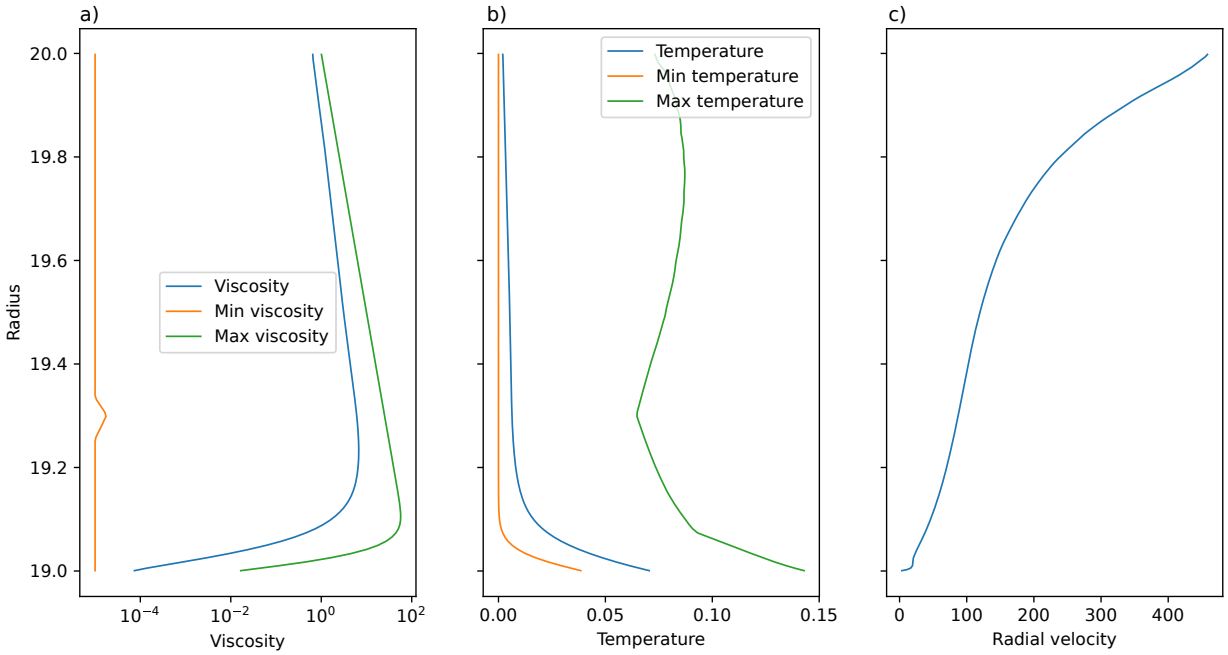

Figure 2.11: Radial profiles of the minimum (orange), maximum (green) and horizontal average (blue) viscosity (a) and temperatures (b). c) shows the RMS radial velocity profile through the HP ice layer. All the panels come from a varying viscosity simulation made with $Ra_q = 10^6$, $\Phi = 10^{-2}$ and a rigid bottom boundary condition.

core, could be transported to the ocean by various processes, as modeled by Kalousová et al. [2018]. This partial melting process has not been considered in this preliminary study, which only takes into account solid-state convection through the HP ice layer, but could have an important impact on the efficiency of the mass transfer. To justify the need of adding this property in future models, we computed the regions where melting would happen and the amount of melt produced in considering Ganymede's HP ice layer if the temperature field we obtained was not too affected by the presence of melt. This is obviously a very crude assumption but it can be useful to provide a first order estimate. For this calculation, we use the same reference values than previously used in § 2.4.3.1 and other parameters from table 2.2. The variations of the melting temperature T_m of ice VI as function of pressure P has been computed from eq. 2.33, with $P = P^+ + \rho g z$, using values given in table 2.2.

Comparing the actual temperature at each point to the melting value at the same position allows to find places that would be expected to partially melt. For regions where the temperature $T > T_m$, the melting temperature at this depth, partial melting should occur and this should limit the temperature to the melting one, at least as long as the melt fraction is lower than 1. We compute the expected melt fraction by equating the energy associated with the temperature in excess to the melting temperature, $\Delta T = T - T_m$, to latent heat of

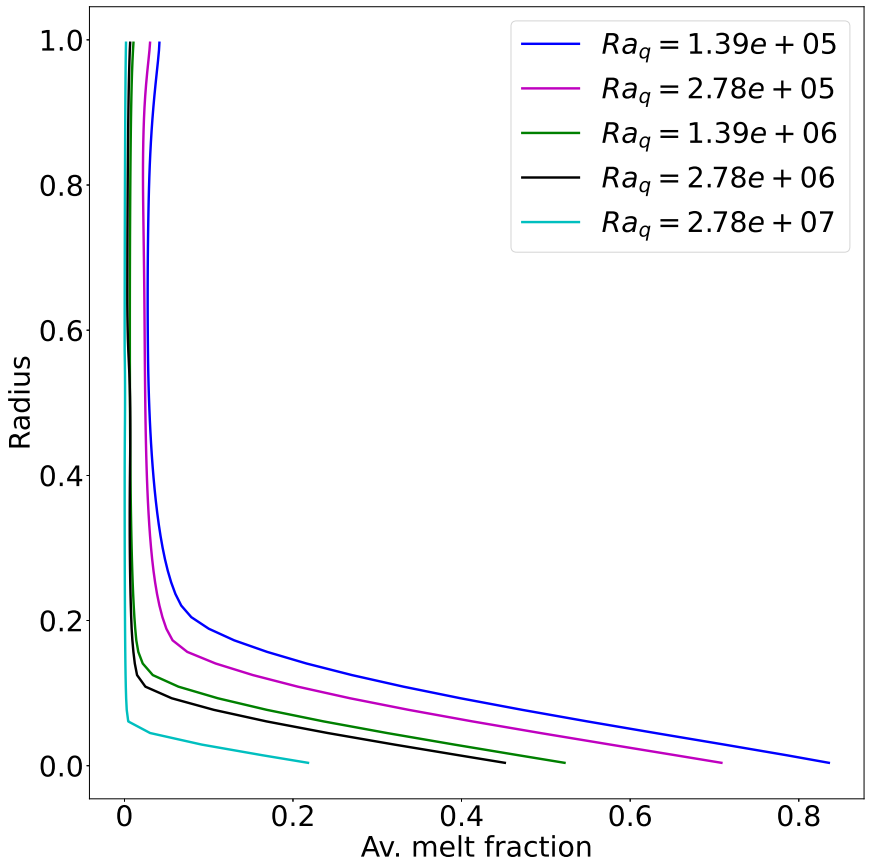

Figure 2.12: This plot shows the horizontal average melt fraction f_M produced in the HP ice layer as function of the radius for a rigid bottom boundary with $\Phi = 10^{-2}$, $\gamma = 0.95$, for various values of Ra_q in the case of Ganymede, using reference parameters values given in table 2.2 for d & q, implying a viscosity in the range 10^{16}–10^{18}Pa s which corresponds more or less to the ranges defined for Ganymede. Note that these figures are an a posteriori prediction from calculations that do not consider partial melting in a self-consistent way (see text for details).

melting. The melt fraction is then

$$f_M = \frac{C_p \Delta T}{L} \tag{2.39}$$

with C_p the heat capacity and L the latent heat as defined in table 2.2. Since this calculation does not account for porous flow, the melt is assumed to stay in place, even for high fractions. In reality, differential motion of liquid and solid resulting from gravity would act to limit this melt fraction within the ice layer. The results presented in this part are therefore only indicative of the relative importance of melt as function of the input parameters.

Figure 2.12 shows the horizontal average of the melt mass fraction produced into the HP ice layer as function of the radius for various values of Ra_q, considering a rigid BC at the

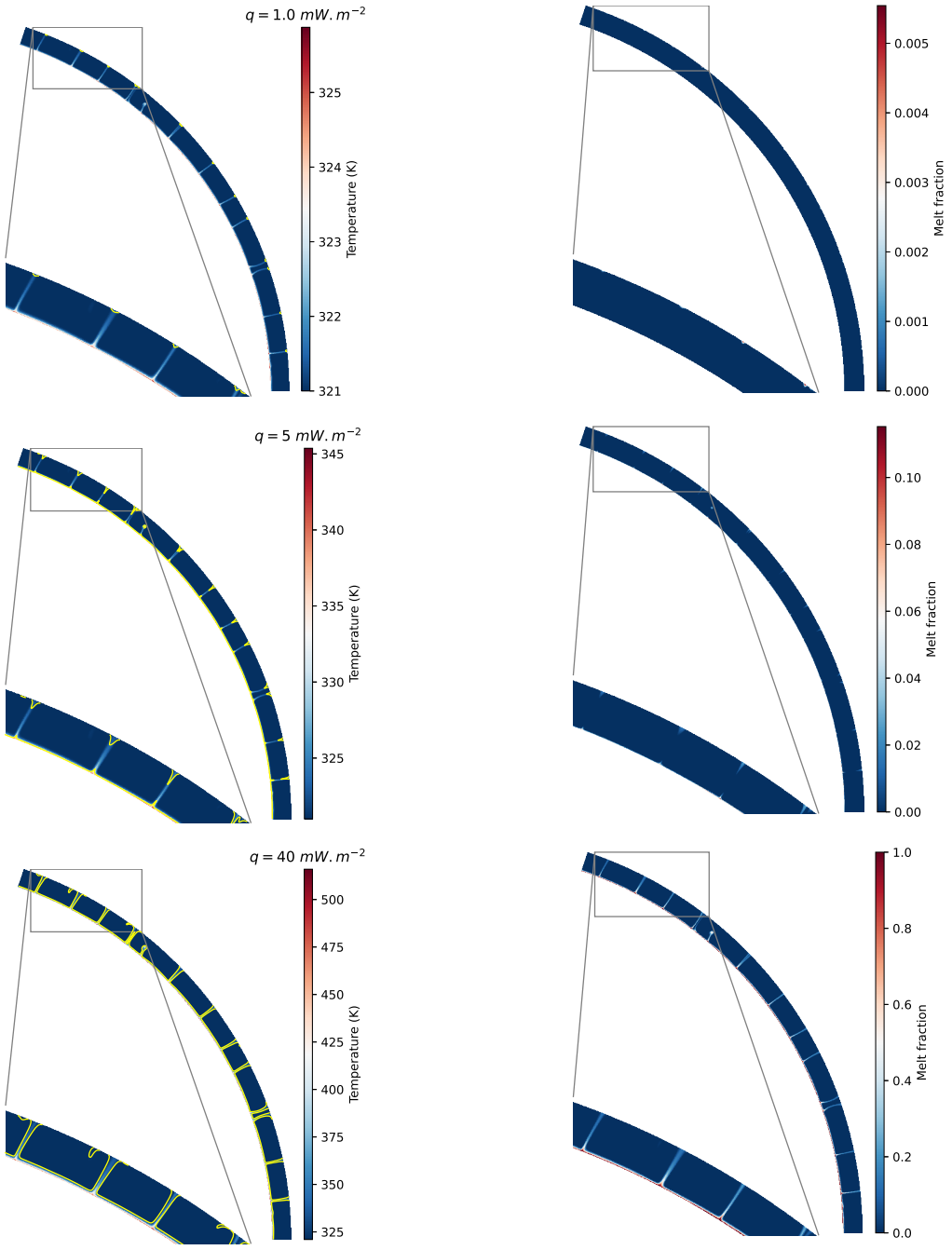

Figure 2.13: Maps of the temperature field (left) and melt fraction (right) for a snapshot at statistically steady-state from the following simulation: $\Phi = 10^{-2}$, $\gamma = 0.95$, $Ra_q \sim 2.8 \times 10^5$, rigid bottom boundary and applied to Ganymede for $d = 100$ km and various values of the heat flux from the core, $q = 1$ mW m^{-2}, $q = 5$ mW m^{-2}, $q = 40$ mW m^{-2}, as labelled. As the Rayleigh number and the thickness of the HP ice layer are fixed while the heat flux is varying, it means that the viscosity is varying in the range 10^{15}–10^{17} Pa s as considered for Ganymede (See table 2.2). The yellow line on left panels shows the points where $\bar{T} = T_m$, which delimits regions of partial melting. Each panel shows the whole computational domain ($1/5^{th}$ of the shell) as well as a zoom on a small fraction of the domain. Note that these figures are an a posteriori prediction from calculations that do not consider partial melting in a self-consistent way (see text for details).

bottom of the ice shell, a phase-change number $\Phi = 10^{-2}$ and the reference values of q and d identified in table 2.2, implying a viscosity in the range 10^{16}–10^{18}Pa s which corresponds more or less to the ranges defined for Ganymede. For all values of the Rayleigh number considered, the melt fraction profiles are similar to the mean temperature profile as shown on figure 2.3. The melt fraction is largest at the bottom boundary and decays with radius in the boundary layer until it reaches a nearly constant value in the bulk. The cases with the lowest values of the Rayleigh number show a slight increase when getting close to the upper boundary.

The melt fraction decreases with the Rayleigh number and reaches zero in the bulk of the layer for $Ra_q \geq 10^7$. In that case, the melt would refreeze during its ascent before remelting upon reaching the ice/ocean interface. As a mass transfer mechanism from the core to the ocean, this situation is likely less efficient than the cases with lower Rayleigh numbers which allow partial melt to be maintained in the whole layer. The amount of melt produced for low Ra_q cases in fig 2.12 reaches very high values which clearly falls out of the range where the assumption of no motion between phases fails. However, the Rayleigh number expected for Ganymede is at least $Ra_q \sim 5 \times 10^8$ as computed in § 2.4.3.1, for which the maximum melt mass fraction produced at the bottom of the HP ice layer would be smaller than for the ones shown in fig 2.12.

Figure 2.13 shows spherical representations of $1/5^{th}$ of the HP ice shell, with a zoom on several plumes. The left panels depict the temperature field for various values of the heat flux coming from the core, the yellow line being the contour on which $\bar{T} = T_m$. The expected melt fraction is shown on the right panels of the figure. Each panel is in fact based on the same snapshot of the results obtained for a rigid BC at the bottom of the HP ice layer when $Ra_q = 10^3 \times Ra_c \sim 2.8 \times 10^5$ and $\Phi = 10^{-2}$ and differ only by the choice of the heat flux to render the results dimensional. It shows that three options are conceivable depending on the heat flux.

In the first case, obtained for small values of the heat flux ($q = 1$ mW m^{-2} on fig 2.13), partial melting only occurs in hot plumes close to the upper boundary where it can reach a fraction of at most 0.5%. Actually taking into account partial melting in the model would make this melt rise faster to the ocean but would probably not change the overall dynamics. Salts can enter the ice layer by contact with the rocky core but is limited by their partitioning behaviour and by diffusion in both solids, a rather inefficient process. We expect therefore that the salt concentration is rather small in the ice layer and its effect on the dynamics should be limited [Hernandez et al., 2022]. However small in quantity, all the salts introduced at the bottom should be efficiently transported by convection in the solid.

For an intermediate value of the heat flux $q = 5$ mW m^{-2} on fig. 2.13, we obtain localised melt pockets in the vicinity of hot plumes, both at their roots and close to the upper boundary, while these are not generally connected with each other. It means the liquid water would refreeze upon ascending in the ice layer and remelt again before reaching the overlying ocean. We expect that the liquid in contact with the rocky core would get enriched in salts, which would help keep it liquid while ascending and potentially making a continuous path toward the ocean, possibly as an independent porous flow [Kalousová and Sotin, 2018, Kalousová et al., 2018, Choblet et al., 2017]. If it crystallises on the way up, the ice-salt mixture is

likely to be denser than pure ice, which could slow down the up-welling flow, depending on the relative effects of salt and temperature on the density. A full treatment of that case requires a model that includes both a two-phase-flow approach [Kalousová and Sotin, 2018, Kalousová et al., 2018] and a proper treatment of composition variations. This will be the topic of our future studies.

Finally, for a large heat flux $q = 40$ mW m^{-2} on fig 2.13, we get melt everywhere at the bottom that even reaches complete melting at places (melt fraction equal to 1). If the melt is so rich in salts that it is denser than pure ice, we expect a full layer of liquid below the ice layer, which would require applying a phase change boundary condition there as well as at the surface. Previous studies [Deguen, 2013, Morison et al., 2019, Morison, 2020] show that we should expect a totally different flow pattern dominated by a degree one mode of convection, a translation of the shell. This is a very efficient heat transport mechanism that would act to cool down the core very efficiently and freezing the dense water. Clearly, a more complete study of that scenario is needed to conclude. On the other hand, in the likely situation where the liquid water contains a small enough fraction of salt to stay less dense than the ice above, it is likely to transport it very efficiently toward the ocean as a porous flow. Even with our purely solid calculations, we predict a continuous connection between the melt layer at the bottom and the upper boundary, a situation that would be reinforced by the presence of salts in the water. We therefore expect this situation to be the most efficient one to transport salts from the core to the ocean.

Several choices have been made for the numerical applications and need to be discussed (See § 2.4.3). First, despite the range estimated for the value of Φ for Ganymede in § 2.3.1.2, we chose $\Phi = 10^{-2}$ for the numerical application (See § 2.4.3.1). This range is a very rough estimate and according to figure 2.9, between $\Phi = 10^{-2}$ and $\Phi \sim 10$, the coefficient a_w of the scaling law for the radial velocity hardly varies. Therefore, we chose the most extreme case among those we have studied for perform these calculations. Also, the scaling laws in § 2.4.2 are established for an aspect ratio in the range 0.9-0.95 (See table 2.1). For Ganymede, this ratio is not yet well constrained, with a value varying from 0.8 to 0.95 depending on the core radius, the thickness of the HP ice layer and the period considered in the different studies. From the study of Bland et al. [2009], in the thermal history of Ganymede, the thickness of the HP ice layer could have vary between 100 km for a heat flux of about 25 mW m^{-2} and 500 km ($\sim$700 km if the ocean is closed) for a heat flux of about 5 mW m^{-2}. The aim of this first numerical application was not to conclude about the actual efficiency of heat and mass transfers from the core to the ocean on Ganymede, but to give an idea of what kind of exchanges could happen through a HP ice layer for that type of planetary objects. Then, we chose to base this numerical application on the study of Kalousová et al. [2018], which considers a large range of combinations between the heat flux from the core and the thickness of the HP ice layer and we decided to represent the extreme case with the smallest values of q and d, which means a minimum of melt at the bottom, in order to observe if melt could occur at the interface between the core and the HP ice shell even in this specific case. In addition, the main parameters currently not well constrained (q, d and η) are kept in clear in the application equations (See eq. 2.28, eq. 2.29 and eq. 2.30) and can be quickly modified to fit another planetary object, as Titan. Finally, future missions should one day

allow to better constrain these parameters for various bodies and this study will allow to quickly conclude about the presence of melt at the bottom and the mass transfer efficiency through the HP ice layer.

2.6 Conclusions

This paper addresses the possibility of convection in a high pressure ice layer between a solid core and a liquid water ocean on icy/water-rich bodies and its heat and mass transfer efficiency. We include an effect not considered previously in this context: the solid-liquid phase change at the upper boundary and its implications for the mechanical boundary condition. As shown by previous papers in other contexts [Deguen, 2013, Deguen et al., 2013, Labrosse et al., 2018, Morison et al., 2019, Agrusta et al., 2020], this leads to a non-zero vertical velocity at the ocean/ice interface, a decreased value for the critical Rayleigh number, a markedly different thermal structure and an enhanced heat and mass transfer efficiency. In order to conclude about the effect of this only aspect of the problem, convection of constant-viscosity pure solid water ice has been considered. Compared to previous papers that consider the effect of the phase change boundary condition, we consider here several aspects that are specific to the application of the HP ice layers in contact with a rocky core: we consider a thin spherical shell, with boundary conditions at the bottom not considered before, an imposed heat flux and either a rigid or free-slip mechanical condition. On the other hand, for the sake of simplicity, we have not included the effect of variable viscosity and partial melting that were considered by some previous studies [Choblet et al., 2017, Kalousová et al., 2018, Kalousová and Sotin, 2018]. Future studies should be performed to combine all these effects.

First of all, our results largely confirm those obtained on the effect of the phase change boundary condition in other contexts. The critical Rayleigh number decreases with a decrease of the phase change number, while the wavelength of the most unstable mode increases [Deguen, 2013, Labrosse et al., 2018, Morison, 2020]. The Rayleigh number expected for the HP ice layer of most icy satellites and planets is expected to be largely supercritical and, in that regime, the radial velocity at the upper boundary and heat transfer efficiency, as measured by the Nusselt number, scale as power laws of the Rayleigh number [Agrusta et al., 2020]. With the setup considered here, the exponents are close to 1/2 and 1/5 for the velocity and the Nusselt number, respectively, for a rigid BC at the bottom and 1/2 and 1/4 for a free-slip BC. The coefficients of the scaling laws increase when the phase change number is decreased, which eases the phase change, by roughly a factor 2 between end-members for the Nusselt number.

The scaling laws obtained in a dimensionless parameter space can be easily applied to any object by choosing the relevant values of all parameters. Section 2.4.3 presents applications to Ganymede and a hypothetical large water exoplanet, imposing values for the best constrained parameters and leaving the possibility of adjusting around reference values for the others, in particular the heat flux from the core, the ice layer thickness and its viscosity. In both cases, we find a typical RMS velocity across the upper boundary of the order of 50 cm yr^{-1} in the limit of a small phase change number. With such values, the mass exchange between the

ice and the overlying ocean should be quite efficient and any salt added to the ice layer by interacting with the underlying core should be easily transported to the ocean. Conversely, if the ocean starts already salted, the efficient mass transfer at the top of the HP ice layer should lead to a rapid chemical equilibrium [Bolrão et al., 2021].

Using the heat transfer scaling laws, we can predict the temperature at the bottom of the HP ice layer as function of the governing parameters. Using the reference values, we predict that the mean temperature at the bottom of the ice layer is close to the melting temperature, both for Ganymede and a large water planet. All parameters being equal, the temperature is lower for a free-slip boundary condition at the bottom than for a no-slip one but in both cases, it is close to the melting one. Considering the lateral variations of the temperature, it means that we should expect the presence of partial melt at least in some areas of the core-ice interface, and the mechanical boundary condition should be intermediate between the two end-members considered in this study. Chemical interaction with the rocky core by hydrothermal activity should enrich this melt in various salts, and its upward motion by porous flow should make it freeze and bring salts in the ice layer. The effect of this salt on convection remains to be studied in details.

Further studies focusing on salts and partial melting will complete the model in order to be more relevant to conclude about mass transfer efficiency through HP ice layer on icy/water-rich bodies. As several parameters are not well constrained yet, these studies will be useful when more information from future exploration missions will be available in order to conclude about the habitability of these bodies from this perspective.

CHAPTER 3

EFFECTS OF SALTS ON THE EXCHANGES THROUGH HIGH-PRESSURE ICE LAYERS OF LARGE OCEAN WORLDS

In chapter 2 we have shown that for pure HP ices, considering the phase-change at the top interface between the ice and the ocean enhances the convection in the HP ice layer and allows efficient heat and mass transfer through the bulk in certain conditions. Many space missions have shown that the oceans of large icy moons as Titan or Ganymede are salty (See § 1,§ 3.2). These salts could come from the formation and differentiation of the moon or be transported from the core to the ocean by convection (See fig. 3.1). Several studies, including our own [Lebec et al., 2023], have shown that under specific conditions the bottom temperature can be greater than the melting one [Choblet et al., 2017, Kalousová and Sotin, 2018, Kalousová et al., 2018, Kalousová and Sotin, 2020]. In that case, the ice melts at the bottom boundary and the water interacts with the core and gets enriched in salts. If this mixture of water and salts is less dense than the ice, it could seep in by porous flow and could either rise through the up-welling hot plumes in the HP ice layer and reach the ocean or at least a part of it could refreeze at a certain depth and be transported through the bulk to the ocean by convection in the solid-state (see fig.3.2), which could also hinder convection because of the effect of salts on the density of the ice. This effect is measured by the buoyancy number B_{salts}, which is the ratio between the increase of the density linked to the enrichment in salts of the ice layer and the decrease of the density linked to the increase of the temperature. Then, the next step is to consider these salts to study their effect on the overall dynamics and on the mass transfer efficiency.

For a comprehensive study of their effect on the system, we model a two-dimensional spherical shell of HP ices of thickness $d = R^+ - R^-$ (See fig. 3.1) in contact with a homogeneous liquid ocean of radius R_o. At the interface between these two layers, we consider the phase-change boundary condition studied in the previous chapter. Also, we add a flux of salts from the core and use Lagrangian tracers to advect them through the HP ice shell. We perform a systematic exploration of the parameter space controlled by the phase-change number Φ, the Rayleigh number Ra_q, the buoyancy number B_{salts} and the partitioning co-

efficient K between the HP ices and the ocean at the upper boundary, which measures the amount of salts trapped in the ice when the ocean refreezes at the top interface. From that, we obtain scaling laws for the bottom temperature and the top radial velocity as function of Ra_q but also for the flux of salts entering the ocean as function of B_{salts} and we are able to determine what percentage of salts from the core are transported to the ocean in order to conclude about the efficiency of the mass transfer by convection in the solid state on large ocean worlds.

In this study, we want to isolate the effect of salts on the dynamics. To do so, we consider only solid convection. This work comes from our second paper submitted to Icarus.

3.1 Abstract

The habitability of large icy moons has long been disputed due to the presence of an high-pressure (HP) ice layer located between the core and the internal liquid ocean, preventing a direct contact and facilitated exchanges between both. In our previous study Lebec et al. [2023], we have shown that under certain conditions and considering the phase-change at the upper boundary of the HP ice shell, heat and mass transfer can occur and be efficient. Now, the aim of this work is to study the effects of impurities inside the HP ices on the flow dynamics and the mass transfer efficiency from the core to the ocean. These salts can enter the ice layer either by diffusion, which is a very inefficient process, or if the temperature at the bottom of the ice layer is high enough to partially melt. In that case, the liquid water can interact with the core and get enriched in salts. This salts/water mixture, which can be lighter than high-pressure ices, could rise through the ice shell and refreeze. The resulting salts/ice mixture can be transported into the ocean by convection in the solid state but could also impede it due to its density compared to pure ice. Therefore, the convection efficiency depends on the buoyancy number B_{salts}, which is the ratio of density increase associated to salts compared to the decrease associated to temperature. For a complete exploration of the impact of salts we modeled a flux of salts from the core and the advection of these salts using Lagrangian tracers in order to study the effects of the Rayleigh number, the buoyancy number and K, which is the partitioning coefficient of the salts between the ocean and the HP ices at the top interface, on the heat and salts transfer efficiency through the HP ice layer, as well as the implications for the evolution of salt concentration in the ocean of large icy moons and ocean worlds. We present a scaling of the bottom temperature and the top radial velocity w_{top} as function of the Rayleigh number Ra_q for various values of the buoyancy number and a scaling of the effective flux of salts across the top interface with the ocean as function of the buoyancy number for various values of the partitioning coefficient. We perform a numerical application for Ganymede and we show that depending on the values of the system parameters a certain percentage of the salts entering the HP ice layer from the core can efficiently flow into the ocean.

3.2 Introduction

Large icy moons have a deep hydrosphere composed of a thin crust of ice Ih at the surface, a liquid ocean and a layer of high-pressure ices trapped between the ocean and the core [Hussmann et al., 2015]. The internal ocean on Ganymede and Titan, which are the two largest moons of the solar system, is composed of salted water. For Ganymede, it has been inferred from electromagnetic measurements from the Galileo missions [Kivelson et al., 2002]. For Titan, it has been deduced from gravity [Iess et al., 2010, 2012, Mitri et al., 2014, Baland et al., 2014], tides [Iess et al., 2012], rotation and shape [Baland et al., 2014] data from the Cassini mission and electromagnetic measurements from the Huygens probe [Béghin et al., 2012]. These moons are mainly composed of rocks and ice and the composition of their rocky part is likely to be close to carbonaceous chondrites [Sotin et al., 2021]. According to Zolotov and Kargel [2009], their ocean's main salt is likely to be $MgSO_4$, which is compatible with the spectra obtained for Ganymede by the Galileo probe [Soderlund et al., 2020]. These salts

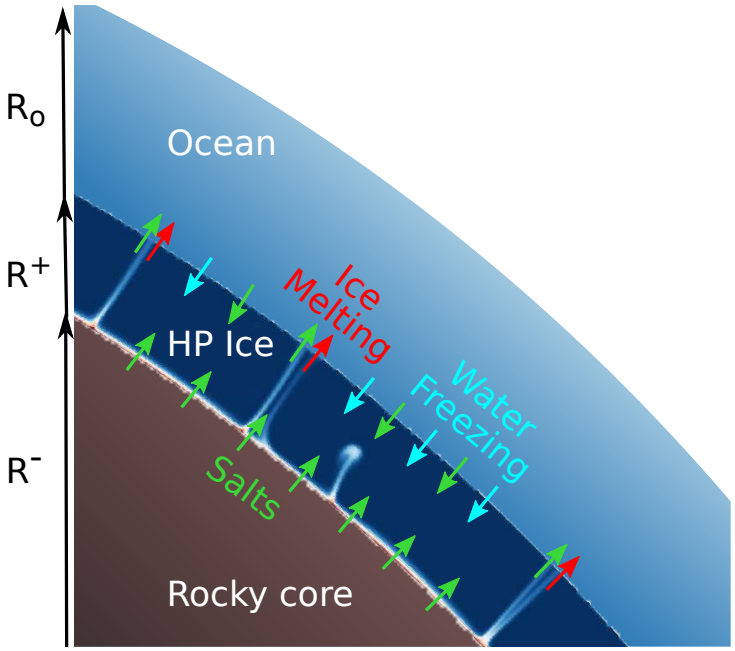

Figure 3.1: Model illustration for the interior of an ocean world with a compositional flux of salts from the core and exchanges of salts between the HP ice layer and the ocean. When the up-welling hot plumes reach the top interface between the ice and the ocean, the ice melts and the salts it contains dissolve in the ocean. Conversely, The water freezes above the down-welling currents and some of the salts it contains are trapped during crystallization, depending on the type of salts and the value of its partitioning coefficient between the water and the ice VI.

could be inherited from the formation and differentiation processes of the moon. They could also come from the core and reach the ocean by convection through the HP ice layer (See fig. 3.1), which would imply the presence of impurities also in this ice shell. In particular, if

melting happens at the bottom of the ice layer in contact with the core [Kalousová et al., 2018, Choblet et al., 2017, Lebec et al., 2023, Kalousová and Sotin, 2018, 2020], the core interacts with the water which gets enriched in salts. If the salty water is less dense than the overlying ice (i.e. if the salt concentration is not too high), it is expected to penetrate in the ice by porous flow. In some conditions, this porous flow can proceed all the way to the ocean [Kalousová et al., 2018, Kalousová and Sotin, 2018, 2020] but, the decrease in temperature with height in the convective boundary layer leads to freezing of part, if not all, of the mixture in some cases (See fig. 3.2). The resulting solid, likely a polycrystalline assemblage of salty ice and hydrated salts, is denser than pure ice. This density increase counteracts the density decrease associated with temperature and the competition between these two effects controls the convective dynamics of the ice layer. This competition is quantified by a dimensionless parameter, classically called buoyancy number B_{salts}, which is the ratio between the density increase associated to salt enrichment and the density decreased associated to temperature increase. In addition to the possibility of salt transfer from the rocky core to the ocean, salts already present in the ocean can be transferred to the ice layer by freezing, provided that the partition coefficient K is greater than zero.

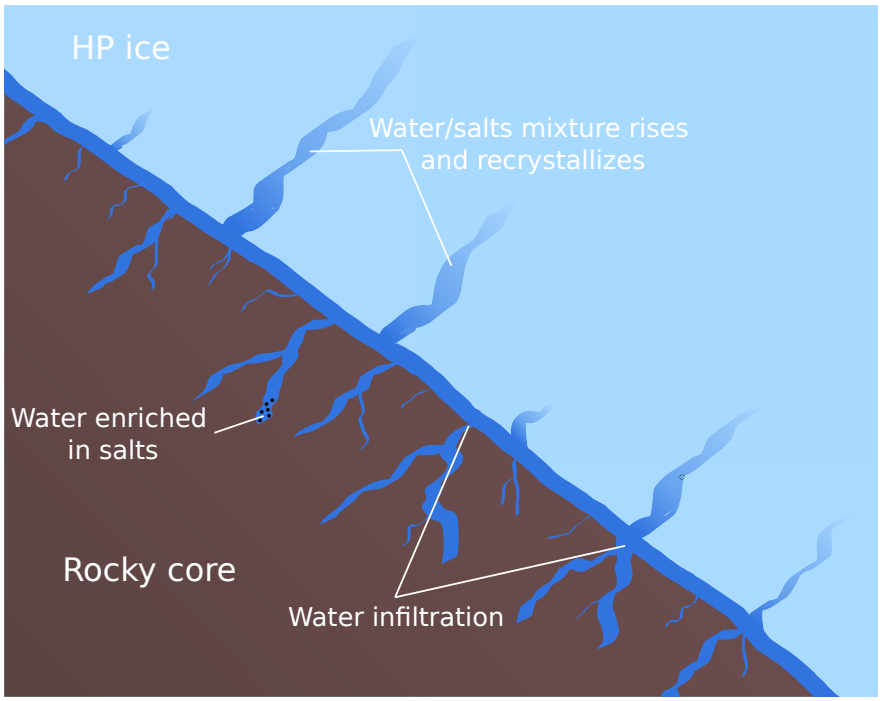

Figure 3.2: Illustration of the process of enriching the HP ice layer with salts from the core. If there is melt at the interface between the HP ice layer and the rocky core, the liquid water will seep into the mantle and this interaction should enrich it with salts. If this salty water is less dense than the ice, it should penetrate into the HP ice layer by porous flow and rise until the temperature decrease along the way makes it recrystallizes at a depth depending on the salts present in the water and the implied solidus.

Hernandez et al. [2022] previously proposed a scaling to estimate whether the salts are impeding convection in the solid state. But despite the fact that the existence of a salty ocean is supported by several studies, a complete exploration of their effects on the mass and heat transfers efficiency through a HP ice layer inside large icy moons, depending on their buoyancy and their partitioning coefficient between HP ices and the ocean, has not been performed yet.

Several papers have already considered convection in high-pressure ice layers of large icy moons: Choblet et al. [2017] modeled a 3D spherical ice layer with a pressure- and temperature-dependent viscosity of the ice. They also considered the ability of the ice to melt at the bottom interface and an instantaneous extraction of the melt to the ocean. Kalousová and Sotin [2018] and Kalousová et al. [2018] studied the evolution of a 2D cartesian HP ice layer. They treated the partial melting in the bulk and the transport of the melt across the ice shell with a variable viscosity, using a two-phase approach. In a previous paper [Lebec et al., 2023], we modeled a two-dimensional spherical HP ice layer treating only solid-state convection for a constant viscosity (except for one case including a temperature- and pressure-dependent viscosity), but contrary to previous studies we considered the effect on the overall dynamics of the phase-change at the interface between the ocean and the ice. Due to convective stresses in the ice, a topography is formed at this interface. These topographic variations are erased by melting and freezing. This process implies a permeable boundary that enhances the heat and mass transfer efficiency through the top interface. It can be modeled as a phase change boundary conditions controlled by a dimensionless parameter Φ. All these previous papers show that, depending on the heat flux from the core, the thickness of the ice and its viscosity, efficient heat and mass transfers may have existed, or may exist, through this layer. Furthermore, all of these studies have shown that under certain conditions, the temperature at the lower boundary between the core and the HP ice layer could reach the melting temperature, which would imply at least pockets of molten ice at the interface and a more efficient mass transfer through the ice shell, either by remaining liquid throughout the ascent or by solid convection if water rises and refreezes in the ascending hot plumes during the ascent.

The present study, while still letting aside the question of two-phase flow, focuses on the effect of salts on the dynamics. We consider a flux of salts from the core and we use a numerical model to solve the convection equations. We perform a systematic exploration of the parameter space, which is composed of the Rayleigh number Ra_q, the phase-change number Φ at the top boundary, the buoyancy number of the salts B_{salts} and the partitioning coefficient K of the salts between the liquid water and the HP ices at the top interface. The value of this coefficient depends on the nature of the salts. In the context of large ocean worlds, the first point is to know which salts could be dissolved in water by interacting with the core. The partition coefficient of most salts between liquid water and ice Ih are well known. On the other hand, this is not the case for the partition coefficient between water and high-pressure ices, with the notable exception of NaCl for which the partition coefficient was measured by Journaux et al. [2017]. According to their study, this coefficient is about 5×10^{-3} for ice VI, which is really low, and about 0.12 for ice VII. Therefore, as this coefficient can vary a lot depending on the salt properties, we decided to use a wide range of

values between 0 and 1 for this coefficient in order to have the largest possible study of the environment to make these results usable when the salts involved will be better identified and to conclude about their effect on the global dynamics.

Section 3.3 presents the physical model and the numerical method used in this study. The results are discussed in section 3.4, including a numerical application to Ganymede in subsection 3.4.4. The limits and perspectives of this work are discussed in section 3.5 and the results are summarized in section 3.6.

3.3 Model

In this study we consider a model made of a HP ice layer topped by an ocean extending from R^+ to R_o (See fig. 3.1) with fixed boundaries in time. Two fluxes are entering the HP ice layer from the core: the heat flux q and the compositional flux of salts F. The ocean is homogeneous by construction but evolves in time by exchanging mass with the HP ice layer. The ice transported by solid convection in the HP ice shell melts on contact with the ocean and the salts contained in the ice dissolve in it. Conversely, a part of the water near the upper interface between the HP ice and the ocean may freeze and be accreted to the ice (fig. 3.1). A certain amount of the salts present in the water during its crystallization is trapped in the process, depending on the salt partitioning coefficient K between HP VI ice and water. All these aspects are considered in our model.

3.3.1 Physical model

3.3.1.1 Governing equations

The primary target of our study is Ganymede but we aim at getting results that can apply equally to any object with a thick enough hydrosphere to host a high-pressure ice layer. We therefore use dimensionless equations in order to reduce the number of parameters of the problem and obtain scaling laws for quantities of interest as function of these parameters. The length scale is taken as the HP ice layer thickness $d = R^+ - R^-$, with R^+ (resp. R^-) the dimensional radius of the top (resp. bottom) HP ice boundary. In the rest of the paper, the aspect ratio between the core and the HP ice layer is $\gamma = R^-/R^+$. The time scale is defined using the thermal diffusivity κ as d^2/κ. As in previous papers on convection in HP ice layers [Choblet et al., 2017, Kalousová et al., 2018, Lebec et al., 2023], we impose a heat flux q at the bottom of the layer and it is used to scale the temperature with $\Delta T = qd/k$, with k the thermal conductivity. Also, the temperature T^+ at the interface between the HP ice and the ocean is set to the melting one at the relevant depth, which depends on the HP ice layer thickness d. The temperature is made dimensionless using the following equation:

$$\tilde{T} = k\frac{T - T^+}{qd}. \tag{3.1}$$

In addition to the temperature, another scalar field is considered in this paper, the mass fraction of salts C (or concentration). Note that the salt concentration we consider is that

for the "fluid parcel" which constitutes the basic element of the hydrodynamics approach used here, which is much larger than the typical grain size of the solid. The salts do not need to be dissolved in the ice crystals and can be in the form of separate crystals. In that sense, the mineral assemblage is similar to the one that forms the rocks constitutive of the mantle of terrestrial planets. As long as they stay at the solid state, the various crystals cannot segregate.

In a first set of runs (see table 3.1 #1), we consider a closed ice/ocean system without an influx of salts from the core and with an initial concentration in the ocean $C^o_{ini} = 1$ as the scaling variable. In a second set of runs (see table 3.1 #2), we impose a fixed flux of salts at the bottom of the ice layer, F (unit of m s^{-1}) which is used to scale the concentration so that the dimensionless salt flux imposed at the bottom is $F_{salts} = 1$.

This problem is solved in a spherical shell under the Boussinesq approximation for an infinite Prandtl number. Indeed, from values in tab 3.4 in the case of Ganymede:

$$Pr = \frac{\eta}{\rho\kappa} \sim 10^{20}, \tag{3.2}$$

with ρ the reference density and η the ice viscosity. In this study η is considered temperature- and pressure-independent through the HP ice shell. The dimensionless conservation equations of mass, momentum and energy are [Tackley and King, 2003, Bolrão et al., 2021]:

$$\boldsymbol{\nabla} \cdot \boldsymbol{u} = \boldsymbol{0}, \tag{3.3}$$

$$0 = -\boldsymbol{\nabla} p + \boldsymbol{\nabla}^2 \boldsymbol{u} + Ra_q \left(T - \bar{T} - B_{salts}(C - \bar{C})\right) \hat{\boldsymbol{r}}, \tag{3.4}$$

$$\frac{\partial T}{\partial t} + \boldsymbol{u} \cdot \boldsymbol{\nabla} T = \boldsymbol{\nabla}^2 T, \tag{3.5}$$

$$\frac{\partial C}{\partial t} + \boldsymbol{u} \cdot \boldsymbol{\nabla} C = 0, \tag{3.6}$$

with $\hat{\boldsymbol{r}}$ the radial unit vector, p the dynamic pressure, $\boldsymbol{u} = (v, w)$ the velocity, $\bar{T}$ the horizontally averaged temperature, $\bar{C}$ the horizontally averaged concentration in salts, and Ra_q the Rayleigh number. In our case of a fixed heat flux from the core and a varying lateral temperature at the interface between the HP ice and the core Ra_q is written as [Choblet et al., 2017]:

$$Ra_q = \frac{\alpha \rho g q d^4}{k \kappa \eta}, \tag{3.7}$$

with g the gravity acceleration and α the thermal expansion.

The equation (3.6) for the evolution of the concentration in salts is a pure advection equation, i.e. we neglect its diffusion in the ice. Its effect on the ice density is controlled by a dimensionless number, the buoyancy number, which is the ratio of density increase

associated to salts $\Delta\rho^c$ compared to the decrease associated to temperature, $\Delta\rho^T = \rho\alpha\Delta T$ [Le Bars and Davaille, 2004]. With $\Delta T = qd/k$, in the case of a closed ice/ocean system without influx of salts from the core, this parameter is written as:

$$B_{salts} = \frac{\Delta\rho^c}{\Delta\rho^T} = \frac{kKC^o_{ini}}{\alpha qd} = \frac{kK}{\alpha qd}, \tag{3.8}$$

while in the case of an imposed flux of salts F from the core, it is written as:

$$B_{salts} = \frac{\Delta\rho^c}{\Delta\rho^T} = \frac{kF}{\alpha\kappa q}, \tag{3.9}$$

A negligible value of B_{salts} would make the flow insensitive to the presence of salts, irrespective of its concentration, while a large value would tend to make salt-enriched regions negatively buoyant and possibly stabilize against thermal diffusion. One of the goals of the present paper is precisely to explore the effects of this parameter on the dynamics of convection in a HP ice layer and resulting transfer efficiency.

The buoyancy number is controlled by the nature of the salts and their amount expected to enter the ice layer if melting occurs at the bottom. These difficult questions depend on the initial composition of the ocean and its chemical interactions with the underlying rocky core, which depend on the pressure and temperature. To our knowledge, the relevant studies are scarce and let us here consider the case of NaCl for which some data exist [Journaux et al., 2013, 2017]. The maximum amount of NaCl for our model to hold is the one which makes the salty water negatively buoyant, since we need it to rise in the ice to freeze. This maximum concentration is 2.5 mol $kg^{-1}_{H_2O}$ [Journaux et al., 2013] or 146 g $kg^{-1}_{H_2O}$, which means that liquid water at high pressure can contain a maximum of about 15% of NaCl to be able to rise through the HP ice layer. According to Journaux et al. [2017], the concentration of NaCl in ice VI cannot exceed 2.1×10^{-2} mol%, or 5.6 g kg^{-1}_{iceVI}. Any additional salts contained in the water would crystallise as salt grains. According to Kalousová et al. [2018], under conditions consistent for Ganymede, the water fraction in the ice layer could be up to 1% and its radial velocity at top is of the order of a few meters per year. Assuming that the radial velocity in the bulk is slightly lower but of the same order of magnitude as at the top, we can estimate the maximum flux of NaCl across the HP ice shell at a given time. This flux depends on the maximum concentration of NaCl in the water at high pressure (0.15), the maximum fraction of liquid in the layer at a given time (0.01) and the radial velocity of the water and salts mixture through the ice (3.2×10^{-8}m s^{-1}), which gives, as their product, $F = 4.8 \times 10^{-11}$ m s^{-1}. Based on this estimate, we can compute the maximum buoyancy number from eq. 3.9 in order to choose wisely the range to be used for this study. For Ganymede, using the values available in table. 3.4, it gives $B_{salts} = 60$. Therefore, we chose a range between 0 and 10, which is sufficiently large to cover the whole range of behaviour, as shown below.

3.3.1.2 Boundary conditions

Our model uses a fixed heat flux from the rocky core and the temperature is therefore free to vary laterally and on average at the bottom of the studied shell. At the interface between the

HP ice and the ocean, the temperature is equal to the liquidus of the overlying ocean assumed to be laterally uniform so that, according to equation 3.1, the dimensionless temperature is set to zero, leading to the following dimensionless temperature top ($^+$) and bottom ($^-$) boundary conditions:

$$\begin{cases} \tilde{T}^+ = 0 \\ \left(\frac{\partial \tilde{T}}{\partial r}\right)^- = -1, \end{cases} \tag{3.10}$$

The mechanical boundary condition that applies at the bottom of the HP ice layer is not obvious [see discussion in Lebec et al., 2023]: if the bottom temperature is below the solidus, the whole shell is solid and the contact with a high viscosity rocky core implies a no-slip boundary condition. On the other hand, in the case of a thick ice layer, the bottom temperature is likely to reach the melting temperature of the HP ice, in places (the temperature being laterally variable) or everywhere. In the extreme case where a liquid is present everywhere between the ice and the core, we can expect a free-slip boundary layer to apply. Intermediate possibilities with a Robin-like boundary condition, that could be laterally variable as a function of the local temperature could be envisioned. As shown by Lebec et al. [2023], heat and mass transfer is more efficient for a free-slip bottom boundary condition and, to be on the conservative side, we consider a no-slip boundary condition in the present study:

$$u^- = w^- = 0. \tag{3.11}$$

The presence of a solid-liquid phase change at the upper boundary of the ice shell imposes a specific boundary condition with important implications for the dynamics and the heat and mass transfer efficiency. The detailed derivation and implications of this boundary condition for a Rayleigh-Bénard convection can be found in several papers [Deguen, 2013, Deguen et al., 2013, Labrosse et al., 2018, Agrusta et al., 2020, Bolrão et al., 2021]. The convection pattern inside a HP ice layer with such a boundary condition at top [Lebec et al., 2023] is made of up-welling hot plumes and a diffuse down-welling current, as shown on top panels of fig.3.8. At the interface with the ocean, the up-welling hot ice plumes melt and join the ocean while a part of the liquid water can solidify and accrete to the ice above the down-welling cold flow. The ease with which this process occurs depends on the competition between two processes: on the one hand, the convective stresses in the solid create a topography at the interface. On the other hand, convection into the ocean erases this topography by melting and freezing. This competition is quantified by the ratio of the two relevant time scales, the one to build the topography, which is:

$$\tau_\eta = \frac{\eta}{\Delta\rho g d}, \tag{3.12}$$

with $\Delta\rho = \rho_s - \rho_l$ the density difference between the solid (ρ_s) and the liquid (ρ_l) at the interface, and the one to erase it by melting and freezing, which is:

$$\tau_\phi = \frac{\rho_s L}{\rho_l c_{pl} u_l \left|\frac{\partial T_m}{\partial r}\right|}, \tag{3.13}$$

with L the latent heat, u_l the flow velocity in the liquid ocean, c_{pl} the specific heat of the liquid and $\partial T_m/\partial r$ the slope of melting temperature with radius [see Labrosse et al., 2018, for a full treatment of this process]. Therefore, the phase change number, defining the efficiency of this mechanical condition, is written as:

$$\Phi = \frac{\tau_\phi}{\tau_\eta}. \tag{3.14}$$

Expressing the continuity of stress across the boundary leads to the dimensionless boundary condition for the radial velocity associated to the phase change considered at the top interface:

$$\Phi w + 2\frac{\partial w}{\partial r} - p = 0. \tag{3.15}$$

When $\Phi \to 0$ the timescale to erase the topography is much lower than the one to create it and the phase-change is efficient at the interface. While for $\Phi \to \infty$, we fall back on the classical non-penetrative boundary condition and the radial velocity at the interface tends to zero, which implies a very inefficient mass transfer between the ice and the ocean. In this study, all the runs have been done considering an efficient phase change of $\Phi = 10^{-2}$, which gives the dynamical regime expected for large rich-water bodies [Lebec et al., 2023].

The equation 3.6 for the composition being hyperbolic, no boundary condition can be applied and a specific treatment is needed to impose an influx of salts at the bottom. As discussed below, in section 3.3.2.2, this is done using Lagrangian tracers. At the bottom of the ice layer, we impose an influx of salts corresponding to a dimensionless flux per surface unit $F_{salts} = Fd/\kappa = 1$. At the upper boundary, there is a mass exchange between the ice and the ocean by phase change, as a result of the mechanical boundary condition just discussed. This mass exchange is treated differently on both sides. At regions of downflow in the ice, water freezes to form newly accreted ice whose composition is set by the partition coefficient, K. Where ice is flowing toward the ocean, it must reach an equilibrium, which implies a modification of its temperature by diffusion and complete melting, irrespective of its composition. The liquid is at the liquidus corresponding to its composition, which could be different from the solidus corresponding to the composition of the solid. In most cases, the solidus of the solid is likely lower than the liquidus of the liquid, in particular if the phase diagram presents a eutectic. In that case, melting of ice is eased, and it could even start before reaching the boundary [Kalousová et al., 2018], a possibility not treated in the present study. If, on the other hand, the liquidus of the liquid is lower than the solidus of the solid, the excess salt in the liquid serves as fusing agent, similarly to the salt spread on snowy roads in mountain regions. In both cases we therefore expect the whole ice flowing through the boundary to melt and its content to mix with the ocean.

3.3.1.3 Evolution of the ocean composition

As explained in the introduction to this section, the ocean evolves in time through mass exchanges with the HP ice layer. The concentration of salts in the ocean C^o evolves over

time as:

$$M^o \frac{dC^o}{dt} = 4\pi (R^+)^2 \rho F^o, \tag{3.16}$$

with F^o the total flux of salts at the interface between the ice and the ocean in m s^{-1} (and ρF^o the total mass flux in kg m^{-2} s^{-1}) and $M^o = (4/3)\pi(R_o^3 - (R^+)^3)\rho$ the ocean mass.

The total flux of salts F^o from the ice to the ocean is composed of an inward flux and an outward flux. The salt/ice mixture transported in the up-welling hot plumes reaches the interface with a radial velocity at top $w_{top} > 0$ and the ice melts at this contact. In this case, the salts contained in the ice melting at the interface are transported from the ice to the ocean. Conversely, above the down-welling currents $w_{top} < 0$ and a certain amount of salts depending on K enters the ice due to freezing at the boundary. The expression of this flux depends on the value of the top radial velocity as:

$$F^o = \begin{cases} w_{top} C^i_{top} & if\ w_{top} > 0 \\ w_{top} K C^o & if\ w_{top} < 0 \end{cases} \tag{3.17}$$

with C^i_{top} the concentration of salts in the ice that melts at the interface.

3.3.2 Numerical method

3.3.2.1 Numerical solution

In this study we used StagYY [Tackley, 2008] to solve the convection equations (§ 3.3.1.1) subject to boundary conditions described in sections § 3.3.1.2. The geometry considered for this model is a two-dimensional spherical annulus [Hernlund and Tackley, 2008]. This convection code, originally developed for convection in rocky mantles, solves the convection equations in various geometries using a finite volume approach and uses Lagrangian tracers to treat composition (more on that below). The longitudinal aperture on which the convection equations are solved is set to $\frac{\pi}{6}$ in all cases, which is enough to capture at least one horizontal period [Lebec et al., 2023]. For the grid, we choose the number of cells in the radial direction $nz_{tot} = 128$ in order to have a high enough resolution to reach the global energy balance. The number of cells in the horizontal direction ny_{tot} is computed in order to make the cells as squared as possible. Therefore, for the runs with an aspect ratio $\gamma = 0.8$, $ny_{tot} = 256$ and for $\gamma = 0.9$, $ny_{tot} = 512$. As we will see in the results, in some cases the salts stack up at the bottom of the HP ice layer. Therefore, the grid is refined in the radial direction by a factor of 6 near the core/ice interface. It is also refined by a factor of 2 near the top boundary to properly solve the phase-change.

Another numerical issue is for high Rayleigh numbers. All the runs of this work are for a Rayleigh number between 10^7 and 10^9 and an efficient phase-change $\Phi = 10^{-2}$ at top. Due to this phase change, the thermal boundary layer at the top interface is $1/w_{top}$ thick. Knowing that the radial velocity at top can be very high, these runs require a very small grid spacing near the interface to be resolved correctly. To this end, we adopt an approach

developed by [Agrusta et al., 2020] and used by [Lebec et al., 2023] which removes the thin boundary layer and applies a Robin boundary condition which allows us to switch from a fixed flux boundary condition to a fixed temperature boundary condition along the interface depending on the value of the radial velocity. This condition is written as [Agrusta et al., 2020]:

$$\Gamma\theta + (1-\Gamma)\frac{\partial\theta}{\partial r} = 0, \tag{3.18}$$

with θ the lateral deviation of the temperature. Γ is the following approximation of the Heaviside function:

$$\Gamma = \frac{1}{2}\left[1 + \tanh\left(\pi\frac{\frac{w_0}{2} - w_{top}}{\frac{w_0}{2}}\right)\right], \tag{3.19}$$

with w_0 the velocity threshold between both conditions, chosen here as $w_0 = 5\times10^{-2}Ra_q^{2/3}$. Depending on the value of w_{top}, representing the up-welling hot plumes and down-welling currents velocity at the interface, this function makes the boundary condition change smoothly from a Neumann boundary condition for which $\frac{\partial\theta}{\partial r} = 0$ in fast upwelling regions to a Dirichlet boundary condition for which $\theta = 0$ in down-welling or slowly upwelling regions.

3.3.2.2 Compositional tracers of salts

To explore the effect of salts on the heat and mass transfer through a HP ice layer, we use Lagrangian tracers distributed throughout the ice shell [Tackley and King, 2003, for more information on the use of tracers and benchmarking]. These tracers are carrying the composition in salts of the HP ice layer. At each time step, the information carried by the tracers is used to compute a salt concentration field on the finite volume grid which, together with the temperature field, is used to compute the total buoyancy force on the right-hand-side of equation 3.4. Using a finite volume approach, the code solves the flow velocity which is then used to compute the evolution of temperature and composition.

As explained before, if the bottom temperature is high enough to melt the ice, the water in contact with the core gets enriched in salts. If this mixture is less dense than the ice, it should rise through the HP ice shell by porous flow and recrystallize. Then, the salts/ice mixture obtained could reach the ocean by convection in the solid state. This process of porous flow requires a full two-phase flow treatment to be modeled self-consistently [Kalousová et al., 2018]. Alternatively, we chose to impose a salt flux at the boundary. However, in the absence of salt diffusion in the equation (3.6), applying a boundary condition does not affect the solution. We adopt the approach proposed by Bouffard et al. [2017] to model this compositional flux: we add a concentration $\delta C(r)$ corresponding to the desired flux directly to the tracers as

$$\int_{r^-}^{r^+} r^2\delta C(r)dr = r^{-^2}F_{salts}\Delta t, \tag{3.20}$$

with r^- (resp. r^+) the dimensionless radius of the bottom (resp. top) boundary of the HP ice layer, knowing $r^+ - r^- = 1$, F_{salts} the dimensionless flux of salts per surface unit and Δt the time step. This additional concentration is added following a Gaussian-like curve centered around a horizontal line just above the bottom interface, as follows:

$$\delta C(r) = \frac{a_F \Delta t}{r^2} exp\left(-\frac{(r-(r^-+h))^2}{\sigma^2}\right), \tag{3.21}$$

with $h = 0.05$ the position of the peak above the bottom boundary and $\sigma = 0.01$ the peak thickness (the values have been chosen empirically), r the position of the tracer inside the HP ice layer to which we add δC and a_F a constant computed from eq.3.20 as:

$$a_F = \frac{2(r^-)^2 F_{salts}}{\sqrt{\pi}\sigma\left(erf\left(\frac{1-h}{\sigma}\right) + erf\left(\frac{h}{\sigma}\right)\right)}. \tag{3.22}$$

Because of the way the flux of salts from the core is modeled, whose associated concentration is distributed in the ice layer according to a Gaussian-like curve, the number of tracers per cell has to be large enough to ensure the smallest possible error on the imposed flux. After some computation to have the best flux quality/computational resources ratio, we fixed it to 500 tracers per cell.

3.4 Results

Two sets of runs have been performed in order to study the effect of salts in the most systematic way, as listed in table 3.1. First of all, we performed a few runs (#1) with a zero salts flux from the core and a non-zero initial salt concentration $C^o_{ini} = 1$ in the ocean to study whether an equilibrium is reached between the ocean and the HP ice layer in term of composition and the time required to reach a steady state in a closed ocean/HP ice system.

For the second set (#2) we added a compositional flux of salts $F_{salts} = 1$ at the bottom of the HP ice layer. Therefore, we never reach a steady-state because the salts continuously enter the ice and the concentration of salts increases with time. These runs all start with a zero initial concentration of salts in the ocean C^o_{ini}, and in the HP ice layer C^i_{ini} and are done for large ranges of values for K, B_{salts}, Ra_q and for two values of the aspect ratio γ.

3.4.1 Closed ocean/HP ice system

Before imposing a flux of salts from the core, let us study the evolution of a closed ocean/HP ice system (See study case #1 in table 3.1). Without an influx from the core, the two layers evolve according to two parameters: B_{salts} and K until reaching a steady-state after a certain amount of time. If the system reaches an equilibrium, the two layers are balanced,

Table 3.1: All simulations are done for a rigid bottom boundary condition and an efficient phase-change at top $\Phi = 10^{-2}$. $\bullet^o$ is for ocean and $\bullet^i$ is for the HP ice layer. C_{ini} is the initial concentration of salts in the designated shell.

#	F_{salts}	C^o_{ini}	C^i_{ini}	K	B_{salts}	Ra_q	γ
1	0	1	0	$0.001, 1$	$0, 3, 10$	10^7	$0.8, 0.9$
2	1	0	0	0,0.001,0.01, 0.1,0.3,1	$0, 0.1, 0.3, 1, 3, 10$	$10^7, 10^8, 10^9$	$0.8, 0.9$
				0.01	$0, 0.1, 0.3, 1, 3, 10$	$3 \times 10^7, 3 \times 10^8$	0.8
				0.01	0.5	10^7,2×10^7,3×10^7,6×10^7,10^8, 2×10^8,3×10^8,6×10^8,10^9	$0.8, 0.9$

each around an equilibrium concentration. A similar study was performed by Bolrão et al. [2021] but with different boundary conditions and geometry, relevant to the magma oceans on Earth.

Starting with a zero concentration in the HP ice shell, we set an initial concentration of salts in the ocean $C^o_{ini} = 1$. If the whole ice layer reaches an equilibrium with the ocean (which is homogeneous by construction of the model), the concentration in the ocean tends to C^o_{eq} and the one in the ice tends to C^i_{eq}, both expressed from the initial concentration C^o_{ini}, the partitioning coefficient K and the volumes of both layers as:

$$C^o_{eq} = C^o_{ini} \frac{V^o}{V^o + KV^i}, \tag{3.23}$$

$$C^i_{eq} = KC^o_{eq} = C^o_{ini} \frac{KV^o}{V^o + KV^i}, \tag{3.24}$$

with V^i (resp. V^o) the volume of the HP ice layer (resp. ocean).

Figure 3.3 shows the evolution of the concentration in salts of the ocean (top panels) and of the ice (bottom panels) for two partitioning coefficients. These graphs are made for various values of the buoyancy number and the red line shows the equilibrium concentrations C^o_{eq} in the ocean and C^i_{eq} in the ice. Figure 3.4 shows snapshots of 1/12 of the HP ice layer at the end of the runs for some of these cases. For both $K = 10^{-3}$ and $K = 1$, the concentration of salts in the ocean decreases as it increases in the ice until the onset of convection in the ice which allows the salts to reach the interface again and to dissolve back in the ocean. These two processes eventually balance each other out and the system ends up reaching a steady-state. For a partitioning coefficient of 1 (see fig. 3.3.a), all salts present in the water at the time of its recrystallization at the ocean/ice interface are trapped in the ice, leading from equations 3.24 and 3.23 to an equal value in both layers of the equilibrium concentration of salts at steady-state. This is what happens in the case $B_{salts} = 0$, for which both concentrations tend to their equilibrium values (eqns. 3.23 and 3.24). The salts are easily transported from

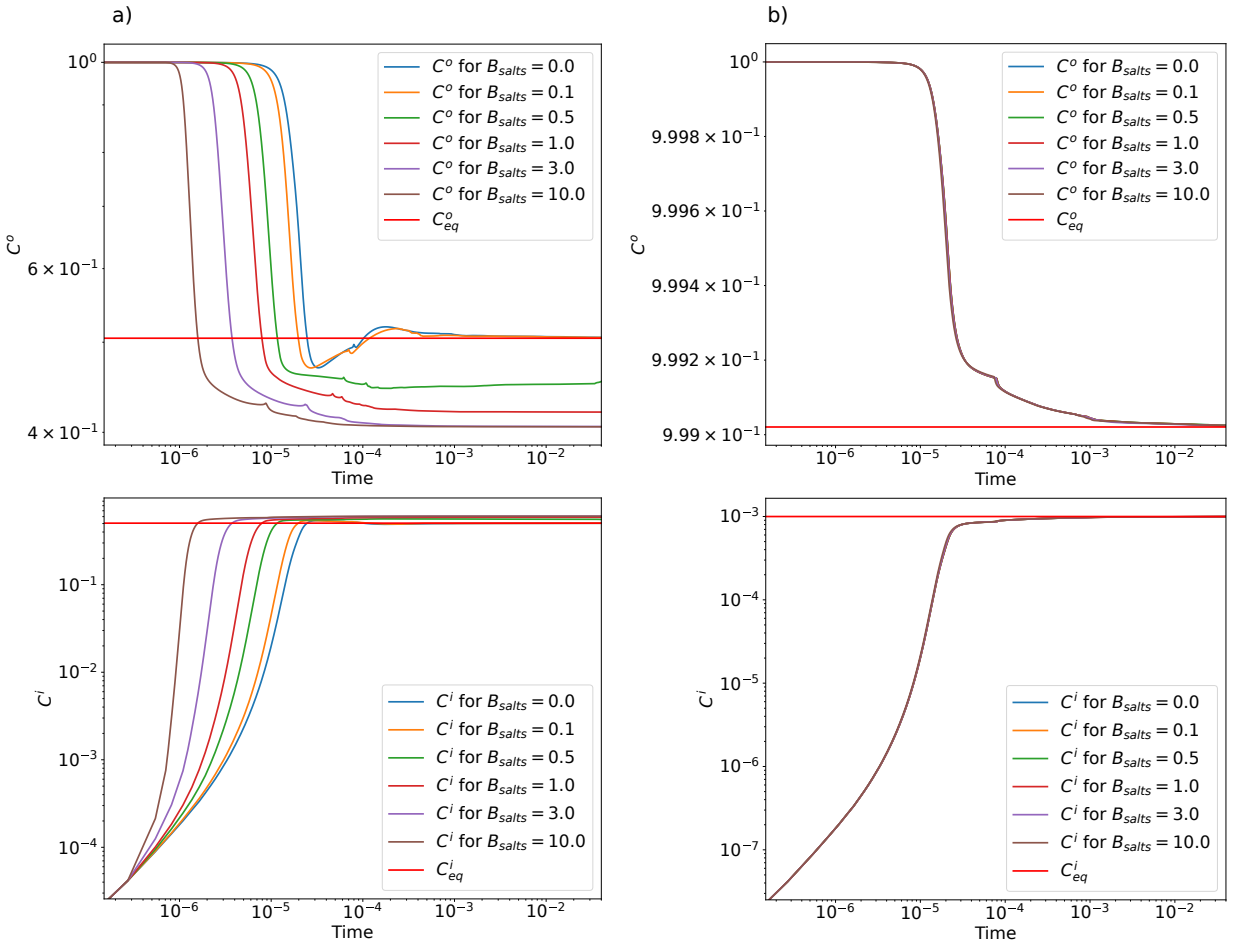

Figure 3.3: Evolution of the concentration in salts of the ocean (top) and the HP ice layer (bottom) with time for a partitioning coefficient a) $K = 1$ and b) $K = 10^{-3}$, a Rayleigh number $Ra_q = 10^7$, an aspect ratio $\gamma = 0.8$ and various values of B_{salts}, as labeled.

one layer to another and it leads at steady-state to an almost homogeneous HP ice layer, as can be seen on fig. 3.4.a. However, these equations do not take into account the effect of the buoyancy number. Contrary to the ocean, the HP ice shell is not considered homogeneous and for $B_{salts} \geq 0.5$, salts from the ocean stack up at the bottom of the HP ice layer. This effect can be observed on fig. 3.4.b on which the concentration is higher in the bottom part of the HP ice shell. Therefore, the salts are difficult to transfer to the ocean by convection and it leads, for $B_{salts} \geq 0.5$, to a mean concentration in the ice larger than the equilibrium value and lower than the equilibrium value in the ocean. The time required to evolve halfway to the steady-state concentration is reported in table 3.2 and named $t^{1/2}$. It shows that, for $K = 1$, the higher the buoyancy number, the faster the steady state is reached. Contrary to all other cases displayed on fig. 3.4, the temperature field in the HP ice layer for $B_{salts} = 10$ and $K = 1$ (see fig. 3.4.b) shows that convection stopped. In this study B_{salts} is an imposed

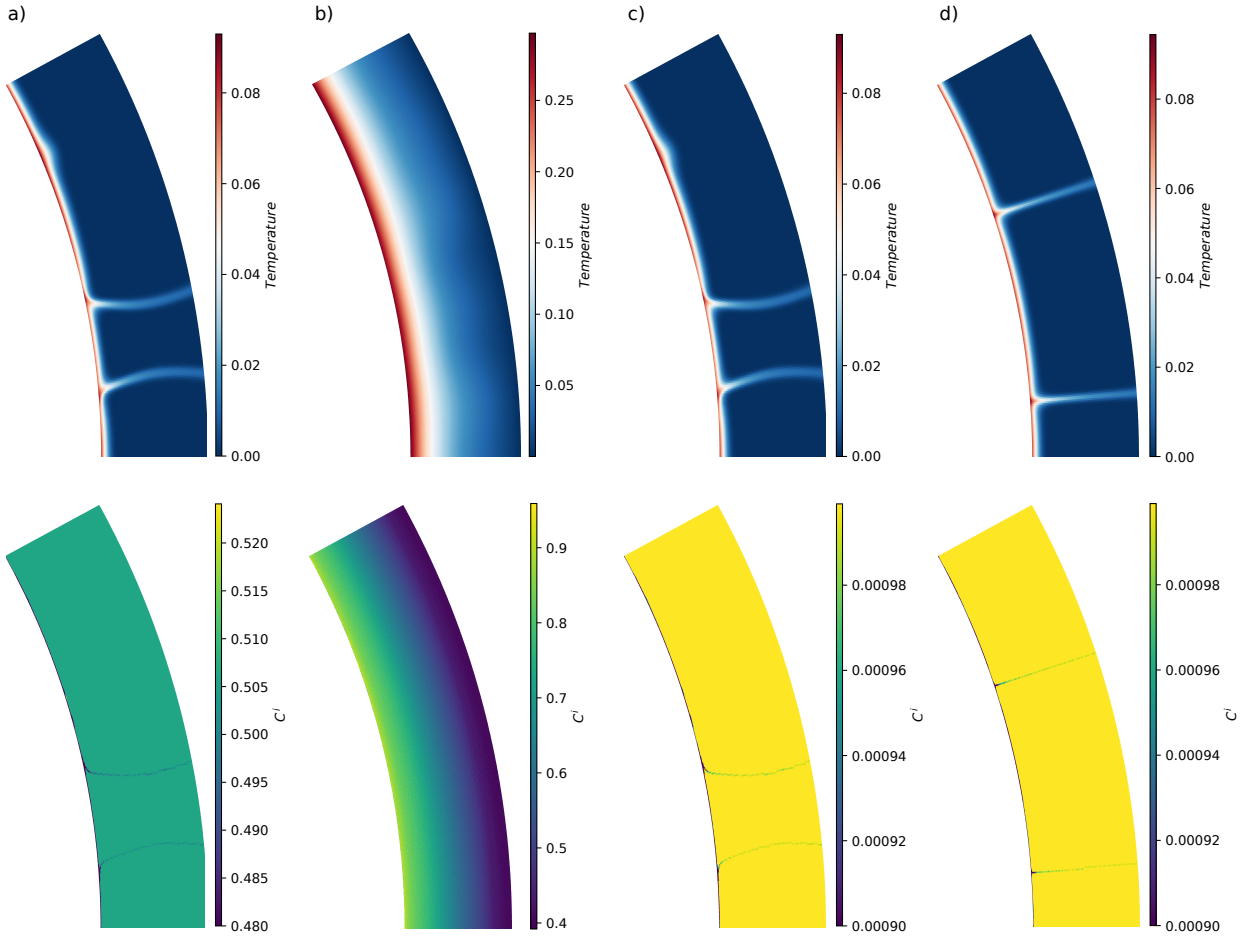

Figure 3.4: Snapshots of 1/12 of the HP ice layer in steady-state at $t \simeq 4 \times 10^{-2}$ for a Rayleigh number $Ra_q = 10^7$, an aspect ratio $\gamma = 0.8$. The top (resp. bottom) panels show the temperature (resp. composition) inside the ice shell for a) $K = 1$ and $B_{salts} = 0$, b) $K = 1$ and $B_{salts} = 10$, c) $K = 10^{-3}$ and $B_{salts} = 0$ and d) $K = 10^{-3}$ and $B_{salts} = 10$. The minimum concentration of salts in the HP ice layer for a),b),c) is 0 but the color bars have been limited to a) 0.48 and c)&d) 9×10^{-4} in order to have more information about what happens in the bulk of the ice shell.

input parameter which is not representative of what will be achieved in the run in terms of concentration and temperature contrast. A posteriori, an effective buoyancy number B_{eff} can be computed based on what has actually been achieved during the run, defined as:

$$B_{eff} = \frac{C^i_{bot} - C^i_{top}}{\tilde{T}_{bot} - \tilde{T}_{top}} B_{salts}. \tag{3.25}$$

In the case of fig. 3.4.b, $B_{eff} = 20$, which is very high and the convection was impeded by the salts stacking at the bottom of the HP ice layer, unlike other cases for which the effective buoyancy number is in the range $0 - 0.1$. To better conclude on this particular case, the

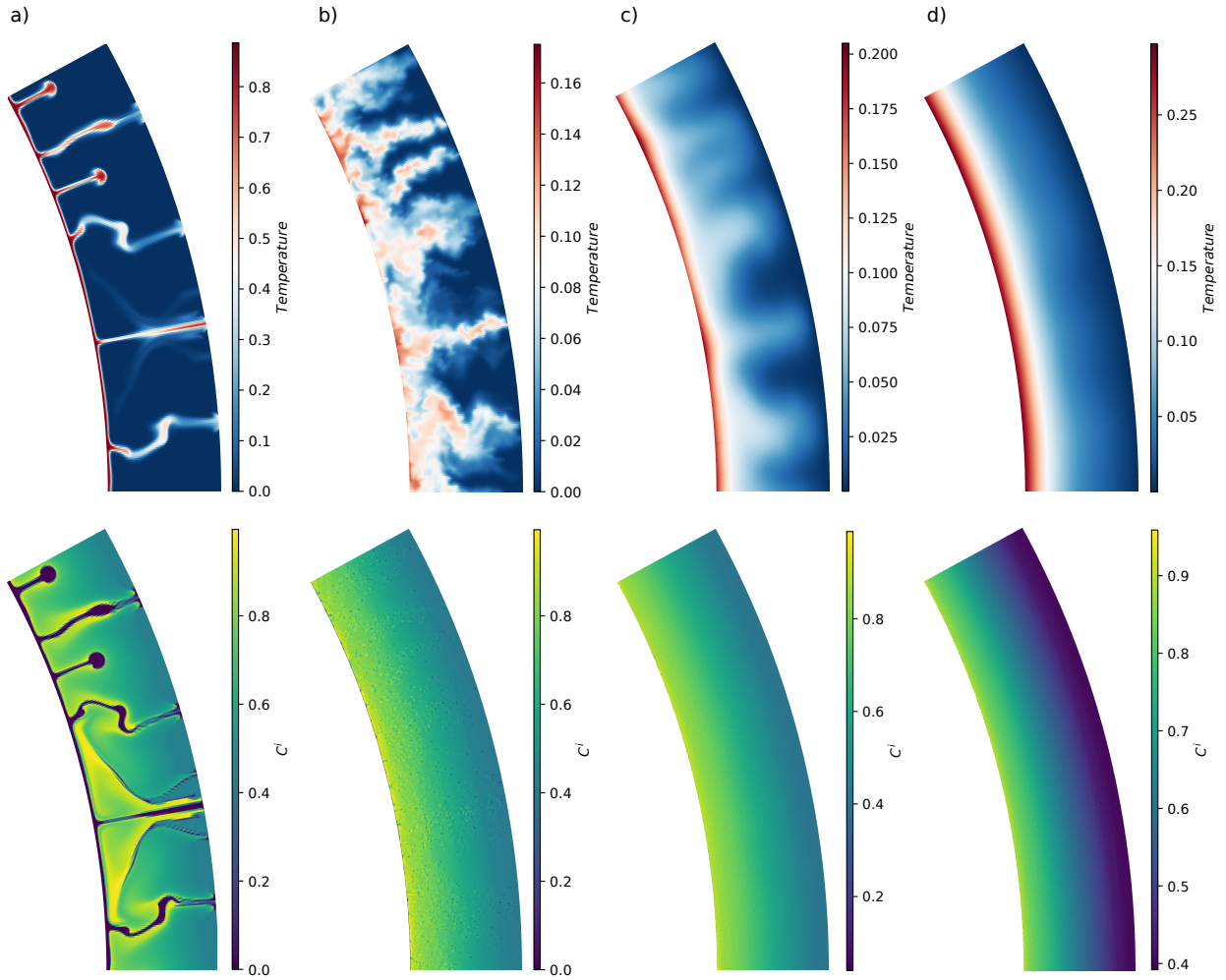

Figure 3.5: Snapshots of the evolution in time of 1/12 of the HP ice layer for a Rayleigh number $Ra_q = 10^7$, an aspect ratio $\gamma = 0.8$, a partitioning coefficient $K = 1$ and a buoyancy number $B_{salts} = 10$. The top (resp. bottom) panels show the temperature (resp. composition) inside the ice shell for a) $t = 10^{-5}$, b) $t = 4.5 \times 10^{-4}$, c) $t = 7.5 \times 10^{-3}$ and d) $t = 4 \times 10^{-2}$.

figure 3.5 shows the evolution in time of the temperature and the concentration fields from an early stage of the run to $t = 4 \times 10^{-2}$ which is the time of figure 3.4.b. On fig. 3.5.a the convection is very strong and the buoyancy number is around 10. At this stage, the heavy salts enter the ice layer from above and therefore help convection which is very fast. The salts are entering the layer above the down-welling currents and the up-welling hot plumes are poor in salts. At the time of fig. 3.5.b, salts have already accumulated at the bottom of the ice layer and the effective buoyancy number is around 60, which is enough to inhibit convection. From that point, the salts continue to enter the ice from the ocean and stack up at the bottom of the ice layer and the convective movements disappear.

Table 3.2: Time $t^{1/2}$ required to evolve halfway to the steady-state concentration.

K	B_{salts}	$t^{1/2}$
1	0	2×10^{-5}
	0.1	1.5×10^{-5}
	0.5	9×10^{-6}
	1	6×10^{-6}
	3	3×10^{-6}
	10	10^{-6}
0.001	0	2×10^{-5}
	0.1	
	0.5	
	1	
	3	
	10	

For a low partitioning coefficient $K = 10^{-3}$ (see fig. 3.3.b), the chosen buoyancy numbers have a very small impact on the dynamics because the concentration of salts trapped in the ice during freezing of water at the ice/ocean interface is very low. In that case, the effective buoyancy number for $B_{salts} = 10$ is $B_{\mathit{eff}} = 0.1$. It means that even for high values of B_{salts} the salts hardly affect the ice density and are still easily transported by convection. This can be observed on fig. 3.4.c and fig. 3.4.d which both show an almost homogeneous HP ice layer with the same amount of salts in the bulk. It confirms that for a very small amount of salts entering the ice from the ocean in a closed ocean/HP ice system the salts do not stack up at the bottom of the ice shell even for $B_{salts} = 10$. In all three cases of fig. 3.4.a,c,d the HP ice layer is almost homogeneous except for a salts-poor thin layer near the lower interface. This is due to the rigid bottom boundary condition, which strongly inhibits vertical flow toward the boundary compared to the case of a free-slip boundary condition. In the case of a low partitioning coefficient, the concentration in the ocean and in the ice layer tend to their respective equilibrium values, C^o_{eq} and C^i_{eq}, irrespective of the buoyancy number chosen here, but the equilibrium concentration in the ice is K times smaller than that in the ocean. Also, the time $t^{1/2}$ to reach half the steady-state concentration is the same whatever the buoyancy number considered in this study because B_{eff} is close to zero in all of those cases. (See table 3.2).

For all values of B_{salts} and K considered in this set of runs, the time to reach half of the steady-state concentration is in the range $10^{-6} - 10^{-5}$ (See table 3.2). For Ganymede, using the values of table 3.4, $t^{1/2}$ is of the order 1.5×10^4 to 1.5×10^5 years.

3.4.2 Effects of an influx of salts on the overall dynamics

Now, adding a flux of salts from the core, we will discuss the qualitative evolution of the system with time depending on the parameters B_{salts} and K before discussing the two main regimes of salts transport through the HP ice layer as a function of the buoyancy number.

3.4.2.1 Qualitative effects of B_{salts} and K on the evolution of the system

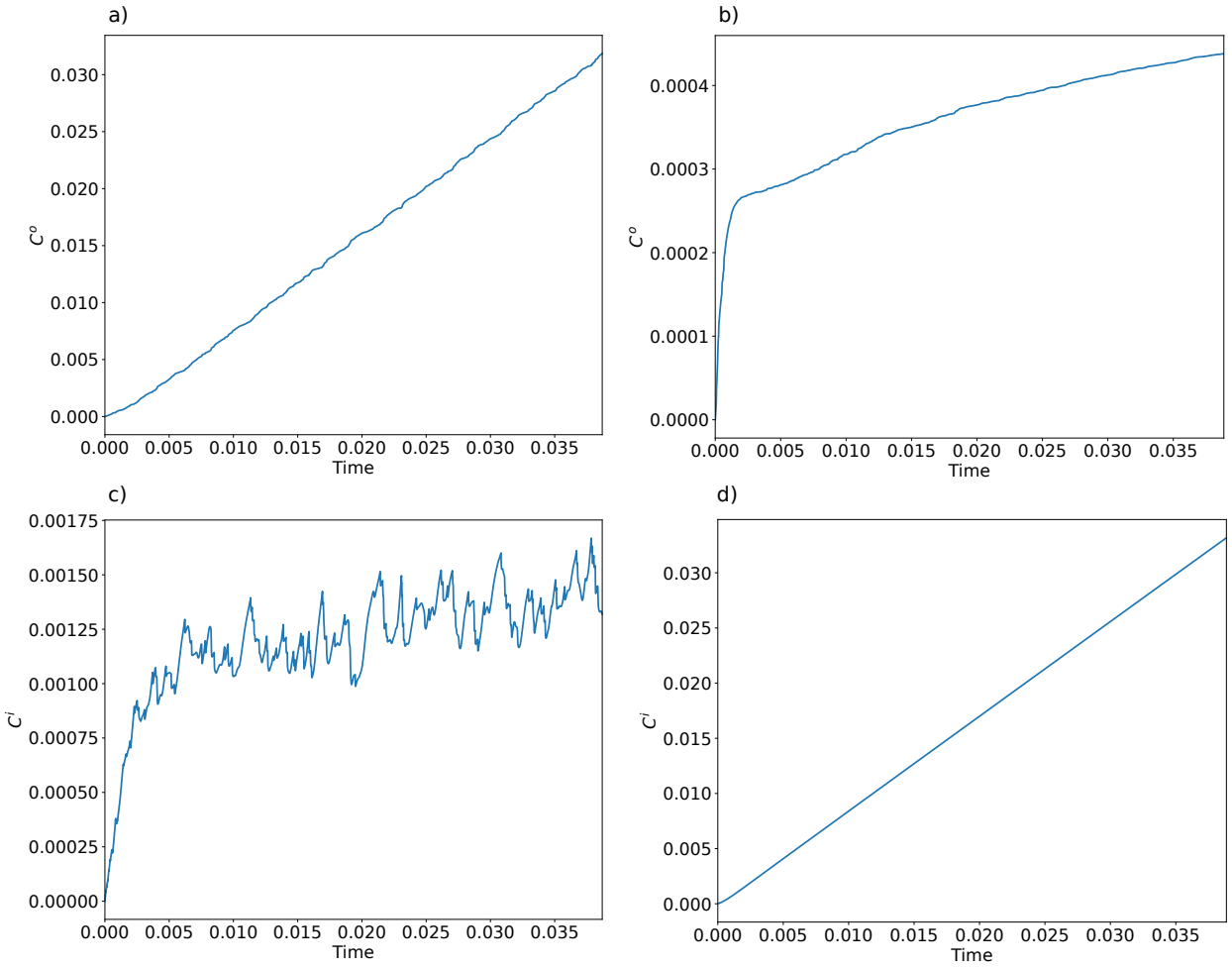

Figure 3.6: Evolution of the ocean a)&b) and HP ice layer c)&d) average concentrations of salts as function of time for a buoyancy number a)&c) $B_{salts} = 0$ and b)&d) $B_{salts} = 10$. Both a)&c) and b)&d) are for a Rayleigh number of 10^8, a partitioning coefficient of the salts between the ocean and the HP ices at the top interface of $K = 10^{-2}$ and an aspect ratio of $\gamma = 0.9$.

In the rest of the results section we analyse the runs of the study case #2 detailed in table 3.1 and we start with a qualitative analysis of the effects of the buoyancy number and the partitioning coefficient on the evolution of the concentrations in salts of the ocean and

the HP ice layer over time. When B_{salts} is 0, the salts have no impact on the ice density and the salts/ice mixture has the same density than pure ice. In that case, the salts are transported passively through the HP ice layer until they reach the ocean. This is what happens on fig. 3.6.a, the concentration of salts in the ocean is increasing steadily with time as the salts are easily transported by thermal convection from the core to the ocean. On the other hand, the higher the buoyancy number, the higher the density of the salts/ice mixture compared to pure ice. As can be seen on fig. 3.6.d for $B_{salts} = 10$, the concentration of salts in the HP ice layer is continuously increasing because the salts mostly accumulate at the bottom of the HP ice layer, the density of the HP ice and salts mixture increasing with time. However, a part of this mixture still rises through the ice and reaches the ocean. At the beginning of the simulation, the concentration of salts in the ice is small enough to allow a part of the salts/ice mixture to rise efficiently through the ice and the ocean concentration of salts increases rather strongly (fig. 3.6.b). After a certain amount of time, the proportion of salts becoming higher in the ice shell, less salts are reaching the ocean and the increase rate of the ocean concentration stabilizes to a smaller value (fig. 3.6.b).

The partitioning coefficient of the salts between the ocean and the HP ices at the top interface controls the amount of salts trapped in the ice when a part of the ocean freezes at the top interface. When $K = 0$, salts are not trapped in the ice during the re-crystallisation of the liquid water and, as can be seen on fig. 3.7.c, after a certain amount of time, the concentration of salts in the HP ice layer reaches a compositional steady state. Indeed, as $B_{salts} = 0$ and $K = 0$, after the onset of convection, the amount of salts entering the HP ice layer from the core is similar to that entering the ocean at each time step, which leads to this quasi-steady state. On the other hand, the higher the partitioning coefficient, the higher the amount of salts trapped during the re-crystallisation at the interface. In the case $B_{salts} = 0$ and $K = 1$, the concentration of salts in the HP ice layer continues to increase over time, as well as the concentration of salts in the ocean, as shown on fig. 3.7.b and fig. 3.7.d.

All the runs have been done for an efficient phase change at top, with a phase change number $\Phi = 10^{-2}$. For this reason, whatever the buoyancy number and the partitioning coefficient, the ice in the ascending hot plumes that reaches the ocean melts at its contact, the boundary is permeable and the radial velocity at the top is much higher than 1. The convection pattern is the same for all cases shown on fig. 3.8, composed of up-welling hot plumes and down-welling cold and broad currents. For the case $B_{salts} = 10$, the salts significantly increase the salts/ice mixture density. Therefore, they stack up just above the interface between the core and the ice, as can be seen on the compositional field of fig. 3.8.c, which increases the bottom temperature (See 3.4.2.3) and leads to an ocean very poor in salts as shown on fig.3.6.b. On the contrary, on fig. 3.8.a and 3.8.b for $B_{salts} = 0$, the salts follow the heat convection pattern, as the salts have no or low effect on the ice density for low values of the buoyancy number. Also, the ice is on average richer in salts on fig. 3.8.a due to the higher partitioning coefficient.

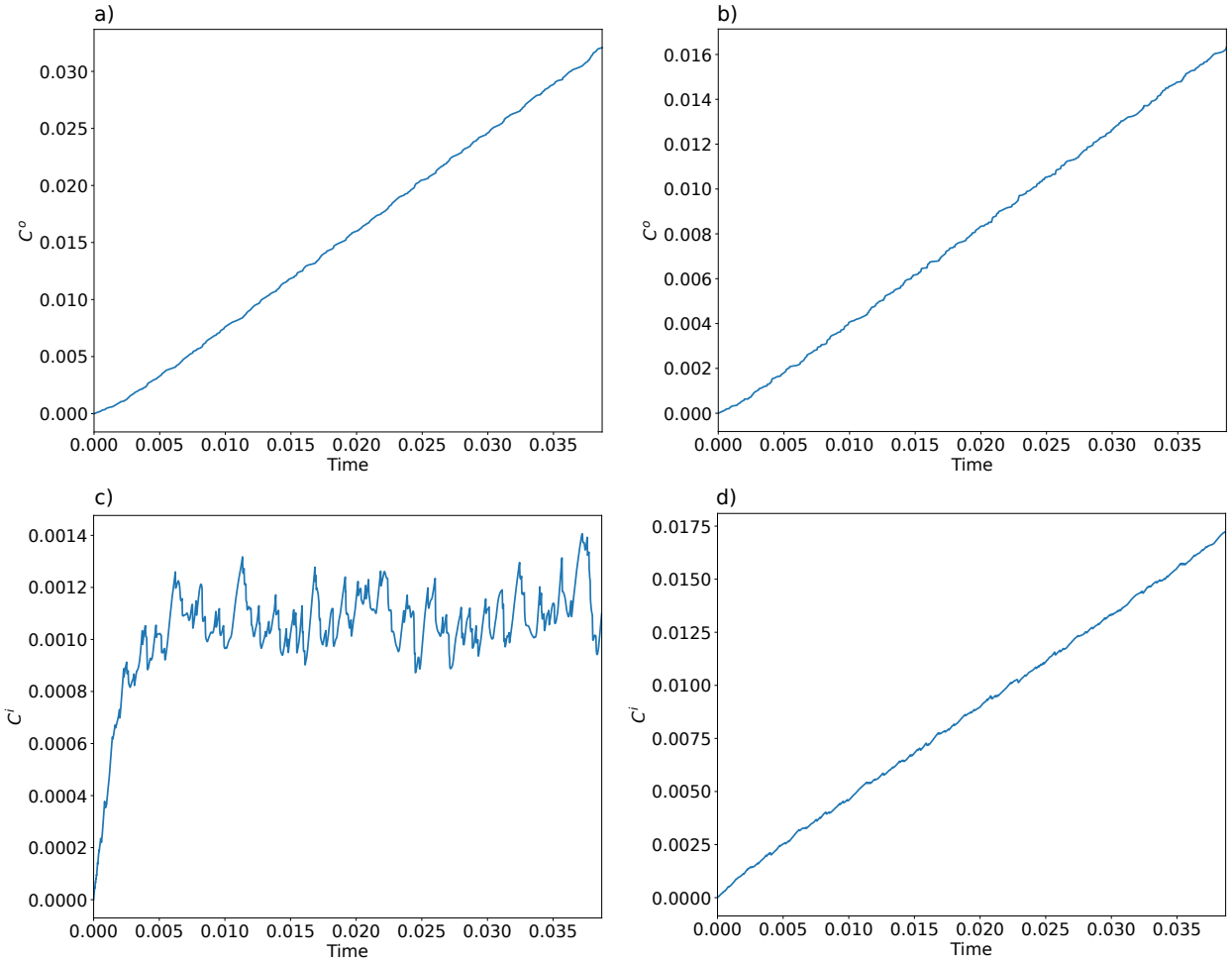

Figure 3.7: Evolution of the ocean a)&b) and HP ice layer c)&d) average concentrations of salts as function of time for a partitioning coefficient of the salts between the ocean and the HP ices at the top interface of a)&c) $K = 0$ and b)&d) $K = 1$. Both a)&c) and b)&d) are for a Rayleigh number of 10^8, a buoyancy number of $B_{salts} = 0$ and an aspect ratio of $\gamma = 0.9$.

3.4.2.2 Compositional flux accuracy

To check the accuracy of the numerical treatment of the flux of salts we impose at the interface between the core and the HP ice layer, defined in 3.3.2.2 and set to $F_{salts} = 1$ in the second series of runs (#2 in table 3.1), we compute the total rate of increase of the salt concentration in both layers and divide it by the surface of the lower interface between the ice and the core, which should be equal to the target flux coming from the core:

$$F_{salts}^{eff} = \frac{\Delta C^i V^i + \Delta C^o V^o}{4\pi r^{-2} \Delta t}, \tag{3.26}$$

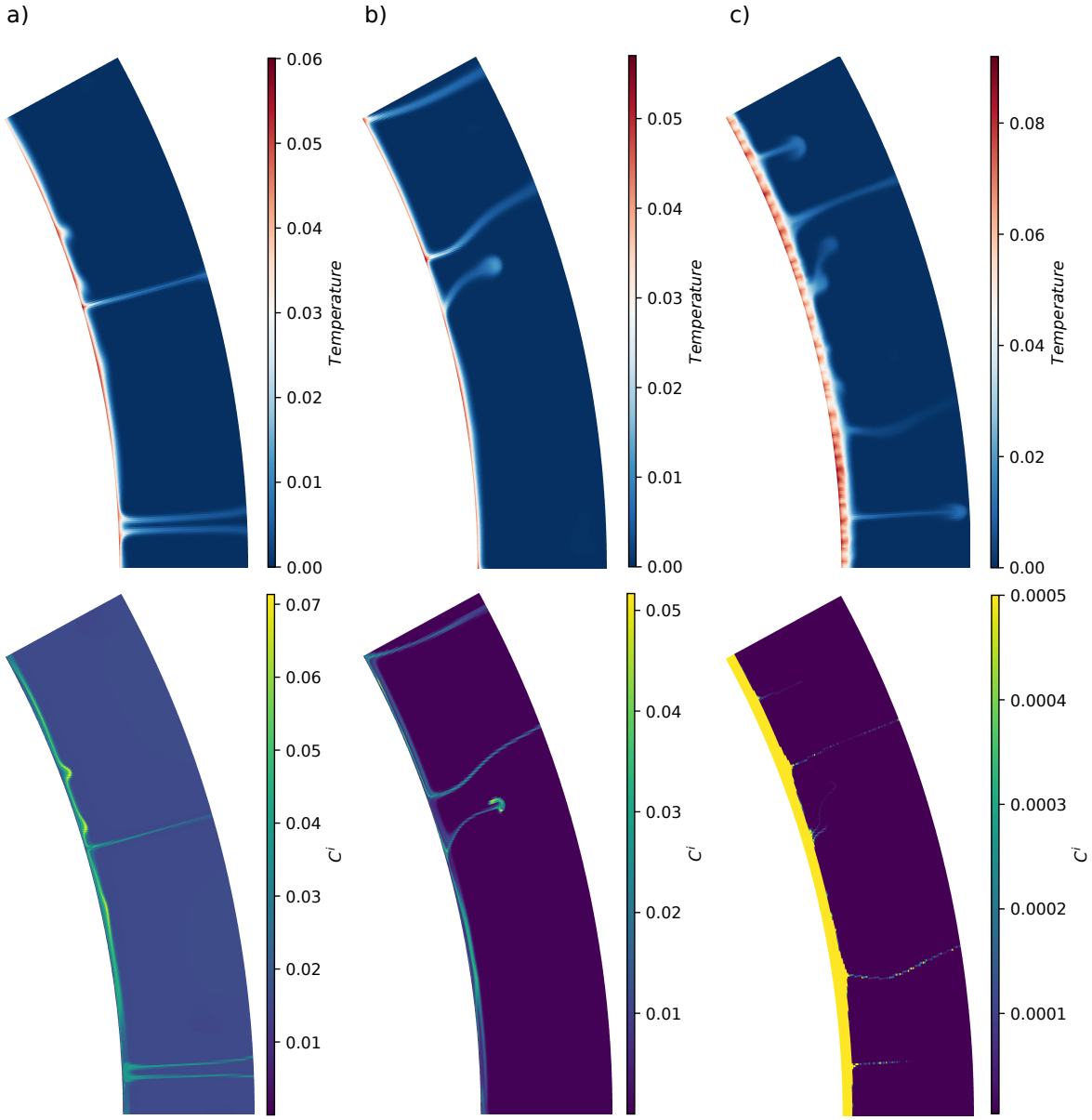

Figure 3.8: Snapshots of 1/12 of the HP ice layer after stabilization of the slopes of concentration increase in the ocean and in the ice over time at $t \simeq 4 \times 10^{-2}$ for a Rayleigh number $Ra_q = 10^8$, an aspect ratio $\gamma = 0.8$. The top (resp. bottom) panels show the temperature (resp. composition) inside the ice shell for a) $K = 1$ and $B_{salts} = 0$, b) $K = 10^{-2}$ and $B_{salts} = 0$, c) $K = 10^{-2}$ and $B_{salts} = 10$. The maximum concentration of salts in the HP ice layer for c) is about 0.57 but the color bars have been limited to 5×10^{-4} in order to have more information about what happens in the bulk of the ice shell.

with ΔC^i (resp. ΔC^o) the variation of the salt concentration in the ice (resp. ocean) over Δt. Figure 3.9 depicts this effective flux of salts as function of the buoyancy number after

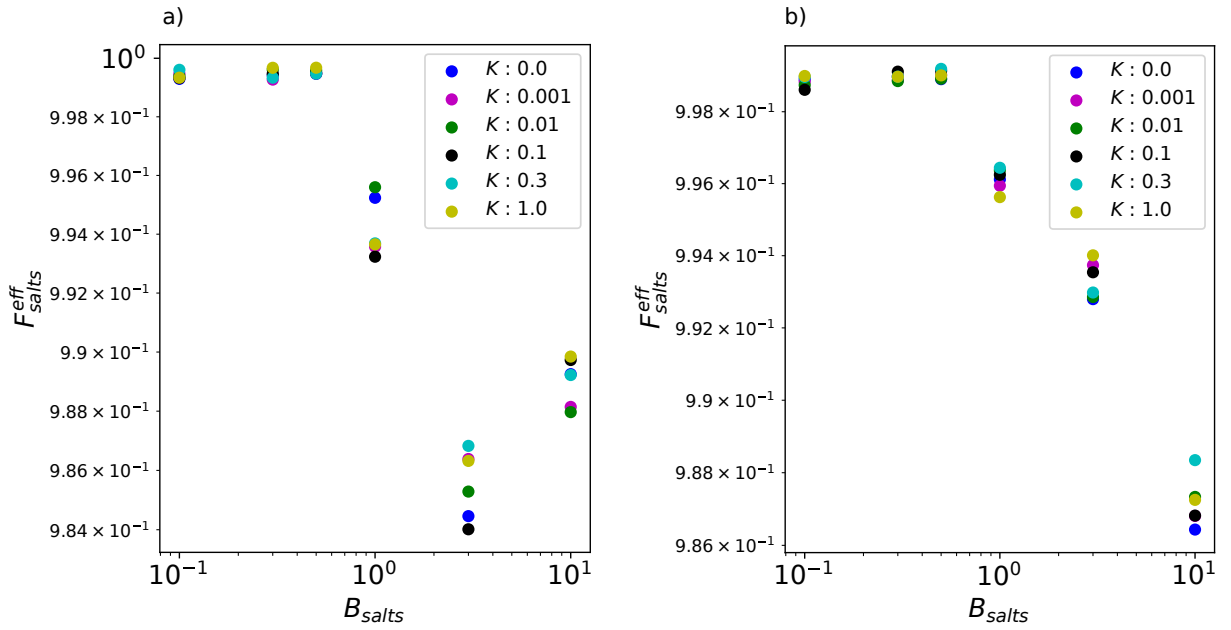

Figure 3.9: Flux of salts from the core as function of the buoyancy number for $Ra_q = 10^9$ and a) $\gamma = 0.8$ and b) $\gamma = 0.9$ for various values of the partitioning coefficient of the salts between the ocean and the HP ices at the top interface. This flux should be equal to 1 for all these simulations, these two figures contain the most extreme cases in terms of flux error for each aspect ratio. The residual error is discussed in the text.

the stabilization of the increase rate of the ocean concentration with time (see § 3.4.2.1 for more details). The two panels show F^{eff}_{salts} for various values of the buoyancy number and partitioning coefficients and contain the worst case among all runs of table 3.1 in term of error flux for $\gamma = 0.8$ (fig. 3.9a), which is for $B_{salts} = 3$ and $K = 10^{-1}$ and for $\gamma = 0.9$ (fig. 3.9b), which is for $B_{salts} = 10$ and $K = 0$. The maximum error, all cases combined, is about 1.6%. This error is mostly due to the resolution at the bottom boundary. In the case of a large buoyancy number, the salts pile up at the bottom of the HP ice layer over time, which explains why the resolution must increase with B_{salts}. The worst case for both values of the aspect ratio in terms of error flux is for a Rayleigh number of 10^9 and the resolution must be finer for higher Rayleigh numbers. Here we chose to refine the grid at the bottom boundary in order to limit this problem, as explained in § 3.3.2.1. We could further refine this boundary layer and increase the resolution of the simulations but increasing the resolution requires more numerical resources for an already very small error.

3.4.2.3 Time evolution

Let us now turn to a systematic exploration of the effect of the various control parameters. The fig. 3.10 shows the rate of change of the concentration in salts of the ocean $\mathrm{d}C^o/\,\mathrm{d}t$ and the HP ice layer $\mathrm{d}C^i/\,\mathrm{d}t$ as function of the salts buoyancy number and for various values

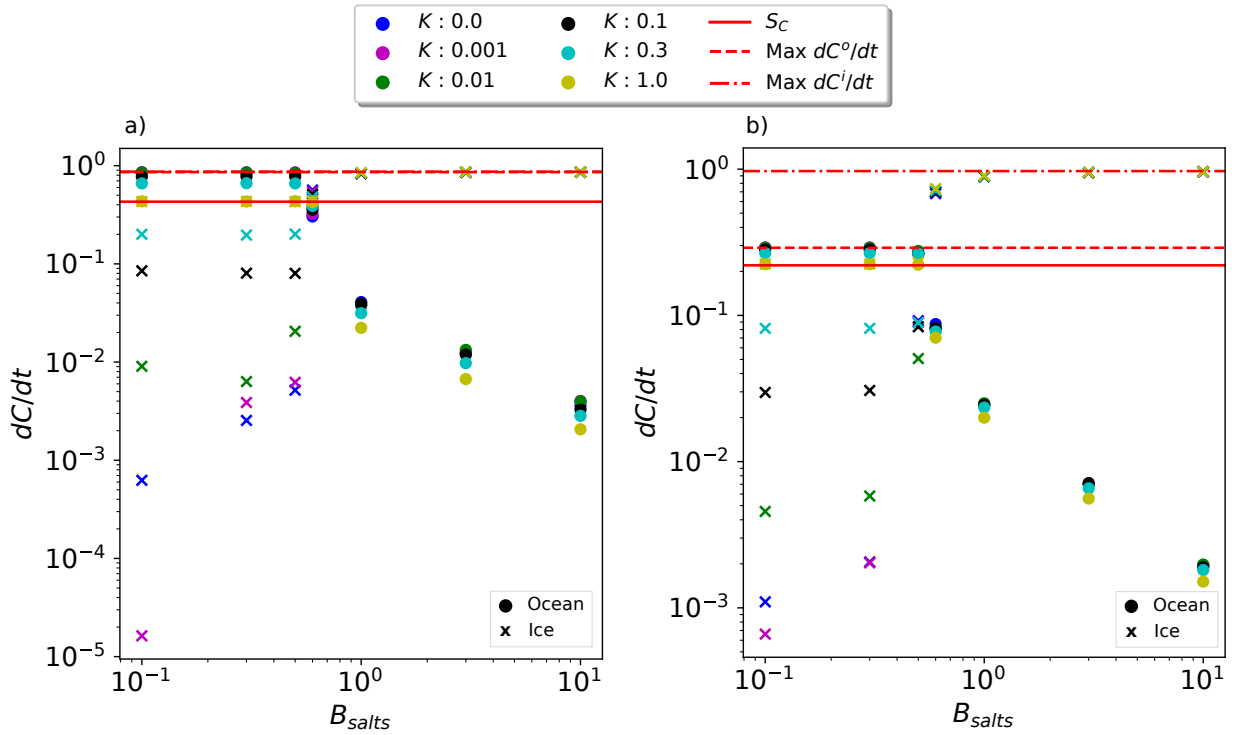

Figure 3.10: Rate of change of the concentration in salts of the ocean (•) and of the HP ice layer (×) over time as function of the salts buoyancy number for an aspect ratio a) $\gamma = 0.8$ and b) $\gamma = 0.9$. This has been computed for various values of K, for a Rayleigh number of $Ra_q = 10^8$ and a zero initial concentration C_{ini} in the ocean and in the HP ice layer. The grey line is the result of eq.3.28 and the two other lines are the maximum rate of change that can be reached in the ocean (red dotted line) and in the ice (orange dashed line).

of the partitioning coefficient K. These rates are computed over a time period chosen after the stabilization of the concentration slope in the two layers (See § 3.4.2.1), here between $t_1 = 10^{-2}$ and the end of the runs $t_2 = 3.8 \times 10^{-2}$. Due to the conservation of salts, the expression of the mass balance is:

$$\frac{(dC^o/dt)V^o + (dC^i/dt)V^i}{V^o + V^i} = \frac{4\pi(r^-)^2 F^{eff}_{salts}}{V^o + V^i}, \tag{3.27}$$

and we note S_C the average rate of increase in solid and liquid concentration:

$$S_C = \frac{4\pi(r^-)^2 F^{eff}_{salts}}{V^o + V^i}. \tag{3.28}$$

Since the salt flux at the bottom of the ice layer is equal to one by our choice of scaling, the value of this sum is purely geometrical and, for the same ocean radius R_o, depends only on the aspect ratio, which defines the thickness of the HP ice layer and, consequently, that of

the ocean. The thickness of the HP ice (resp. ocean) layer increases (resp. decreases) for decreasing values of the aspect ratio (there is a factor 2.25 on the thickness d between $\gamma = 0.8$ and $\gamma = 0.9$). For the ocean radius defined in § 3.3.2.1 corresponding to a Ganymede-like case, the theoretical value of S_C is about 0.43 for $\gamma = 0.8$ and about 0.22 for $\gamma = 0.9$ (See grey line on fig. 3.10.a and fig. 3.10.b). As shown on fig. 3.10, for low values of the buoyancy number ($B_{salts} \leq 0.6$ for $\gamma = 0.8$ and $B_{salts} \leq 0.5$ for $\gamma = 0.9$), the value of both rates of change (ocean and ice) equals the value of S_C for $K = 1$. From eq. 3.27, we can compute the two extreme cases for which the rate of change in the ice dC^i/dt or in the ocean dC^o/dt is 0, meaning that all the salts are transported to the other layer, which gives us its maximum rate of change. These maximum values, around $0.86 - 0.87$ for both layers for $\gamma = 0.8$ (because both volumes are similar in that case) and about 0.29 in the ocean and 0.97 in the ice for $\gamma = 0.9$, are represented on fig. 3.10 by a red dotted line for the ocean and an orange dashed line for the ice. As can be expected, dC^i/dt tends towards its maximum value for increasing values of the buoyancy number, irrespective of the value of K. On the other hand, dC^o/dt tends towards its maximum value for decreasing values of the buoyancy number and low values of K.

According to fig. 3.10, the proportion of salts in the ocean compared to the proportion in the ice shell reverses at a certain buoyancy number, which is the limit between the low buoyancy number regime and the high buoyancy number regime. For $Ra_q = 10^8$ this limit is around $B_{salts} = 0.6$ for $\gamma = 0.8$ (see fig. 3.10.a) and between $B_{salts} = 0.5$ and 0.6 for $\gamma = 0.9$ (see fig. 3.10.b). For each partitioning coefficient, the closer the buoyancy number is to this limit value, the closer dC^o/dt and dC^i/dt become. For B_{salts} ranging from ~ 1 to 10, dC^i/dt is close to the maximum value identified with eq. 3.28, leading to a similar concentration in salts in the ice at the end of the runs in all three cases presented here. The rate of change of the concentration in the ocean dC^o/dt in those cases is $< 10^{-1}$. This is consistent with the fact that the salts stack up at the bottom of the ice shell, preventing an efficient transfer of salts toward the ocean. For low values of the buoyancy number, $B_{salts} < 0.6$, the salts have a very low impact on the ice density and are transported easily by convection in the solid state through the HP ice layer. In those cases, the range covered by dC^i/dt as function of B_{salts} is really large, because almost the entire amount of salts coming from the core are transported into the ocean and the evolution of the salts concentration in the ice shell depends mostly on the amount of salts trapped into the ice when a part of the ocean at the interface with the HP ices refreezes and is accreted to the ice, which is controlled by K. On fig. 3.10, this is reflected in the fact that dC^i/dt decreases with decreasing values of the partitioning coefficient, while it is exactly equal to dC^o/dt for $K = 1$, for which the amount of salts trapped into the ice at the interface is maximal. For the concentration of salts in the ice, the value of K has nearly no effect for $B_{salts} \geq 1$ but a significant effect for $B_{salts} < 0.6$.

While the ocean is considered homogeneous by construction of the model, the salts concentration is not uniform in the HP ice layer and their distribution in the shell is controlled by the values of the partitioning coefficient and the buoyancy number. The figure 3.11 shows the profiles of temperature (left panels) and composition (right panels) in the HP ice layer for a partitioning coefficient of 1 and various values of the buoyancy number at different times of the runs. These times are similar between the three presented cases, $B_{salts} = 0$,

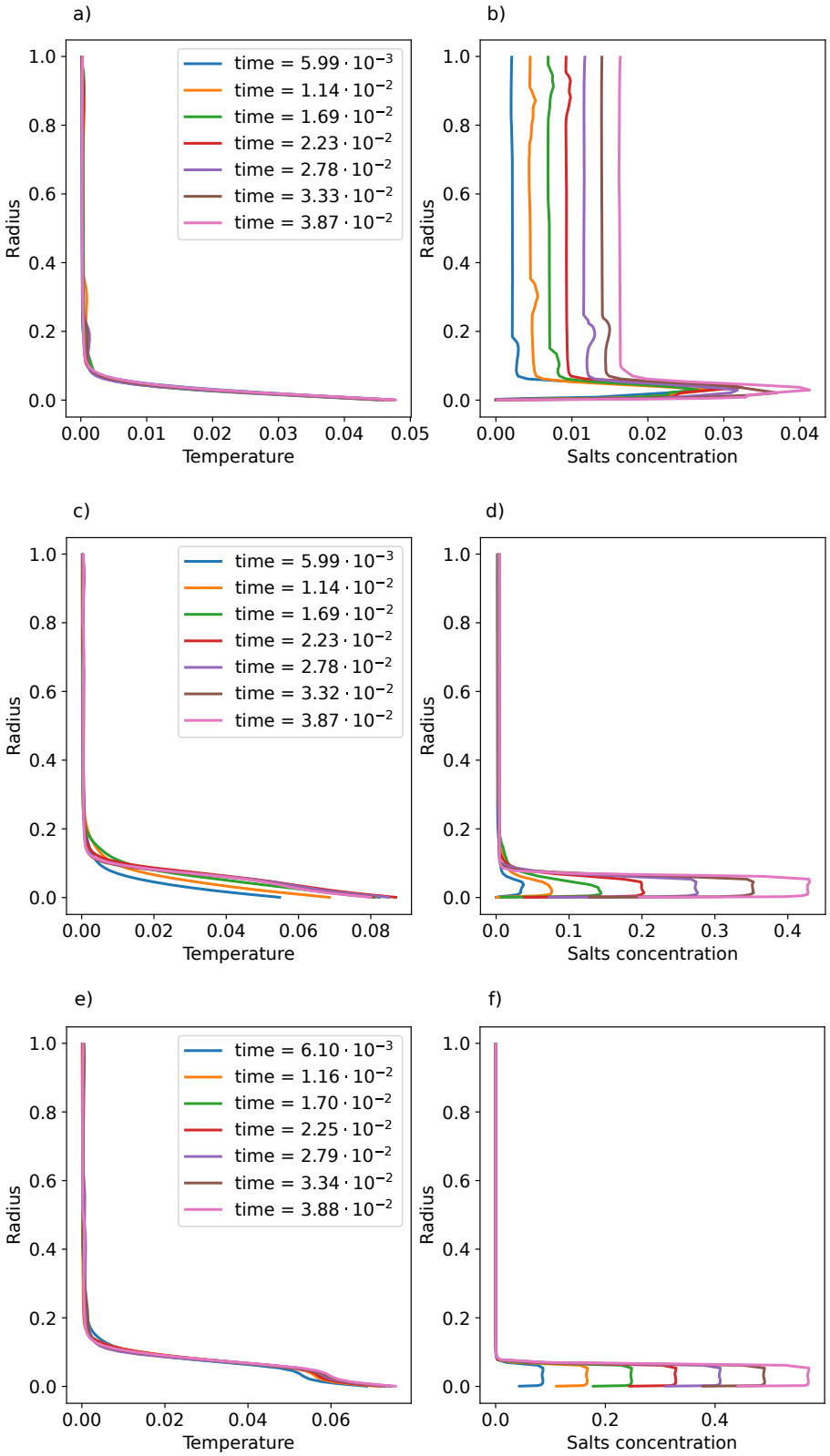

Figure 3.11: Profiles of the temperature and the salts concentration in the HP ice layer as function of the radius at different times of the simulation. This figure has been done for a partitioning coefficient $K = 1$, a Rayleigh number $Ra_q = 10^8$ and an aspect ratio $\gamma = 0.8$. Panels a) & b) are for $B_{salts} = 0$, c) & d) for $B_{salts} = 0.7$ and e) & f) for $B_{salts} = 10$.

$B_{salts} = 0.7$ and $B_{salts} = 10$ in order to make the comparisons relevant. For a buoyancy number $B_{salts} = 0$ the salts have no effect on the density. Therefore, the temperature curves through the ice shell (fig. 3.11.a) has a classical shape for the boundary conditions of the problem, with $\tilde{T}^+ = 0$ as set in equation 3.21 and a thermal boundary layer at the bottom, which does not thicken in time. In terms of composition (fig. 3.11.b), the concentration in salts is slightly higher around the height at which they are added to the ice shell (see § 3.3.2.2) but the overall layer is poor in salts because they are easily transported by convection as they have no impact on density in that case. Due to the value of the partitioning coefficient, $K = 1$, the concentration of salts in the bulk increases as fast as in the ocean with time. For $B_{salts} = 0.7$, a buoyancy number just above the limit value for $Ra_q = 10^8$ and $\gamma = 0.8$ (see fig.3.10), the temperature profile evolves a lot more with time (fig. 3.11.c). At the onset of convection and until $t \sim 1.69 \times 10^{-2}$, there is a classical thermal boundary layer at the bottom, which thickens with time. Around this time, a layering seems to happen and there are two separate thermal boundary layers. In that case, a salts-rich layer develops at the bottom of the ice shell and it thickens with time (fig. 3.11.d). Finally, for a very high buoyancy number $B_{salts} = 10$, there is already a layering of the convection and two thermal boundary layers at the bottom early in the simulation. Also, the mixture of salts and ice that forms the lower, highly salted layer is so dense that the salts can hardly be carried by convection to the upper layer, which thus remains lighter than this salts-rich lower layer.

3.4.2.4 Salts transport

In this part, we study the effect of the buoyancy number on the salts distribution through the HP ice layer (fig. 3.12.a) and the evolution of the maximum concentration in salts with time (fig. 3.12.b) and as function of B_{salts} (fig. 3.12.c). We also analyze the temperature, radial velocity, thermal and compositional advection profiles for high (fig. 3.14) and low (fig. 3.13) values of the buoyancy number separately. The thermal advection reflects how heat is transferred through the shell and can be written from eq. 3.5 as $w\Delta\tilde{T}$. The compositional advection reflects how the salts are transported by convection and can be written from eq. 3.6 as $w\Delta C^i$. We chose a time period after the stabilization of the concentration slope in the ocean and in the ice (See § 3.4.2.1), here from $t_1 = 2.6 \times 10^{-2}$ to the end of the simulation $t_2 = 3.8 \times 10^{-2}$. The panels a) and c) of fig.3.12 and all profiles of figures 3.13 and 3.14 are time-averaged on this period. This period is long enough for these parameters to evolve a lot, in particular the concentration in salts and the temperature. Therefore, these two curves are built by dividing the relevant parameter by a reference value: the bottom temperature $\tilde{T}^-$ for figures 3.13.a and 3.14.a and the maximum concentration $max(C^i)$ for fig.3.12.a, before averaging over time. The fig. 3.12.b shows the evolution of the maximum concentration as function of time for $Ra_q = 10^8$ and various values of the buoyancy number, while fig. 3.12.c shows the time-averaged value of the maximum value as function of the buoyancy number for various Rayleigh numbers.

It is clear in all panels of fig.3.12 that there is a very marked separation between two regimes: one for low values of the buoyancy number and one for high values of the buoyancy

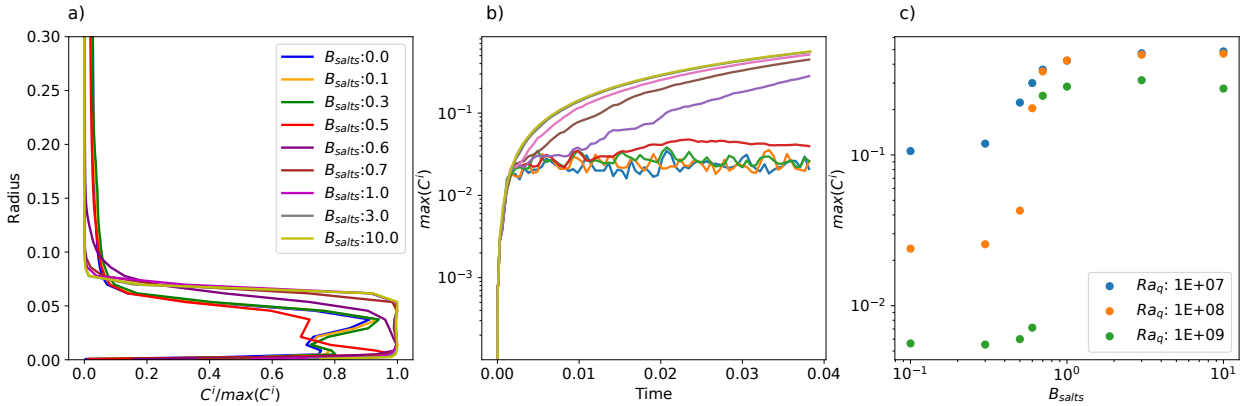

Figure 3.12: a) Profile of the concentration in salts at the bottom of the HP ice layer divided by the maximum concentration $max(C^i)$ as function of the radius for various values of the buoyancy number. b) Maximum concentration in salts of the HP ice layer $max(C^i)$ as function of time. c) Maximum concentration in salts of the HP ice layer $max(C^i)$ for various values of the Rayleigh number as function of B_{salts}. This figure has been done for a partitioning coefficient $K = 10^{-2}$ and an aspect ratio $\gamma = 0.8$. a) and b) are for a Rayleigh number $Ra_q = 10^8$. a) and c) are time-averaged over a period between $t_1 = 2.6 \times 10^{-2}$, chosen after the stabilization of the concentration slopes (See § 3.4.2.1) in the ocean and in the ice, and $t_2 \simeq 3.9 \times 10^{-2}$ the end of the simulation.

number. On fig. 3.12.c, we can observe that the difference in maximum concentration between low and high values of the buoyancy number gets larger with higher values of Ra_q. Also, the limit between low and high values of the buoyancy number for $Ra_q = 10^8$ is very clear on fig. 3.12.c, with an inflexion point between $B_{salts} = 0.5$ and $B_{salts} = 0.6$. These limit values increase with increasing Rayleigh numbers (See fig. 3.12.c). These two regimes are also visible on fig.3.12.b. For low values of the buoyancy number the salts are easily transported through the HP ice layer and most of the salts coming from the core go into the ocean. As the partitioning coefficient is small here, $K = 10^{-2}$, the amount of salts trapped in the ice at the interface with the ocean is very low and the HP ice layer reaches a compositional steady-state. The case $B_{salts} = 0.5$ is an intermediate case, with a final maximum concentration slightly higher than that for low values of B_{salts} but it seems to also reach a compositional steady-state unlike the cases for high values of B_{salts}. Regarding the concentration in salts divided by the maximum concentration (fig. 3.12.a), in the upper part of the HP ice layer it does not depend on B_{salts}. In this part the buoyancy number has no effect on the thermal convection because the salts concentration is small for large values of B_{salts} and does not affect the density for small values of B_{salts} and all the salts reaching this part goes into the ocean. The value of the concentration in this upper part is mainly controlled by the partitioning coefficient K. In the lower part, two regimes can be observed, depending on the value of the buoyancy number. In the first case, for a buoyancy number $B_{salts} \leq 0.5$, the lower part is slightly enriched in salts, as can be seen on fig. 3.12.c, due to the way the

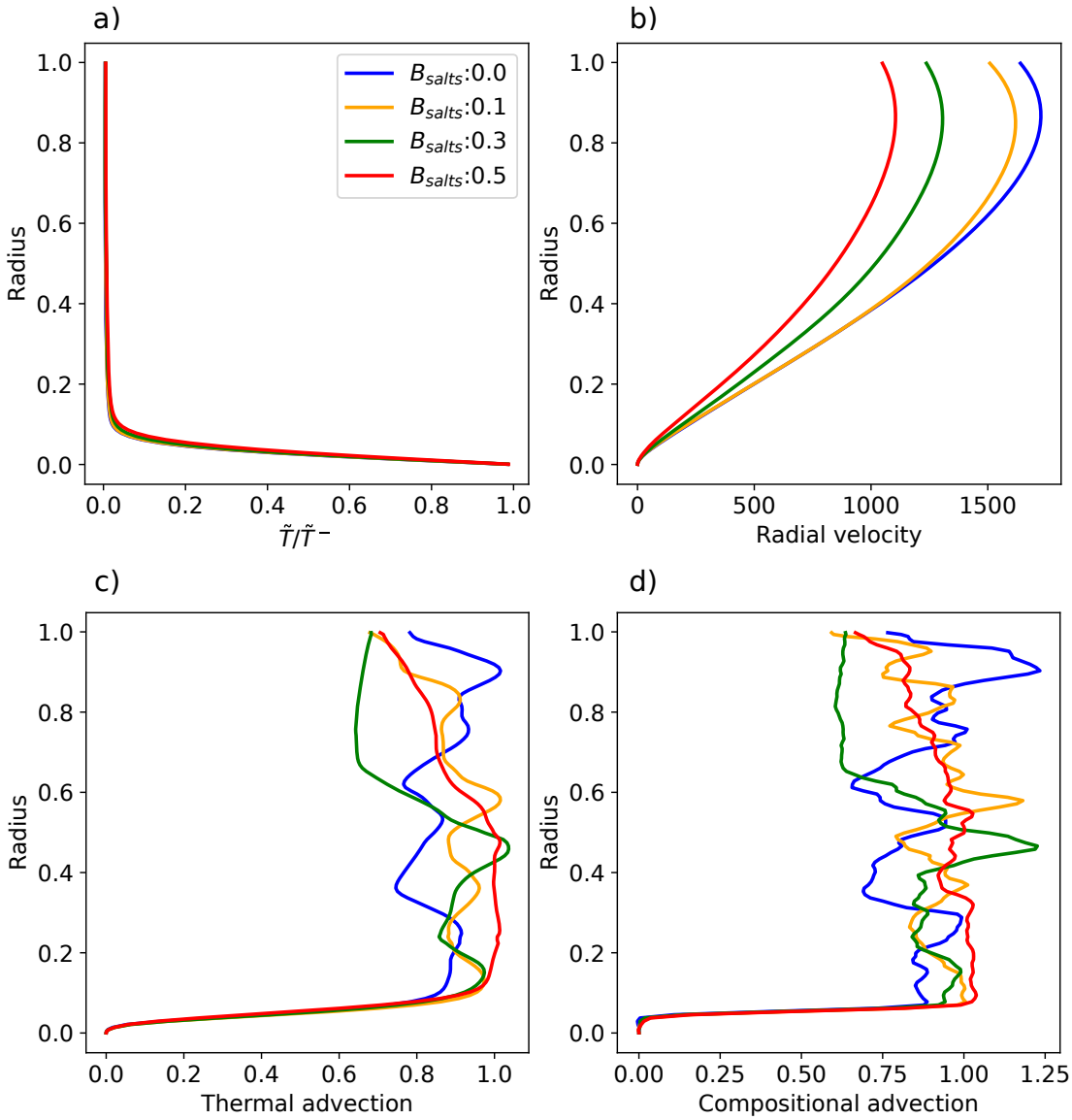

Figure 3.13: Profiles of a) the temperature divided by the bottom temperature, b) the radial velocity, c) the thermal advection and d) the compositional advection in the HP ice layer as function of the radius for small buoyancy number $B_{salts} < 0.6$. This figure has been done for a partitioning coefficient $K = 10^{-2}$, a Rayleigh number $Ra_q = 10^8$ and an aspect ratio $\gamma = 0.8$. The parameters shown on the five panels are time-averaged over a period between $t_1 = 2.6 \times 10^{-2}$, chosen after the stabilization of the concentration slopes (See § 3.4.2.1) in the ocean and in the ice, and $t_2 \simeq 3.9 \times 10^{-2}$ the end of the simulation.

flux of salts is modeled. A concentration of salts corresponding to the desired compositional flux is directly added to the ice shell at each time step at a certain height, here $h = 0.05$ (See § 3.3.2.2), which corresponds more or less to the maximum of the concentration in this

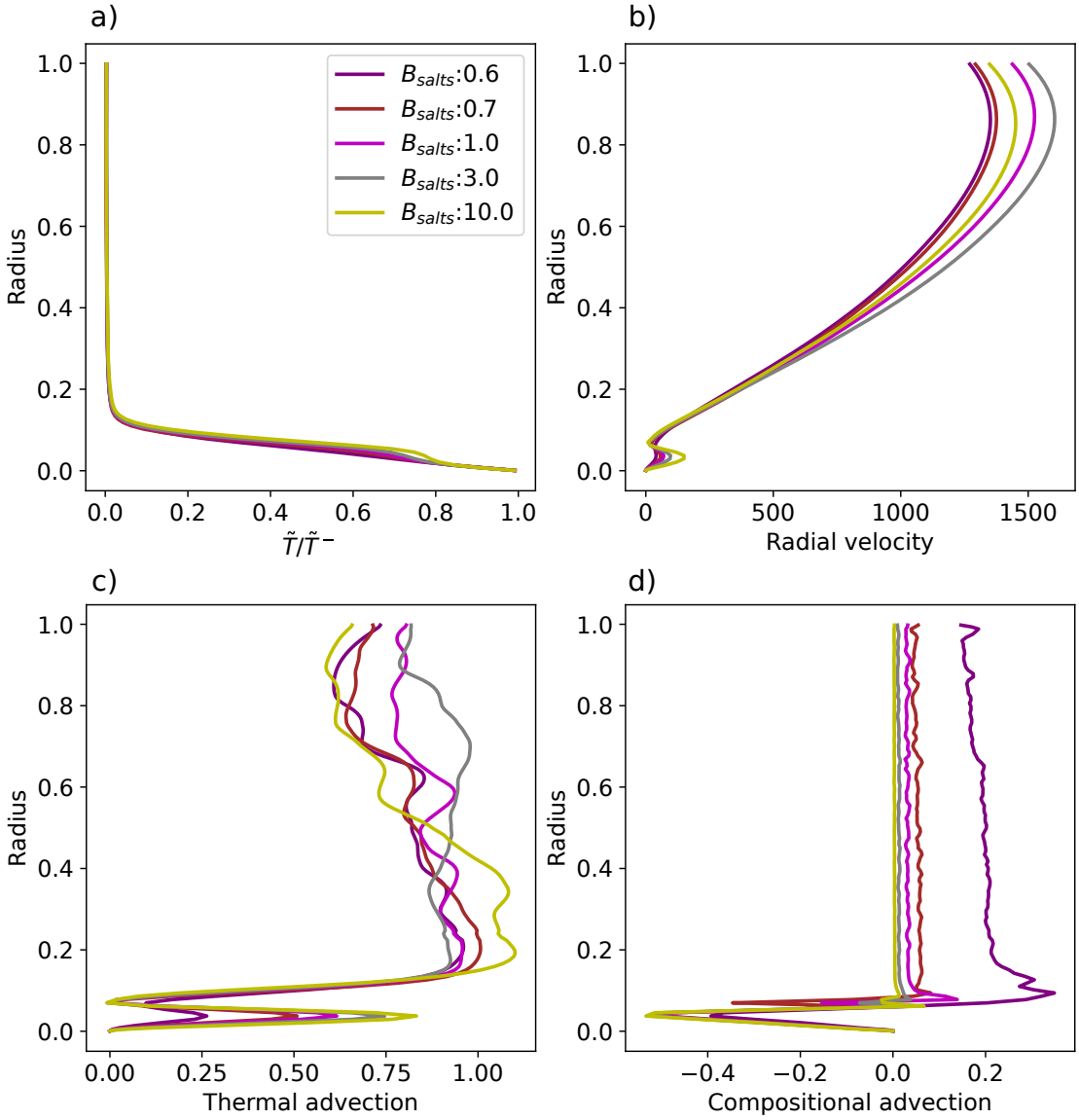

Figure 3.14: Profiles of a) the temperature divided by the bottom temperature, b) the radial velocity, c) the thermal advection and d) the compositional advection in the HP ice layer as function of the radius for high values of the buoyancy number $B_{salts} \geq 0.6$. This figure has been done for a partitioning coefficient $K = 10^{-2}$, a Rayleigh number $Ra_q = 10^8$ and an aspect ratio $\gamma = 0.8$. The parameters shown on the five panels are time-averaged over a period between $t_1 = 2.6 \times 10^{-2}$, chosen after the stabilization of the concentration slopes (See § 3.4.2.1) in the ocean and in the ice, and $t_2 \simeq 3.9 \times 10^{-2}$ the end of the simulation.

salt-poor layer, while the regime for high values of the buoyancy number, $B_{salts} > 0.5$, the density of the salts/ice mixture is so much larger than that of pure ice that the salts stack up at the bottom of the HP ice layer, which creates a highly salted layer (See fig. 3.12.c)

thicker than in the cases for a low buoyancy number. This thickening is probably due to a modest entrainment by the thermal convection above which transports a small part of the salts to the top and leaves the rest at the bottom.

On fig. 3.13, for low values of the buoyancy number, the shape of the different curves corresponds to what we could expect with pure ice [Lebec et al., 2023]. On fig. 3.13.a there is a classical thermal boundary layer at the bottom of the shell and a temperature of almost 0 in the rest of the layer due to the temperature boundary conditions (See § 3.3.1.2). Also, the thermal boundary layer does not change significantly with variable values of B_{salts}. In this regime, the thermal advection curves represented on fig. 3.13.c increase with radius in the thermal boundary layer until reaching a value around ~ 1 in the rest of the shell, which is the value needed to balance the imposed flux at the bottom boundary. The compositional advection, fig. 3.13.d, on the other hand, is just slightly negative under the part where the salts are added to the HP ice layer and increases in the rest of the thermal boundary layer until reaching ~ 1, which is also the value of the imposed influx at the bottom. Concerning the radial velocity, fig. 3.13.b, the inflexion at the bottom is due to the rigid boundary condition and in the rest of the shell it decreases for increasing values of B_{salts}.

For the high buoyancy number regime, the same parameters are displayed on fig. 3.14. In those cases, on fig. 3.14.a, there is an inflexion point of temperature at a radius grossly set by the position at which salts are introduced in the shell (See 3.3.2.2) and there are two thermal boundary layers, which is a sign of layering of the convection. The inflexion gets more pronounced for increasing values of the buoyancy number B_{salts}. The thermal advection, fig. 3.14.b, increases with height classically along the first thermal boundary layer at the bottom, then decreases until reaching a local minimum between the two convective layers before increasing again along a second thermal boundary layer. The compositional advection, fig. 3.14.c, is negative at the bottom of the HP ice layer, implying that the salts are transported downwards, which is consistent with a layering of the convection. The compositional advection is low in the rest of the HP ice layer due to the fact that most of the salts remain at the bottom of the shell. The point where the thermal and compositional advection profiles reach their local minima is the interface between the two distinct convective layers. The thickness of the lower convective layer is essentially set by the height at which the salts are added, which is somewhat arbitrary in the model. Therefore, the exact value of the thickness of this layer is not relevant, but we think this effect would occur naturally because of the way the salts/water mixture should rise through the ice before recrystallizing (See fig. 3.2). This layering of the convection is also affecting the radial velocity profile, which shows a local maximum in the middle of the lower layer while the upper layer has a shape similar to that obtained for the whole ice layer in the low buoyancy number regime.

3.4.3 Scaling laws

Several scaling laws can be proposed in order to quantify the effect of salts on the mass transfer efficiency through a HP ice layer, as the root-mean-square (RMS) radial velocity at the top interface with the ocean and the temperature at the bottom interface with the core as function of the Rayleigh number and the ratio of outflow to the ocean and inflow from

the core as function of the buoyancy number.

Both the radial velocity at the top and the bottom temperature are important output parameters to conclude about the efficiency of the heat and mass transfer through the HP ice layer. A higher radial velocity at the interface with the ocean means a more efficient mass transfer through the boundary, while the bottom temperature is directly related to the amount of melt at the interface between the core and the HP ice shell. According to Lebec et al. [2023], a relation exists between the radial velocity and the Rayleigh number $w_{top} = c_w Ra_q^{p_w}$ and also between the Nusselt number Nu, the dimensionless heat flux, and the Rayleigh number $Nu = c_T Ra_q^{p_T}$, with c_w, p_w and c_T, p_T the scaling coefficients for these two laws. In our case of a fixed heat flux, the Nusselt number is defined as $Nu = 1/\Delta\tilde{T}$, with $\Delta\tilde{T} = \tilde{T}^+ - \tilde{T}^-$ the mean dimensionless temperature difference between the upper and the lower boundaries, which allows us to compute the dimensional horizontal average bottom temperature T^-. For a rigid bottom boundary condition we obtained the following scaling exponents: $p_w = 1/2$ and $p_T = 1/5$.

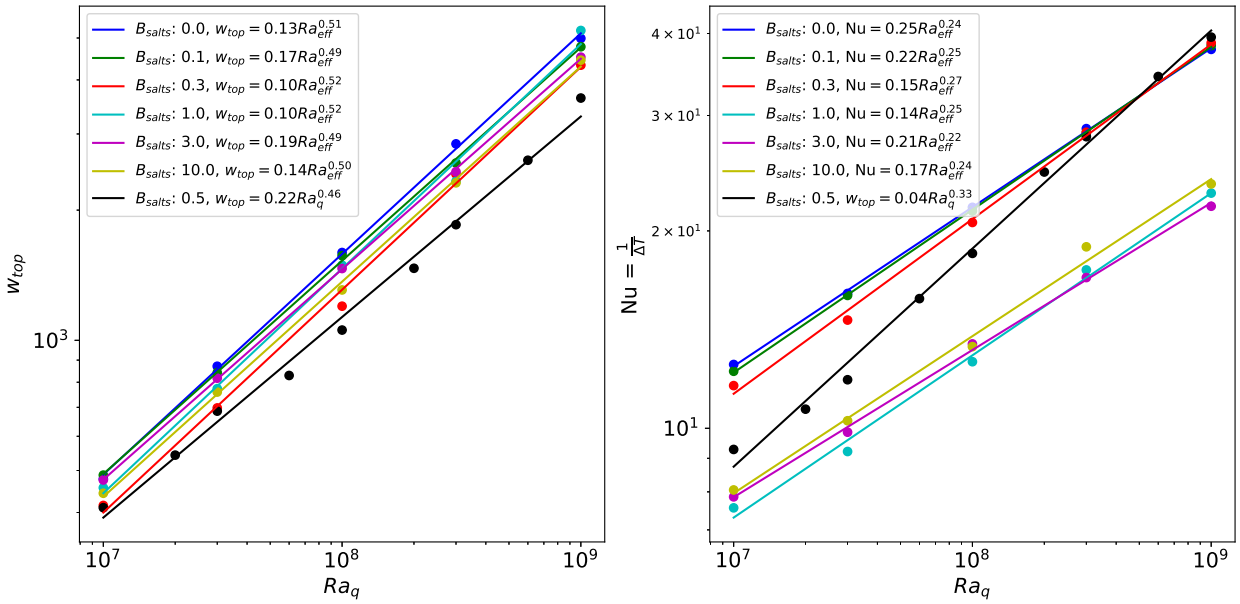

Figure 3.15: a) Dimensionless radial velocity at the top boundary of the HP ice layer and b) Nusselt number, $Nu = \frac{1}{\Delta T}$ with ΔT the dimensionless temperature through the ice shell, as functions of the Rayleigh number for various values of B_{salts}, an aspect ratio $\gamma = 0.8$ and a partitioning coefficient of salts between the ice and the ocean fixed to $K = 10^{-2}$.

These two relations have been plotted in fig. 3.15 for various values of the buoyancy number and there are several important points to note. First of all, the scaling exponents are in the range $p_w = 0.49 - 0.52$ for w_{top}, which is about $1/2$, and $p_T = 0.22 - 0.27$ for Nu, which is about $1/4$. The exponent for the Nusselt number is slightly higher than the one obtained in Lebec et al. [2023] for an aspect ratio of $\gamma = 0.95$. The scaling coefficient p_T presented in table 3.3 for an aspect ratio $\gamma = 0.9$ is between $1/5$ for low values of the

Table 3.3: Values of the scaling coefficients for the laws $w_{top} = c_w Ra_q^{p_w}$ and $Nu = c_T Ra_q^{p_T}$ for $\gamma = 0.8$ and $\gamma = 0.9$.

	$\gamma = 0.8$				$\gamma = 0.9$			
	w_{top}		Nu		w_{top}		Nu	
B_{salts}	c_w	p_w	c_T	p_T	c_w	p_w	c_T	p_T
0.0	0.13	0.51	0.25	0.24	0.18	0.5	0.3	0.23
0.1	0.17	0.49	0.22	0.25	0.15	0.51	0.25	0.24
0.3	0.1	0.52	0.15	0.27	0.14	0.5	0.21	0.25
0.5	0.22	0.46	0.04	0.33	0.36	0.44	0.03	0.35
1	0.1	0.52	0.14	0.25	0.17	0.49	0.22	0.22
3	0.19	0.49	0.21	0.22	0.19	0.49	0.29	0.2
10	0.14	0.5	0.17	0.24	0.18	0.49	0.3	0.2

buoyancy number, which corresponds to the power we obtained in Lebec et al. [2023] for the same aspect ratio, and 1/4 for high values of the buoyancy number, which corresponds to the power we obtain here for $\gamma = 0.8$. This could explain the higher value obtained in fig.3.15.b for $\gamma = 0.8$. The very high power coefficient $p_T = 0.33$ obtained for $B_{salts} = 0.5$ has been excluded from the previous ranges as it seems to be a transitional case between the low and high buoyancy numbers regimes. For a Rayleigh number $Ra_q = 10^7$, $B_{salts} = 0.5$ falls in the high buoyancy number regime, the salts have a large effect on the ice density and the Nusselt number is closer to the ones for high buoyancy numbers, while for $Ra_q = 10^9$ the salts have almost no effect on the density and the Nusselt number is closer to the values for low buoyancy numbers.

The addition of salts in the problem, irrespective of the value of the buoyancy number, does not seem to have a significant effect on the radial velocity at the top, at least for this range of Rayleigh numbers, meaning that the buoyancy affects the amount of salts transported via the salt/ice mixture into the ocean through the HP ice layer, but not so much the velocity at which the transfer occurs. Also, as the salts stack up more and more at the bottom of the HP ice layer when the buoyancy increases, one would think that the radial velocity at top is likely to be lower for higher values of B_{salts}. But it is not what is observed on fig. 3.15.a, on which the lowest radial velocities are obtained for the cases $B_{salts} = 0.3$ and 0.5. This could be due to the layering of the convection for high values of the buoyancy number. In that case, the salts accumulate in the lower convective layer and the amount of salts in the upper convective layer, closer to the surface, is low enough for the convection to remain efficient. Therefore, the radial velocity is only slightly affected, but the ice reaching the ocean is less enriched in salts. On the other hand, for $B_{salts} = 0.3$ and 0.5, the salts are sufficient to affect the ice density and slow down the exchanges with the ocean, but this effect is too small to create a layering of the convection, which would allow, as in the

previous case for high values of the buoyancy number, to maintain an efficient convection in the upper layer. In this range of values, the ice reaching the ocean is more enriched in salt but the overall mass transfer across the interface is slowed by their effect on the ice density.

On the other hand, the salts have a strong effect on the Nusselt number for high buoyancy number and the temperature is increased by a factor between 1.5 and 2. As already stated, the fact the salts accumulate at the bottom of the HP ice layer for high buoyancy numbers leads to a significant increase of the bottom temperature, meaning more melt at the interface between the core and the HP ice.

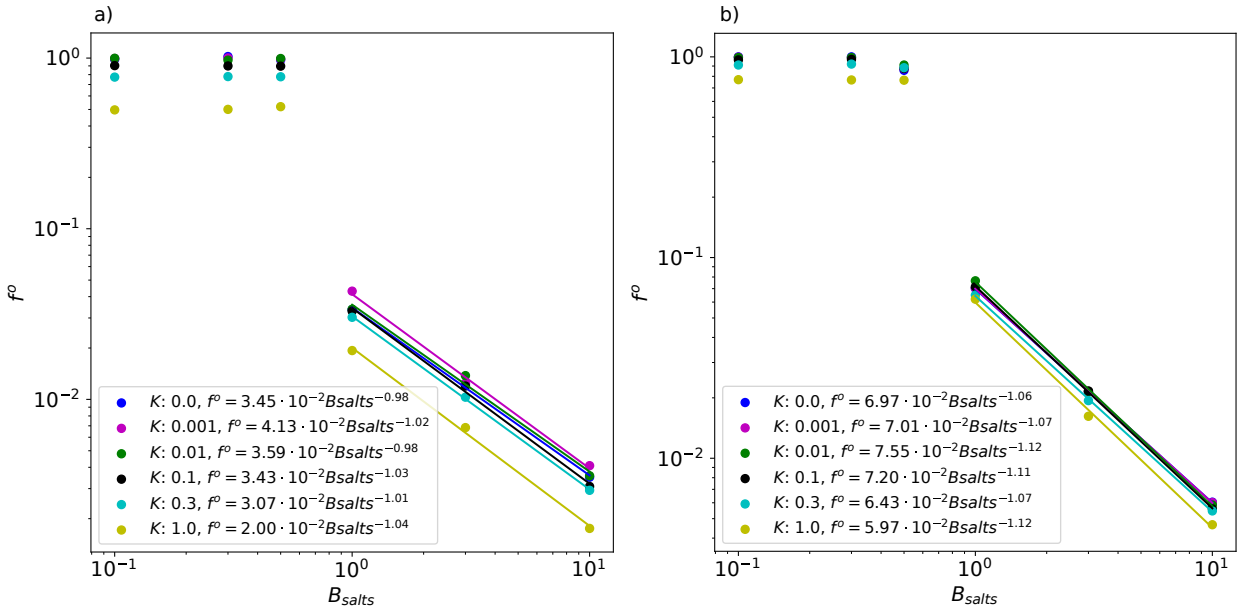

Figure 3.16: Flow ratio of salts through the ocean/ice interface f^o as function of the buoyancy number B_{salts} for various values of K and a Rayleigh number $Ra_q = 10^8$. a) is for an aspect ratio $\gamma = 0.8$ and b) for $\gamma = 0.9$. Both panels display the relation $f^o = c_F B_{salts}^{p_F}$ (straight lines) for high values of the buoyancy number with c_F, p_F the scaling coefficient.

Regarding the percentage of salts entering from the core that reach the ocean, it can be computed from the flow ratio f^o which is the ratio of the total flux of salts across the upper boundary F^o_{salts}, which includes salts flowing into the ocean by melting of the topography at the interface and salts accreted to the ice by freezing of a small portion of the ocean, to the total flux of salts coming from the core F^{eff}_{salts}:

$$f^o = \frac{F^o_{salts}(r^+)^2}{F^{eff}_{salts}(r^-)^2} \tag{3.29}$$

with F^o_{salts} the dimensionless flux of salts per surface unit across the boundary between the HP ices and the ocean $F^{eff}_{salts} \sim 1$ the actual flux of salts from the core computed by eq. 3.26.

This parameter is represented on fig. 3.16 as function of the buoyancy number for various values of the partitioning coefficient. As can be seen comparing fig. 3.16.a and fig. 3.16.b the flow ratio of salts f^o at the interface between the ice and the ocean is higher for an aspect ratio $\gamma = 0.9$. The same can be observed for the bottom temperature and the top radial velocity, which are higher in that case (According to the scaling laws coefficients available in table. 3.3). On figure fig. 3.16.a we can observe that the flux of salts through the top interface is independent of B_{salts} for small values of B_{salts} but decreases with the buoyancy number for values larger than around 1. It is consistent with the fact that even if the radial velocity is relatively stable, the quantity of salts transported through the HP ice layer decreases with an increase of the buoyancy number. f^o also decreases with increasing values of the partitioning coefficient, because the greater the quantity of salts trapped in the ice during freezing at the top boundary, the lower the net flux of salts towards the ocean. Finally, figure 3.16 shows that f^o is roughly inversely proportional to B_{salts}, $f^o = c_F B_{salts}^{-1}$, which can easily be explained. Indeed, for $B_{salts} \geq 1$, the amount of salts transported by convection in the upper layer decreases for increasing values of the buoyancy number. In those cases, the effective buoyancy number in the upper convective layer is proportional to $\Delta C^i B_{salts}$, with ΔC^i the concentration of salts effectively realised in the upper layer, and should be less than or nearly equal to 1 for the salts to be easily transported by convection in the upper convective layer. It means that ΔC^i scales as $1/B_{salts}$. Also, as the convection in the upper layer is efficient ($B_{\mathit{eff}} \leq 1$), the flux of salts F^o_{salts} across the ice/ocean interface is the same than the flux of salts entering the upper layer from the lower one and should be $F^o_{salts} \sim \Delta C^i w_{top}$. Therefore, for a fixed radial velocity at top, F^o_{salts} scales as $1/B_{salts}$. From eq. 3.29, for a fixed value of the flux of salts F^{eff}_{salts} entering the ice from the core, f^o also scales as $1/B_{salts}$.

As shown on fig. 3.16, for high values of the buoyancy number, the amount of salts from the core that ends up in the ocean is on the order of 0.1 to a few percent, depending on the buoyancy number and the partitioning coefficient, while it is around 50% for low values of the buoyancy number and a partitioning coefficient of 1 and in the range $75 - 100\%$ for low values of the buoyancy number and lower partitioning coefficients.

3.4.4 Applications to Ganymede

The results discussed in the previous section can be applied to specific planetary bodies. We use Ganymede as an example because its thick layer of HP ices makes it interesting in order to estimate the efficiency of salt transfer from the core to the ocean in an unfavourable environment. With a core radius of about 1 800 km and a total radius of 2 634 km [Hussmann et al., 2015], Ganymede is composed of a thick hydrosphere of about 834 km (See table 3.4 for more details). The thickness of the HP ice layer is written as function of the core radius and the aspect ratio γ as:

$$d = R^- \left(\frac{1-\gamma}{\gamma} \right). \tag{3.30}$$

For the aspect ratios considered in table 3.1, it gives a HP ice thickness between 200 and

Table 3.4: Numerical application table for Ganymede. Most values (if not indicated otherwise) are coming from Kalousová et al. [2018].
[a] Hussmann et al. [2015].
[b] Grasset et al. [2013], Sotin and Tobie [2004].
[c] Computed from R^- for $\gamma = 0.8$ (max thickness) and $\gamma = 0.9$ (min thickness).

Parameter	Symbol	Ganymede	Unit
Thermal expansivity	α	1.5×10^{-4}	K^{-1}
Gravity	g	1.6	m s^{-2}
Thermal conductivity	k	1.6	$Wm^{-1}K^{-1}$
Thermal diffusivity	κ	4.3×10^{-7}	m^2s^{-1}
Reference density	ρ	1390	kgm^{-3}
HP ice viscosity	η	$10^{15} - 10^{17}$	Pa s
Heat flux for silicate core	q	$10 - 40$	mWm^{-2}
Radius	R	2 634[a]	km
Core radius	R^-	1 800[a]	km
Ocean radius	R_o	$734 - 784$	km
Hydrosphere thickness	d_h	834	km
Crust Ih thickness	d_{Ih}	$50 - 100$[b]	km
HP ice thickness	d	$200 - 450$[c]	km
Bottom melting temperature	T_m^-	332	K

450 km, which is in the actual range considered for Ganymede [Bland et al., 2009]. As the aspect ratio $\gamma = 0.8$ is the less favourable one in terms of radial velocity at top, bottom temperature and effective flux of salts towards the ocean, all the following calculations are made for this case. First of all, to perform this numerical application we choose (table 3.4) a viscosity of ice VI $\eta = 10^{15}$ Pa s and a heat flux from the core $q = 20$ mW m^{-2} as reference values [Kalousová et al., 2018]. The values chosen for d, q and η are different from the ones used in Lebec et al. [2023], which were very conservative, but the scaling laws obtained in both studies are consistent with each other. For the chosen reference values we can compute a Rayleigh number:

$$Ra_q = \frac{\alpha g q \rho d^4}{k\kappa\eta} = 4 \times 10^{11} \left(\frac{q}{20 \text{ mW m}^{-2}}\right) \left(\frac{d}{450 \text{ km}}\right)^4 \left(\frac{\eta}{10^{15} \text{ Pa s}}\right)^{-1}, \tag{3.31}$$

which puts the HP ice layer of Ganymede in the large Rayleigh number regime of convection for any reasonable choice of parameter values.

We can use the scaling laws obtained earlier (fig. 3.15) to compute the radial velocity at top and the bottom temperature for $\gamma = 0.8$ and various values of the buoyancy number, using the same reference values as for the Rayleigh number computed in eq. 3.31. Here we

Table 3.5: Results of the numerical application for Ganymede from values of table 3.4 for rescaling. Results for $\gamma = 0.9$ are computed from scaling laws available in table 3.3. Values for T^+ comes from Kalousová et al. [2018] for $d = 200$ km and extrapolated for $d = 450$ km.

γ	Ra_q	B_{salts}	w_{top}(m yr^{-1})	$1/\Delta T$(K^{-1})	T^-(K)	T^+(K)
		0	3.2	2.7×10^{-2}	312	275
0.8	4×10^{11}	10	2.7	1.8×10^{-2}	331	275
		0	1.5	2.7×10^{-2}	346	309
0.9	1.6×10^{10}	10	1.2	1.3×10^{-2}	386	309

start with $B_{salts} = 10$ (other values are available for comparison in table 3.5):

$$w_{top} = 0.14 Ra_q^{0.5} \frac{\kappa}{d} = 2.7 \text{ m yr}^{-1} \left(\frac{q}{20 \text{ mW m}^{-2}} \right)^{0.48} \left(\frac{d}{450 \text{ km}} \right)^{0.92} \left(\frac{\eta}{10^{15} \text{ Pa s}} \right)^{-0.48}, \tag{3.32}$$

$$\frac{1}{\Delta T} = 0.17 Ra_q^{0.24} \frac{k}{qd} = 1.8 \times 10^{-2} \text{ K}^{-1} \left(\frac{q}{20 \text{ mW m}^{-2}} \right)^{-0.78} \left(\frac{d}{450 \text{ km}} \right)^{-0.12} \left(\frac{\eta}{10^{15} \text{ Pa s}} \right)^{-0.22}. \tag{3.33}$$

Extrapolating the values from Kalousová et al. [2018] for a HP ice thickness of 450 km, the temperature T^+ at the interface between the ice and the ocean is equal to the melting temperature which is about 275 K. Therefore, still for $B_{salts} = 10$, the dimensional horizontal average bottom temperature $\bar{T}^-$ for the reference values of all parameters is:

$$\bar{T}^- = \Delta \bar{T} + T^+ = 331 \text{ K} \tag{3.34}$$

In comparison to the melting temperature at the bottom, which is $T_m^- = 332$ K, the ice at the bottom boundary is in average very close to the melting temperature, which would imply the existence of at least pockets of melt at the interface with the core. The buoyancy number being very high, the salts entering the ice will continue to accumulate along the interface and to increase this temperature until the entire layer between the interface and the point of refreezing has melted.

We have also performed these calculations for $\gamma = 0.9$ from the data available in table 3.3 and for $B_{salts} = 0$ and $B_{salts} = 10$ in order to compare the effect of low and high values of the buoyancy number on these two parameters. All the results are displayed in table 3.5. For $B_{salts} = 0$, the salts have no effect on the ice density and are transported passively through the HP ice layer. Therefore, the salts do not affect the dynamics and we fall back on the pure ice study case [Lebec et al., 2023]. On the other hand, for a high buoyancy number $B_{salts} = 10$ the top radial velocity is lower, but of the same order of magnitude as for low values of B_{salts}, and the bottom temperature is about 25 K higher. In addition, the accumulation of salts decreases the melting temperature, which means that the higher the

amount of salts, the higher the melting capacity. For $\gamma = 0.9$, the bottom temperature is much higher, but the Nusselt is very close to the one obtained for the corresponding runs with $\gamma = 0.8$ due to the thinner HP ice shell. The top radial velocity is in average two times smaller for $\gamma = 0.9$, for a Rayleigh number 25 times smaller, also a consequence of the thinner HP ice layer.

The effective dimensional flux of salts F from the core per unit surface can be estimated for values of the buoyancy number from 0 to 10, using the eq. 3.9 and values from table 3.4. Considering the reference value of the heat flux $q = 20$ mW m^{-2}, it gives us a range $F = 0 - 2.5 \times 10^{-4}$m yr^{-1}. It can be used in accordance with fig. 3.16 for $\gamma = 0.8$ to estimate a first range of the amount of salts transported across the ocean boundary per unit time. For high values of the buoyancy number the quantity of salts passing through the top boundary is on average (depending on the value of K) 0.3% for $B_{salts} = 10$ and 3% for $B_{salts} = 1$. It means that for high values of the buoyancy number the average flux of salts across the top boundary is around 7×10^{-7}m yr^{-1}. For a low buoyancy such as $B_{salts} = 0.1$, the quantity of salts passing through the top boundary is about 50 to nearly 100% depending on K, the flux of salts across the ice/ocean interface is of the order of 10^{-6}m yr^{-1}.

3.5 Discussion

In this study we considered a model with a uniform ice viscosity, while it should depend on pressure, temperature, salt concentration and on the fraction of liquid contained in the shell. We already performed a run with a varying viscosity in a previous study [Lebec et al., 2023] in order to check the reliability of this hypothesis and the results for a model considering only convection in the solid-state was pretty close to the one obtained with a constant viscosity. The difference here is the presence of salts, that would increase the temperature of the ice and decrease its melting temperature. Also, the salts have a double effect on the efficiency of the convection, by allowing the salts/water mixture to remain liquid longer during the ascent through the bulk, but conversely to increase the ice density which tends to impede the convection. Therefore, an improvement to this model would be to consider a two-phase model of convection in the HP ice layer to study all of these aspects.

Another limitation of this model that has already been pointed out in § 3.4.2.4 comes from the way the salts are added to the HP ice layer (See § 3.3.2.2) which affects the results of the runs. Indeed, for low values of the buoyancy number, the maximum concentration of salts in the shell is around the height at which the salts are added. Also, for high values of the buoyancy number, a layering of the convection happens and the two independent convective layers separate around this height. As shown on fig. 3.2 and explained in the introduction, if a thin layer or isolated pockets of melt below the H_2O ice layer interact with the core and if this salted water is less dense than pure HP ices, it should rise through the HP ice layer. Its temperature would start to decrease until it partially, or totally, refreezes along its path (see fig. 3.2). As we consider only convection in the solid state, this new salts/ice mixture is the focus of our study. Therefore, the salts we are studying are integrated into the ice at a given height above the bottom boundary, certainly close to the bottom interface, but not directly

in contact with the core. This makes our model consistent, even if the height at which the salts are added to the ice is chosen arbitrarily and should not be interpreted quantitatively, as this height would undoubtedly depend on the type of salt and the implied solidus.

The present study shows that the presence of salts and their negative buoyancy makes the bottom temperature higher. Combined with their effect as fusing agent in water (which is not modeled here) increases the chances of melting at the bottom of the HP ice layer compared to pure ice cases. In the case of a large buoyancy number which leads to progressive enrichment in salts in a lower sublayer, when a certain quantity of salts stacked at the bottom is reached, increasing the temperature at the interface with the core and decreasing the melting temperature, a thin secondary ocean between the HP ice layer and the core may appear. This ocean is likely to be very salty and it could be interesting to study its stability and its effect on the overall dynamics and on heat and mass transfer efficiency through the HP ice layer.

3.6 Conclusions

With this work, we address the question of the effect of salts on the dynamics of a high-pressure ice shell between a solid core and a liquid ocean and on the efficiency of the transfer of these salts between these two layers. Salts affect the dynamics through their effect on the density of the ice/salts mixture whose increase is quantified with respect to the decrease from temperature by the buoyancy number, B_{salts}. We model an influx of salts from the core, with a fixed heat flux at the bottom boundary, and we consider a mechanical phase change boundary condition at the top interface between the ice and the ocean, whose effects on the dynamics and on the heat and mass transfer through a HP ice layer have already been studied previously [Lebec et al., 2023]. For the sake of simplicity and to conclude about the effect of salts only, we chose to consider a uniform viscosity in the HP ice layer and convection in the solid state. Partial melting has already been considered in several studies [Kalousová and Sotin, 2018, Kalousová et al., 2018, Choblet et al., 2017] but with pure ice. All of these effects could be interesting to combine in a future and more exhaustive study.

This paper sheds light on some of the questions that had been raised in our previous paper [Lebec et al., 2023]. First of all, as already studied by Bolrão et al. [2021] in the context of magma oceans, if the ocean starts already salted and without an influx of salts from outside of the system, it ends up reaching a steady-state. For what can be considered as low values of the effective buoyancy number, depending on the partitioning coefficient K of salts between the HP ice and the ocean at the top interface (see eq. 3.8), the system even reaches a chemical equilibrium.

Modeling an influx of salts from the core by adding a corresponding concentration of salts slightly above the interface between the core and the ice, corresponding to what would happen if the salts-enriched water at the bottom boundary rose through the bulk before recrystallizing at a certain height, two very distinct regimes can be observed. For low values of the buoyancy number, the salts are easily entrained by solid convection and all the salts entering the ice from the core reach the ocean. On the contrary, for high values of the

buoyancy number, the salts stack up at the bottom of the HP ice layer and a layering of the convection happens at a depth corresponding more or less to the one at which the salts are added to the shell. This height corresponds to the crystallization point of the water/salt mixture. It depends on the salts properties and would determine at which depth is the boundary between the two convective layers. Also, for high values of the buoyancy number, the salts that accumulate at the bottom of the HP ice layer should increase the temperature of the salts/ice mixture and decrease the melting temperature, causing the formation of a thin secondary salty ocean between the HP ice layer and the core. Therefore, if this ocean is dense enough to be stable, the highly salted water could infiltrate the ice and rise through the HP ice layer with greater chance of staying liquid all the way to the ocean. To conclude about this aspect a study of this secondary ocean including partial melting in the HP ice shell is necessary.

Interestingly, the radial velocity at the ocean interface scales as a power 1/2 of the Rayleigh number, as for convection in pure ice [Lebec et al., 2023] and is only slightly affected by the concentration in salts of the HP ice layer. Regarding the Nusselt number, it scales as a power 1/5 of the Rayleigh number and the bottom temperature increases with the buoyancy numbers. We also obtained a scaling of the ratio of the salts flux across the ocean interface to that from the core as function of the buoyancy number and the exponent obtained is -1. These dimensionless scaling laws can be applied to any planetary body with an internal structure corresponding to our model. It has been done for the case of Ganymede in § 3.4.4, choosing values in a relevant range for the least well-constrained parameters, as the thickness of the ice, its viscosity and the heat flux from the core. This gives a radial velocity at the ice/water upper boundary around 3 m yr^{-1} for a HP ice thickness $d = 200$ km and 1.3 m yr^{-1} for a HP ice thickness $d = 450$ km, which would imply an efficient mass transfer through the interface and the salts reaching the interface should all goes easily into the ocean. Regarding the flux of salts through the interface between the ice and the ocean, it is more complicated to conclude without knowing the composition in salts of the core and the flux of salts coming from it, but a first rough approximation for a large range of the buoyancy number gave us a maximum flux around 10^{-6}m yr^{-1}.

Finally, if the temperature at the interface between the core and the ice reaches the melting temperature, all the salts that would enrich the ocean in the case of small icy moons with a core in direct contact with a liquid ocean would end up in the ice in our case. From here, two scenarios are possible. If the flux of salts from the core is low, the buoyancy number is small and the effect of the small amount of salts entering the ice on the density is also low. In that case, the mass transfer of salts through the HP ice layer is likely to be easy and all the salts coming from the core would end up in the ocean, just as it would be for small icy moons without a HP ice layer. On the other hand, if the flux of salts is strong, the salts affect the density of the ice, meaning a high buoyancy number. In that case, we saw that most of the salts accumulate at the bottom of the HP ice layer and that the upper convective layer is likely to be poor in salts. The convection in this upper layer is not impeded by the salts and all the salts entering this layer are transported through the HP ice layer and reach the ocean. In that case, only a small part of the salts coming from the core would reach the ocean, but considering a stronger flux of salts entering the ice, this small amount could

be comparable to the one entering the ice and reaching the ocean in the case of a low flux from the core. To conclude about this aspect it would require a better knowledge of the salts available in these moons. Therefore, future studies and space missions will be needed to better constrain the internal structure and composition of these water-rich bodies in order to conclude on their habitability.

CHAPTER 4

A SECONDARY OCEAN BETWEEN THE CORE AND THE HP ICE LAYER

As explained in the previous chapter, the salts have an important effect on the dynamics. If the amount of salts in the ice becomes too large, their effect on the ice density is very high and the salts stack up at the bottom of the shell. The salts also decrease the melting temperature of the ice and when it reaches it an entire layer of highly salted ice could melt. If this water layer is less dense than the HP ice, it would rise through the HP ice shell. But if it is denser than the ice, a thin stable, salt-rich, warm secondary ocean may form between the core and the HP ice layer. The concentration of salts at which salty water is denser than ice VI depends on the salt nature and is still lacking for most of the salts that could be found in the rocky core of these moons but, according to Journaux et al. [2013], the concentration of NaCl to make salty water more buoyant than ice VI and to form this stable layer is 146 g $kg^{-1}_{H_2O}$, or about 15%. In both cases, it would have an important impact on the overall dynamics and these are interesting points to discuss.

To study the case of the stable secondary ocean between the ice and the core, we model a closed system composed of the HP ice layer between two oceans (See fig. 4.1). The lower ocean extends from the core (radius R_c) to the bottom of the HP ice layer (radius R^-), the thickness of the HP ice layer is still defined by $d = R^+ - R^-$ and the upper ocean goes from the top of the HP ice layer (radius R^+) to the bottom of the icy surface (radius R_o). As we saw in § 3.4.1, in the case of a closed system without an influx of salts from the core, it should tend towards a steady-state and the concentration in all the layers reach a final value. Under certain conditions, the steady-state is that of a chemical equilibrium and the equilibrium concentration is computed from the initial conditions in § 4.2.

This study is a preliminary work.

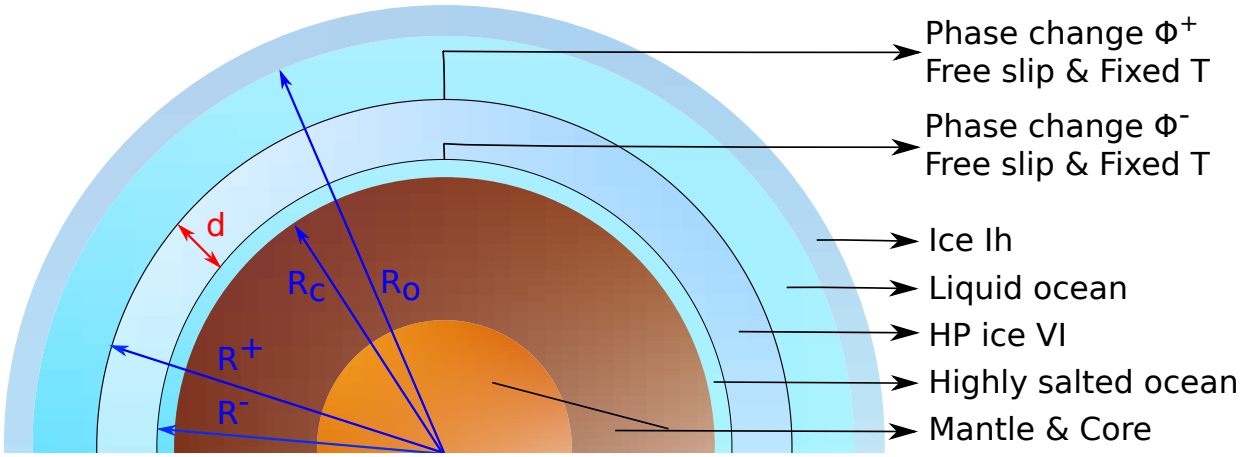

Figure 4.1: Model illustration for the interior of an ocean world with a HP ice layer between two liquid oceans. The bottom one is a thin and very salty ocean and is in direct contact with the rocky core at the lower boundary.

4.1 Model

4.1.1 Physical model

4.1.1.1 Governing equations

In the same way as for chapter 2 and 3, the number of control parameters for which the values are not well-known is important and we reduce it using dimensionless numbers. The scales for length and time are, respectively, the thickness of the HP ice layer $d = R^+ - R^-$ and the diffusion time d^2/κ, with κ the thermal diffusivity. Unlike the problems studied in chapters 2 and 3, we impose a temperature, not a heat flux, at the bottom boundary and the temperature scales as $\Delta\tilde{T} = \tilde{T}^- - \tilde{T}^+$ and is made dimensionless by:

$$T = \frac{\tilde{T} - \tilde{T}^+}{\Delta\tilde{T}}. \tag{4.1}$$

In this study, the ice is not pure and the concentration of salts is denoted C. We consider a closed system composed of the HP ice layer and both liquid oceans without an influx of salts from the core. To lead to the complete melting of the bottom of the ice layer the quantity of salts stacked at the bottom must be very large and the resulting ocean should be highly salted. Therefore, the initial salt concentration in the ice and in the overlying ocean should be negligible compared to that of the ocean below. In the following, we consider a zero initial concentration in the ice and in the ocean above and an initial concentration $C^{bo}_{ini} = 1$ in the bottom ocean, used as scaling variable. We consider the same partitioning coefficient K for salts at the upper ocean/ice boundary and at the lower ocean/ice boundary. Also, the

Rayleigh number Ra is written as:

$$Ra = \frac{\alpha g \rho \Delta T d^3}{\kappa \eta}. \tag{4.2}$$

As in chapter 3 we consider a viscosity independent of the pressure, temperature and salt concentration variations. The conservation equations 3.3- 3.6 are solved under the Boussinesq approximation for an infinite Prandtl number (See eq 3.2) and an infinite Lewis number, meaning that we neglect chemical diffusion in the ice and $\frac{1}{Le}\boldsymbol{\nabla}^2 C = 0$ in eq. 3.6.

For a fixed bottom temperature, the buoyancy number is written as:

$$B_{salts} = \frac{K C_{ini}^{bo}}{\alpha \Delta T}. \tag{4.3}$$

4.1.1.2 Boundary conditions

Due to the basal ocean between the core and the HP ice layer, there is a phase-change at the bottom interface R^- in addition to the one existing at the top interface R^+. The equation 2.7 of the timescale to build the topography at the interface becomes [Labrosse et al., 2018]:

$$\tau_\eta^\pm = \frac{\eta}{|\Delta\rho^\pm| \, g d}, \tag{4.4}$$

with $\Delta\rho^\pm = \rho_s - \rho_l^\pm$ depending on whether we are talking about the phase-change at top $^+$ or at the bottom $^-$ of the HP ice layer. In a similar way, the equations 2.8 of the timescale to erase the topography becomes [Labrosse et al., 2018]:

$$\tau_\phi^\pm = \frac{\rho_s L}{\rho_l^\pm c_{pl}^\pm u_l^\pm \left| \frac{\partial T_m}{\partial r} \right|}. \tag{4.5}$$

The phase-change number which controls its efficiency at the top Φ^+ or bottom Φ^- interface is the ratio between these two timescales [Labrosse et al., 2018]:

$$\Phi^\pm = \frac{\tau_\phi^\pm}{\tau_\eta^\pm}, \tag{4.6}$$

and the boundary condition for the radial velocity can be written as [Labrosse et al., 2018]:

$$\pm\Phi^\pm w + 2\frac{\partial w}{\partial r} - p = 0. \tag{4.7}$$

At both interfaces, the temperature is equal to the melting temperature at the corresponding depth, which leads to the following temperature boundary conditions by rendering the temperature dimensionless:

$$T^+ = 0, \tag{4.8}$$

$$T^- = 1. \tag{4.9}$$

4.1.1.3 Evolution of the oceans composition

In this study, both oceans are considered homogeneous but evolve in time by exchanging mass and salts with the HP ice shell. As in chapter 3, the evolution of the concentration in salts C^{to} of the upper ocean can be written as:

$$M^{to}\frac{dC^{to}}{dt} = 4\pi(R^{+})^2\rho^{to}F^{to}, \tag{4.10}$$

with ρ^{to} the density of the upper ocean, $M^{to} = (4/3)\pi(R_o^3 - (R^{+})^3)\rho^{to}$ (see fig. 4.1) the upper ocean mass and F^{to} the flux of salts across the upper ocean/HP ice interface. On the other hand, the concentration in salts of the basal ocean C^{bo} evolves as:

$$M^{bo}\frac{dC^{bo}}{dt} = 4\pi(R^{-})^2\rho^{bo}F^{bo}, \tag{4.11}$$

with ρ^{bo} the density of the basal ocean, $M^{bo} = (4/3)\pi((R^{-})^3 - (R_c)^3)\rho^{bo}$ (see fig. 4.1) the basal ocean mass and F^{bo} the flux of salts across the basal ocean/HP ice interface.

The flux of salts F^{to} across the upper ocean/HP ice interface can be computed from the flux of salts entering the ocean from the ice and the one entering the ice from the ocean as it was done in chapter 3:

$$F^{to} = \begin{cases} w_{top}C^{i}_{top} & if\ w_{top} > 0 \\ w_{top}KC^{to} & if\ w_{top} < 0 \end{cases} \tag{4.12}$$

with C^{i}_{top} the salts concentration contained in the ice melting at the interface with the upper ocean. On the other hand, the flux of salts F^{bo} across the HP ice/basal ocean interface can also be decomposed into two fluxes as:

$$F^{bo} = \begin{cases} w_{bot}C^{i}_{bot} & if\ w_{bot} < 0 \\ w_{bot}KC^{bo} & if\ w_{bot} > 0 \end{cases} \tag{4.13}$$

with C^{i}_{bot} the salts concentration contained in the ice melting at the interface with the basal ocean and w_{bot} the radial velocity at the bottom boundary of the HP ice layer, which is greater than zero for the flux of salts entering the ice from the basal ocean and is less than zero for the flux of salts entering the basal ocean by melting at the bottom boundary of the HP ice shell.

4.1.2 Numerical parameterization

We use StagYY to solve the convection equations on a two-dimensional spherical shell with two phase-change boundary conditions: at the lower and upper interfaces and a fixed temperature at the bottom boundary. All the runs in this study are done for an aspect ratio $\gamma = 0.8$ and various values of the partitioning coefficient K and buoyancy number B_{salts}. The phase-change is considered efficient and the phase-change number at both boundaries

is set to $\Phi^{\pm} = 10^{-2}$. For a large aspect ratio, we are getting closer to a Cartesian geometry and, according to Labrosse et al. [2018], Morison [2020], the critical Rayleigh number to onset convection for a large aspect ratio and $\Phi^{+} = \Phi^{-}$ is:

$$\lim_{\gamma \to 1} Ra_c = 24\Phi^{\pm} = 0.24, \tag{4.14}$$

which is really small. Therefore, in order to be supercritical as in chapter 3, but still able to solve the convection equations, we chose a Rayleigh number of $Ra = 10^4$ for all the runs performed in this study. The linear stability for this kind of three-layers configuration has already been performed by Morison [2020] for lower values of the Rayleigh number, which could lead to a slightly different flow in our case. The convection equations are solved on the entire shell and the grid size is 128 in the radial direction and 2048 in the horizontal one. Both boundaries are refined by a factor of 6 at the lower interface, in order to properly solve the phase-change and the possible accumulation of salts at the bottom of the HP ice layer, and 2 at the upper one to properly solve the phase-change.

As the Rayleigh number can already be considered as highly super-critical, a Robin boundary condition is needed at both boundaries to smoothly solve the phase-change and is defined as [Agrusta et al., 2020]:

$$\Gamma^{\pm}\theta + (1 - \Gamma^{\pm})\frac{\partial \theta}{\partial r} = 0, \tag{4.15}$$

with θ the temperature lateral deviation and $\Gamma^{\pm}$ the approximation of the Heaviside function:

$$\Gamma^{\pm} = \frac{1}{2}\left[1 + \tanh\left(\pi \frac{\mp w + \frac{w_0}{2}}{\frac{w_0}{2}}\right)\right]. \tag{4.16}$$

The velocity threshold between both conditions w_0 is the same as before (See § 2.3.2.2). The radial velocity towards the boundary at the top is $w = w_{top} > 0$, while at the bottom it is $w = w_{bot} < 0$.

4.2 Results

In this chapter, we study the evolution of a closed system composed of the two liquid layers surrounding a HP ice layer for several values of the buoyancy number B_{salts} and partitioning coefficient K, which is considered the same between at the basal ocean/HP ice interface and at the HP ice/upper ocean interface. As we consider no influx of salts from the core, all three layers evolve until reaching a steady-state. Depending on the values of B_{salts} and K, the system can also reach an equilibrium [Bolrão et al., 2021].

This study follows the hypothesis of the formation of a liquid layer between the core and the HP ice shell due to a very high amount of salts accumulated at the bottom of the HP ice layer. Therefore, we decided to start with a zero concentration in the upper ocean and the HP ice layer, while setting an initial concentration of $C_{ini}^{bo} = 1$ in the basal ocean as scaling

variable. The two oceans are considered homogeneous in the model and if an equilibrium is reached, they both tend to the same equilibrium concentration C^o_{eq}, which is:

$$C^o_{eq} = \frac{C^{bo}_{ini} V^{bo}}{V^{bo} + KV^i + V^{to}}. \tag{4.17}$$

with V^{bo}, V^{to} and V^i the volumes of the basal ocean, upper ocean and HP ice layers, respectively. On the other hand, the concentration in salts of the ice tends to another equilibrium concentration C^i_{eq}, which is:

$$C^i_{eq} = KC^o_{eq}. \tag{4.18}$$

To study whether an equilibrium is reached or not, fig. 4.2 shows the evolution of the concentration in the three layers (upper ocean at the top, ice in the middle and basal ocean at the bottom) as a function of time for two values of K and various values of B_{salts}. The equilibrium value is displayed by a red straight line. In order to be more comparable, for each run we impose a value for the input parameter B_{salts} which correspond to a unique range of effective buoyancy numbers $B_{\mathit{eff}} = [0, 0.1, 0.5, 1, 3, 10]$ whatever the partitioning coefficient. This effective buoyancy number represents the actual concentration and temperature contrasts that have been achieved during the run. In both cases $K = 10^{-1}$ and $K = 1$, the concentration in salts starts to increase in the ice first without increasing in the upper ocean. After a certain amount of time, for what could be considered as low values of the buoyancy number, which seems to be around $B_{\mathit{eff}} \leq 1$ for $K = 10^{-1}$ and $B_{\mathit{eff}} \leq 3$ for $K = 1$, the concentration decreases a lot in the basal ocean and increases above the equilibrium concentration in the ice. From that point, it starts increasing in the upper ocean until reaching the equilibrium value in all three layers. In the case $K = 1$, the equilibrium concentration reached at steady-state is the same in all three layers, which was also the case in chapter 3, while the equilibrium concentration reached in both oceans is twice the one reached in the ice for $K = 0.1$. For high values of the buoyancy number, the steady-state is reached without ever reaching this equilibrium value.

As in the previous study, we can compute the time $t^{1/2}$ required to evolve halfway to the steady-state concentration. In contrast to what we saw in the previous chapter for a two-layers system composed of a HP ice layer topped by a liquid ocean (see § 3.4.1), in the case of this three-layers system the steady-state is reached faster for decreasing values of the buoyancy number. Indeed, there is roughly a factor of 5 for $K = 1$ and 2 for $K = 10^{-1}$ between $B_{\mathit{eff}} = 0$ and $B_{\mathit{eff}} = 10$ (See tab. 4.1). As shown in tab. 4.1, $t^{1/2}$ is very close for $K = 10^{-1}$ and $K = 1$ and is in the range $3 \times 10^{-4} - 1.5 \times 10^{-3}$. Applied to Ganymede using table 3.4, it corresponds to a time of the order of 4.5×10^6 to 2×10^7 years. It is interesting to compare these results with the ones obtained in chapter 3 for a two-layers system composed of a HP ice layer topped by an ocean. However, in this chapter $Ra_q = 10^4$, while it is 10^8 in chapter 3, so we need to bring them to the same value to be able to compare the results. To do so, we refer to the study of Agrusta et al. [2020] which shows that, for a system composed of two liquid layers enclosing a solid one, the radial velocity scales as Ra_q^1. In our study, the

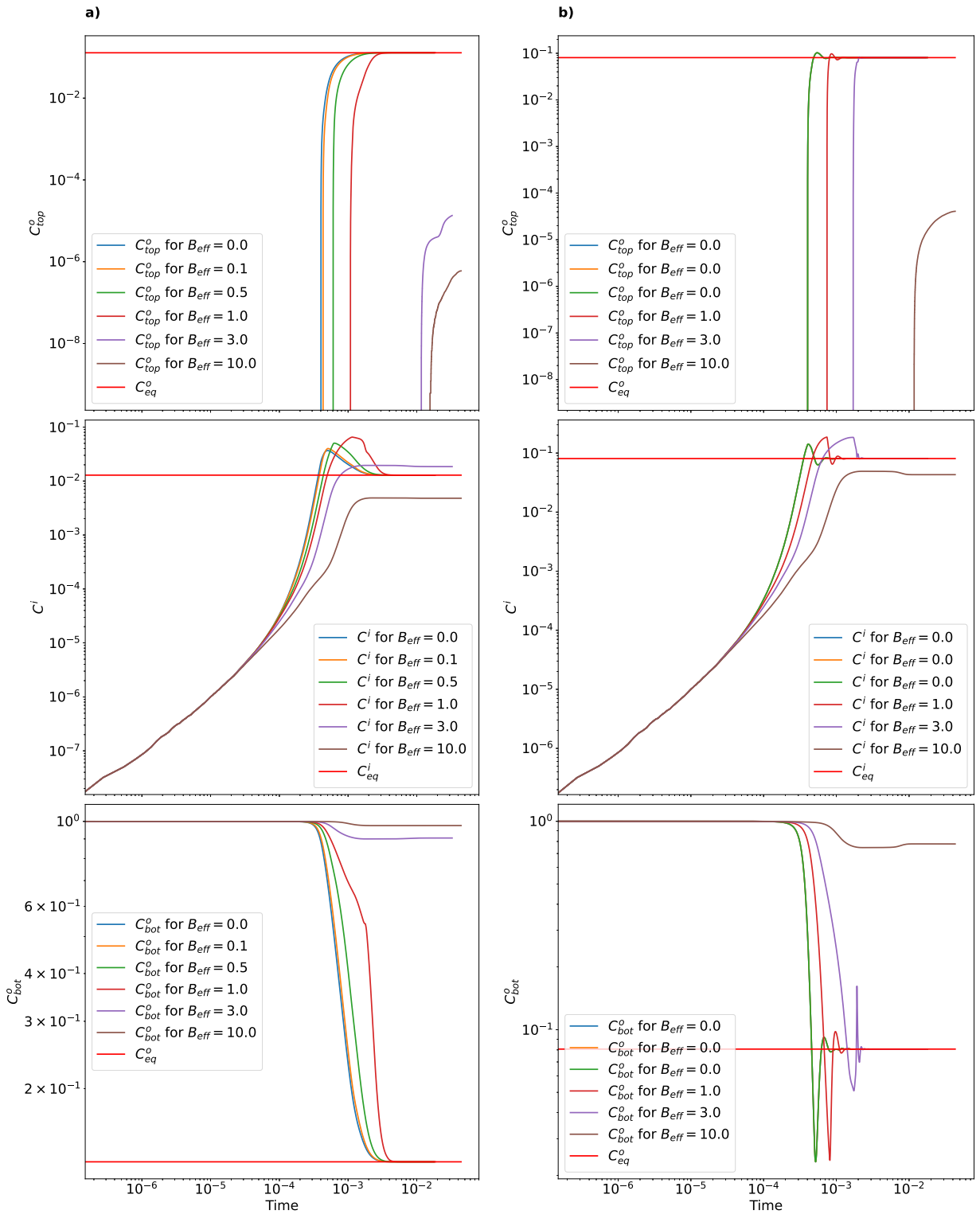

Figure 4.2: Evolution of the salt concentration in the upper ocean (top), HP ice layer (middle) and basal ocean (bottom) with time for a partitioning coefficient a) $K = 10^{-1}$ and b) $K = 1$ for various values of the effective buoyancy number B_{eff}. The straight red line is the equilibrium concentration corresponding to each layer and computed from eq. 4.18 and 4.17.

time should scale as w^{-1}, with w the radial velocity. Therefore, for a three-layers system and a Rayleigh number of 10^8, the time $t^{1/2}_{10^8}$ required to travel halfway to the concentration at steady-state is computed from the average time $t^{1/2}_{10^4}$ obtained for a Rayleigh number of 10^4 and $K = 1$ (see tab. 4.1):

$$t^{1/2}_{10^8} = t^{1/2}_{10^4} \frac{10^4}{10^8} = 5 \times 10^{-8}. \tag{4.19}$$

In § 3.4.1, we obtained on average $t^{1/2} \sim 9 \times 10^{-6}$ for $K = 1$ (see tab. 3.2), which is 180 times slower than for the current three-layers study.

Table 4.1: Time $t^{1/2}$ required to travel halfway to the concentration at steady-state.

K	B_{eff}	$t^{1/2}$
0.1	0	3×10^{-4}
	0.1	3×10^{-4}
	0.5	3.5×10^{-4}
	1	4×10^{-4}
	3	6×10^{-4}
	10	-
1	0	3×10^{-4}
	0.1	3×10^{-4}
	0.5	3×10^{-4}
	1	4×10^{-4}
	3	5×10^{-4}
	10	1.5×10^{-3}

In order to better visualize the evolution of the system with time for various values of B_{eff} and K, figures. 4.3 to 4.6 show the time evolution of the temperature (left panels) and salts concentration (right panels) in the HP ice layer. Starting with $B_{\mathit{eff}} = 0$ and $K = 10^{-1}$ (see fig. 4.3), at an early stage of the run (fig. 4.2.a), the salts enter the ice from the basal ocean only. As $B_{salts} = 0$, the salts are easily transported by convection through the HP ice layer and, as can be seen on fig. 4.2.a and fig. 4.3.a, they start entering the upper ocean from $t \sim 4 \times 10^{-2}$. From the beginning of the run until $t \sim 3 \times 10^{-3}$, the convection pattern is dominated by a degree-two mode with large cold down-welling and hot up-welling currents and engaging small deformations in the HP ice layer. Finally, the flow pattern changes from a degree-two to a degree-one mode of convection around $t \sim 3 \times 10^{-3}$. Also from fig. 4.2.a, the average concentration in salts of the ice starts decreasing from $t \sim 5 \times 10^{-4}$. It can be observed on the different fields of fig. 4.3 in which the maximum concentration decreases with time until reaching the equilibrium concentration around 1.3×10^{-2}.

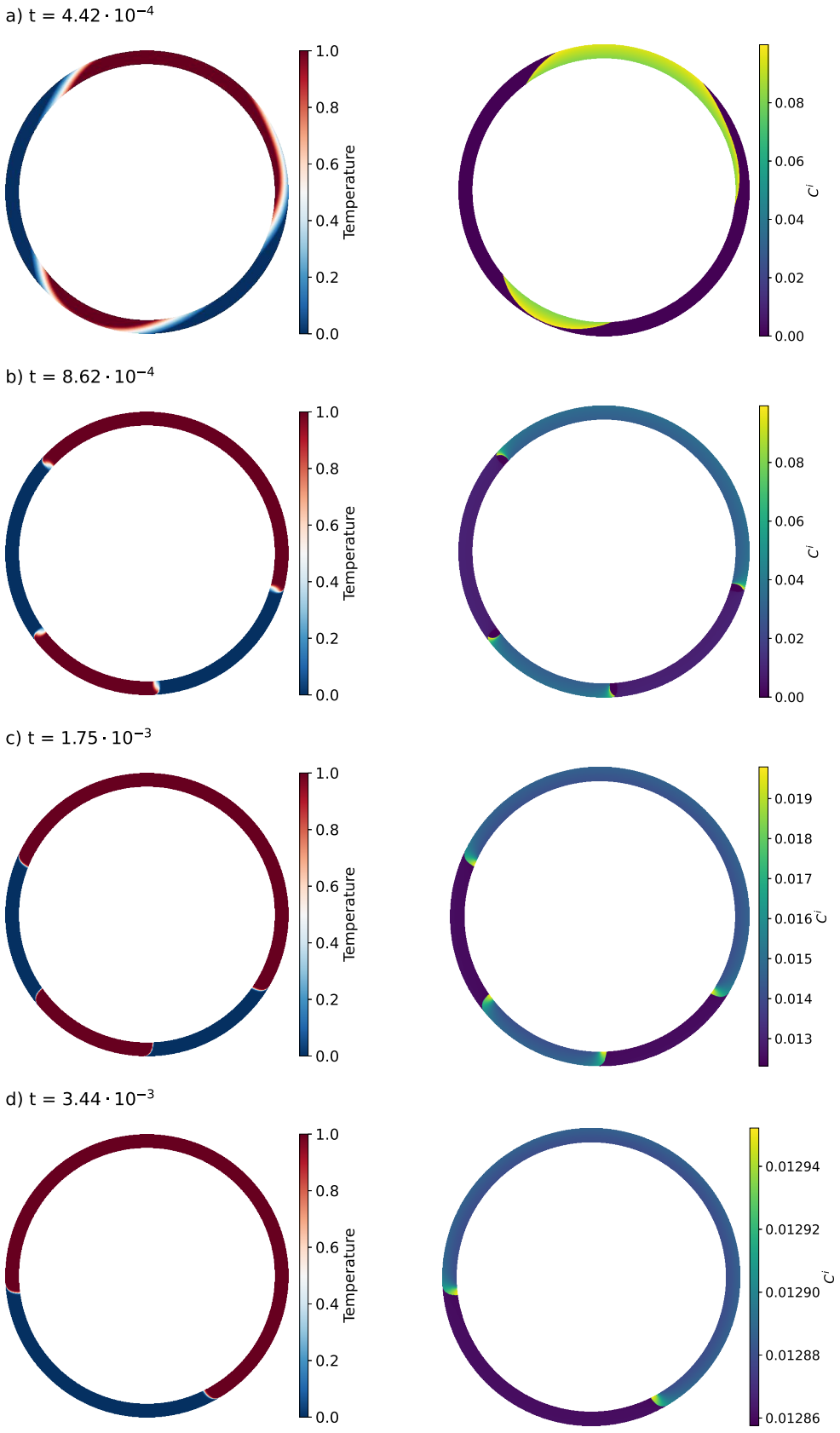

Figure 4.3: Snapshots of the evolution in time of the temperature (left) and salt concentration (right) in the HP ice layer for a partitioning coefficient $K = 10^{-1}$ and an effective buoyancy number $B_{eff} = 0$.

For a higher buoyancy number $B_{eff} = 1$, at an early stage of the run the flow pattern is already dominated by a degree 1 mode (see fig. 4.4.a). As the partitioning coefficient K is the same than in the previous case, the same amount of salts enters the ice layer, but their effect on the density being more important for $B_{eff} = 1$, the salts take more time to reach the ocean and the ocean concentration in salts starts increasing only around $t = 10^{-3}$ (see fig. 4.2.a). Around $t = 2 \times 10^{-3}$, the flow pattern switch from a degree 1 to a degree 2 mode. At the end of the run, the flow pattern is once again dominated by a degree one mode and looks like the final field of fig. 4.3.d.

On both fig. 4.3 and fig. 4.4, around $t \sim 8.6 \times 10^{-4}$ and $t \sim 2.2 \times 10^{-3}$, respectively, we can observe a sort of "ying-yang" effect at the crossroads of up-welling and down-welling currents. This effect and its evolution with time can be observed on fig. 4.7. The hot up-welling plumes and the cold down-welling plumes spread out and wrap around each other. In these two runs, the entire process takes a time of the order of $\Delta t = 7 \times 10^{-3}$.

In the case of a partitioning coefficient $K = 1$ and an effective buoyancy number $B_{eff} = 1$, the flux of salts entering the ice from the basal ocean increases by a factor of 10. Therefore, at the early stage of the run, the convection pattern is the same than the one observed on fig. 4.4.a but the concentration is 10 times higher (fig. 4.5.a). During the entire run, the flow pattern is dominated by a degree one mode. At the end of the run, the ice is highly homogeneous as the concentration tends toward the equilibrium concentration, with a difference of the order of 10^{-15} between the up-welling and down-welling currents.

In all previous examples, the effective buoyancy number was low enough for the salts to be transported easily through the HP ice layer by thermal convection. But in the case of $B_{eff} = 10$, even for a low partitioning coefficient $K = 10^{-1}$, the effect on the density is very high and the salts accumulate at the bottom of the HP ice layer (fig. 4.6). The maximum concentration in salts stays around 8×10^{-2} during the entire run. On fig. 4.6, the salts concentration has been limited to 10^{-9} in order to see what happens in the bulk of the HP ice layer, but the salts/ice mixture density is too high and nothing seems to move upwards before $t \sim 10^{-2}$. On the other hand, the thermal convection pattern evolves a lot. The flow pattern is dominated by a degree 1 mode during the entire run and the width of the hot up-welling current reduces with time. An important point to note is that the extreme accumulation of salts at the bottom of the HP ice layer forms a stable highly-salted layer which kills the phase change at the interface with the core. Therefore, we fall back on the case of a two-layers system as in chapter 3.

In the case of a three-layers system with a HP ice layer between two oceans we can also observe, comparing the two panels of fig. 4.8 and comparing figures 4.9 and 4.10, two main and very distinct regimes for low ($B_{eff} < 3$) and high ($B_{eff} \geq 3$) values of the effective buoyancy number. All the profiles displayed in these figures are time-averaged over a period from $t_1 = 1.43 \times 10^{-2}$ to $t_2 = 1.49 \times 10^{-2}$ (the end of the run). For low values of the buoyancy number, the salts have only a small effect on the ice density and are easily transported through the HP ice layer by convection. As these profiles are taken towards the end of the run, the equilibrium is already reached for low values of the buoyancy number, which explains why the salts are evenly distributed in the ice shell on fig. 4.8.a. As for these

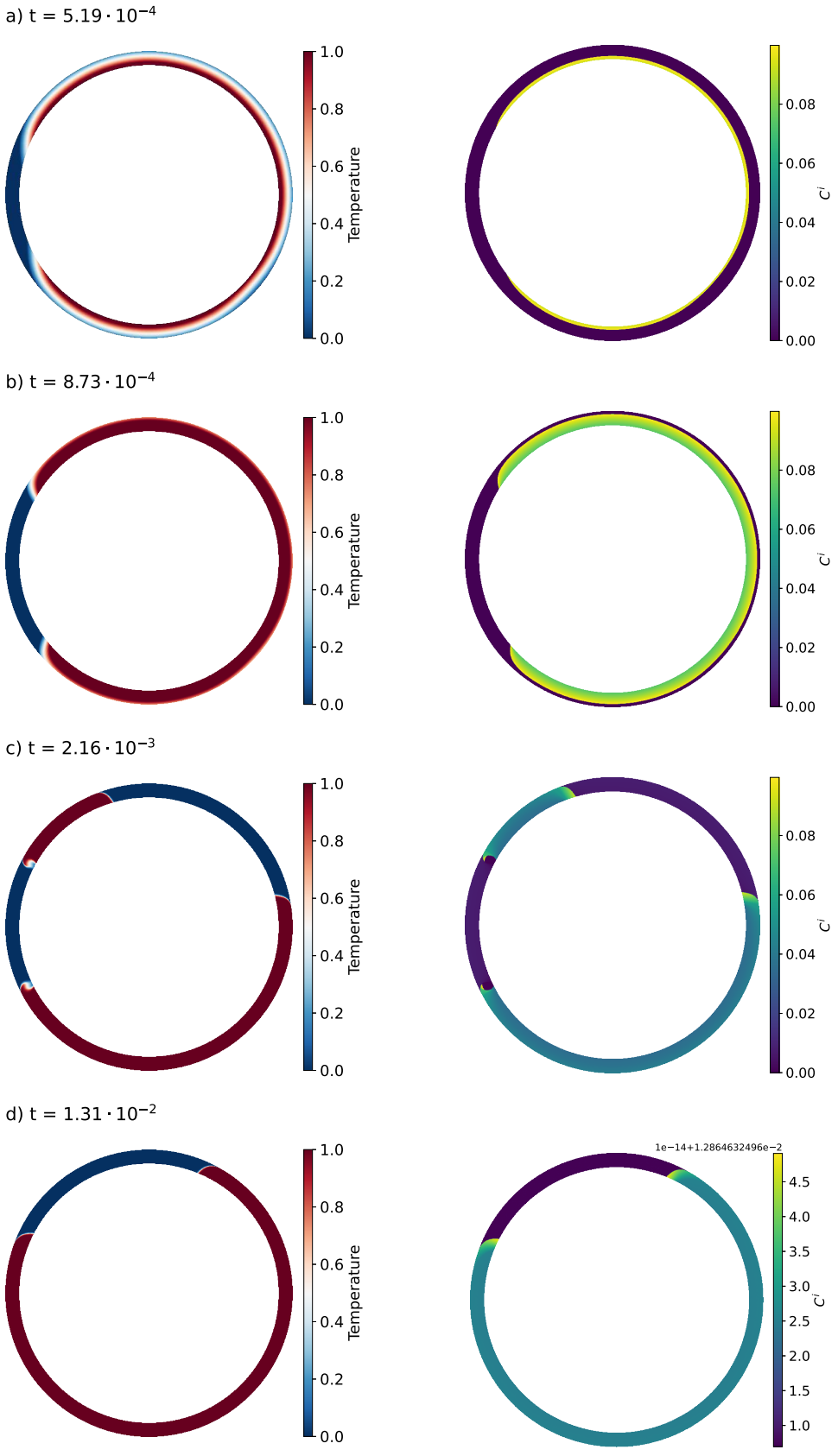

Figure 4.4: Snapshots of the evolution in time of the temperature (left) and salt concentration (right) in the HP ice layer for a partitioning coefficient $K = 10^{-1}$ and an effective buoyancy number $B_{eff} = 1$.

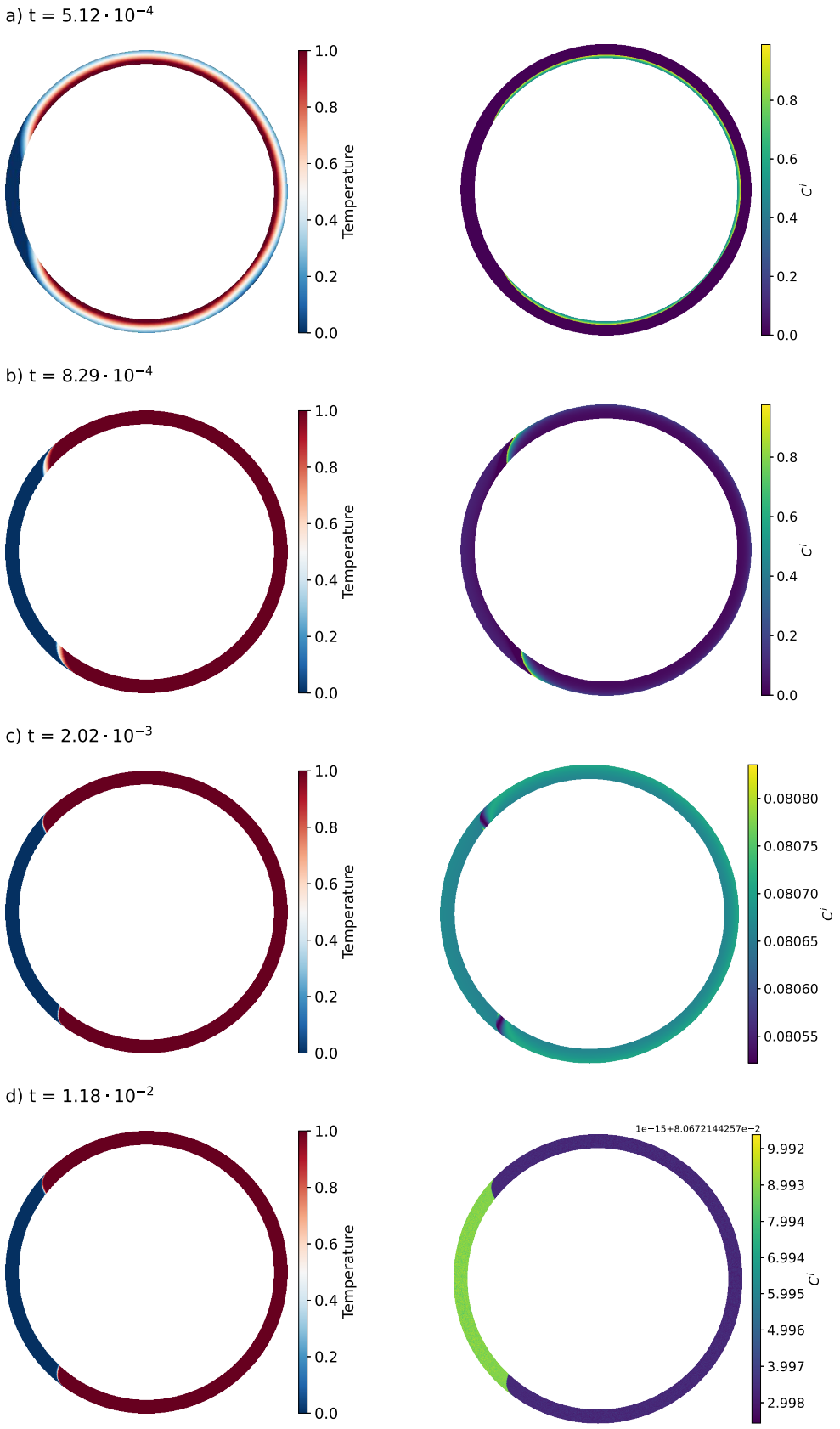

Figure 4.5: Snapshots of the evolution in time of the temperature (left) and salt concentration (right) in the HP ice layer for a partitioning coefficient $K = 1$ and an effective buoyancy number $B_{eff} = 1$.

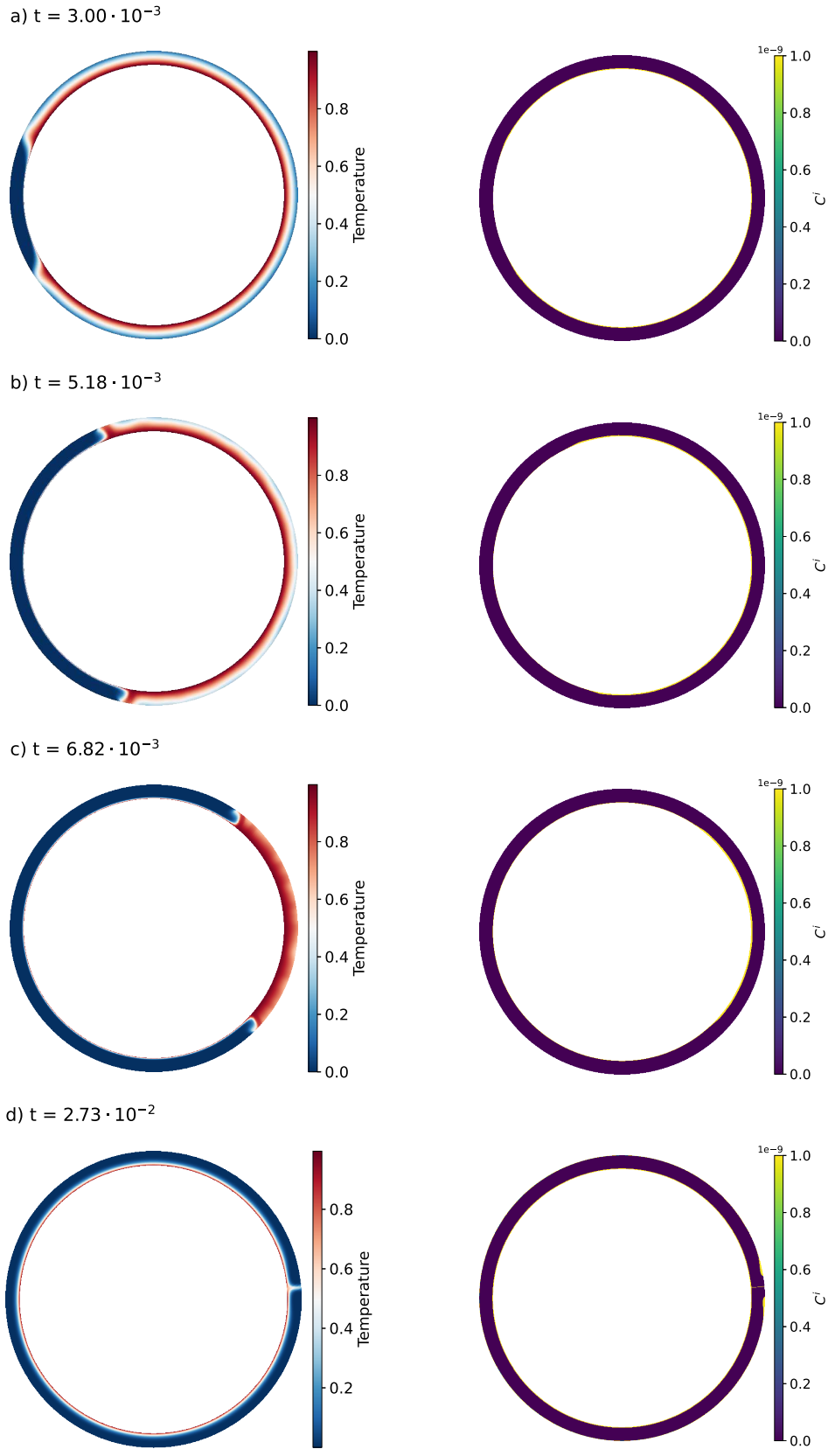

Figure 4.6: Snapshots of the evolution in time of the temperature (left) and salt concentration (right) in the HP ice layer for a partitioning coefficient $K = 10^{-1}$ and an effective buoyancy number $B_{eff} = 10$. The maximum concentration of salts in the HP ice layer during the entire run is 8×10^{-2}, but the color bars have been limited to 10^{-9} in order to have more information about what happens in the bulk of the ice shell.

range of B_{eff} the system reaches an equilibrium value, the concentration variations between the various values of B_{eff} are only about 10^{-13}. On the other hand, in the second regime for high values of the buoyancy number, the salts accumulate at the bottom of the HP ice layer (fig. 4.8.b) and their maximum concentration is about 7 times higher than the one for low values of the buoyancy number. In chapter 3, we observed that the thickness of the bottom layer formed by the accumulation of the salts was always around the height where the salts were added to the layer. In the case of this three-layers closed system we can observe that this layer is about 3 times thicker for $B_{eff} = 3$ than for $B_{eff} = 10$. It can be explained by the fact that for $B_{eff} = 3$ the salts have a lower effect on the ice density and can be transported higher, which forms a thicker bottom highly-salted layer but with a maximum concentration in salts about 10% lower than for $B_{eff} = 10$.

These regimes are also clearly visible comparing profiles of temperature, radial velocity, thermal advection and compositional advection for low (fig. 4.9) and high (fig. 4.10) values of the buoyancy number. Starting with fig. 4.9, the temperature is almost homogeneous in the layer with a difference of about 4% between the top and bottom boundaries. All three profiles fig. 4.9.b,c,d are nearly linear and decrease with radius, which is probably due to a geometrical effect. The radial velocity, thermal advection and composition advection increase slightly for increasing values of the effective buoyancy number.

For the second regime for high values of the buoyancy number (fig. 4.10), a highly-salted layer forms at the bottom of the HP ice shell, as already stated in chapter 3, but with two different heights depending on the value of the buoyancy number, as previously observed for the concentration. There is a layering of the convection and the limit between the two layers can be identified as the height at which the radial velocity and the thermal advection fall to 0, which is around 5×10^{-2} for $B_{eff} = 10$ and just above 2×10^{-1} for $B_{eff} = 3$. The compositional advection (fig. 4.10.d) seems to be nearly 0 and the small variations of the order of 10^{-3} are probably just noise, which means that at steady-state all the salts are accumulated at the bottom of the layer and are no longer entrained by convection. A major difference with the results obtained in chapter 3 is that the radial velocity at the interface between the upper ocean and the HP ice layer is completely different between low and high values of B_{eff}, while we saw on fig. 3.15.a that the buoyancy number did not have a significant effect of the top radial velocity in the case of a two-layers system. From fig. 3.15.a, we can compute an average value of the radial velocity at top for a Rayleigh number $Ra_q = 10^4$, which gives us $w_{top} = 13$ in order to compare it with the values obtained here for low and high values of the effective buoyancy number. In the regime for high values of B_{eff} (fig. 4.10) the radial velocity at top is nearly of the same order of magnitude, while in the regime for small values of B_{eff} (fig. 4.9) it is about 600 times higher. It means that if the salts have nearly no effect on the ice density, the mass transfer across the interface between the HP ice and the upper ocean is much more efficient for a three-layers system with a basal ocean between the core and the ice than for a two-layers system.

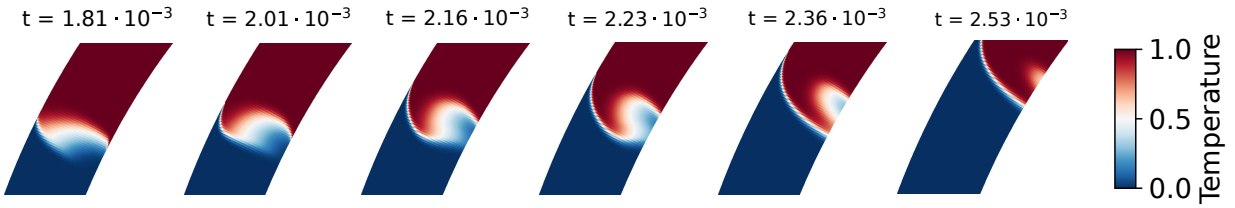

Figure 4.7: Snapshots of the evolution in time of the ying-yang effect in the thermal structure of the HP ice layer for a partitioning coefficient $K = 10^{-1}$ and an effective buoyancy number $B_{eff} = 1$.

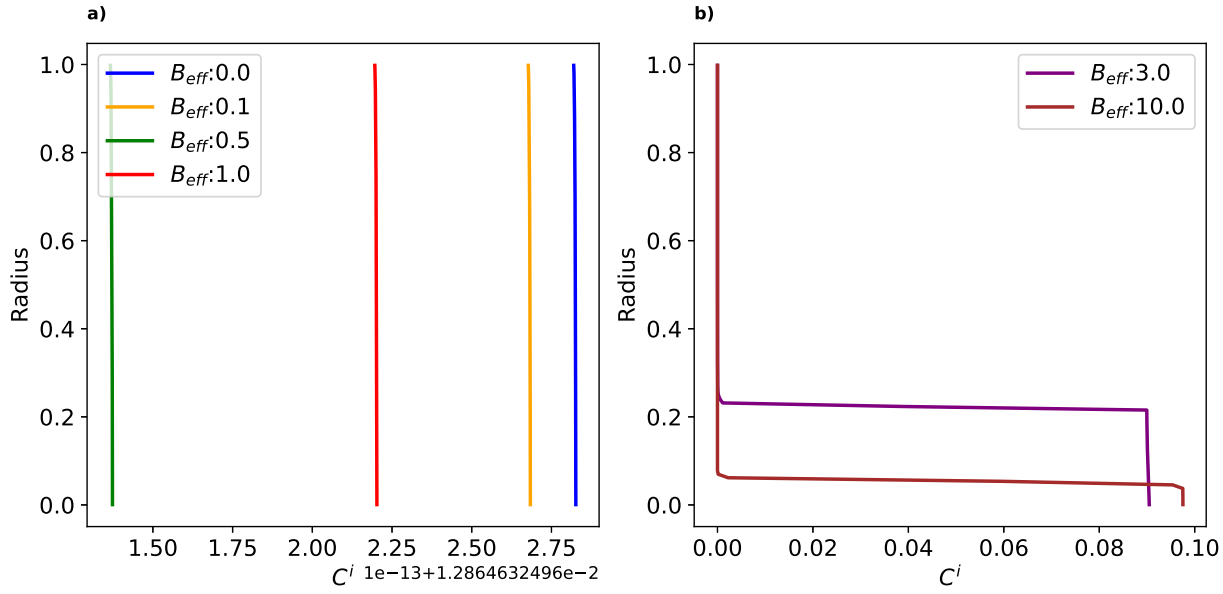

Figure 4.8: Profiles of the concentration in salts in the HP ice layer for a) $B_{eff} \leq 1$ and b) $B_{eff} > 1$. This figure is for a partitioning coefficient $K = 10^{-1}$ and the concentration is time-averaged over a period from $t_1 = 1.43 \times 10^{-2}$ to $t_2 = 1.49 \times 10^{-2}$, the end of the simulation.

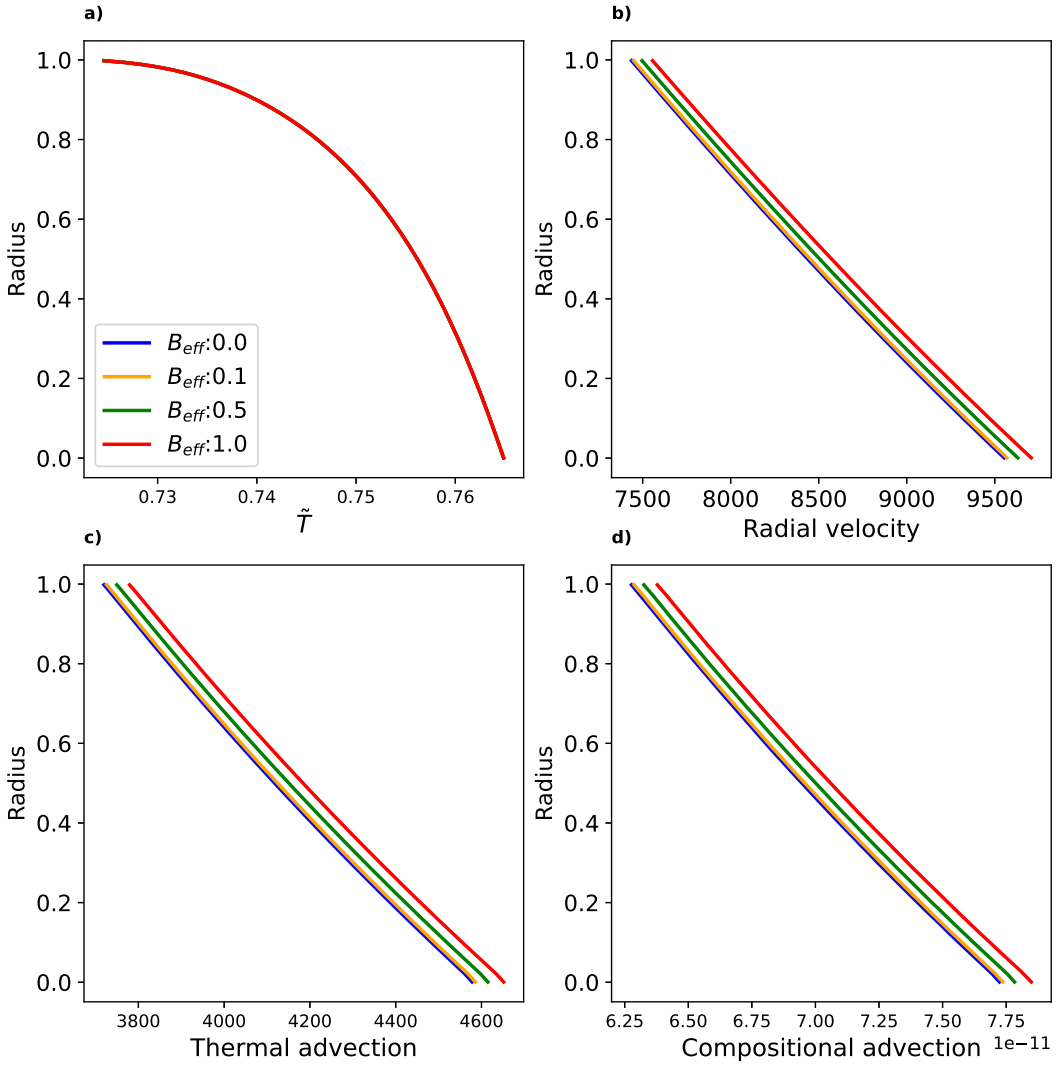

Figure 4.9: Profiles of a) the temperature divided by the bottom temperature, b) the radial velocity, c) the thermal advection and d) the compositional advection for $B_{eff} \leq 1$. This figure is for a partitioning coefficient $K = 10^{-1}$ and all profiles are time-averaged over a period from $t_1 = 1.43 \times 10^{-2}$ to $t_2 = 1.49 \times 10^{-2}$, the end of the simulation.

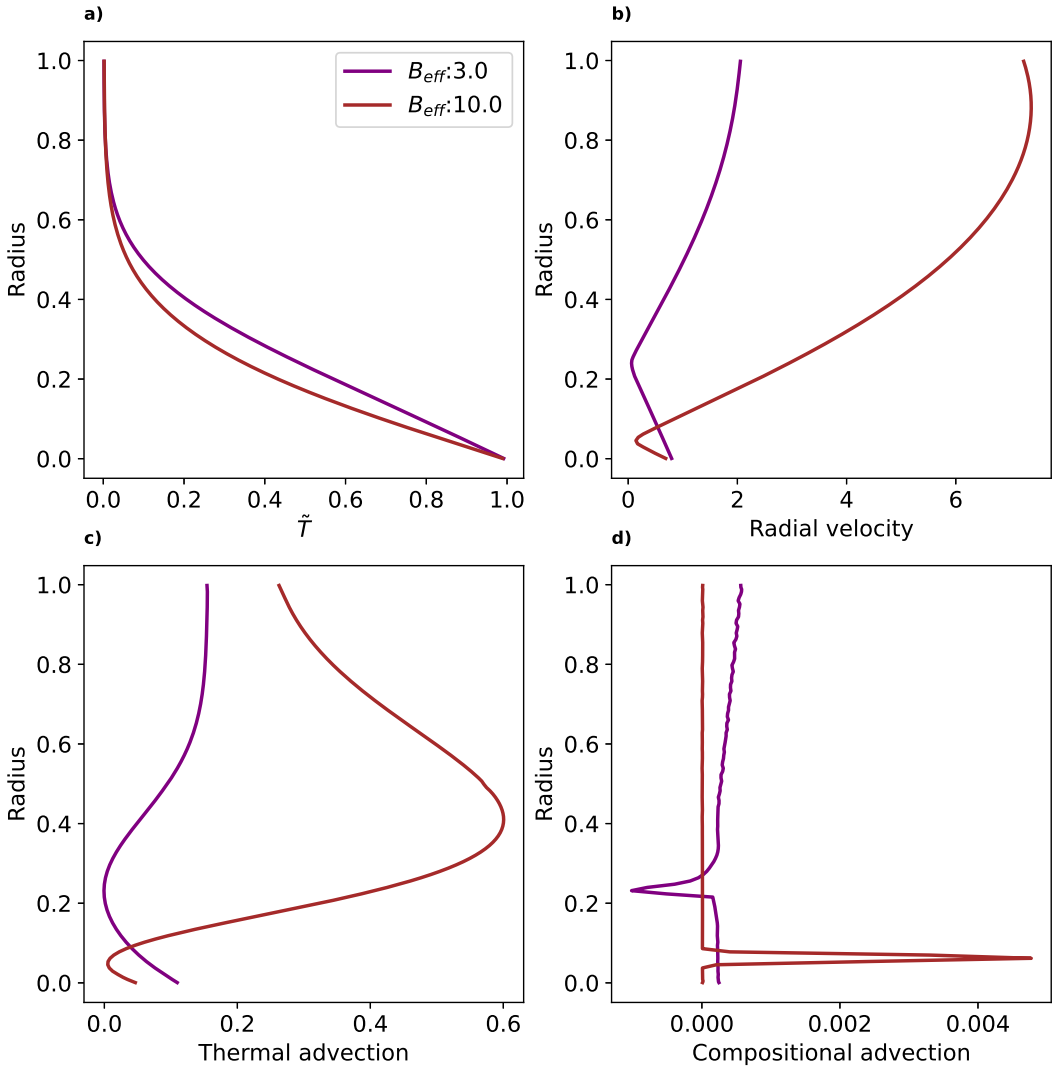

Figure 4.10: Profiles of a) the temperature divided by the bottom temperature, b) the radial velocity, c) the thermal advection and d) the compositional advection for $B_{eff} = 3$ and $B_{eff} = 10$. This figure is for a partitioning coefficient $K = 10^{-1}$ and all profiles are time-averaged over a period from $t_1 = 1.43 \times 10^{-2}$ to $t_2 = 1.49 \times 10^{-2}$, the end of the simulation.

4.3 Discussion & Perspectives

The formation of a basal ocean between the HP ice layer and the core in large icy moons or ocean worlds is predicted by the extreme accumulation of salts at the bottom of the HP ice shell in the regime for high values of the buoyancy number. But the feasibility of this solution depends mainly on the amount of chemical elements originally present in the core after differentiation and capable of forming salts through interactions with liquid water and, therefore, on the flux of salts expected to come from the core. On large icy moons such as Ganymede or Titan, because of their very deep hydrosphere, the water/rocks ratio is pretty high and, during the differentiation process, most of these chemical elements could have been trapped in the hydrosphere. The small amount of these chemical elements expected to be found in the core after differentiation does not support the hypothesis of the formation of a basal ocean between the ice and the core, as we need a lot of salts to accumulate at the interface between both for this highly-salted layer to melt and form an ocean. However, according to Reynard and Sotin [2023], in rich-silicate mantles, a natural pyrolysis reaction releases hydrocarbons and volatiles as CO_2 and leads to dehydration of the silicates. These hydrocarbons are not stable and it leads to the carbonization of the carbonaceous matter initially present in icy moon's mantle. This mechanism could still exist today for icy moons larger than 1 000 km, which is the case of Ganymede and Titan, and provide organics and volatiles to the ocean. According to Castillo-Rogez et al. [2022], icy moons are rich in NH_3 and CO_2, which can participate to increase ocean salinity and electrical conductivity. Indeed, during the differentiation of the moon, these volatiles are trapped in the mantle, for example in carbonates for CO_2, and released later thanks to thermal metamorphism. These volatiles could interact between them and with water and provide more anions and cations as NH_4^+, HCO_3^- and CO_3^{2-}, for salts to form in the ocean. The processes presented in Reynard and Sotin [2023] and Castillo-Rogez et al. [2022] could counteract the lack of chemical elements initially present in the core after differentiation and capable of forming salts through interactions with liquid water, but to conclude about all of these aspects, more information is required.

As we have already observed in chapter 3, the system tends to a steady-state and even to a chemical equilibrium for low values of the effective buoyancy number. For the same Rayleigh number, the three-layers system presented in this chapter tends to the steady-state 180 times faster than the two-layers system studied in chapter 3. The two regimes identified in chapter 3 can also be easily identified in the case of a three-layers system. However, if the radial velocity was virtually not affected by the value of the buoyancy number in the case of chapter 3, it has a huge impact on it in the case of two oceans surrounding a solid layer. In the present case, the radial velocity is of the order of 600 times higher for low values than for high values of the buoyancy number, meaning that if the salts have a low effect on the ice density, the efficiency of the mass transfer through the HP ice layer is much higher if a basal ocean exists between the ice and the core than in the case of a two-layers system as presented in chapter 3. Also, for high values of the buoyancy number, the salts accumulate at the bottom of the HP ice layer, forming a highly-salted stable layer which kills the phase-change boundary condition. Therefore, we fall back on a two-layers system composed of a

HP ice layer topped by an ocean. In that particular case, it could be interesting to run a simulation with a Rayleigh number of about 10^8, as in chapter 3, to compare the evolution of the HP ice layer and the steady-state in both cases.

CHAPTER 5

CONCLUSION

The aim of this PhD thesis is to contribute to the improvement of the dynamical models of the high-pressure ice layers and to characterize the water/rock interactions in large ocean worlds. There are only a few studies published on this question so far and contributing to this work is important to improve our knowledge on the internal activity and the habitability of large icy moons. These studies could also be used in the future to define the habitability of water-rich exoplanets. Therefore, this thesis is in line with the few previous studies on this topic and focuses on several aspects not considered before in order to answer the questions addressed in the introduction part of this manuscript.

Is mass transfer through a high-pressure ice layer possible and how efficient is it?

Through the results presented in the previous chapters, we can conclude that mass transfer through the high-pressure ice layers on large icy moons as Ganymede is possible and that its efficiency depends on several factors. First of all, it depends on parameters such as the thickness of the high-pressure ice shell, the heat flux from the core and the viscosity of the ice, whose values are currently ill-constrained. In the range of values considered relevant for Ganymede, we found in chapter 2 that in most cases at least an indirect contact between the core and the ocean could exist, which means that melt is produced at the interface with the core, which rises through the HP ice layer and recrystallizes on the way. It also depends on the efficiency of the phase change at the interface between the ice and the ocean and on the melting ability of the ice at the bottom boundary between the ice and the core.

How does the phase-change at the top boundary between the ice and the ocean impact the efficiency of the heat and mass transfer through the high-pressure ice layer?

The conclusion of chapter 2 is that considering the phase-change existing between the high-pressure ice layer and the ocean greatly eases the convection and improves the heat and mass exchanges between the core and the ocean through the high-pressure ice layer. Indeed the easiest this phase-change is, the higher the radial velocity at the interface with the ocean, allowing a more efficient mass transfer through the boundary. In most cases studied in the context of Ganymede, this temperature reaches the melting temperature and melt forms at the interface between the core and the ice. It means that salts and nutrients from the core could also be transported to the ocean in the liquid state during at least a part of the ascent. This point has not been studied in this PhD thesis but the preliminary study in the discussion part of chapter 2 showed that in the case of Ganymede, depending on the values chosen for our ill-constrained parameters, several types of contacts could exist between the core and the ocean, going from no exchanges at all if the temperature at the bottom of the high-pressure ice shell is not high enough for the ice to melt, to direct exchanges if the ice in the up-welling hot plumes remains liquid during the entire ascent, which is the best scenario in terms of mass transfer efficiency.

How does a flux of salts from the core impact the mass transfer efficiency and the overall dynamics? Can these salts be efficiently transferred from the core to the ocean?

In the case of melt formation at the interface between the core and the high-pressure ice, it allows liquid water to interact with the core and get enriched in salts. Then, if this mixture is less dense than the ice, it should rise through it and either recrystallise on the way or stay liquid until reaching the ocean. We studied the case where the mixture of water and salts recrystallizes into a mixture of salts and high-pressure ices that can be transported through the ice shell by convection in the solid state. It leads to two very different regimes depending on the value of the buoyancy number. In the case of a small buoyancy number regime, the salts do not have a significant effect on the ice density and are easily transported through the high-pressure ice layer. In that case they do not impede the convection, neither nor the efficiency of the mass transfer and all the salts entering the ice from the core are reaching the ocean. In the case of a large buoyancy number regime, the salts accumulate at the bottom the high-pressure ice layer and it leads to a layering of the convection. But even in that case, the accumulation of the salts does not impede the convection in the upper convective layer and does not affect significantly the radial velocity at the interface between the ice and the ocean, which is still of the order of several meters per year. As explained in the conclusion of chapter 3, we switch in this second regime for a high flux of salts from the core, meaning that even if only a small part of these salts are reaching the upper convective layer, the total amount of salts transported through this upper layer to the ocean could be comparable to the amount of salts coming from the core and reaching the ocean in the case

of the first regime. Finally, in the case of Ganymede we found that the mass transfer is still efficient, but to conclude about the habitability the question is "What is the amount of salts contained in this salt/ice mixture reaching the ocean?". This is a tricky question to answer because of the lack of information about the internal and chemical composition of these moons.

How would the existence of a thin liquid ocean composed of highly salted water between the core and the high-pressure ice shell change the dynamics and affect the mass transfer efficiency?

Another consequence of the high buoyancy number regime that we found in chapter 3 is the possibility of the formation of a thin, entirely liquid layer between the core and the high-pressure ice shell. Indeed, in the case of a continuous accumulation of salts at the bottom of the high-pressure ice layer progressively decreasing the melting temperature, the entire layer could reach this temperature and melt. In that case, a thin, highly-salted water ocean could form between the ice and the core. First, the three-layers closed system formed by this basal ocean, the HP ice layer and the upper ocean tend to a steady-state, and even to a chemical equilibrium for low values of the effective buoyancy number B_{eff}. Depending on its value, two regimes are observed, as in chapter 3, but in the case of a three-layers system, the buoyancy number has a huge effect on the radial velocity, which is much higher for low values of B_{eff}. It means that the mass transfer through the HP ice layer for a system composed of two oceans is much more efficient for low values of B_{eff}. Finally, for high values of B_{eff}, the salts accumulate so much at the bottom of the HP ice shell that it kills the phase-change boundary condition at the interface with the core. The feasibility of the formation of such a basal ocean has yet to be demonstrated because of the unknown amount of salts that could accumulate at the bottom of the HP ice layer. It has been discussed in § 4.3.

Finally, is the existence of a HP ice layer between the core and the ocean a real obstacle to habitability?

According to the results obtained during this PhD thesis and the ones from the few previous studies on this topic, efficient exchanges are possible through this high-pressure ice layer, either by convection in the solid state but also in the liquid state during at least a part of the ascent, under certain conditions. Therefore, the existence of a high-pressure ice layer between the core and the ocean on large icy moons and ocean worlds is not a real obstacle to habitability. However, it is obviously not enough to conclude about the habitability of these moons. If mass exchanges are efficient, we need more information about the internal structure of these planetary objects, to better constrained our models, and about their rocky core chemical composition in order to estimate the amount of salts we could expect to be transported from the core to the ocean. This knowledge should hopefully be provided by future missions.

Perspectives

Despite the many aspects covered over these three years, this PhD thesis has obviously not answered all the questions on this vast subject. First of all, there is still work to be done on the possible formation of the basal ocean between the core and the high-pressure ice shell (chapter 4) and its effect on the overall dynamics and on the mass transfer efficiency through the ice. We could extend this study to consider other values of the Rayleigh number and the addition of a flux of salts from the core at the interface with the basal ocean.

An important point that has not been considered in this PhD thesis is the full treatment of the two-phase flow composed of convection in the solid and liquid states. If the bottom temperature at the interface between the core and the ice reaches the melting temperature, melt forms at the bottom boundary and can rise through the ice by convection in the liquid state, as stated in the preliminary study in § 2.5. This key aspect changes a lot the dynamics and greatly increases the efficiency of the mass transfer through the high-pressure ice shell. Unlike models considering only convection in the solid state for which we have shown in § 2.5 that a constant viscosity is reliable, considering the viscosity variations with pressure, temperature, salts concentration and melt fraction is necessary in the case of a two-phase flow.

APPENDIX A

SCALING OF CONVECTION IN HIGH-PRESSURE ICE LAYERS OF LARGE ICY MOONS AND IMPLICATIONS FOR HABITABILITY - SUPPLEMENTARY MATERIALS

This supplementary material contains the fully detailed results tables and figures corresponding to the exploration of the parameters space for all cases.

Table A.1: Detailed results for cases $Ra_q \sim Ra_c$ for a rigid bottom BC, $\gamma = 0.95$ and various values of Φ from 10^{-2} to ∞. Cases solved for $nz_{tot} = 32$ (most of the time, otherwise 64) and $ny_{tot} = 2k\pi z_{tot}(R^- + 0.5)$ with $2k\pi$ the longitudinal aperture considered for each simulation (Here $k = 1$ or $k = \frac{1}{10}$). A refinement has been applied at the top $dresl_{R^+} = 5$ and the bottom $dresl_{R^-} = 2$ interfaces with 4 points in the boundary layers.

Φ	γ	Ra_q/Ra_c	Ra_q	$\bar{T}_{bot}$	Nu	w_{top}
0.01	0.95	2.00	556.07	0.71	1.40	3.33
0.01	0.95	3.00	834.10	0.61	1.65	4.79
0.01	0.95	4.00	1112.14	0.55	1.82	5.94
0.01	0.95	5.00	1390.17	0.50	1.99	7.08
0.01	0.95	6.00	1668.20	0.48	2.08	7.88
0.01	0.95	7.00	1946.24	0.46	2.18	8.57
0.01	0.95	8.00	2224.27	0.45	2.23	9.16
0.01	0.95	9.00	2502.31	0.43	2.32	9.79
0.01	0.95	10.00	2780.34	0.42	2.35	10.41
0.1	0.95	1.10	308.98	0.91	1.10	1.04
0.1	0.95	2.00	561.78	0.71	1.40	3.31

Continued on Next Page

Table A.1: Detailed results for cases $Ra_q \sim Ra_c$ for a rigid bottom BC, $\gamma = 0.95$ and various values of Φ from 10^{-2} to ∞. Cases solved for $nz_{tot} = 32$ (most of the time, otherwise 64) and $ny_{tot} = 2k\pi z_{tot}(R^- + 0.5)$ with $2k\pi$ the longitudinal aperture considered for each simulation (Here $k = 1$ or $k = \frac{1}{10}$). A refinement has been applied at the top $dresl_{R^+} = 5$ and the bottom $dresl_{R^-} = 2$ interfaces with 4 points in the boundary layers.

Φ	γ	Ra_q/Ra_c	Ra_q	T_{bot}	Nu	w_{top}
0.1	0.95	3.00	842.66	0.60	1.66	4.91
0.1	0.95	4.00	1123.55	0.55	1.83	5.96
0.1	0.95	5.00	1404.44	0.50	1.99	7.04
0.1	0.95	6.00	1685.33	0.48	2.07	7.82
0.1	0.95	7.00	1966.22	0.46	2.18	8.53
0.1	0.95	8.00	2247.11	0.45	2.23	9.24
0.1	0.95	9.00	2527.99	0.43	2.31	9.71
0.1	0.95	10.00	2808.88	0.42	2.36	9.93
1	0.95	1.10	338.98	0.91	1.10	1.00
1	0.95	2.00	616.32	0.71	1.42	3.24
1	0.95	3.00	924.49	0.60	1.66	4.68
1	0.95	5.00	1540.81	0.50	1.99	6.74
1	0.95	6.00	1848.97	0.48	2.10	7.51
1	0.95	7.00	2157.13	0.46	2.16	7.96
1	0.95	8.00	2465.29	0.45	2.23	8.86
1	0.95	9.00	2773.46	0.43	2.30	9.32
1	0.95	10.00	3081.62	0.42	2.36	9.65
10	0.95	1.10	541.02	0.91	1.10	0.72
10	0.95	3.00	1475.51	0.58	1.71	3.35
10	0.95	4.00	1967.35	0.53	1.89	4.06
10	0.95	5.00	2459.18	0.49	2.02	4.65
10	0.95	6.00	2951.02	0.46	2.15	5.18
10	0.95	7.00	3442.86	0.45	2.23	5.49
10	0.95	8.00	3934.69	0.44	2.27	5.97
10	0.95	9.00	4426.53	0.43	2.30	6.13
10	0.95	10.00	4918.37	0.40	2.51	7.16
100	0.95	1.10	859.75	0.90	1.11	0.17
100	0.95	2.00	1563.19	0.66	1.51	0.57
100	0.95	3.00	2344.78	0.55	1.82	0.80
100	0.95	4.00	3126.37	0.49	2.03	1.03
100	0.95	5.00	3907.96	0.46	2.18	1.23
100	0.95	6.00	4689.56	0.43	2.32	1.40

Continued on Next Page

Table A.1: Detailed results for cases $Ra_q \sim Ra_c$ for a rigid bottom BC, $\gamma = 0.95$ and various values of Φ from 10^{-2} to ∞. Cases solved for $nz_{tot} = 32$ (most of the time, otherwise 64) and $ny_{tot} = 2k\pi z_{tot}(R^- + 0.5)$ with $2k\pi$ the longitudinal aperture considered for each simulation (Here $k = 1$ or $k = \frac{1}{10}$). A refinement has been applied at the top $dresl_{R^+} = 5$ and the bottom $dresl_{R^-} = 2$ interfaces with 4 points in the boundary layers.

Φ	γ	Ra_q/Ra_c	Ra_q	T_{bot}	Nu	w_{top}
100	0.95	7.00	5471.15	0.42	2.40	1.57
100	0.95	8.00	6252.74	0.39	2.58	1.61
100	0.95	9.00	7034.33	0.39	2.58	1.88
100	0.95	10.00	7815.93	0.38	2.66	2.00
∞	0.95	1.10	948.95	0.90	1.11	0
∞	0.95	2.00	1725.36	0.66	1.51	0
∞	0.95	3.00	2588.04	0.56	1.78	0
∞	0.95	4.00	3450.72	0.50	2.00	0
∞	0.95	5.00	4313.40	0.46	2.16	0
∞	0.95	6.00	5176.08	0.44	2.30	0
∞	0.95	7.00	6038.76	0.42	2.40	0
∞	0.95	8.00	6901.44	0.40	2.50	0
∞	0.95	9.00	7764.11	0.39	2.59	0
∞	0.95	10.00	8626.79	0.37	2.67	0

Table A.2: Detailed results for cases $Ra_q \sim Ra_c$ for a rigid bottom BC, $\gamma = 0.9$ and various values of Φ from 10^{-2} to ∞. Cases solved for $nz_{tot} = 32$ (most of the time, otherwise 64) and $ny_{tot} = 2k\pi z_{tot}(R^- + 0.5)$ with $2k\pi$ the longitudinal aperture considered for each simulation (Here $k = 1$ or $k = \frac{1}{10}$). A refinement has been applied at the top $dresl_{R^+} = 5$ and the bottom $dresl_{R^-} = 2$ interfaces with 4 points in the boundary layers.

Φ	γ	Ra_q/Ra_c	Ra_q	T_{bot}	Nu	w_{top}
0.01	0.90	1.10	321.01	0.86	1.16	1.07
0.01	0.90	3.00	875.48	0.58	1.73	4.86
0.01	0.90	4.00	1167.31	0.53	1.88	5.86
0.01	0.90	6.00	1750.96	0.47	2.15	7.59
0.01	0.90	7.00	2042.79	0.45	2.22	8.19
0.01	0.90	8.00	2334.62	0.43	2.34	9.41

Continued on Next Page

Table A.2: Detailed results for cases $Ra_q \sim Ra_c$ for a rigid bottom BC, $\gamma = 0.9$ and various values of Φ from 10^{-2} to ∞. Cases solved for $nz_{tot} = 32$ (most of the time, otherwise 64) and $ny_{tot} = 2k\pi z_{tot}(R^- + 0.5)$ with $2k\pi$ the longitudinal aperture considered for each simulation (Here $k = 1$ or $k = \frac{1}{10}$). A refinement has been applied at the top $dresl_{R^+} = 5$ and the bottom $dresl_{R^-} = 2$ interfaces with 4 points in the boundary layers.

Φ	γ	Ra_q/Ra_c	Ra_q	T_{bot}	Nu	w_{top}
0.01	0.90	9.00	2626.44	0.42	2.36	9.67
0.01	0.90	10.00	2918.27	0.41	2.44	9.90
0.1	0.90	1.10	324.42	0.86	1.16	1.06
0.1	0.90	2.00	589.85	0.67	1.50	3.41
0.1	0.90	3.00	884.77	0.58	1.73	4.84
0.1	0.90	4.00	1179.70	0.53	1.88	5.83
0.1	0.90	5.00	1474.62	0.50	1.99	6.33
0.1	0.90	6.00	1769.55	0.47	2.14	7.74
0.1	0.90	7.00	2064.47	0.44	2.27	8.40
0.1	0.90	8.00	2359.40	0.44	2.28	9.20
0.1	0.90	9.00	2654.32	0.43	2.33	9.21
0.1	0.90	10.00	2949.25	0.41	2.41	10.35
1	0.90	2.00	648.99	0.66	1.51	3.27
1	0.90	3.00	973.48	0.58	1.74	4.64
1	0.90	4.00	1297.98	0.54	1.85	5.25
1	0.90	5.00	1622.47	0.50	2.00	6.21
1	0.90	6.00	1946.97	0.47	2.11	7.26
1	0.90	7.00	2271.46	0.46	2.18	7.39
1	0.90	8.00	2595.96	0.43	2.34	8.54
1	0.90	9.00	2920.45	0.43	2.33	9.37
1	0.90	10.00	3244.95	0.41	2.47	9.28
10	0.90	1.10	574.62	0.86	1.16	0.71
10	0.90	3.00	1567.14	0.56	1.77	3.23
10	0.90	4.00	2089.51	0.51	1.97	3.99
10	0.90	5.00	2611.89	0.48	2.09	4.58
10	0.90	6.00	3134.27	0.46	2.19	5.09
10	0.90	7.00	3656.65	0.43	2.35	5.32
10	0.90	8.00	4179.03	0.41	2.45	6.18
10	0.90	9.00	4701.41	0.38	2.64	6.91
10	0.90	10.00	5223.79	0.38	2.62	6.70
100	0.90	1.10	912.57	0.85	1.17	0.16
100	0.90	3.00	2488.84	0.53	1.90	0.81

Continued on Next Page

Table A.2: Detailed results for cases $Ra_q \sim Ra_c$ for a rigid bottom BC, $\gamma = 0.9$ and various values of Φ from 10^{-2} to ∞. Cases solved for $nz_{tot} = 32$ (most of the time, otherwise 64) and $ny_{tot} = 2k\pi z_{tot}(R^- + 0.5)$ with $2k\pi$ the longitudinal aperture considered for each simulation (Here $k = 1$ or $k = \frac{1}{10}$). A refinement has been applied at the top $dresl_{R^+} = 5$ and the bottom $dresl_{R^-} = 2$ interfaces with 4 points in the boundary layers.

Φ	γ	Ra_q/Ra_c	Ra_q	T_{bot}	Nu	w_{top}
100	0.90	6.00	4977.67	0.42	2.39	1.40
100	0.90	8.00	6636.89	0.39	2.58	1.71
100	0.90	9.00	7466.51	0.37	2.67	1.84
∞	0.90	1.10	1006.30	0.85	1.17	0
∞	0.90	3.00	2744.44	0.53	1.90	0
∞	0.90	4.00	3659.26	0.47	2.12	0
∞	0.90	5.00	4574.07	0.44	2.27	0
∞	0.90	6.00	5488.89	0.41	2.42	0
∞	0.90	7.00	6403.70	0.39	2.54	0
∞	0.90	8.00	7318.52	0.38	2.64	0
∞	0.90	9.00	8233.33	0.37	2.73	0
∞	0.90	10.00	9148.14	0.36	2.81	0

Table A.3: Detailed results for cases $Ra_q \sim Ra_c$ for a free-slip bottom BC, $\gamma = 0.95$ and various values of Φ from 10^{-2} to ∞. Cases solved for $nz_{tot} = 32$ and $ny_{tot} = 2k\pi z_{tot}(R^- + 0.5)$ with $2k\pi$ the longitudinal aperture considered for each simulation ($k = 1$ in this case due to degree 1 mode). A refinement has been applied at the top $dresl_{R^+} = 5$ and the bottom $dresl_{R^-} = 2$ interfaces with 4 points in the boundary layers.

Φ	γ	Ra_q/Ra_c	Ra_q	T_{bot}	Nu	w_{top}
0.01	0.95	1.10	68.61	0.95	1.05	0.00
0.01	0.95	2.00	124.74	0.86	1.17	1.10
0.01	0.95	3.00	187.11	0.74	1.35	2.25
0.01	0.95	4.00	249.48	0.65	1.54	3.13
0.01	0.95	5.00	311.85	0.61	1.64	3.53
0.01	0.95	6.00	374.21	0.56	1.79	4.19
0.01	0.95	7.00	436.58	0.53	1.87	4.43
0.01	0.95	8.00	498.95	0.50	1.99	5.29

Continued on Next Page

Table A.3: Detailed results for cases $Ra_q \sim Ra_c$ for a free-slip bottom BC, $\gamma = 0.95$ and various values of Φ from 10^{-2} to ∞. Cases solved for $nz_{tot} = 32$ and $ny_{tot} = 2k\pi z_{tot}(R^- + 0.5)$ with $2k\pi$ the longitudinal aperture considered for each simulation ($k = 1$ in this case due to degree 1 mode). A refinement has been applied at the top $dresl_{R^+} = 5$ and the bottom $dresl_{R^-} = 2$ interfaces with 4 points in the boundary layers.

Φ	γ	Ra_q/Ra_c	Ra_q	T_{bot}	Nu	w_{top}
0.01	0.95	9.00	561.32	0.48	2.08	5.37
0.01	0.95	10.00	623.69	0.47	2.15	5.85
0.1	0.95	1.10	70.76	0.95	1.05	0.00
0.1	0.95	2.00	128.66	0.85	1.18	1.32
0.1	0.95	3.00	192.99	0.75	1.34	2.07
0.1	0.95	4.00	257.32	0.64	1.57	3.18
0.1	0.95	5.00	321.65	0.60	1.66	3.42
0.1	0.95	6.00	385.98	0.56	1.77	4.12
0.1	0.95	7.00	450.31	0.53	1.88	4.63
0.1	0.95	8.00	514.64	0.50	2.01	5.15
0.1	0.95	9.00	578.97	0.48	2.10	5.34
0.1	0.95	10.00	643.30	0.46	2.18	5.82
1	0.95	1.10	92.33	0.95	1.05	0.00
1	0.95	2.00	167.86	0.82	1.22	1.39
1	0.95	3.00	251.80	0.69	1.46	2.55
1	0.95	4.00	335.73	0.62	1.61	3.42
1	0.95	5.00	419.66	0.56	1.77	3.82
1	0.95	6.00	503.59	0.54	1.86	4.27
1	0.95	7.00	587.52	0.50	1.99	5.23
1	0.95	8.00	671.46	0.46	2.16	5.52
1	0.95	9.00	755.39	0.46	2.18	5.67
1	0.95	10.00	839.32	0.44	2.25	6.56
10	0.95	1.10	234.56	0.92	1.08	0.43
10	0.95	2.00	426.47	0.73	1.37	1.49
10	0.95	3.00	639.70	0.58	1.72	2.45
10	0.95	4.00	852.93	0.52	1.92	2.75
10	0.95	5.00	1066.16	0.47	2.11	3.39
10	0.95	6.00	1279.40	0.43	2.35	3.90
10	0.95	7.00	1492.63	0.40	2.48	4.44
10	0.95	8.00	1705.86	0.40	2.53	4.65
10	0.95	9.00	1919.09	0.38	2.63	5.15
10	0.95	10.00	2132.33	0.35	2.82	5.44

Continued on Next Page

Table A.3: Detailed results for cases $Ra_q \sim Ra_c$ for a free-slip bottom BC, $\gamma = 0.95$ and various values of Φ from 10^{-2} to ∞. Cases solved for $nz_{tot} = 32$ and $ny_{tot} = 2k\pi z_{tot}(R^- + 0.5)$ with $2k\pi$ the longitudinal aperture considered for each simulation ($k = 1$ in this case due to degree 1 mode). A refinement has been applied at the top $dresl_{R^+} = 5$ and the bottom $dresl_{R^-} = 2$ interfaces with 4 points in the boundary layers.

Φ	γ	Ra_q/Ra_c	Ra_q	T_{bot}	Nu	w_{top}
100	0.95	1.10	406.57	0.91	1.10	0.12
100	0.95	2.00	739.22	0.66	1.52	0.40
100	0.95	3.00	1108.83	0.54	1.86	0.59
100	0.95	4.00	1478.44	0.48	2.10	0.77
100	0.95	5.00	1848.06	0.43	2.30	0.91
100	0.95	6.00	2217.67	0.42	2.40	1.07
100	0.95	7.00	2587.28	0.39	2.56	1.19
100	0.95	8.00	2956.89	0.37	2.70	1.30
100	0.95	9.00	3326.50	0.36	2.79	1.41
100	0.95	10.00	3696.11	0.35	2.87	1.53
∞	0.95	1.10	451.20	0.90	1.11	0
∞	0.95	2.00	820.37	0.66	1.52	0
∞	0.95	3.00	1230.55	0.54	1.85	0
∞	0.95	4.00	1640.73	0.48	2.10	0
∞	0.95	5.00	2050.92	0.43	2.31	0
∞	0.95	6.00	2461.10	0.40	2.48	0
∞	0.95	7.00	2871.28	0.38	2.62	0
∞	0.95	8.00	3281.47	0.36	2.74	0
∞	0.95	9.00	3691.65	0.35	2.85	0
∞	0.95	10.00	4101.84	0.34	2.96	0

Table A.4: Detailed results for cases $Ra_q \sim Ra_c$ for a free-slip bottom BC, $\gamma = 0.9$ and various values of Φ from 10^{-2} to ∞. Cases solved for $nz_{tot} = 32$ and $ny_{tot} = 2k\pi z_{tot}(R^- + 0.5)$ with $2k\pi$ the longitudinal aperture considered for each simulation ($k = 1$ in this case due to degree 1 mode). A refinement has been applied at the top $dresl_{R^+} = 5$ and the bottom $dresl_{R^-} = 2$ interfaces with 4 points in the boundary layers.

Φ	γ	Ra_q/Ra_c	Ra_q	T_{bot}	Nu	w_{top}
0.01	0.90	1.10	71.37	0.90	1.11	0.00
0.01	0.90	2.00	129.77	0.81	1.23	1.31
0.01	0.90	3.00	194.65	0.71	1.42	2.14
0.01	0.90	4.00	259.53	0.63	1.59	3.28
0.01	0.90	5.00	324.41	0.57	1.74	3.67
0.01	0.90	6.00	389.30	0.52	1.91	4.14
0.01	0.90	7.00	454.18	0.51	1.96	4.54
0.01	0.90	8.00	519.06	0.51	1.96	4.36
0.01	0.90	9.00	583.94	0.46	2.15	5.19
0.01	0.90	10.00	648.83	0.45	2.23	5.62
0.1	0.90	1.10	73.73	0.90	1.11	0.00
0.1	0.90	2.00	134.06	0.81	1.23	1.21
0.1	0.90	3.00	201.09	0.70	1.44	2.33
0.1	0.90	4.00	268.12	0.62	1.61	2.92
0.1	0.90	5.00	335.15	0.57	1.77	3.97
0.1	0.90	6.00	402.18	0.54	1.84	3.78
0.1	0.90	7.00	469.21	0.50	1.99	4.89
0.1	0.90	8.00	536.24	0.47	2.11	5.01
0.1	0.90	9.00	603.27	0.45	2.21	6.01
0.1	0.90	10.00	670.29	0.44	2.27	5.30
1	0.90	1.10	97.31	0.90	1.11	0.00
1	0.90	2.00	176.94	0.78	1.29	1.58
1	0.90	3.00	265.40	0.67	1.48	2.39
1	0.90	4.00	353.87	0.61	1.65	2.94
1	0.90	5.00	442.34	0.56	1.79	3.27
1	0.90	6.00	530.81	0.52	1.93	4.19
1	0.90	7.00	619.27	0.48	2.09	4.74
1	0.90	8.00	707.74	0.45	2.23	5.23
1	0.90	9.00	796.21	0.44	2.29	5.91
1	0.90	10.00	884.68	0.42	2.36	6.55
10	0.90	1.10	252.74	0.87	1.15	0.44

Continued on Next Page

Table A.4: Detailed results for cases $Ra_q \sim Ra_c$ for a free-slip bottom BC, $\gamma = 0.9$ and various values of Φ from 10^{-2} to ∞. Cases solved for $nz_{tot} = 32$ and $ny_{tot} = 2k\pi z_{tot}(R^- + 0.5)$ with $2k\pi$ the longitudinal aperture considered for each simulation ($k = 1$ in this case due to degree 1 mode). A refinement has been applied at the top $dresl_{R^+} = 5$ and the bottom $dresl_{R^-} = 2$ interfaces with 4 points in the boundary layers.

Φ	γ	Ra_q/Ra_c	Ra_q	T_{bot}	Nu	w_{top}
10	0.90	2.00	459.53	0.69	1.45	1.37
10	0.90	3.00	689.30	0.57	1.75	2.33
10	0.90	4.00	919.07	0.48	2.07	2.91
10	0.90	5.00	1148.83	0.43	2.31	3.57
10	0.90	6.00	1378.60	0.41	2.43	4.04
10	0.90	7.00	1608.37	0.38	2.60	4.48
10	0.90	8.00	1838.13	0.38	2.61	4.59
10	0.90	9.00	2067.90	0.38	2.65	5.10
10	0.90	10.00	2297.67	0.35	2.90	5.55
100	0.90	1.10	436.31	0.86	1.17	0.11
100	0.90	2.00	793.30	0.62	1.61	0.39
100	0.90	3.00	1189.94	0.51	1.96	0.58
100	0.90	4.00	1586.59	0.45	2.23	0.74
100	0.90	5.00	1983.24	0.41	2.43	0.89
100	0.90	6.00	2379.89	0.39	2.57	1.03
100	0.90	7.00	2776.53	0.37	2.73	1.14
100	0.90	8.00	3173.18	0.35	2.88	1.25
100	0.90	9.00	3569.83	0.34	2.94	1.37
100	0.90	10.00	3966.48	0.33	3.06	1.47
∞	0.90	1.10	483.56	0.86	1.17	0
∞	0.90	2.00	879.20	0.62	1.61	0
∞	0.90	3.00	1318.81	0.51	1.95	0
∞	0.90	4.00	1758.41	0.45	2.22	0
∞	0.90	5.00	2198.01	0.41	2.44	0
∞	0.90	6.00	2637.61	0.38	2.62	0
∞	0.90	7.00	3077.22	0.36	2.76	0
∞	0.90	8.00	3516.82	0.35	2.90	0
∞	0.90	9.00	3956.42	0.33	3.02	0
∞	0.90	10.00	4396.02	0.32	3.12	0

Table A.5: Detailed results for cases $Ra_q \geq 50 * Ra_c$ for a rigid bottom BC, $\gamma = 0.95$ and various values of Φ from 10^{-2} to ∞. Cases solved for $nz_{tot} = 64$ (most of the time, otherwise 128 or 256) and $ny_{tot} = 2k\pi z_{tot}(R^- + 0.5)$ with $2k\pi$ the longitudinal aperture considered for each simulation (Here $k = \frac{1}{5}$ or $k = \frac{1}{10}$). A refinement has been applied at the top $dresl_{R^+} = 2$ and the bottom $dresl_{R^-} = 2$ interfaces with 4 points in the boundary layers.

Φ	γ	Ra_q/Ra_c	Ra_q	$\bar{T}_{bot}$	Nu	w_{top}
0.01	0.95	50	13901.70	0.29	3.45	22.83
0.01	0.95	100	27803.40	0.25	4.07	35.21
0.01	0.95	500	139016.99	0.18	5.52	69.18
0.01	0.95	1000	278033.97	0.16	6.33	93.03
0.01	0.95	5000	1390169.87	0.12	8.50	201.28
0.01	0.95	10000	2780339.73	0.10	9.68	279.26
0.01	0.95	100000	27803397.34	0.06	15.93	878.73
0.1	0.95	50	14044.41	0.30	3.34	21.92
0.1	0.95	100	28088.82	0.24	4.11	33.53
0.1	0.95	500	140444.08	0.18	5.57	67.20
0.1	0.95	1000	280888.16	0.16	6.30	92.70
0.1	0.95	5000	1404440.78	0.12	8.53	198.77
0.1	0.95	10000	2808881.57	0.10	9.71	278.30
0.1	0.95	100000	28088815.69	0.06	16.03	866.86
1	0.95	50	15408.09	0.29	3.48	21.07
1	0.95	100	30816.18	0.25	4.01	29.92
1	0.95	500	154080.90	0.18	5.65	66.46
1	0.95	1000	308161.79	0.15	6.50	91.47
1	0.95	5000	1540808.96	0.11	8.78	193.52
1	0.95	10000	3081617.91	0.10	9.87	269.24
1	0.95	100000	30816179.13	0.06	16.21	832.94
10	0.95	50	24591.83	0.25	3.92	18.26
10	0.95	100	49183.66	0.22	4.49	25.11
10	0.95	500	245918.30	0.16	6.27	53.01
10	0.95	1000	491836.59	0.14	7.02	72.27
10	0.95	5000	2459182.97	0.11	9.51	150.73
10	0.95	10000	4918365.94	0.09	10.87	208.32
10	0.95	100000	49183659.45	0.05	19.23	639.44
100	0.95	50	39079.64	0.25	4.02	5.01
100	0.95	100	78159.27	0.23	4.39	7.82

Continued on Next Page

Table A.5: Detailed results for cases $Ra_q \geq 50 * Ra_c$ for a rigid bottom BC, $\gamma = 0.95$ and various values of Φ from 10^{-2} to ∞. Cases solved for $nz_{tot} = 64$ (most of the time, otherwise 128 or 256) and $ny_{tot} = 2k\pi z_{tot}(R^- + 0.5)$ with $2k\pi$ the longitudinal aperture considered for each simulation (Here $k = \frac{1}{5}$ or $k = \frac{1}{10}$). A refinement has been applied at the top $dresl_{R^+} = 2$ and the bottom $dresl_{R^-} = 2$ interfaces with 4 points in the boundary layers.

Φ	γ	Ra_q/Ra_c	Ra_q	$\bar{T}_{bot}$	Nu	w_{top}
100	0.95	500	390796.36	0.16	6.22	19.11
100	0.95	1000	781592.73	0.14	7.35	27.81
100	0.95	5000	3907963.63	0.09	10.65	69.38
100	0.95	10000	7815927.26	0.08	12.58	92.36
100	0.95	100000	78159272.64	0.05	21.37	276.72
∞	0.95	50	43133.97	0.26	3.88	0
∞	0.95	500	431339.72	0.17	5.72	0
∞	0.95	1000	862679.44	0.16	6.26	0
∞	0.95	5000	4313397.20	0.11	8.96	0
∞	0.95	10000	8626794.41	0.10	10.42	0
∞	0.95	100000	86267944.07	0.06	17.70	0

Table A.6: Detailed results for cases $Ra_q \geq 50 * Ra_c$ for a rigid bottom BC, $\gamma = 0.9$ and various values of Φ from 10^{-2} to ∞. Cases solved for $nz_{tot} = 64$ (most of the time, otherwise 128 or 256) and $ny_{tot} = 2k\pi z_{tot}(R^- + 0.5)$ with $2k\pi$ the longitudinal aperture considered for each simulation (Here $k = \frac{1}{5}$ or $k = \frac{1}{10}$). A refinement has been applied at the top $dresl_{R^+} = 2$ and the bottom $dresl_{R^-} = 2$ interfaces with 4 points in the boundary layers.

Φ	γ	Ra_q/Ra_c	Ra_q	$\bar{T}_{bot}$	Nu	w_{top}
0.01	0.90	50	14591.35	0.28	3.54	23.05
0.01	0.90	100	29182.70	0.24	4.09	33.10
0.01	0.90	500	145913.49	0.17	5.80	69.52
0.01	0.90	1000	291826.99	0.16	6.27	92.26
0.01	0.90	5000	1459134.93	0.12	8.59	199.03
0.01	0.90	10000	2918269.86	0.10	9.80	274.21
0.01	0.90	100000	29182698.59	0.06	16.19	861.13

Continued on Next Page

Table A.6: Detailed results for cases $Ra_q \geq 50 * Ra_c$ for a rigid bottom BC, $\gamma = 0.9$ and various values of Φ from 10^{-2} to ∞. Cases solved for $nz_{tot} = 64$ (most of the time, otherwise 128 or 256) and $ny_{tot} = 2k\pi z_{tot}(R^- + 0.5)$ with $2k\pi$ the longitudinal aperture considered for each simulation (Here $k = \frac{1}{5}$ or $k = \frac{1}{10}$). A refinement has been applied at the top $dresl_{R^+} = 2$ and the bottom $dresl_{R^-} = 2$ interfaces with 4 points in the boundary layers.

Φ	γ	Ra_q/Ra_c	Ra_q	$\bar{T}_{bot}$	Nu	w_{top}
0.1	0.90	50	14746.23	0.28	3.55	23.14
0.1	0.90	100	29492.47	0.24	4.10	29.94
0.1	0.90	500	147462.33	0.18	5.71	65.90
0.1	0.90	1000	294924.66	0.15	6.52	90.34
0.1	0.90	5000	1474623.32	0.12	8.57	199.24
0.1	0.90	10000	2949246.63	0.10	10.12	273.71
0.1	0.90	100000	29492466.33	0.06	16.41	852.82
1	0.90	50	16224.74	0.27	3.65	21.96
1	0.90	100	32449.48	0.25	4.05	30.49
1	0.90	500	162247.42	0.17	5.88	69.18
1	0.90	1000	324494.84	0.15	6.55	89.25
1	0.90	5000	1622474.19	0.11	8.97	191.14
1	0.90	10000	3244948.38	0.10	10.16	267.67
1	0.90	100000	32449483.77	0.06	16.50	810.57
10	0.90	50	26118.93	0.25	3.97	16.12
10	0.90	100	52237.85	0.22	4.63	25.71
10	0.90	500	261189.26	0.16	6.36	51.82
10	0.90	1000	522378.53	0.14	7.29	73.65
10	0.90	5000	2611892.63	0.10	9.58	146.45
10	0.90	10000	5223785.26	0.09	11.38	201.89
10	0.90	100000	52237852.59	0.05	19.55	627.38
100	0.90	50	41480.59	0.25	4.02	5.11
100	0.90	100	82961.17	0.21	4.78	7.19
100	0.90	500	414805.85	0.16	6.28	17.34
100	0.90	1000	829611.70	0.13	7.56	28.63
100	0.90	5000	4148058.52	0.09	10.97	66.63
100	0.90	10000	8296117.05	0.08	13.09	92.05
100	0.90	100000	82961170.48	0.04	22.41	266.22
∞	0.90	50	45740.72	0.25	4.05	0
∞	0.90	100	91481.44	0.22	4.51	0
∞	0.90	500	457407.20	0.17	6.01	0

Continued on Next Page

Table A.6: Detailed results for cases $Ra_q \geq 50 * Ra_c$ for a rigid bottom BC, $\gamma = 0.9$ and various values of Φ from 10^{-2} to ∞. Cases solved for $nz_{tot} = 64$ (most of the time, otherwise 128 or 256) and $ny_{tot} = 2k\pi z_{tot}(R^- + 0.5)$ with $2k\pi$ the longitudinal aperture considered for each simulation (Here $k = \frac{1}{5}$ or $k = \frac{1}{10}$). A refinement has been applied at the top $dresl_{R^+} = 2$ and the bottom $dresl_{R^-} = 2$ interfaces with 4 points in the boundary layers.

Φ	γ	Ra_q/Ra_c	Ra_q	$\bar{T}_{bot}$	Nu	w_{top}
∞	0.90	1000	914814.41	0.14	7.11	0
∞	0.90	5000	4574072.03	0.11	9.32	0
∞	0.90	10000	9148144.07	0.09	10.95	0
∞	0.90	100000	91481440.66	0.05	18.42	0

Table A.7: Detailed results for cases $Ra_q \geq 50 * Ra_c$ for a free-slip bottom BC, $\gamma = 0.95$ and various values of Φ from 10^{-2} to ∞. Cases solved for $nz_{tot} = 128$ or 256 and $ny_{tot} = 2k\pi z_{tot}(R^- + 0.5)$ with $2k\pi$ the longitudinal aperture considered for each simulation (Here $k = 1$, $k = \frac{1}{5}$ or $k = \frac{1}{10}$). A refinement has been applied at the top $dresl_{R^+} = 2$ or 4 and the bottom $dresl_{R^-} = 2$ interfaces with 4 or 6 points in the boundary layers.

Φ	γ	Ra_q/Ra_c	Ra_q	$\bar{T}_{bot}$	Nu	w_{top}
0.01	0.95	50	3118.45	0.29	3.48	14.65
0.01	0.95	100	6236.90	0.24	4.24	20.80
0.01	0.95	500	31184.51	0.16	6.26	44.08
0.01	0.95	1000	62369.03	0.14	7.24	60.52
0.01	0.95	5000	311845.14	0.10	10.34	121.18
0.01	0.95	10000	623690.27	0.08	12.82	179.15
0.1	0.95	50	3216.49	0.29	3.47	15.11
0.1	0.95	100	6432.98	0.24	4.25	19.93
0.1	0.95	1000	64329.85	0.14	7.25	62.33
1	0.95	50	4196.59	0.27	3.65	15.51
1	0.95	100	8393.19	0.22	4.53	21.12
1	0.95	500	41965.94	0.15	6.78	43.20
1	0.95	1000	83931.89	0.13	7.99	61.37
1	0.95	5000	419659.44	0.09	11.27	131.08
1	0.95	10000	839318.87	0.07	13.65	184.79

Continued on Next Page

Table A.7: Detailed results for cases $Ra_q \geq 50 * Ra_c$ for a free-slip bottom BC, $\gamma = 0.95$ and various values of Φ from 10^{-2} to ∞. Cases solved for $nz_{tot} = 128$ or 256 and $ny_{tot} = 2k\pi z_{tot}(R^- + 0.5)$ with $2k\pi$ the longitudinal aperture considered for each simulation (Here $k = 1$, $k = \frac{1}{5}$ or $k = \frac{1}{10}$). A refinement has been applied at the top $dresl_{R^+} = 2$ or 4 and the bottom $dresl_{R^-} = 2$ interfaces with 4 or 6 points in the boundary layers.

Φ	γ	Ra_q/Ra_c	Ra_q	T_{bot}	Nu	w_{top}
10	0.95	50	10661.63	0.22	4.55	14.20
10	0.95	100	21323.27	0.18	5.61	19.99
10	0.95	500	106616.34	0.12	8.51	41.69
10	0.95	1000	213232.68	0.10	10.02	56.21
10	0.95	5000	1066163.39	0.07	13.57	122.96
10	0.95	10000	2132326.78	0.06	17.11	152.00
10	0.95	100000	21323267.83	0.04	28.36	444.76
100	0.95	100	36961.10	0.17	5.96	5.43
100	0.95	500	184805.50	0.13	7.80	15.36
100	0.95	1000	369611.01	0.11	9.20	20.48
100	0.95	5000	1848055.03	0.08	13.33	53.13
100	0.95	10000	3696110.05	0.06	15.70	79.08
100	0.95	100000	36961100.54	0.04	27.23	240.14
∞	0.95	50	20509.18	0.21	4.67	0
∞	0.95	100	41018.36	0.18	5.52	0
∞	0.95	500	205091.78	0.14	7.16	0
∞	0.95	1000	410183.55	0.12	8.35	0
∞	0.95	5000	2050917.77	0.09	11.59	0
∞	0.95	10000	4101835.54	0.07	14.39	0
∞	0.95	100000	41018355.40	0.04	24.50	0

Table A.8: Detailed results for cases $Ra_q \geq 50 * Ra_c$ for a free-slip bottom BC, $\gamma = 0.9$ and various values of Φ from 10^{-2} to ∞. Cases solved for $nz_{tot} = 128$ or 256 and $ny_{tot} = 2k\pi z_{tot}(R^- + 0.5)$ with $2k\pi$ the longitudinal aperture considered for each simulation (Here $k = 1$, $k = \frac{1}{5}$ or $k = \frac{1}{10}$). A refinement has been applied at the top $dresl_{R^+} = 2$ or 4 and the bottom $dresl_{R^-} = 2$ interfaces with 4 or 6 points in the boundary layers.

Φ	γ	Ra_q/Ra_c	Ra_q	T_{bot}	Nu	w_{top}
0.01	0.90	50	3244.14	0.28	3.58	13.50
0.01	0.90	100	6488.28	0.24	4.14	21.00
0.01	0.90	500	32441.38	0.15	6.50	41.66
0.01	0.90	1000	64882.77	0.14	7.39	54.52
0.01	0.90	5000	324413.83	0.09	10.86	123.33
0.01	0.90	100000	6488276.58	0.06	17.78	481.47
0.10	0.90	50	3351.47	0.28	3.60	13.10
0.10	0.90	100	6702.94	0.23	4.37	21.49
0.10	0.90	500	33514.72	0.17	5.99	41.33
0.10	0.90	1000	67029.45	0.13	7.42	56.75
0.10	0.90	5000	335147.25	0.10	10.35	137.91
0.10	0.90	100000	6702944.90	0.06	17.50	426.20
1.00	0.90	50	4423.39	0.26	3.79	14.21
1.00	0.90	100	8846.78	0.23	4.36	19.62
1.00	0.90	500	44233.90	0.15	6.46	42.04
1.00	0.90	1000	88467.79	0.12	8.21	61.32
1.00	0.90	5000	442338.97	0.08	11.94	125.59
1.00	0.90	100000	8846779.38	0.05	20.37	600.05
10.00	0.90	100	22976.67	0.16	6.10	18.42
10.00	0.90	500	114883.36	0.12	8.59	40.78
10.00	0.90	1000	229766.73	0.09	10.73	54.61
10.00	0.90	5000	1148833.65	0.07	14.83	107.35
10.00	0.90	10000	2297667.30	0.06	17.17	143.60
10.00	0.90	100000	22976672.96	0.03	30.28	437.86
100.00	0.90	50	19832.38	0.20	5.10	3.28
100.00	0.90	100	39664.77	0.17	5.80	5.90
100.00	0.90	500	198323.85	0.12	8.08	14.61
100.00	0.90	1000	396647.70	0.11	9.36	20.65
100.00	0.90	5000	1983238.49	0.07	14.02	48.23
100.00	0.90	10000	3966476.99	0.06	16.66	68.22
100.00	0.90	100000	39664769.87	0.04	28.38	235.37

Continued on Next Page

Table A.8: Detailed results for cases $Ra_q \geq 50 * Ra_c$ for a free-slip bottom BC, $\gamma = 0.9$ and various values of Φ from 10^{-2} to ∞. Cases solved for $nz_{tot} = 128$ or 256 and $ny_{tot} = 2k\pi z_{tot}(R^- + 0.5)$ with $2k\pi$ the longitudinal aperture considered for each simulation (Here $k = 1$, $k = \frac{1}{5}$ or $k = \frac{1}{10}$). A refinement has been applied at the top $dresl_{R^+} = 2$ or 4 and the bottom $dresl_{R^-} = 2$ interfaces with 4 or 6 points in the boundary layers.

Φ	γ	Ra_q/Ra_c	Ra_q	T_{bot}	Nu	w_{top}
∞	0.90	100	43960.25	0.17	5.83	0
∞	0.90	500	219801.23	0.13	7.42	0
∞	0.90	1000	439602.47	0.12	8.66	0
∞	0.90	5000	2198012.34	0.08	12.36	0
∞	0.90	10000	4396024.67	0.07	14.55	0
∞	0.90	100000	43960246.72	0.04	24.80	0

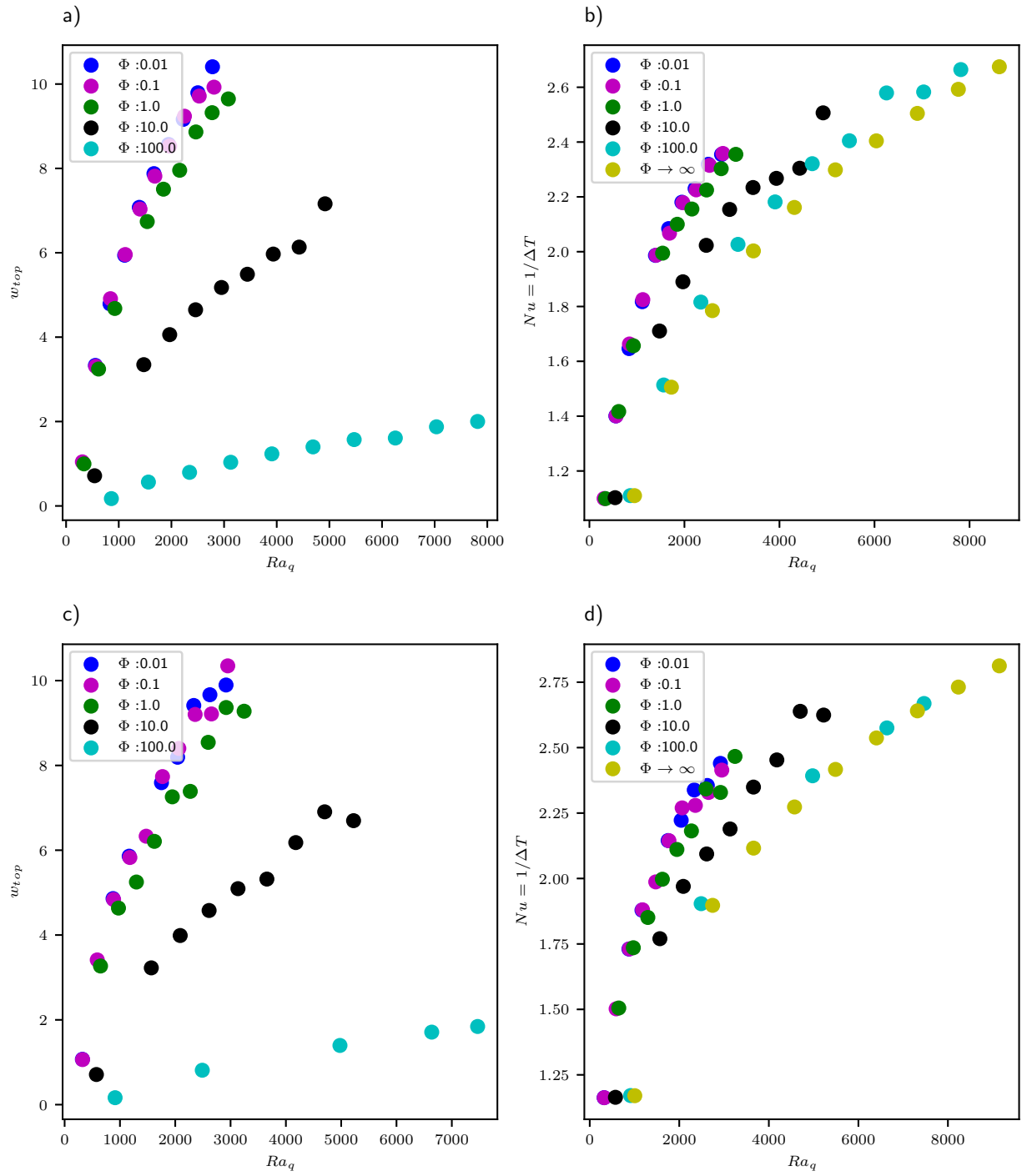

Figure A.1: Cases $Ra_q \sim Ra_c$ for a rigid bottom BC, (a)&(b) being for $\gamma = 0.95$ and (c)&(d) being for $\gamma = 0.9$. Left panels (a)&(c) show the dimensionless radial velocity at the top boundary of the HP ice layer, w_{top}. Right panels (b)&(d) show the dimensionless heat flux (Nusselt number). Both parameters in function of the Rayleigh Number Ra_q and for various values of Φ.

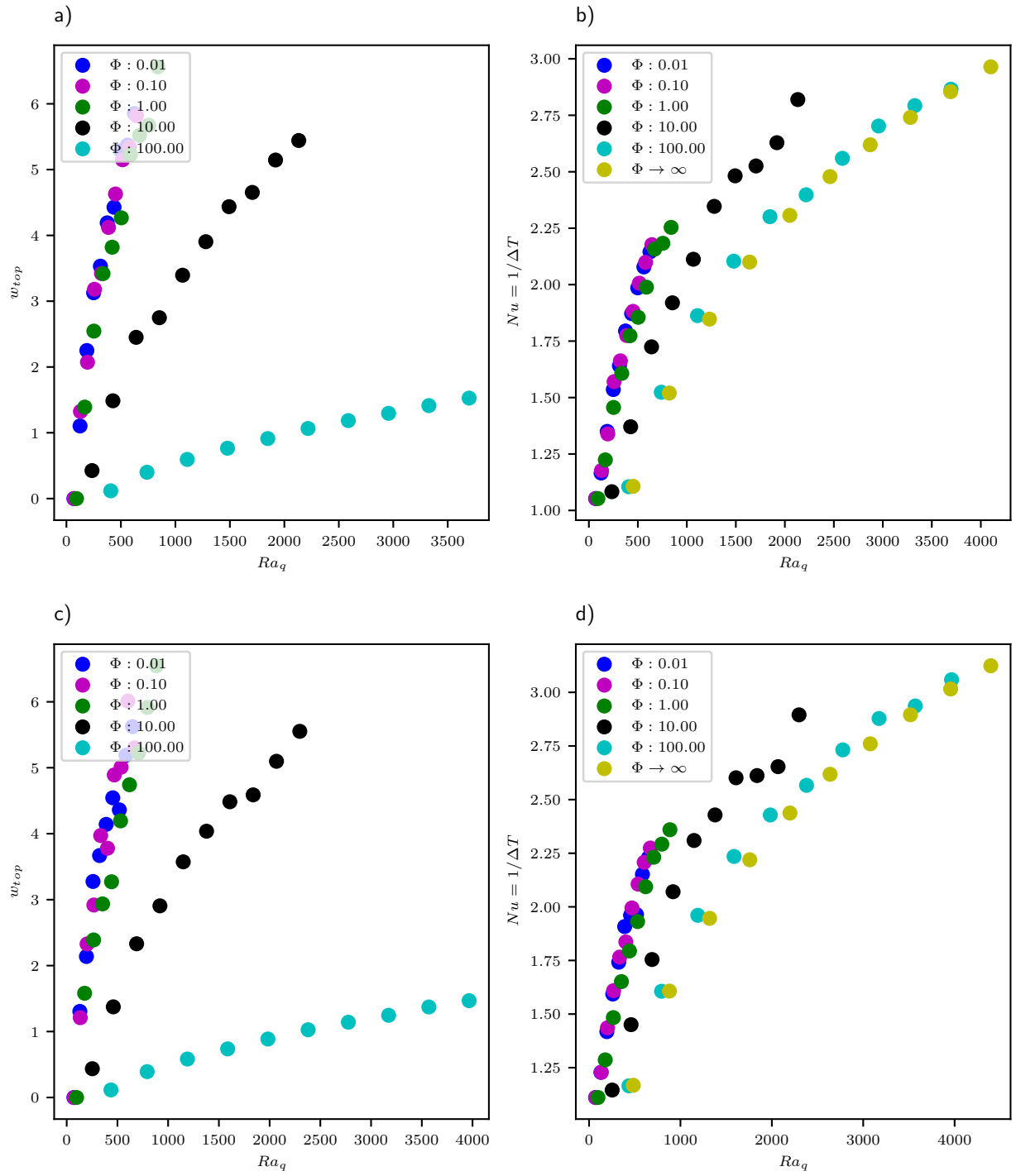

Figure A.2: Cases $Ra_q \sim Ra_c$ for a free-slip bottom BC, (a)&(b) being for $\gamma = 0.95$ and (c)&(d) being for $\gamma = 0.9$. Left panels (a)&(c) show the dimensionless radial velocity at the top boundary of the HP ice layer, w_{top}. Right panels (b)&(d) show the dimensionless heat flux (Nusselt number). Both parameters in function of the Rayleigh Number Ra_q and for various values of Φ.

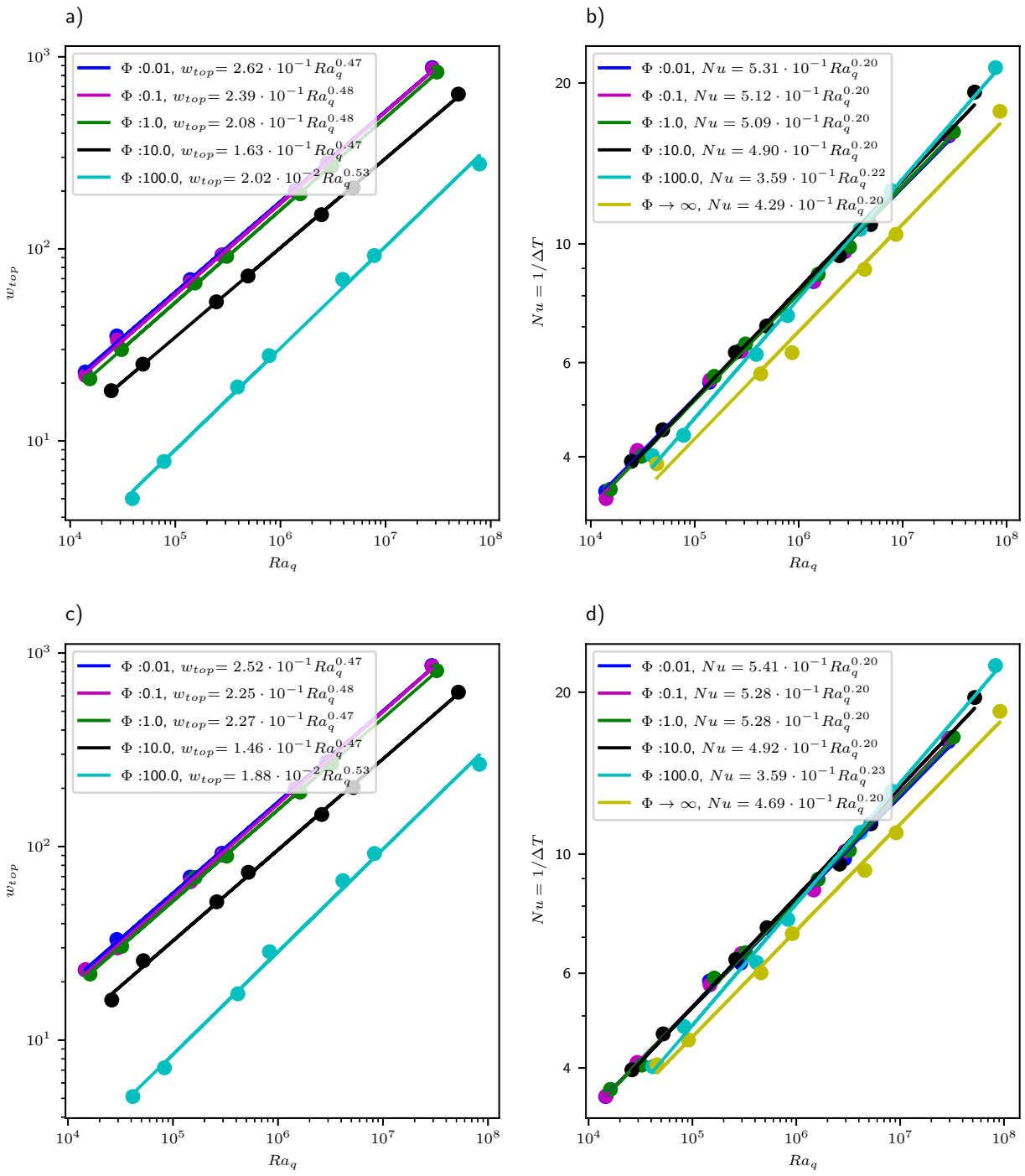

Figure A.3: Cases $Ra_q > 50 * Ra_c$ for a rigid bottom BC, (a)&(b) being for $\gamma = 0.95$ and (c)&(d) being for $\gamma = 0.9$. Left panels (a)&(c) show the dimensionless radial velocity at the top boundary of the HP ice layer. Right panels (b)&(d) show the dimensionless heat flux (Nusselt number). Both parameters in function of the Rayleigh Number Ra_q and for various values of Φ.

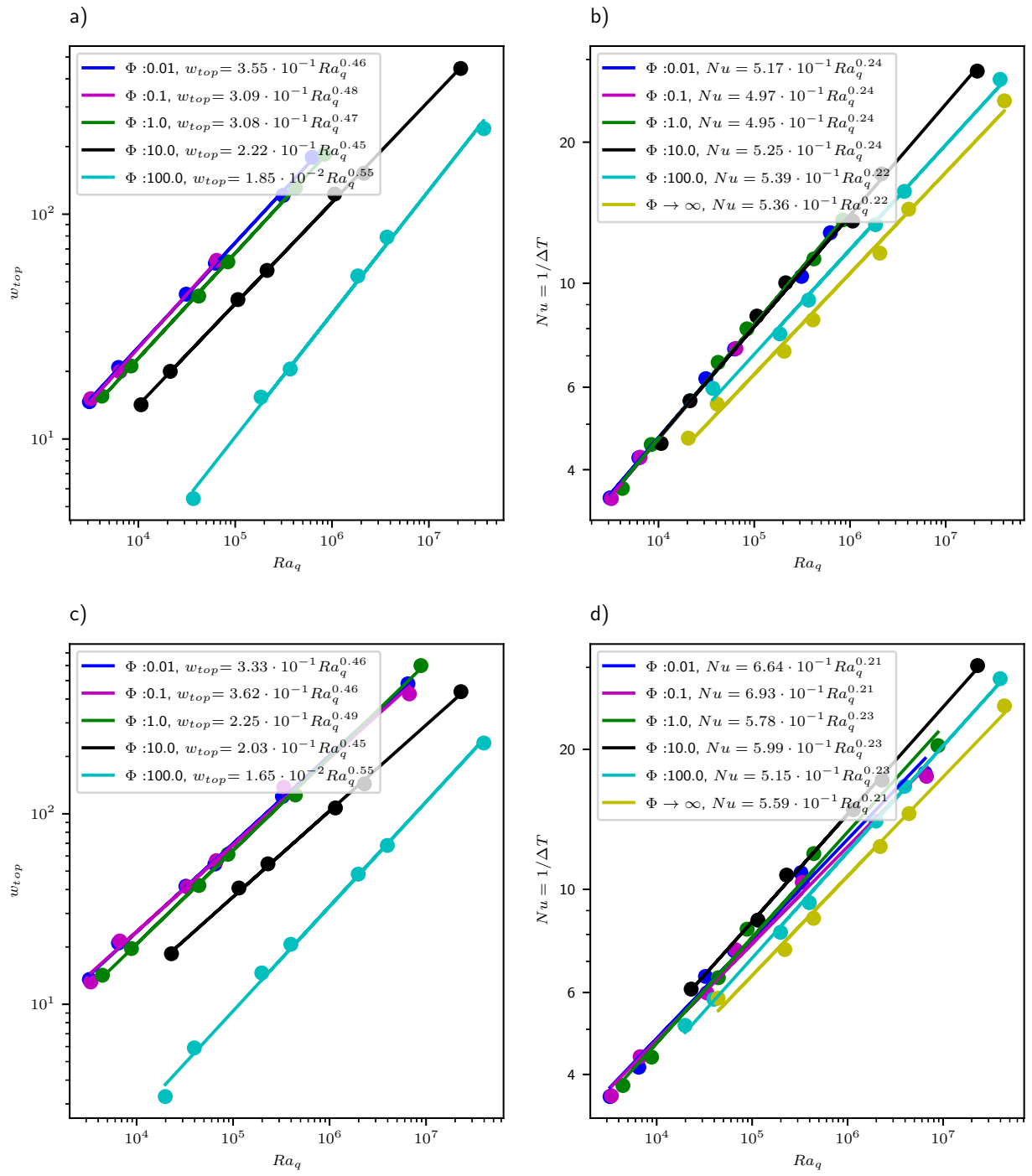

Figure A.4: Cases $Ra_q > 50 * Ra_c$ for a free-slip bottom BC, (a)&(b) being for $\gamma = 0.95$ and (c)&(d) being for $\gamma = 0.9$. Left panels (a)&(c) show the dimensionless radial velocity at the top boundary of the HP ice layer. Right panels (b)&(d) show the dimensionless heat flux (Nusselt number). Both parameters in function of the Rayleigh Number Ra_q and for various values of Φ.

BIBLIOGRAPHY

R. Agrusta, A. Morison, S. Labrosse, R. Deguen, T. Alboussière, P. J. Tackley, and F. Dubuffet. Mantle convection interacting with magma oceans. *Geophys. J. Int.*, 220(3):1878–1892, 2020. doi: 10.1093/gji/ggz549.

F. Albarède. Time-dependent models of U–Th–He and K–Ar evolution and the layering of mantle convection. *Chem. Geol.*, 145(3-4):413–429, 1998. doi: 10.1016/S0009-2541(97)00152-6.

R.-M. Baland, G. Tobie, A. Lefèvre, and T. Van Hoolst. Titan's internal structure inferred from its gravity field, shape, and rotation state. *Icarus*, 237:29–41, 2014. doi: 10.1016/j.icarus.2014.04.007.

G.I. Barenblatt. *Scaling, Self-Similarity, and Intermediate Asymptotics*. Cambridge University Press, Cambridge, 1996.

J.W. Barnes, E.P. Turtle, M.G. Trainer, R.D. Lorenz, S.M. MacKenzie, W.B. Brinckerhoff, M.L. Cable, C.M. Ernst, C. Freissinet, K.P. Hand, A.G. Hayes, S.M. Hörst, J.R. Johnson, E. Karkoschka, D.J. Lawrence, A. Le Gall, J.M. Lora, C.P. McKay, R.S. Miller, S.L. Murchie, C.D. Neish, C.E. Newman, J. Núñez, M.P. Panning, A.M. Parsons, P.N. Peplowski, L.C. Quick, J. Radebaugh, S.C.R. Rafkin, H. Shiraishi, J.M. Soderblom, K.S. Sotzen, A.M. Stickle, E.R. Stofan, C. Szopa, T. Tokano, T. Wagner, C. Wilson, R.A. Yingst, K. Zacny, and S.C. Stähler. Science Goals and Objectives for the Dragonfly Titan Rotorcraft Relocatable Lander. *Planet. Sci. J.*, 2(4):130, 2021. doi: 10.3847/PSJ/abfdcf.

T. W. Becker, J. B. Kellogg, and R. J. O'Connell. Thermal constraints on the survival of primitive blobs in the lower mantle. *Earth Planet. Sci. Lett.*, 171(3):351–365, 1999. doi: 10.1016/S0012-821X(99)00160-0.

M.T. Bland, A.P. Showman, and G. Tobie. The orbital–thermal evolution and global expansion of Ganymede. *Icarus*, 200(1):207–221, 2009. doi: 10.1016/j.icarus.2008.11.016.

D.P. Bolrão, M.D. Ballmer, A. Morison, A.B. Rozel, P. Sanan, S. Labrosse, and P.J. Tackley. Timescales of chemical equilibrium between the convecting solid mantle and over- and underlying magma oceans. *Solid Earth*, 12(2):421–437, 2021. doi: 10.5194/se-12-421-2021.

M. Bouffard, S. Labrosse, G. Choblet, A. Fournier, J. Aubert, and P.J. Tackley. A particle-in-cell method for studying double-diffusive convection in the liquid layers of planetary interiors. *J. Comput. Phys.*, 346:552–571, 2017. doi: 10.1016/j.jcp.2017.06.028.

P. W. Bridgman. Water, in the liquid and five solid forms, under pressure. *Proc. Amer. Acad. Arts Sci.*, 47:441–558, 1912. doi: 10.2307/20022754.

P. W. Bridgman. The phase diagram of water to 45,000 kg/cm^2. *J. Chem. Phys.*, 5:964–966, 1937. doi: 10.1063/1.1749971.

C. Béghin, O. Randriamboarison, M. Hamelin, E. Karkoschka, C. Sotin, R.C. Whitten, J.-J. Berthelier, R. Grard, and F. Simões. Analytic theory of Titan's Schumann resonance: Constraints on ionospheric conductivity and buried water ocean. *Icarus*, 218(2):1028–1042, 2012. doi: 10.1016/j.icarus.2012.02.005.

J. C. Castillo-Rogez, M. M. Daswani, C. R. Glein, S. D. Vance, and C. J. Cochrane. Contribution of Non-Water Ices to Salinity and Electrical Conductivity in Ocean Worlds. *Geophys. Res. Lett.*, 49(16), 2022. doi: 10.1029/2021GL097256.

S. Chandrasekhar. *Hydrodynamic and hydromagnetic stability*. Oxford university press, 1961.

G. Choblet, G. Tobie, C. Sotin, K. Kalousová, and O. Grasset. Heat transport in the high-pressure ice mantle of large icy moons. *Icarus*, 285:252–262, 2017. doi: 10.1016/j.icarus.2016.12.002.

C.S. Cockell, T. Bush, C. Bryce, S. Direito, M. Fox-Powell, J.P. Harrison, H. Lammer, H. Landenmark, J. Martin-Torres, N. Nicholson, L. Noack, J. O'Malley-James, S.J. Payler, A. Rushby, T. Samuels, P. Schwendner, J. Wadsworth, and M.P. Zorzano. Habitability: A Review. *Astrobiology*, 16(1):89–117, 2016. doi: 10.1089/ast.2015.1295.

N. Coltice and Y. Ricard. Geochemical observations and one layer mantle convection. *Earth Planet. Sci. Lett.*, 174(1-2):125–137, 1999. doi: 10.1016/S0012-821X(99)00258-7.

A. Davaille. Simultaneous generation of hotspots and superswells by convection in a heterogeneous planetary mantle. *Nature*, 402(6763):756–760, 1999. doi: 10.1038/45461.

R. Deguen. Thermal convection in a spherical shell with melting/freezing at either or both of its boundaries. *J. Earth Sci.*, 24(5):669–682, 2013. doi: 10.1007/s12583-013-0364-8.

R. Deguen, T. Alboussière, and P. Cardin. Thermal convection in Earth's inner core with phase change at its boundary. *Geophys. J. Int.*, 194(3):1310–1334, 2013. doi: 10.1093/gji/ggt202.

A.J. Friedson and D.J. Stevenson. Viscosity of rock-ice mixtures and applications to the evolution of icy satellites. *Icarus*, 56(1):1–14, 1983. doi: 10.1016/0019-1035(83)90124-0.

T. Gastine, J. Wicht, and J. Aubert. Scaling regimes in spherical shell rotating convection. *J. Fluid Mech.*, 808:690–732, 2016. doi: 10.1017/jfm.2016.659. Publisher: Cambridge University Press.

O. Grasset, M.K. Dougherty, A. Coustenis, E.J. Bunce, C. Erd, D. Titov, M. Blanc, A. Coates, P. Drossart, L.N. Fletcher, H. Hussmann, R. Jaumann, N. Krupp, J.-P. Lebreton, O. Prieto-Ballesteros, P. Tortora, F. Tosi, and T. Van Hoolst. JUpiter ICy moons Explorer (JUICE): An ESA mission to orbit Ganymede and to characterise the Jupiter system. *Planet. Spa. Sci.*, 78:1–21, 2013. doi: 10.1016/j.pss.2012.12.002.

J.-A. Hernandez, R. Caracas, and S. Labrosse. Stability of high-temperature salty ice suggests electrolyte permeability in water-rich exoplanet icy mantles. *Nature Commun.*, 13 (1):3303, 2022. doi: 10.1038/s41467-022-30796-5.

J.W. Hernlund and P.J. Tackley. Modeling mantle convection in the spherical annulus. *Phys. Earth Planet. Inter.*, 171:48–54, 2008. doi: 10.1016/j.pepi.2008.07.037.

A. W. Hofmann. Mantle geochemistry: the message from oceanic volcanism. *Nature*, 385 (6613):219–229, 1997. doi: 10.1038/385219a0.

L. N. Howard. Convection at high Rayleigh number. In H. Gortler, editor, *Proceedings of the Eleventh International Congress of Applied Mechanics*, pages 1109–1115, New York, 1964. Springer-Verlag.

H Hussmann, C. Sotin, and J.I. Lunine. 10.18 - Interiors and Evolution of Icy Satellites. *Treatise on Geophys.*, 10:605–635, 2015. doi: 10.1016/B978-0-444-53802-4.00178-0.

L. Iess, N.J. Rappaport, R.A. Jacobson, P. Racioppa, D.J. Stevenson, P. Tortora, J.W. Armstrong, and S.W. Asmar. Gravity Field, Shape, and Moment of Inertia of Titan. *Science*, 327(5971):1367–1369, 2010. doi: 10.1126/science.1182583.

L. Iess, R.A. Jacobson, M. Ducci, D.J. Stevenson, J.I. Lunine, J.W. Armstrong, S.W. Asmar, P. Racioppa, N.J. Rappaport, and P. Tortora. The Tides of Titan. *Science*, 337(6093): 457–459, 2012. doi: 10.1126/science.1219631.

B. Journaux, I. Daniel, R. Caracas, G. Montagnac, and H. Cardon. Influence of NaCl on ice VI and ice VII melting curves up to 6GPa, implications for large icy moons. *Icarus*, 226 (1):355–363, 2013. doi: 10.1016/j.icarus.2013.05.039.

B. Journaux, I. Daniel, S. Petitgirard, H. Cardon, J.-P. Perrillat, R. Caracas, and M. Mezouar. Salt partitioning between water and high-pressure ices. implication for the dynamics and habitability of icy moons and water-rich planetary bodies. *Earth Planet. Sci. Lett.*, 463:36–47, 2017. doi: 10.1016/j.epsl.2017.01.017.

K. Kalousová and C. Sotin. Melting in High-Pressure Ice Layers of Large Ocean Worlds—Implications for Volatiles Transport. *Geophys. Res. Lett.*, 45:8096–8103, 2018. doi: 10.1029/2018GL078889.

K. Kalousová and C. Sotin. Dynamics of Titan's high-pressure ice layer. *Earth Planet. Sci. Lett.*, 545:116416–116416, 2020. doi: 10.1016/j.epsl.2020.116416.

K. Kalousová, C. Sotin, G. Choblet, G. Tobie, and O. Grasset. Two-phase convection in Ganymede's high-pressure ice layer — Implications for its geological evolution. *Icarus*, 299:133–147, 2018. doi: 10.1016/j.icarus.2017.07.018.

L. H. Kellogg, B. H. Hager, and R. D. Van Der Hilst. Compositional Stratification in the Deep Mantle. *Science*, 283(5409):1881–1884, 1999. doi: 10.1126/science.283.5409.1881.

M. G. Kivelson, K. K. Khurana, C. T. Russell, R. J. Walker, J. Warnecke, F. V. Coroniti, C. Polanskey, D. J. Southwood, and G. Schubert. Discovery of Ganymede's magnetic field by the Galileo spacecraft. *Nature*, 384(6609):537–541, 1996. doi: 10.1038/384537a0.

M.G. Kivelson, K.K. Khurana, C.T. Russell, R.J. Walker, P.J. Coleman, F.V. Coroniti, J. Green, S. Joy, R.L. McPherron, C. Polanskey, D.J. Southwood, L. Bennett, J. Warnecke, and D.E. Huddleston. Galileo at Jupiter: Changing states of the magnetosphere and first looks at Io and Ganymede. *Adv. Space Res.*, 20(2):193–204, 1997. doi: 10.1016/S0273-1177(97)00533-4.

M.G. Kivelson, K.K. Khurana, C.T. Russell, M. Volwerk, R.J. Walker, and C. Zimmer. Galileo Magnetometer Measurements: A Stronger Case for a Subsurface Ocean at Europa. *Science*, 289(5483):1340–1343, 2000. doi: 10.1126/science.289.5483.1340.

M.G. Kivelson, K.K. Khurana, and M. Volwerk. The Permanent and Inductive Magnetic Moments of Ganymede. *Icarus*, 157(2):507–522, 2002. doi: 10.1006/icar.2002.6834.

S. Labrosse, A. Morison, R. Deguen, and T. Alboussière. Rayleigh–Bénard convection in a creeping solid with melting and freezing at either or both its horizontal boundaries. *J. Fluid Mech.*, 846:5–36, 2018. doi: 10.1017/jfm.2018.258.

H. Lammer. *Origin and Evolution of Planetary Atmospheres - Implications for Habitability.* Springer, 2013. ISBN 9781461459170.

M. Le Bars and A. Davaille. Large interface deformation in two-layer thermal convection of miscible viscous fluids. *Journal of Fluid Mechanics*, 499:75–110, 2004. doi: 10.1017/S0022112003006931.

L. Lebec, S. Labrosse, A. Morison, and P.J. Tackley. Scaling of convection in high-pressure ice layers of large icy moons and implications for habitability. *Icarus*, page 115494, 2023. doi: https://doi.org/10.1016/j.icarus.2023.115494.

W. V. R. Malkus. The heat transport and spectrum of thermal turbulence. *Proc. Roy. Soc. A*, 225:196–212, 1954.

W.B. McKinnon. Effect of Enceladus's rapid synchronous spin on interpretation of Cassini gravity: Enceladus: global ocean, thick ice shell. *Geophys. Res. Lett.*, 42(7):2137–2143, 2015. doi: 10.1002/2015GL063384.

G. Mitri, R. Meriggiola, A. Hayes, A. Lefevre, G. Tobie, A. Genova, J.I. Lunine, and H. Zebker. Shape, topography, gravity anomalies and tidal deformation of Titan. *Icarus*, 236: 169–177, 2014. doi: 10.1016/j.icarus.2014.03.018.

M. Monnereau and F. Dubuffet. Is Io's mantle really molten. *Icarus*, 158(2):450–459, 2002. doi: 10.1006/icar.2002.6868.

A. Morison. *Convection in the primitive mantle in interaction with global magma oceans.* PhD thesis, Université de Lyon - ENS de Lyon, 2020. URL `http://www.theses.fr/2019LYSEN061/document`.

A. Morison, S. Labrosse, R. Deguen, and T. Alboussière. Timescale of overturn in a magma ocean cumulate. *Earth Planet. Sci. Lett.*, 516:25–36, 2019. doi: 10.1016/J.EPSL.2019.03.037.

L. Noack, D. Höning, A. Rivoldini, C. Heistracher, N. Zimov, B. Journaux, H. Lammer, T. Van Hoolst, and J. H. Bredehöft. Water-rich planets: How habitable is a water layer deeper than on Earth? *Icarus*, 277:215–236, 2016. doi: 10.1016/J.ICARUS.2016.05.009.

R. Pappalardo, T. Becker, D. Blaney, D. Blankenship, J. Burch, P. Christensen, K. Craft, I. Daubar, M. Gudipati, A. Hayes, S. Howell, S. Kempf, M. Kivelson, R. Klima, H. Korth, E. Mazarico, B. Paczkowski, C. Phillips, J. Rathbun, T. Ray, K. Retherford, C. Richey, J. Roberts, A. Rymer, B. Schmidt, D. Senske, E. Shock, E. Turtle, and J. Westlake. The Europa Clipper Mission: Understanding Icy World Habitability and Blazing a Path for Future Exploration. *Bulletin of the AAS*, 53(4), 2021. doi: 10.3847/25c2cfeb.08489926.

A. Picard and I. Daniel. Pressure as an environmental parameter for microbial life — A review. *Biophys. Chem*, 183:30–41, 2013. doi: 10.1016/J.BPC.2013.06.019.

F. Postberg, S. Kempf, J. Schmidt, N. Brilliantov, A. Beinsen, B. Abel, U. Buck, and R. Srama. Sodium salts in E-ring ice grains from an ocean below the surface of Enceladus. *Nature*, 459(7250):1098–1101, 2009. doi: 10.1038/nature08046.

M. A. Ravine, C. J. Hansen, G. C. Collins, P. M. Schenk, M. A. Caplinger, L. Lipkaman Vittling, D. J. Krysak, R. P. Zimdar, J. B. Garvin, and S. J. Bolton. Ganymede Observations by JunoCam on Juno Perijove 34. *Geophys. Res. Lett.*, 49(23), 2022. doi: 10.1029/2022GL099211.

B. Reynard and C. Sotin. Carbon-rich icy moons and dwarf planets. *Earth Planet. Sci. Lett.*, 612:118172, 2023. doi: 10.1016/j.epsl.2023.118172.

Y. Ricard. 7.02 - physics of mantle convection. In G. Schubert, editor, *Treatise on Geophys.*, pages 23–71. Elsevier, Oxford, 2 edition, 2015. ISBN 978-0-444-53803-1. doi: 10.1016/B978-0-444-53802-4.00127-5.

Y. Ricard, S. Labrosse, and F. Dubuffet. Lifting the cover of the cauldron: Convection in hot planets. *Geochem. Geophys. Geosyst.*, 15(12):4617–4630, 2014. doi: 10.1002/2014GC005556.

G. O. Roberts. Fast viscous bénard convection. *Geophys. Astrophys. Fluid Dyn*, 12(1): 235–272, 1979. doi: 10.1080/03091927908242692.

J. Saur, S. Duling, L. Roth, X. Jia, D.F. Strobel, P.D. Feldman, U.R. Christensen, K.D. Retherford, M.A. McGrath, F. Musacchio, A. Wennmacher, F.M. Neubauer, S. Simon, and O. Hartkorn. The search for a subsurface ocean in Ganymede with Hubble Space Telescope observations of its auroral ovals. *J. Geophys. Res.*, 120(3):1715–1737, 2015. doi: 10.1002/2014JA020778.

K.M. Soderlund. Ocean dynamics of outer solar system satellites. *Geophys. Res. Lett.*, 46 (15):8700–8710, 2019. doi: 10.1029/2018GL081880.

K.M. Soderlund, K. Kalousová, J.J. Buffo, C.R. Glein, J.C. Goodman, G. Mitri, G.W. Patterson, F. Postberg, M. Rovira-Navarro, T. Rückriemen, J. Saur, B.E. Schmidt, C. Sotin, T. Spohn, G. Tobie, T. Van Hoolst, S.D. Vance, and B. Vermeersen. Ice-Ocean Exchange Processes in the Jovian and Saturnian Satellites. *Space Sci. Rev.*, 216(5):80, 2020. doi: 10.1007/s11214-020-00706-6.

C. Sotin and S. Labrosse. Three-dimensional thermal convection in an iso-viscous, infinite Prandtl number fluid heated from within and from below: applications to the transfer of heat through planetary mantles. *Phys. Earth Planet. Inter.*, 112(3-4):171–190, 1999. doi: 10.1016/S0031-9201(99)00004-7.

C. Sotin and G. Tobie. Internal structure and dynamics of the large icy satellites. *Comptes Rendus Physique*, 5(7):769–780, 2004. doi: 10.1016/j.crhy.2004.08.001.

C. Sotin, K. Kalousová, and G. Tobie. Titan's Interior Structure and Dynamics After the Cassini-Huygens Mission. *Annual Review of Earth and Planet. Sci.*, 49(1):579–607, 2021. doi: 10.1146/annurev-earth-072920-052847.

P. J. Tackley. Three-dimensional simulations of mantle convection with a thermo-chemical basal boundary layer: D"? In M. Gurnis, M. E. Wysession, E. Knittle, and B. A. Buffett, editors, *The Core-Mantle Boundary Region*, volume 28, pages 231–253. American Geophysical Union, Washington, D. C., 1998. ISBN 978-0-87590-530-3. doi: 10.1029/GD028p0231.

P. J. Tackley. Mantle Convection and Plate Tectonics: Toward an Integrated Physical and Chemical Theory. *Science*, 288(5473):2002–2007, 2000. doi: 10.1126/science.288.5473.2002.

P.J. Tackley. Modelling compressible mantle convection with large viscosity contrasts in a three-dimensional spherical shell using the yin-yang grid. *Phys. Earth Planet. Inter.*, 171 (1):7–18, 2008. doi: 10.1016/j.pepi.2008.08.005.

P.J. Tackley and S.D. King. Testing the tracer ratio method for modeling active compositional fields in mantle convection simulations. *Geochem. Geophys. Geosyst.*, 4(4), 2003. doi: 10.1029/2001GC000214.

V. Tchijov. Heat capacity of high-pressure ice polymorphs. *J. Phys. Chem. Solids*, 65(5): 851–854, 2004. doi: 10.1016/j.jpcs.2003.08.019.

G. Tobie, J.I. Lunine, J. Monteux, O. Mousis, and F. Nimmo. The Origin and Evolution of Titan. 2014.

S.D. Vance, M.P. Panning, S. Stähler, F. Cammarano, B.G. Bills, G. Tobie, S. Kamata, S. Kedar, C. Sotin, W.T. Pike, R. Lorenz, H.-H. Huang, J. M. Jackson, and B. Banerdt. Geophysical Investigations of Habitability in Ice-Covered Ocean Worlds. *J. Geophys. Res. Planets*, 123(1):180–205, 2018. doi: 10.1002/2017JE005341.

J.T. Wasson and G.W. Kallemeyn. Compositions of chondrites. *Phil. Trans. R. Soc. Lond. A*, 325:535–544, 1988. doi: 10.1098/rsta.1988.0066.

M. Y. Zolotov and J. S. Kargel. On the chemical composition of europa's icy shell, ocean, and underlying rocks. *Tucson, AZ: University of Arizona Press*, 431:431 – 458, 2009. doi: 10.2307/j.ctt1xp3wdw.

O. Čadek, G. Tobie, T. Van Hoolst, M. Massé, G. Choblet, A. Lefèvre, G. Mitri, R.-M. Baland, M. Běhounková, O. Bourgeois, and A. Trinh. Enceladus's internal ocean and ice shell constrained from Cassini gravity, shape, and libration data. *Geophys. Res. Lett.*, 43 (11):5653–5660, 2016. doi: 10.1002/2016GL068634.